Verständis und Vorhersage von Oberflächen- und Grenzflächeneigenschaften komplexer Übergangsmetalloxide mittels Dichtefunktionaltheorie-Rechnungen

Dissertation an der Fakultät für Geowissenschaften der
Ludwig-Maximilians-Universität München
zur Erlangung des Grades

DOCTOR RERUM NATURALIUM

vorgelegt am
23. 10. 2012
von
Katrin Maria Otte

1. Gutachter	Priv.-Doz. Dr. Rossitza Pentcheva
2. Gutachter	Prof. Dr. Wolfgang W. Schmahl
Tag der Disputation:	22.04.2013

Contents

Synopsis

Surfaces and interfaces of transition metal oxides exhibit a variety of intriguing phenomena. Owing to their unique physical and chemical properties, they find application as catalysts, magnetic data storage materials, sensors, and more recently in the field of spintronics and electronics. The vast variety of structures of transition metal oxides offer outstanding opportunities to explore novel phenomena.

For gaining a fundamental understanding of their properties, density functional theory (DFT) is a powerful tool. But the complex structures and the description of electronic correlations represent a challenge to this method. However, supercomputers are capable to perform electronic structure calculations for these large and computationally demanding systems.

In this work two different classes of materials are addressed based on DFT calculations: the iron oxyhydroxide (FeOOH) polymorphs and the perovskites $LaAlO_3$ and $SrTiO_3$. At first the properties of bulk FeOOH are discussed, followed by the study of water and arsenate adsorption on the goethite(101), the akaganeite(100), and the lepidocrocite(001) surfaces. In the second part interface effects between thin films of the perovskites $LaAlO_3$ and $SrTiO_3$ are explored.

The FeOOH polymorphs

Among the transition metal oxides, iron oxides represent an important class of materials. They are widely distributed minerals in aquifers, in sediments, and in the earth's crust. [1] The high-pressure behavior of hydrous iron bearing minerals is important for understanding processes in the earth's crust and upper mantle. In this respect the iron oxyhydroxides, FeOOH, can be regarded as a model system for achieving a better understanding of the role of hydrogen bonding at high pressures.[2, 3]

The FeOOH polymorphs are structurally related to hematite, Fe_2O_3, replacing one half of the oxygen by hydroxyl groups. Their structures differ in the linkage of bands of $Fe(O,OH)_6$ octahedra as presented in Fig. 0.1.

Arsenic contamination of ground waters and mine wastes represents a significant environmental hazard. [4] An efficient method to control arsenic transport and distribution in aqueous environments is the binding at water/mineral interfaces. In the form of nanoparticles the FeOOH polymorphs possess a high specific surface area [1] and show high adsorption affinities for aqueous solutes [5, 6]. These properties render them as attractive adsorbants for toxic anions [1, 7, 8], *e.g.* arsenic complexes. Therefore, the FeOOH polymorphs play an important role in the sorption and retention of contaminants in a series of environmental processes and receive attention as potential filter material for water treatment purposes. [4, 9, 10]

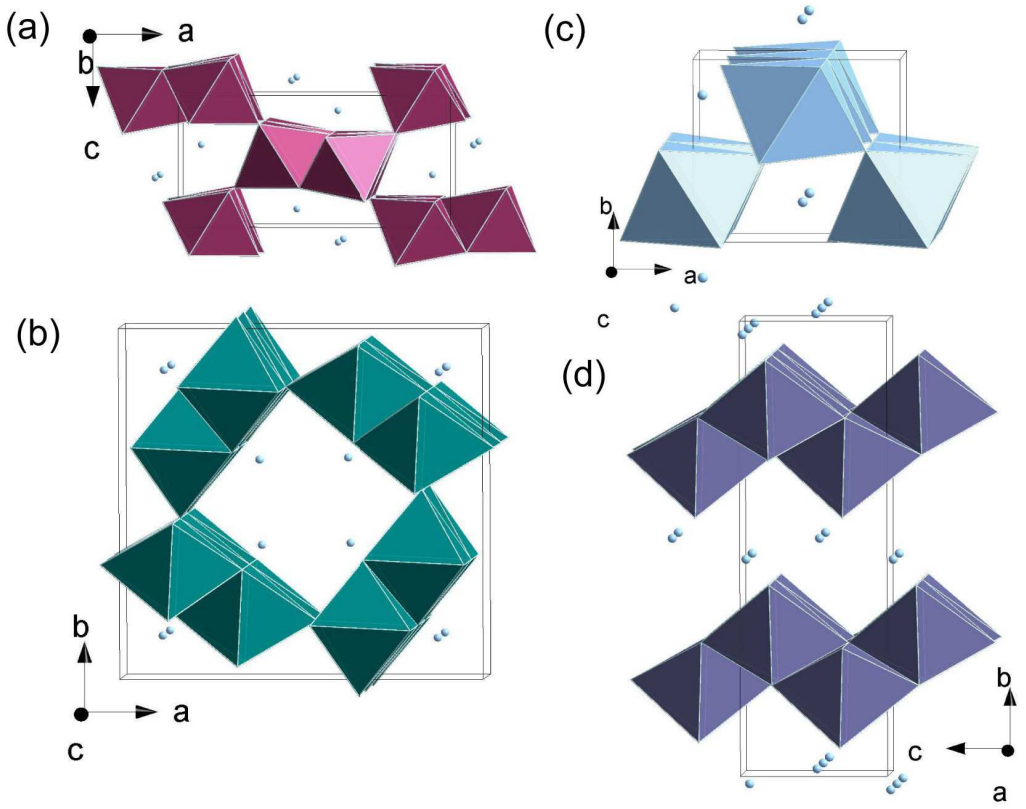

Figure 0.1: The structures of the FeOOH polymorphs consist of $Fe(O,OH)_6$ octahedra. a) Goethite (α-FeOOH) with 2×1 channels, b) akaganeite (β-FeOOH) with 1×1 and large 2×2 tunnels and c) the $hp(\epsilon)$ phase composed of corner sharing single bands of octahedra in a dense 1×1 arrangement with interstitial hydrogen have framework structures. In contrast, d) lepidocrocite (γ-FeOOH) consists of zigzag-sheets of edge sharing double bands connected to each other via hydrogen bonds.

Structural and electronic transitions in bulk FeOOH In **Manuscript 1** the results on bulk properties of the FeOOH polymorphs are presented. Unlike their well realized variety of structures, their energetic relations are poorly known. In this work the energetic stability of the four FeOOH polymorphs goethite (α-FeOOH), akaganeite(β-FeOOH), lepidocrocite (γ-FeOOH), and the high pressure phase ($hp(\epsilon)$-FeOOH). Furthermore, pressure induced structural and electronic transitions were investigated using DFT calculations. The energy-volume curves obtained were used to extract the equilibrium volume, the equation of state, bulk moduli, and the relative stability of the FeOOH phases. Additionally, the pressure dependence of the bond lengths are presented as well as the electronic properties, *i.e.* the density of states and the band gaps.

All FeOOH phases show antiferromagnetic (AFM) coupling between iron ions as ground state. Calculations performed within the GGA and GGA+U methods reveal that the inclusion of an on-site Coulomb repulsion term U is necessary to correctly describe the insulating behavior with band gaps of ∼2.0 eV close to the experimentally determined values [1]. Goethite (α-FeOOH) is identified as lowest energy phase at ambient conditions, consistent with calorimetric mearsurements [11]. The

following energetic relations between the phases were found in order of decreasing stability:

$$E_\alpha < E_\beta < E_{hp(\epsilon)} < E_\gamma$$

The results show that the framework structures of goethite (α-FeOOH), akaganeite (β-FeOOH), and the high pressure phase ($hp(\epsilon)$-FeOOH) are energetically favored compared to the sheet-like structured polymorph lepidocrocite (γ-FeOOH). The results presented here predict a transformation from the α phase to the high-pressure $hp(\epsilon)$ phase around 6–7 GPa as depicted in Fig. 0.2a).

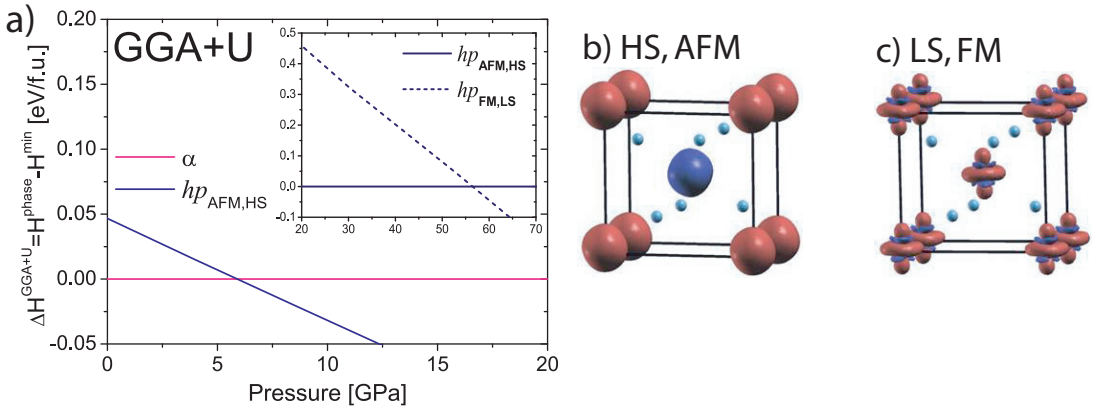

Figure 0.2: a) The enthalpy-pressure relation $\Delta H(p)$ for the different polymorphs within GGA+U. The results predict a structural transition at ∼7 GPa from α-FeOOH to $hp(\epsilon)$-FeOOH, followed by a spin transition within in the $hp(\epsilon)$ phase from HS to LS at 56 GPa shown in the inset of a). Δ **H**(p) <0 indicates phases that are more stable than goethite or $hp(\epsilon)_{\mathrm{AFM,HS}}$ for a given pressure. Furthermore, the spin-density distribution of $hp(\epsilon)$-FeOOH at 56.5 GPa is displayed for Fe^{3+} in b) HS, AFM and c) LS, FM state. Fe is octahedrally coordinated by oxygen (light blue/gray), the hydrogen positions are not shown.

This transition is experimentally supported by IR data [2]. Pernet et al. [12] synthesized $hp(\epsilon)$-FeOOH at pressures around 8 GPa. Furthermore, a boundary line between α and $hp(\epsilon)$ phase in the range between 6 and 7.5 GPa is reported by Voigt and Will [13] confirmed by x-ray diffraction (XRD) measurements [3]. The structural transformation is followed by a high-spin (HS) to low-spin (LS) transition in $hp(\epsilon)$-FeOOH accompanied by a switch to ferromagnetic (FM) coupling of the irons. GGA+U tends to stabilize the HS state and the spin crossover takes place at 56.6 GPa (Fig. 0.2a). The spin density distributions of Fe^{3+} at the spin transition pressure (GGA+U) in Fig. 0.2b) and c) show the change in orbital occupation. While in the HS state, Fig. 0.2b), all Fe 3d orbitals are singly occupied, leading to a spherical spin density distribution, the LS state, Fig. 0.2c), exhibits a clear t_{2g} character with lobes pointing to the faces of the surrounding oxygen octahedron. Still, this transition pressure is much lower than values reported for other currently discussed iron bearing materials, e.g. magnesiowüstite [14]. This suggests that the presence of OH^- in the coordination shell of Fe^{3+} facilitates the spin crossover. One possible explanation may be the symmetry breaking caused by having both OH^-

and O^{2-} in the coordination polyhedron. If this is a general phenomenon, it may indicate an unanticipated connection between water content and the spin-transition pressure in the Earth's mantle.

Water adsorption at the most common FeOOH surfaces Prior to modeling the adsorption of contaminants, it is necessary to understand the geometric and electronic structures as well as the stability of the water/FeOOH interfaces at the atomic level. In **Manuscript 2** the most common surfaces of the FeOOH polymorphs, *i.e.* goethite(101), akaganeite(100), and lepidocrocite(010), and their interaction with water were studied. Both molecular and dissociative water adsorption were considered. The stability of different surface terminal groups (Fe, Fe-OH, Fe-OH_2) was investigated within the framework of *ab initio* thermodynamics [15]. As a result of the different orientation of surface octahedra, two distinct surface iron sites are exposed at goethite(101) and akaganeite(100): fivefold coordinated Fe1 and fourfold coordinated Fe2. The relaxed Fe/Fe termination for α-FeOOH(101) is displayed in Fig. 0.3. The zigzag layered polymorph lepidocrocite exposes only Fe2 sites at its (010) surface.

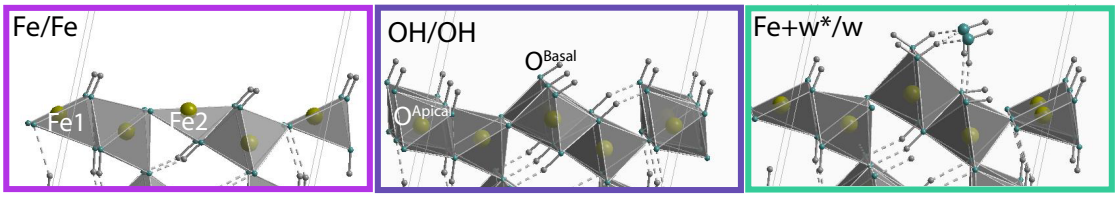

Figure 0.3: The relaxed surface structures of the stable terminations Fe/Fe, OH/OH, and Fe+w*/w of goethite(101). The adsorbed hydroxyl and aquo terminal groups are mononuclear coordinated to Fe1 and binuclear to Fe2. Upon relaxation, the aquo group preferentially physisobs at Fe1, denoted as w*, but chemisorbs at Fe2, w. The frames correspond to the color coding in the surface phase diagram of Fig. 0.4a).

Despite the different surface structures, the trends in surface stability of these polymorphs are remarkably similar. A main finding is that the coordination of surface iron strongly influences the surface reactivity as well as the binding mechanism of water. In particular, a strong preference is found for binuclear water adsorption at Fe2, thereby restoring the octahedron around Fe2. In contrast, water binds weaker to Fe1 with hydrogen instead of oxygen pointing towards the surface. The surface phase diagrams displayed in Fig. 0.4 obtained within the framework of *ab initio* thermodynamics reveal several stable terminations: iron terminations at oxygen and water poor conditions, water terminations at water rich and oxygen poor conditions, and a hydroxylated termination at ambient conditions. Different types of surface hydroxyl and aquo groups are identified according to their coordination at the FeOOH surfaces. The variation in protonation state can be directly related to changes in pH conditions.

Interestingly, the stability of the FeOOH surfaces at 298 K reveals a reverse order as compared to the bulk FeOOH polymorphs. These *ab initio* results are in

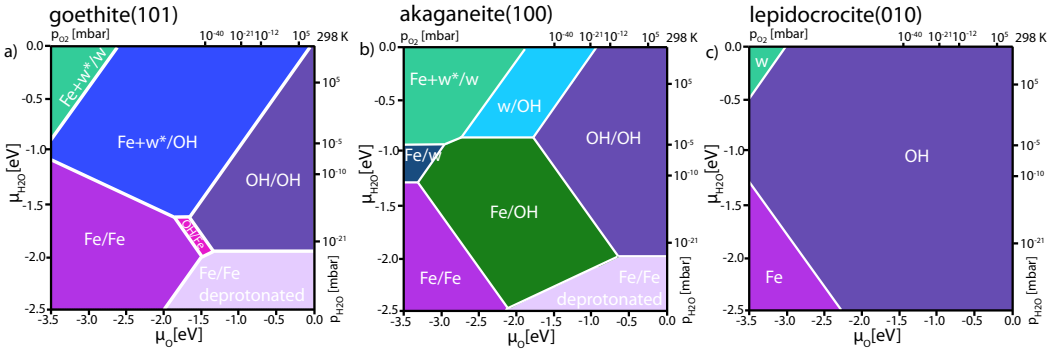

Figure 0.4: Stable surface terminations at a) goethite(101), b) akaganeite(100), and c) lepidocrocite(010) with respect to the chemical potentials of oxygen and water, μ_{O} and $\mu_{\mathrm{H_2O}}$. Additionally, μ_{O} and $\mu_{\mathrm{H_2O}}$ are converted into pressures at room temperature (298 K). With increasing oxygen concentration there is a transition from water terminations to hydroxylated surface terminations.

agreement with calorimetric measurements [5, 16, 17]:

$$E_{\gamma(010)} < E_{\beta(100)} < E_{\alpha(101)}$$

The results presented here show that the composition of the surface has a strong influence on the surface electronic and magnetic properties. In particular, iron and water terminated surfaces exhibit ferrous iron, *i.e.* Fe^{2+}, in the surface layer and a reduced band gap, while oxo-species lead to higher valent cations. However, the fully hydroxylated FeOOH surfaces with restored surface octahedra which are the stable surface configurations at standard conditions, show properties closest to bulk FeOOH where only ferric iron, *i.e.* Fe^{3+}, is present. Thus by varying the environmental pH conditions, namely the partial pressures of water and oxygen, the ferric/ferrous iron ratio at the FeOOH surfaces can be controlled.

Inner sphere Arsenate Adsorption at FeOOH surfaces Finally, the inner sphere arsenate adsorption at the FeOOH surfaces is addressed in **Manuscript 3**. It is well established that arsenic species form inner sphere complexes at hydrous iron oxide surfaces via ligand exchange. [18, 19, 20, 21, 22] However, the exact inner sphere bonding geometry of arsenate (mono- or bidentate) on the FeOOH surfaces is still a matter of ongoing debate.

Depending on the orientation of the surface octahedra, arsenate can bind either at the fivefold coordinated Fe1 and/or the fourfold coordinated Fe2 surface sites as schematically illustrated in Fig. 0.5. For mono- and bidentate adsorption it was further distinguished between the coordination of the adsorbate to the underlying iron, that can be either mono- or binuclear. In this study various arsenate adsorption geometries were considered. The results presented here show that the arsenate adsorption configuration depends critically on the local environment, in particular on the coordination of surface iron and the presence of surface functional groups,

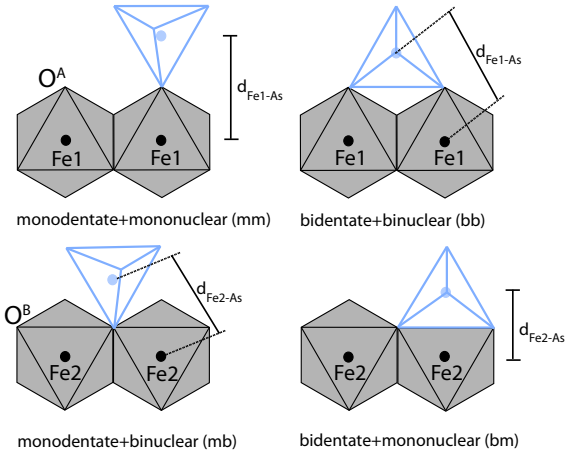

Figure 0.5: Schematic illustration of possible adsorption geometries of the AsO_4 complex (blue/light grey tetrahedron) at the tip/apex and in the basal plane of edge sharing FeO_6 octahedra, depicted in gray. Fe and As are represented as black and blue dots located in the center of the respective polyhedron. O^A and O^B refer to the oxygen at the tip and in the basal plane of the octahedra, respectively. Mono- or bidentate specify the linkage between tetra- and octahedra via one or two oxygen, whereas mono- or binuclear indicate the coordination of As to one or two Fe atoms via oxygen.

e.g. hydroxyl (-OH) or aquo ($-OH_2$) groups.

In EXAFS (extended x-ray absorption fine structure) experiments [19, 23, 24, 25] extracted Fe–As distances are used to determine adsorption geometries through comparison to schematic models or related compounds [26, 27, 28]. However, the interpretation of the extracted Fe–As distances is not unambiguous. Distances of 3.50 to 3.60 Å are commonly associated with a monodentate coordination, whereas distances of 2.70 to 3.45 Å with a bidentate one. Accordingly, the Fe–As distance of ∼3.30 Å measured in EXAFS experiments indicates a predominantly bidentate binuclear adsorption geometry [8, 19, 29, 30]. The DFT optimized geometries render both Fe–As distances and Fe–O–As angles of the extended surfaces. The effect of protonation is investigated and the energetic ordering of different binding modes is compared taking into account different adsorption pathways: arsenate can bind either directly at different iron surface sites or alternatively via ligand exchange. Furthermore, the effect of the arsenate complex on the surface electronic properties is discussed.

Using *ab initio* thermodynamics, our calculations reveal the stability of monodentate adsorption configurations at ambient conditions. In Fig. 0.6 the surface phase diagram is depicted for goethite(101) together with the relaxed stable adsorption geometries. On goethite(101) a protonated monodentate mononuclear arsenate binds at Fe1 at ambient conditions. Such a configuration was considered in EXAFS studies by Waychunas et al. [19], Fendorf et al. [24], but the relaxed geometry shows a reduced Fe–As distance of 3.45 Å due to a strong Fe–O–As tilt, consistent with the model proposed by Loring et al. [31]. A protonated monodentate binuclear complex at Fe2 is favored at akaganeite(100) with $d_{\mathrm{Fe2–As}}$=3.29 Å and at lepidocrocite(010)

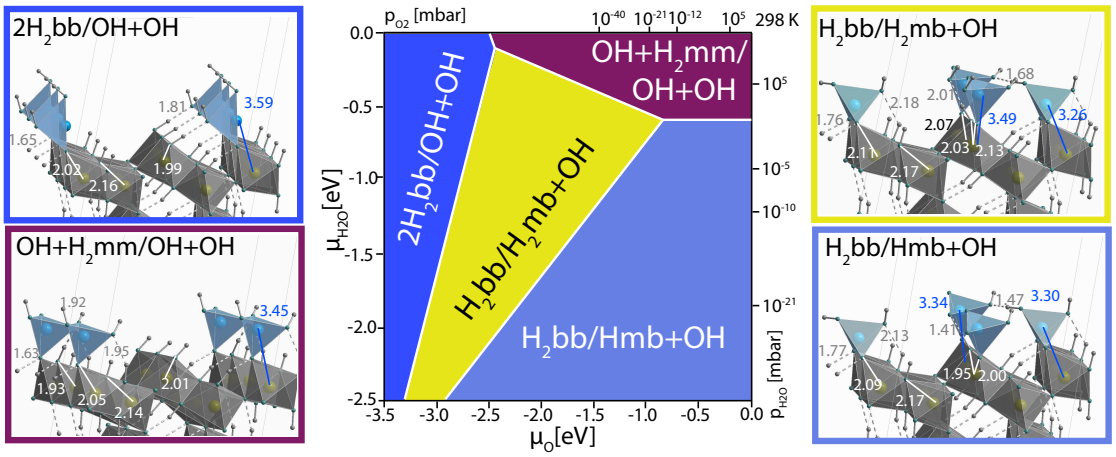

Figure 0.6: Side views of the relaxed structure of stable arsenate complexes at α-FeOOH(101). Relevant Fe–O/OH bond lengths are marked in white and hydrogen bonds are indicated by gray dashed lines. Additionally, the distances of As to the nearest and next nearest Fe ions are shown together with the corresponding Fe–O–As angle. The hydroxyl groups at the surfaces are coordinated either mononuclear to Fe1 (-O^{A}H) or binuclear to Fe2 (μ-O^{B}H) restoring the surface octahedra. The colors of the frames correspond to the color used in the surface phase diagram with stable surface terminations with respect to μ_O and μ_{H_2O} in the middle. In the top and right axis μ_O and μ_{H_2O} are converted into pressures for room temperature (298 K).

with $d_{Fe2–As}$=3.38 Å. With decreasing oxygen pressure a mixed configuration of a protonated bidentate binuclear complex at Fe1 and a monodentate binculear one at Fe2 is stabilized at goethite(101) and akaganeite(100). Here the Fe–As distances for bidenate binculear ($d_{Fe1–As}$=3.26-3.34 Å) and mondenate binuclear ($d_{Fe2–As}$=3.31-3.50 Å) adsorbed arsenate complexes are not distinguishable. Finally, at low oxygen pressures two protonated bidentate binuclear complexes at Fe1 and hydroxyl groups at Fe2 are stabilized which show remarkably long Fe1–As bond lengths of 3.55-3.59 Å due to adsorbate-adsorbate repulsion. On α-FeOOH(101) and β-FeOOH(100) there is no evidence for a bidentate mononuclear coordinated complex. However, it is stabilized at low oxygen pressure at lepidocrocite(010) with $d_{Fe1–As}$=3.10 Å. Formation of hydrogen bonds to surface hydroxyl and aquo groups as well as to neighboring adsorbates plays an important role in the stabilization of these complexes. The DFT results reveal that the protonation state of the complex, the coverage, and the presence of surface functional groups are the main factors that determine the bond lengths and to a much lesser extent the bonding configuration. This indicates that the Fe–As bond length is not a reliable criterion to identify the adsorption mode.

Concerning the electronic properties, the most stable adsorbate configurations at α-FeOOH(101) and β-FeOOH(100) exhibit ferric iron in the surface layer. Reduced magnetic moments, indicative of Fe^{2+}, are found underneath bidentate complexes or water molecules and lead to reduced band gaps and even a metallic state.

The explicit treatment of a solvation layer goes beyond the scope if this work, however, it may influence surface relaxation. Its influence on surface relaxation and bonding geometries needs to be explored in future work. Another interesting aspect

is the study of the binding mechanism of arsenate complexes in the wide channels of akaganeite. This might provide information for further applications of the iron oxyhydroxides as storage materials.

The n-type $LaAlO_3/SrTiO_3(001)$ Interface and Influence of an $SrTiO_3$ Overlayer

A further topic of this study are the interfaces of a different class of transition metal oxides: the perovskites $LaAlO_3$ and $SrTiO_3$. In the perovskite structure (general formula: ABO_3) the A and B subsites are occupied by ions in complementary oxidation states (A: +I, +II, +III and B: +V, +IV, +III). The interfaces contain alternating $AO\text{-}BO_2$ layers in the [001] direction. Upon variation of the valence state of both A and B subsites, a charge discontinuity arises naturally at the $AO\text{-}BO_2$ interfaces. This gives rise to technologically relevant phenomena which are highly requested in the electronic industry due to progressing miniaturization of devices.

$SrTiO_3$ is a II-IV perovskite and in the [001] direction it consists of alternating layers of charge neutral SrO and TiO_2, while the III-III perovskite $LaAlO_3$ is built up by positively charged LaO^+ and negatively charged AlO_2^- layers. $LaAlO_3$ grown on a TiO_2 terminated $SrTiO_3(001)$ leads to an n type interface due to charge mismatch as displayed in Fig. 0.7 a). In contrast, a p type interface is generated between an AlO_2^- layer and a SrO terminated $SrTiO_3(001)$ substrate.

At this interface between the two simple band insulators $LaAlO_3$ and $SrTiO_3$ Ohtomo and Hwang [32] discovered electrical conductivity. Later on, superconductivity [33], magnetism [34], and even their coexistence [35, 36, 37] have been reported. Thiel et al. [38] investigated the thickness dependence of N monolayers of $LaAlO_3$ deposited via pulsed laser deposition (PLD) on a $SrTiO_3(001)$ substrate. They observed a sharp transition from an insulating to a conducting state at a critical thickness of four $LaAlO_3$ monolayers. [38]. This has been confirmed by periodic density functional theory calculations [39] where the closing of the band gap is attributed to a quantum size effect in the polar $LaAlO_3$ film. In contrast to the sharp insulator-to-metal transition around four monolayers of $LaAlO_3$ on $SrTiO_3(001)$ [38, 39], the coupled $SrTiO_3/LaAlO_3/SrTiO_3(001)$ system shows a gradual change in the sheet resistance between two and six monolayers for $LaAlO_3$ films covered by a $SrTiO_3$ film. [40] This heterostructure contains both n and p type interfaces. Motivated by these findings, an extensive study of the role of a $SrTiO_3$ capping layer was carried out.

In this work it is shown how the insulator to metal transition can be triggered in thin $LaAlO_3$ films on $SrTiO_3(001)$ by adding a $SrTiO_3$ capping layer. Systems consisting of a varying number of M=0-2 monolayers of capping $SrTiO_3$ on top of N=1-3 monolayers of $LaAlO_3$ on a $SrTiO_3(001)$ substrate were studied. Fig. 0.7 displays the ionic relaxation of a) two monolayers of $LaAlO_3$ on a $SrTiO_3(001)$ substrate ($2LaAlO_3/SrTiO_3(001)$) and of b) where the $LaAlO_3$ films are covered by a $SrTiO_3$ capping layer ($1SrTiO_3/2LaAlO_3/SrTiO_3(001)$). A strong lattice polarization allows the $LaAlO_3/SrTiO_3(001)$ system to remain insulating until a crossover to an electronic reconstruction takes place [39]. While the potential build-up that

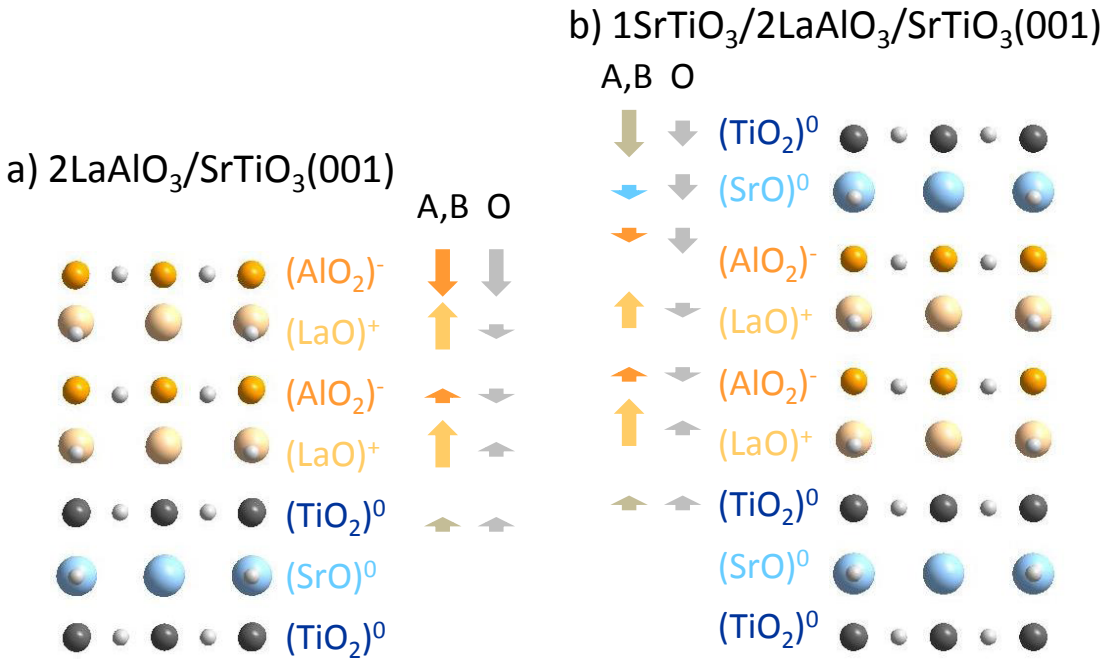

Figure 0.7: Ionic relaxation of a) $2LaAlO_3/SrTiO_3(001)$ [39] and b) $1SrTiO_3/2LaAlO_3/SrTiO_3(001)$. In the uncapped case, a), the insulating behavior of the system up to a critical thickness of $LaAlO_3$ is associated with a lattice distortion. Here the outward relaxation of the La atoms leads to a buckling within the layer and induces a uniform polar distortion. The lattice distortion compensates the induced dipole and sustains the insulating behavior up to a critical thicknes of 4-5 $LaAlO_3$ monolayers. While the surface AlO_2^- layer in the uncapped system shows negligible polarization, the surface TiO_2^0 layer in the capping $SrTiO_3$ layer buckles, leading to a negative dipole moment.

arises from the polarity of the $LaAlO_3$ on a nonpolar $SrTiO_3(001)$ substrate for two monolayers of $LaAlO_3$ is not large enough for electronic reconstruction, a $SrTiO_3$ capping provides further potential shift inducing a insulator to metal transition: dispersive surface O $2p$ states (TiO_2 terminated surface) were identified as origin for the early closing of the band gap (Fig. 0.8b). In contrast, when the system is terminated by a SrO layer (using a 1.5 monolayers of $SrTiO_3$ overlayer) the band gap of approximately 1 eV of the uncapped system $2LaAlO_3/SrTiO_3(001)$ is preserved. In the $1SrTiO_3/2LaAlO_3/SrTiO_3(001)$ system an electronic reconstruction mechanism comes into play with two spatially separated conducting sheets: one electron-like, the other one hole-like. Increasing the number of $LaAlO_3$ and $SrTiO_3$ capping layers enhances the overlap of the valence and conduction bands at the Fermi level as displayed in Fig. 0.8b). The electron density distribution in $2SrTiO_3/2LaAlO_3/SrTiO_3(001)$ in Fig. 0.8c) shows electrons of Ti $3d_{xy}$ character in the interface layer and holes in the O $2p_\pi$ bands at the surface. The effective mass of holes (1.4 m_e), determined from the curvature of the electron and hole bands at the Γ and M points is significantly higher as compared to the lighter electrons

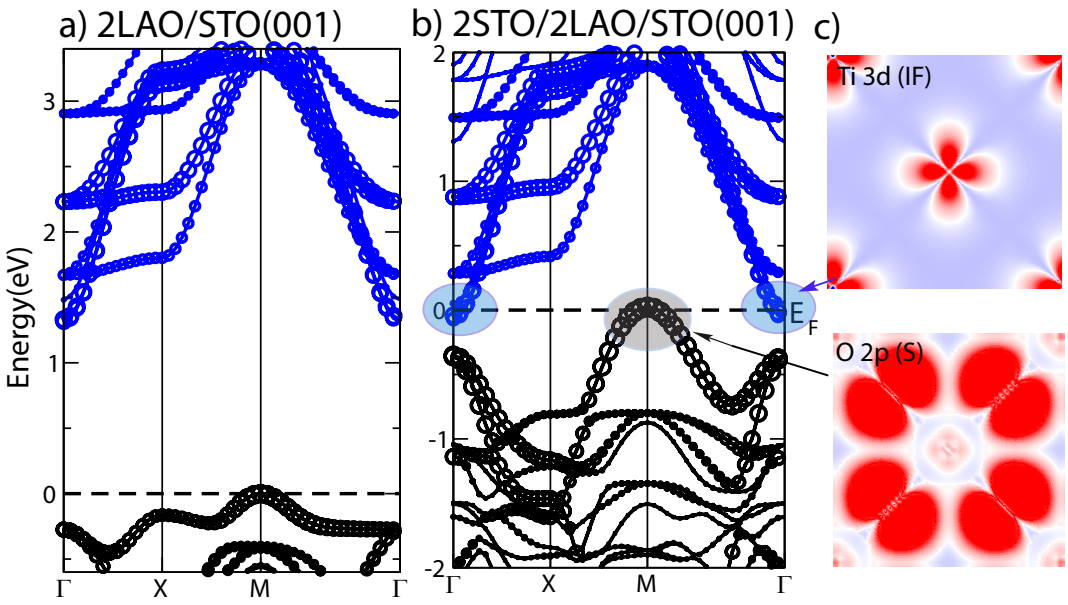

Figure 0.8: Band structure of a) $2LaAlO_3/SrTiO_3(001)$ with an indirect band gap and b) $2SrTiO_3/2LaAlO_3/SrTiO_3(001)$ with a closed band gap due to overlap of an electron band at Γ and a hole band at M. c) integrated electron density around the Fermi level shows electrons of Ti $3d_{xy}$ character at Γ and holes of O $2p_\pi$ type at M.

(0.4 m_e). The two types of carriers and their different mobilities are confirmed in Hall and magnetoresistance measurements [41]. In summary, the presence of a nonpolar $SrTiO_3$ capping layer appears to stabilize the system with respect to surface defects and adsorbates that are likely to eliminate holes in the uncapped systems. Various parameters, such as surface and interface termination, defects and adsorbates have been identified so far to enable tuning of electronic behavior of the $LaAlO_3/SrTiO_3(001)$ system. The control those parameters remains a further challenge in future studies.

The results are published in **Manuscript 4** and **Manuscript 5**. **Manuscript 4** represents a combined theoretical and experimental approach.

Outline

This thesis is organized as follows. In **Chapter 1** the theoretical framework and in particular density functional theory (DFT) and its implementation in the used WIEN2k [42] and VASP [43, 44, 45, 46, 47] codes are introduced. Furthermore, the methodology of *ab initio* thermodynamics [15, 48, 49, 50, 51] is presented.

The following chapters include the manuscripts published in this work.
The FeOOH polymorphs in **Chapter 2**:

- *Pressure Induced Structural and Electronic Transitions in FeOOH from First Principles*, K. Otte, R. Pentcheva, W.W. Schmahl, and J.R. Rustad, Physical Review B **80**, 205116 (2009).
- *Density Functional Theory Study of Water Adsorption on FeOOH Surfaces*, K. Otte, W.W. Schmahl, and R. Pentcheva, Surface Science **606**, 1623 (2012).
- *DFT+U Study of Arsenate Adsorption on FeOOH Surfaces: Evidence for Competing Binding Mechanisms*, K. Otte, W.W. Schmahl, and R. Pentcheva, Journal of Physical Chemistry C, submitted.

Interfaces between the perovskites $LaAlO_3$ and $SrTiO_3$ in **Chapter 3**:

- *Parallel Electron-Hole Bilayer Conductivity from Electronic Interface Reconstruction*, R. Pentcheva, M. Huijben, K. Otte, W. E. Pickett, J. E. Kleibeuker, J. Huijben, H. Boschker, D. Kockmann, W. Siemons, G. Koster, H. J. W. Zandvliet, G. Rijnders, D. H. A. Blank, H. Hilgenkamp, and A. Brinkman, Physical Review Letters **104**, 166804 (2010).
- *Termination Control of Electronic Phases in Oxide Thin Films and Interfaces: $LaAlO_3/SrTiO_3(001)$*, R. Pentcheva, R. Arras, K. Otte, V.Ruiz, and W. E. Pickett, Philosophical Transactions of the Royal Society A **370**, 4904-4926 (2012).

1 Methods

A crystalline material represents a many-particle problem and it is described by the time-independent Schrödinger equation

$$\mathbf{H}\Psi(\{\mathbf{r_i}\},\{\mathbf{R_I}\}) = E\Psi(\{\mathbf{r_i}\},\{\mathbf{R_I}\}), \tag{1.1}$$

where the wave function Ψ includes all information about the system.

Because the mass of the electron and the nucleus differ by three orders of magnitude, it is possible to decouple the electronic and nuclear degrees of freedom. This so called adiabatic or Born-Oppenheimer approximation helps to reduce substantially the complexity of the many body problem. It assumes that the electrons adapt instantaneously to the current position of the nuclei. What remains is the Hamiltonian of the electrons moving in the external field of the nuclei:

$$\mathbf{H}_{elec} = -\sum_{i=1}^{N}\frac{1}{2}\nabla_i^2 + \sum_{i=1}^{N}\sum_{j>1}^{N}\frac{1}{r_{ij}} + \sum_{i=1}^{N}V_{ext} \tag{1.2}$$

The individual terms, given in atomic units [1], represent the kinetic energy of the electrons, the Coulomb interactions between electron-electron, electrons-nuclei as well as nuclei-nuclei, expressed in the external potential, respectively.

One way to express the many-electron wave function is to build it up by a product of single-electron states, i.e. states of single, non-interacting electrons. This is done in the Hartree approximation. An electron is not only described by the three spatial coordinates $\mathbf{r}_i$ but also by a spin coordinate σ_i, which can take one of the two values $\sigma_i = \pm 1$ for spin up or down. Thus the exact wave function not only has to satisfy the Schrödinger equation, it also must be antisymmetric in the sense of the Pauli exclusion principle, that no two electrons with the same spin can occupy the same energy level. The requirement of antisymmetry is enforced by using Slater determinants. The variational principle leads to the Hartree-Fock (HF) equations. The so called HF-approximation includes the correlation for electrons with parallel spins, which leads to a Fermi-hole, i.e. electrons with parallel spin avoid each other. HF methods are widely used in quantum chemistry to calculate electronic properties of atoms and molecules.

As long-range ordered crystalline materials are in the focus of this thesis and the numerical cost of using Slater determinants scales with the size of the sytem, a different approach is needed and established in density functional theory.

[1] In atomic units, the energy E is measured in Rydbergs ($1Ry = 13.6058eV$) with the setting $\hbar = 1$, $m_e = \frac{1}{2}$, $e^2 = 2$, and lengths are defined in units of Bohr's radius $a_0 = 0.529177$Å.

1.1 Density functional theory

While the Born Oppenheimer approximation substantially reduces the complexity, it is still not feasible to find the exact solution of the Schrödinger equation and to determine the many-particle wave function. Here, the development of density functional theory (DFT) accomplished a breakthrough in electronic structure calculations of crystalline materials: the main idea is that the energy, as well as all physical quantities can be described as functionals of the electron- or particle-density $n(\mathbf{r})$. In DFT, the N-particle problem is formally transformed into a single quasi-particle problem in an effective potential V_{eff}. Furthermore, correlation effects between electrons are taken into account via the so called exchange-correlation functional.

1.1.1 The theorems of Hohenberg and Kohn

DFT is based on two theorems stated by Hohenberg and Kohn (1964)[52]:

- All physical quantities are functionals of the electron- or particle-density and are therefore uniquely determined by it. This is particularly true for the ground-state energy $E[n(\mathbf{r})]$.

$$n(\mathbf{r}) = N \int d^3\mathbf{r_2}...d^3\mathbf{r_N} |\psi(\mathbf{r}, \mathbf{r_2}, ..., \mathbf{r_N})|^2 \tag{1.3}$$

  There is an one-to-one correspondence between the particle-density $n(\mathbf{r})$ and the external potential V_{ext} containing all material specific information.

- The energy functional has variational property and reaches its minimal value for the ground state density $n_0(\mathbf{r})$ for a given V_{ext}.

$$E_{V_{ext}}[n_0(\mathbf{r})] \leq E_{V_{ext}}[n(\mathbf{r})] \tag{1.4}$$

Extension of the HK-theorems to magnetic systems

For the spin polarized case the particle density $n(\mathbf{r})$ and the spin magnetization $m(\mathbf{r})$ are determined by the up ($^+$) and down ($^-$) spin densities $n^+(\mathbf{r}), n^-(\mathbf{r})$.

$$n(\mathbf{r}) = n^+(\mathbf{r}) + n^-(\mathbf{r}), \qquad m(\mathbf{r}) = n^+(\mathbf{r}) - n^-(\mathbf{r}) \tag{1.5}$$

The energy becomes a functional of both the up and down spin densities $E[n(\mathbf{r})] = E[n^+(\mathbf{r}), n^-(\mathbf{r})]$ and is minimized with respect to $(n^+(\mathbf{r}), n^-(\mathbf{r}))$ as it is provided by the HK-theorems, and is extended in this sense.

1.1.2 The Kohn-Sham equations

Kohn and Sham [53] mapped the many body problem onto that of solving a system of decoupled Schrödinger equations of non-interacting quasi-particles. For that purpose the exact energy functional is rewritten as

$$E[n(\mathbf{r})] = T_s[n(\mathbf{r})] + U[n(\mathbf{r})] + E_{xc}[n(\mathbf{r})]. \tag{1.6}$$

The term $T_s[n(\mathbf{r})]$ is the kinetic energy of single, non-interacting quasi-particles, $U[n(\mathbf{r})]$ combines the average Coulomb interaction between the electrons as well as the external potential. $E_{xc}[n(\mathbf{r})]$ in contrast is the sum of the exchange (x) and correlation (c) energy.

The single terms are discussed in the following section. The kinetic energy $T[n(\mathbf{r})]$ is resolved into $T_s[n(\mathbf{r})]$ (non-interacting) and a contribution to the kinetic energy, $T_c[n(\mathbf{r})]$, due to interaction.

$$T[n(\mathbf{r})] = T_s[n(\mathbf{r})] + T_c[n(\mathbf{r})] \tag{1.7}$$

Using the Thomas-Fermi description of a homogeneous electron gas, the particle density is determined by single electron states $\phi_{\mathbf{k}\nu}$, reintroduced by Kohn and Sham.

$$n(\mathbf{r}) = \sum_{\mathbf{k}\nu} |\phi_{\mathbf{k}\nu}(\mathbf{r})|^2 \tag{1.8}$$

Simultaneously the kinetic energy can be presented as:

$$T_s[n(\mathbf{r})] = \sum_{\mathbf{k}\nu} \int d^3\mathbf{r} \phi^*_{\mathbf{k}\nu}(\mathbf{r})(-\nabla^2)\phi_{\mathbf{k}\nu}(\mathbf{r}) \tag{1.9}$$

The indices $\mathbf{k}, \nu$ denote the state in $\mathbf{k}$-space, the band index, respectively. Hence T_s depends on the full set of occupied orbitals. The term $U[n(\mathbf{r})]$ contains the potential energy of the nuclei in the external potential of the electrons and the averaged Coulomb interaction energy between the electrons, which is the Hartree term.

$$U[n(\mathbf{r})] = \int d^3r V_{ext}(\mathbf{r}) n(\mathbf{r}) + \int d^3\mathbf{r} d^3\mathbf{r}' \frac{n(\mathbf{r})n(\mathbf{r}')}{|\mathbf{r} - \mathbf{r}'|} \tag{1.10}$$

Applying the variational principle of Eq.(1.8) leads to a decoupled system of one electron Schrödinger equations, the so called *Kohn-Sham equations*

$$(-\nabla^2 + V_{eff}(\mathbf{r}))\phi_{\mathbf{k}\nu} = \epsilon_{\mathbf{k}\nu}\phi_{\mathbf{k}\nu} \tag{1.11}$$

with V_{eff} being the effective potential

$$V_{eff}(\mathbf{r}) = V_{ext}(\mathbf{r}) + \int d^3\mathbf{r}' \frac{n(\mathbf{r}')}{|\mathbf{r} - \mathbf{r}'|} + \frac{\delta E_{xc}[n(\mathbf{r})]}{\delta n(\mathbf{r})}. \tag{1.12}$$

Spin density functional theory (SDFT)

As already discussed, the extension to spin polarized systems leads to a dependence of the variables on the spin and its spin direction up or down ($\sigma = \pm\frac{1}{2}$). For a spin polarized system, the Kohn-Sham equations are:

$$(-\nabla^2 + V^\sigma_{eff}(\mathbf{r}))\phi^\sigma_{\mathbf{k}\nu} = \epsilon^\sigma_{\mathbf{k}\nu}\phi^\sigma_{\mathbf{k}\nu}, \tag{1.13}$$

where the effective potential consists of

$$V_{eff}^{\sigma}(\mathbf{r}) = V_{ext}^{\sigma}(\mathbf{r}) + \int d^3\mathbf{r}' \frac{n^{\sigma}(\mathbf{r}')}{|\mathbf{r}-\mathbf{r}'|} + \frac{\Delta E_{xc}[n(\mathbf{r})]}{\Delta n^{\sigma}(\mathbf{r})}. \tag{1.14}$$

1.1.3 Approximations for the exchange-correlation functionals

Besides the Born-Oppenheimer approximation DFT is an exact theory. However, the form of the exchange-correlation potential is not known. In a second approximation, the exchange-correlation $E_{xc}[n(\mathbf{r})]$ can be reasonably approximated as a local or a nearly local functional of the electron-density.

Linear density and linear spin density approximation (LDA and LSDA)

- Local *ansatz* of the L(S)DA
  In the local density approximation (LDA) or more generally in the local spin density approximation (LSDA), the exchange-correlation energy function $\epsilon_{xc}(n^+(\mathbf{r}), n^-(\mathbf{r}))$ is locally approximated by the exchange-correlation density of a homogeneous electron gas.

$$E_{xc}^{LSDA}[n^+, n^-] = \int d^3 n(\mathbf{r}) \epsilon_{xc}^{hom}(n^+(\mathbf{r}), n^-(\mathbf{r})) \tag{1.15}$$

  $\epsilon_x^{hom}(n)$ is the exchange energy of the unpolarized gas. For non-spin-polarized systems the LDA is found simply by setting $n^+ = n^- = \frac{n(\mathbf{r})}{2}$.

- Expressions for the potential $V_{xc}^{\sigma}(\mathbf{r})$
  The derivative of the exchange-correlation energy functional with respect to the electron density gives the potential in the form

$$V_{xc}^{\pm}(\mathbf{r}) = \frac{\delta E_{xc}[n(\mathbf{r}), m(\mathbf{r})]}{\delta n(\mathbf{r})} \pm \frac{\delta E_{xc}[n(\mathbf{r}), m(\mathbf{r})]}{\delta m(\mathbf{r})}, \tag{1.16}$$

  and can also be expressed in terms of functions of the local density of each spin $n^{\sigma}(\mathbf{r})$.

$$V_{xc}^{\sigma}(\mathbf{r}) = \frac{\partial n(\mathbf{r}) \epsilon_{xc}[n(\mathbf{r}), m(\mathbf{r})]}{\partial n^{\sigma}(\mathbf{r})}. \tag{1.17}$$

This approximation is widely used and gives reliable results for many systems. It works well, because (i) the errors in the approximations for E_x and E_c cancel each other, (ii) LDA satisfies the sum rule for the exchange-correlation hole. Common shortcomings are: too high bulk moduli, the cohesive energy E_{coh} is over-, bond length are underestimated (overbinding), typically obtained values of the lattice parameter are about 2% smaller than the experimental ones. Furthermore, LDA predicts for bulk iron paramagnetic fcc ground state instead ferromagnetic bcc [54].

Generalized gradient approximation (GGA)

For open systems (e.g. on surfaces) where strong variations of the electronic density take place, the local density approximation is less suitable. Here the generalized gradient approximation has gained importance in the last years, where the exchange-correlation energy is a function both of the electron density and its gradient at each position. [55]

In the *generalized* form of

$$E_{xc}^{GGA}[n^+, n^-] = \int d^3n(\mathbf{r})\epsilon_x^{hom}(n)F_{xc}(n^+, n^-, |\nabla n^+|, |\nabla n^-|, ...), \tag{1.18}$$

F_{xc} is the dimensionless exchange-correlation enhancement factor.

- The exchange-correlation enhancement factor F_{xc}
  F_{xc} is denoted as the sum of the exchange and correlation factor.

  $$F_{xc} = F_x + F_c \tag{1.19}$$

  There are different forms of $F_x(n, s)$, where $s = s_1$, with different physical conditions for $s \to \infty$. Three widely used forms are of Becke (B88)[56], Perdew and Wang (PW91)[57], and Perdew, Burke and Enzerhof (PBE)[58]. The latter drops the non-uniform scaling condition in favor of a simplified parametrization with $F_x^{PBE-GGA}(s) \sim const.$.

  As $F_x \geq 1$, all the GGAs lead to an E_x lower than the LDA. In atoms, there are more rapidly varying regions than in condensed matter which results in a greater lowering of the E_x in the atoms. This reduces the binding energy, corrects the LDA overbinding (resulting in slightly overestimated bond length), and most importantly, improves the consistency with experimental evidence, e.g. the ground state of bulk Fe is predicted correctly (ferromagnetic bcc) [54].

  Typically, the contribution of correlation to the total energy is much smaller than the exchange and is added into the lowest order gradient expansion at high density. For large density gradients the magnitude of the correlation energy decreases and vanishes for $s \to \infty$.

- Expressions for the potential $V_{xc}^{\sigma}(\mathbf{r})$

  $$V_{xc}^{\sigma}(\mathbf{r}) = [\epsilon_{xc} + n\frac{\delta\epsilon_{xc}}{\delta n^{\sigma}} - \nabla(n\frac{\delta\epsilon_{xc}}{\delta\nabla n^{\sigma}})]_{\mathbf{r},\sigma} \tag{1.20}$$

  This method requires higher order derivatives of the density which can lead to pathological potentials or numerical difficulties near the nucleus of the outer regions of atoms, where the density is rapidly varying or is very small.

1.1.4 Description of strongly correlated systems

To provide a better description of electronic correlation, Anisimov et al. [54, 59, 60] introduced the LDA+U approximation. To describe the localized d- or f-electrons, a Hubbard-like term $\frac{1}{2}U\sum_{i\neq j} n_i n_j$ is added to the Hamiltonian, while the delocalized s- and p-electrons are treated with L(S)DA/GGA. The functional has the form

$$E^{LDA+U} = E^{LDA} - \frac{1}{2}UN(N-1) + \frac{1}{2}U\sum_{i\neq j} n_i n_j \tag{1.21}$$

where N is the number of d-electrons.

"LDA+U" therefore stands for methods that involve L(S)DA- or GGA-type calculations coupled with an additional orbital-dependent interaction. The effect of the added term is to shift the localized orbitals relative to the other orbitals, which attempts to correct errors in the usual LDA or GGA calculations. The "U"-parameter is defined as the Coulomb-energy cost to place two atoms at the same site:

$$U = E(d^{n+1}) + E(d^{n-1}) - 2E(d^n) \tag{1.22}$$

1.2 Electrons in periodic solids

An ordered crystalline solid is characterized by translational symmetry: $\mathbf{R_n} = n_1\mathbf{a_1} + n_2\mathbf{a_2} + n_3\mathbf{a_3}$A result of the translation symmetry is that the potential is periodic:

$$V(\mathbf{r} + \mathbf{R_n}) = V(\mathbf{r}) \tag{1.23}$$

1.2.1 Basic formulation: Bloch's theorem

The application of *Bloch's theorem* simplifies all calculations performed on ordered solids. Due to the periodicity of the potential, the wave function $\phi_{\mathbf{k}\nu}(\mathbf{r})$ can be written as a product of a periodic function $u_{\mathbf{k}\nu}(\mathbf{r} + \mathbf{R_n}) = u_{\mathbf{k}\nu}(\mathbf{r})$ and a plane wave $e^{i\mathbf{k}\cdot\mathbf{r}}$:

$$\phi_{\mathbf{k}\nu}(\mathbf{r}) = e^{i\mathbf{k}\cdot\mathbf{r}} u_{\mathbf{k}\nu}(\mathbf{r}) \tag{1.24}$$

and, because of the periodicity, may be written as a sum of plane wave functions, where $u_{\mathbf{k}\nu}(\mathbf{r})$ is expanded in three-dimensional Fourier series.

$$\phi_{\mathbf{k}\nu}(\mathbf{r}) = \sum_n P_{\mathbf{k}\nu}(\mathbf{K_n}) exp[i(\mathbf{k} + \mathbf{K_n})\cdot r] \tag{1.25}$$

Note that for each Bloch vector $\mathbf{k}$ there is a discrete set of energies $E = E_\nu(\mathbf{k})$ with the corresponding wave function $\phi_{\mathbf{k}\nu}(\mathbf{r})$. The periodicity in reciprocal space implies that

$$\phi_{\mathbf{k}+\mathbf{K_n},\nu}(\mathbf{r}) = \phi_{\mathbf{k}\nu}(\mathbf{r}) \qquad \text{and} \qquad E_\nu(\mathbf{k} + \mathbf{K_n}) = E_\nu(\mathbf{k}) \tag{1.26}$$

where K_n is a lattice vector in reciprocal space[2]. Thus, no new information is generated by considering $\mathbf{k}$ vectors, that are located outside the unit cell in reciprocal space.The probability that an electron in the state $\phi_{\mathbf{k}\nu}(\mathbf{r})$ has one of the possible values of momentum $\mathbf{k}+\mathbf{K_n}$ is proportional to $|P_{\mathbf{k}\nu}(\mathbf{K_n})|^2$. Due to the rules for the Fourier series, the magnitudes of $P_{\mathbf{k}}(\mathbf{K_n})$ will be appreciable even for large $\mathbf{K_n}$. Near any lattice site, $u_{\mathbf{k}\nu}(\mathbf{r})$ must reproduce an electronic wave function very similar to an atomic wave function, which is a very localized function. In transition metals and their oxides the wave function shows strong oscillations close to the nucleus. To describe these, a very high cutoff of the Fourier series is needed to represent the wave function by plane waves.

1.2.2 Basis functions: APW and LAPW method

The difficulty in a solid is to deal accurately with the oscillations of wave functions both near the nucleus and in the smoother bonding regions. To solve this problem, in the augmented plane waves (APW) and linear augmented plane waves (LAPW) method the space is divided into two regions: spheres around the atomic position and an interstitial region inbetween.

The APW method

In the APW method the potential function has the *muffin-tin* form:

$$V(\mathbf{r}) = \sum_n v(\mathbf{r}-\mathbf{R_n}) \tag{1.27}$$

Initially a spherically symmetric potential around the lattice point $\mathbf{R_n}$ was used. The chosen radius $\mathbf{R_{MT}}$ is small enough such that the muffin-tin spheres do not overlap. Space is therefore divided into two regions with different basis expansions:

$$\phi^{APW}(\mathbf{r}) = \begin{cases} \frac{1}{\sqrt{\Omega}} \sum_{\mathbf{K}} c_{\mathbf{K}} e^{i(\mathbf{k}+\mathbf{K})} & \mathbf{r} \in I \\ \sum_{lm} A_{lm} R_l(\mathbf{r}) Y_{lm}(\mathbf{r}) & \mathbf{r} \in S \end{cases} \tag{1.28}$$

Planewaves in the interstitial region I with $c_{\mathbf{K}}$ being an expansion coefficient. $\mathbf{R}_l(E,\mathbf{r})$ are solutions of th radial part of the Schrödinger equation inside the muffin-tin spheres S and $Y_{lm}(\theta,\Phi)$ is a spherical harmonic. A_{lm} is an expansion coefficient determined by matching the wave function at the sphere boundary. Therefore, it is completely described by the planewave coefficients $c_{\mathbf{K}}$ and the energy parameters E_l, both being the variational coefficients, and $\mathbf{R}_l(E,\mathbf{r})$ a solution of

$$-\frac{1}{\mathbf{r}^2}\frac{d}{d\mathbf{r}}\left(\mathbf{r}\frac{d\mathbf{R}_l}{d\mathbf{r}}\right) + \left[\frac{l(l+1)}{\mathbf{r}^2} + v(\mathbf{r}) - E_l\right]\mathbf{R}_l = 0. \tag{1.29}$$

[2]The reciprocal lattice vector is composed of the basis vectors in reciprocal space $\mathbf{b_j}$ which are constructed so that $\mathbf{a_i}\cdot\mathbf{b_j} = 2\pi\delta_{ij}$, and the integers m_j. It may be written $K_n = m_1\mathbf{b_1} + m_2\mathbf{b_2} + m_3\mathbf{b_3}$.

The augmented plane wave is defined to be continuous at the surface of the muffin-tin sphere: The radial functions are automatically orthogonal to any eigenstate of the same Hamiltonian that vanishes on the sphere boundary [61]. In order to find a numerical solution, truncation at some values of l_{max} is necessary. Nodes correspond to a given l_{max} for which $Y_{l_{max}m}(\theta, \Phi)$ is zero with a maximum number of $\frac{2l_{max}}{2\pi \mathbf{R_{MT}}} = \frac{l_{max}}{\pi \mathbf{R_{MT}}}$ nodes per unit of length. The shortest period of a plane wave $\frac{2\pi}{K_{max}}$ has $\frac{2}{2\pi/K_{max}} = \frac{K_{max}}{\pi}$ nodes per unit of length. K_{max} and l_{max} are the *cut-off* for the plane waves and the angular functions, respectively. The relation $\mathbf{R_{MT}} K_{max} = l_{max}$ is true for an identical number of nodes per unit of length. Therefore, the individual muffin-tin radii of the different atoms should not vary too much, as a suitable l_{max} for each atom would not be able to be found. The set of $\sum_{l=1}^{l_{max}} 2l_{max} + 1$ coefficients A_{lm}^{α} for each atom α seal the match.
To completely determine the coefficients $c_{\mathbf{K}}$ the parameter E_l first has to be set equal to the eigenvalue ϵ of the eigenstate $\phi(\mathbf{r})$. Since the value of E is to be determined, it starts with a guessed value for ϵ, and hence for E. Now the APW's are determined, and, as the APW's are not orthogonal, after calculating the hamiltonian matrix elements H as well as the overlap matrix elements F, the secular equation is determined. The guessing continues until a root of the secular equation is found. However, for every eigenvalue a diagonalization needs to be performed which makes the APW method inherently slow. Another problem occurs as the derivatives of the APW's are not continuous at the surface of the muffin-tin sphere.

The LAPW method

Anderson [61], Koelling and Arbman [62] extended the APW method to a scheme where the basis functions inside the muffin tin and its energy derivatives are made continuous.
The radial function R_l is developed around the selected reference energy E_l in a Taylor expansion to a linear term in order to reduce the dependence on the single particle energy.

$$R_l(\mathbf{r}, \epsilon) = R_l(\mathbf{r}, E_l) + (\epsilon - E_l)\dot{R}_l(\mathbf{r}) + O(\epsilon - E_l)^2 \tag{1.30}$$

Furthermore, by a linear combination of the radial function R_l at a chosen fixed E_l and its energy derivative $\dot{R}_l = \frac{\delta R_l(\mathbf{r}, E_l)}{\delta \epsilon}|_{\epsilon = E_l}$ the basis functions are fully described. The form of eq.(1.28) can be adapted:

$$\phi^{LAPW}(\mathbf{r}) = \begin{cases} \frac{1}{\sqrt{\Omega}} \sum_{\mathbf{K}} c_{\mathbf{K}} e^{i(\mathbf{k}+\mathbf{K})} & \mathbf{r} \in I \\ \sum_{lm} \left[A_{lm} R_l(\mathbf{r}) + B_{lm} \dot{R}_l(\mathbf{r}) \right] Y_{lm}(\mathbf{r}) & \mathbf{r} \in S \end{cases} \tag{1.31}$$

Due to the boundary conditions of the basis functions, the coefficients A_{lm} and B_{lm} for the energy derivative are determined by matching the plane both in value and slope at the sphere boundary.
The criterion for the accuracy or convergence of the APW or rather LAPW basis set is the cutoff parameter.

In essence, via linearization a simplification to a finite basis as well as an increase of flexibility of the basis is achieved. This facilitates the construction of a full

potential LAPW (FP-LAPW) method.

1.2.3 Representation of the potential: FP-LAPW

Initially, spherically symmetric potentials within the atomic sphere approximation (ASA) were used. However, for systems containing *d*-electrons and directional bonds, non-spherical contributions become important. In the FP-LAPW method a similar representation is used for the potential and the density as for the wave function. This allows adding non-spherical contributions to the potential and warping terms in the interstitial. Thus no shape approximations are made - hence the denotation as *full potential* LAPW or FP-LAPW method [63, 64].
The potential and, in line with that, the charge density are expanded as follows

$$V(r) = \begin{cases} \sum_{\mathbf{K}} V_{\mathbf{K}} e^{i(\mathbf{Kr})} & \mathbf{r} \in I \\ \sum_{lm} V_{lm}(\mathbf{r}) Y_{lm}(\hat{\mathbf{r}}) & \mathbf{r} \in S \end{cases} \tag{1.32}$$

where the potential inside the spheres is expanded into spherical harmonics. Similar to the wave function, these sums are truncated at some l_{max} and G_{max} in order to handle this problem numerically. Because the density is quadratic in the wave function, the plane wave cutoff has to be at least twice of the wave function cutoff $|G^{pot}_{max}| \geq 2K^{WF}_{max}$.
Symmetry adapted expansions are used to reduce storage capacity:

- *stars* in the interstitial
  The constructed planewaves with $|\mathbf{K_n}| \leq \mathbf{K_{max}}$ are both sorted by length and subdivided symmetry related into sublists. The lists consisting of the individual sublists form the *stars*.

  and

- *lattice harmonics* instead of spherical harmonics within the nonequivalent atoms
  Lattice harmonics are symmetrized spherical harmonics, constructed around the center of the atom α at $\mathbf{R}_\alpha$ under the explicit use of point symmetry. Only one representative for all symmetrically equivalent positions needs to be calculated which simplifies the calculation.

The FP-LAPW method is an all-electron approach, where both core and valence states are explicitely taken into account making it one of the methods with the highest accuracy. The Schrödinger equation of the core electrons is solved for a spherically symmetric potential.

1.2.4 The WIEN2k code

WIEN is a full-potential LAPW code developed by Blaha, Schwarz, Sorantin, and Trickey [65]. The most recent version WIEN2k is used in this work. The package consists of separate programs which are controlled via shell scripts. The flow of the program for a calculation on a crystalline solid will now be briefly presented. [42]

Initialization: Generation of the inputs for the main programs

The case.struct file contains all information on the structure and atom types (Z) of the material. This includes the symmetry class of the cell and, together with the site symmetry of the individual atoms, the program sgroup can determine the space group of the system. After running symmetry all symmetry matrices are written. During a volume optimization, care has to be taken that the chosen muffin tin spheres do not overlap. nn calculates the distances to the neighboring atoms and is therefore a useful tool to fix the muffin tin radii especially when the volume is reduced during a volume optimization.

The starting density: lstart and dstart lstart generates a superposition of the atomic densities. Here the type of exchange correlation potential has to be chosen, e.g. 13 for GGA (PBE)[58]. Because the Fe 3s-states are not completely localized withing the MT sphere, we chose to treat them as valence states. The energy which separates the core and valence states for iron compounds is located at -7.0Ry in order to include the Fe 3s-states into the valence band to enhance accuracy.
The calculation of integrals in the reciprocal space (e.g. the density of states (DOS)) necessitates a good sampling over the Brillouin zone. Therefore, a sufficient number of **k**-points needs to be generated. Here again, the symmetry in reciprocal space is utilized and the **k**-mesh is generated on a special point grid in the irreducible wedge of the Brillouin zone (IBZ). This is done by kgen.

dstart extends the core density to the interstitial region and generates thereby a starting density.

In the following the essential programs for running an SCF cycle are described in the order of flow.

Construction of the effective potential: lapw0

The effective potential V_{eff} which is to be used in the KS equations is constructed by lapw0 from the electron (spin) density. V_{eff} consists of an exchange-correlation term V_{xc} and a Coulomb term V_C which are treated as follows:

- The exchange correlation potential V_{xc} is calculated on a grid in real space where it is diagonal. Inside the spheres a least squares procedure is used to compute V_{xc} at each grid point with an expansion in lattice harmonics.
  The interstitial charge is first represented in real space by a fast Fourier transformation (FFT). V_{xc} is subsequently constructed in real space and transformed back to reciprocal space to a planewave representation via FFT.

- The Hartree potential V_H which is the averaged electron-electron interaction, and the nuclear potential produce the Coulomb potential V_C obtained from the density via Poisson's equation:

$$\nabla^2 V_C(\mathbf{r}) = 4\pi n(\mathbf{r}) \tag{1.33}$$

This equation Eq.(1.33) can be solved easily in reciprocal space.

$$V_C(\mathbf{K}) = \frac{4\pi n(\mathbf{K})}{\mathbf{K}^2} \tag{1.34}$$

However, problematic are the oscillating behavior of the density and the delta function-like shape of the nuclear charge density. Therefore, the so called *pseudo-charge* method [66] is used. The *multipoles* of the charges inside and outside the spheres are calculated constructing the pseudo-charges.
Instead of the true charge density pseudo-charges are chosen which generate the same potential in the interstitial region as the real density. The interstitial Coulomb potential V_{PW} is calculated in reciprocal space.
Via a standard Green's function approach the integration of Poisson's equation is finally performed in real space to compute the potential in the sphere.

Calculation of orbital dependent potentials: ORB

The potential for a given atom and orbital number l which is nonzero in the atomic spheres and depends on the orbital state numbers l, m is an *orbital dependent potential*. For strongly correlated systems the LDA+U (fully localized limit) method [67]. The resulting potential is a Hermitean $(2l+1) \times (2l+1)$ matrix. There exist another two LDA+U methods: LDA+U (around mean field = AMF) [68] and LDA+U (HMF) [54] where in addition the Hubbard model in the mean field approximation is also implemented. Besides the LDA+U implementation, there are also potentials implemented for orbital polarization and interaction with the external magnetic field.

Solution of the Generalized Eigenvalue Problem: lapw1

The next and most time consuming step after the construction of the effective potentials is to set up and diagonalize the Hamiltonian, and to solve the Kohn-Sham equation. In the LAPW basis set expansion, the eigenfunctions from the KS equation can be calculated by finding the variational coefficients $c_{\mathbf{K}}$. This is done by setting up the Hamiltonian $\mathbf{H}$ and the overlap matrix $\mathbf{S}$ including both interstitial and spherical contributions. As the LAPW transform as planewaves, they are not orthogonal and this results in a generalized eigenvalue problem:

$$\{\mathbf{H} - \epsilon_{\mathbf{k}\nu}\mathbf{S}\}\, c_{\mathbf{k}\nu} = 0 \tag{1.35}$$

In the case of inversion symmetry, the matrices $\mathbf{H}$ and $\mathbf{S}$ are symmetric (making their construction and diagonalization more efficient). Otherwise complex matrix elements additionally slow down this already very time-consuming step in the program. Next to several efforts to speed up this part, e.g. modifications of LAPACK routines, a good performance can be obtained by parallel execution. For the numerically intensive parts (lapw1 and lapw2), the $\mathbf{k}$-points are parallelized over processors, where subsets of the k-mesh are distributed to different processors, and the results are subsequently summarized. Additionally, a fine grain MPI parallelization is used.

Computation of the valence electron density: lapw2

In the next step, the Fermi energy is computed and the valence electron density is generated from the eigenvectors by evaluating integrals over the Brillouin zone.

$$n(\mathbf{r}) = \frac{1}{V_{BZ}} \int_{BZ} \sum_{\epsilon_{\mathbf{k}\nu} < E_F} |\Psi_\nu(\mathbf{k}, \mathbf{r})|^2 d^3k \tag{1.36}$$

This integration is performed numerically on a finite set of **k**-points in the IBZ. Two approaches can be applied: On the one hand the tetrahedron method [69, 70, 71, 72, 73] and on the other hand the special points method [74, 75, 76]. The Fermi energy can be determined by the requirement that over all occupied states the total number of valence electrons is equal to the integral. Furthermore, the integral can be substituted by a weighted sum[3] with a broadened occupation function:

$$F_{\mathbf{k},\nu} = \frac{1}{e^{\frac{\epsilon_{\mathbf{k},\nu} - E_F}{k_B T}} + 1} \tag{1.37}$$

The energy has to be extrapolated to $T \to 0$ to obtain the ground state energy.

The treatment of the core electrons: lcore

The core electrons are treated separately in lcore and the all-electron method fulfills the conditions: The valence states are orthogonal to the core states and the core states are calculated self-consistently in the crystal potential. The core states are calculated using the spherical part of the crystal potential, whereas the valence states are calculated from the full potential.

Generating the input density for the next iteration: mixer

According to Hohenberg and Kohn, the ground state energy is uniquely determined by the ground-state electron density $n(\mathbf{r})$ which is calculated self-consistently in order to minimize the energy functional. A new output density $n^m_{out}(\mathbf{r})$ is obtained after each iteration cycle. The mixer now generates a new input density $n^{m+1}_{in}(\mathbf{r})$ from the input and output density of the m^{th} iteration. In order to stabilize the self consistent field (SCF) cycle, an effificient method for mixing the output and old input densities has to be applied.

- The Pratt mixing scheme [77] is a simple method with a linear mixing factor Q:
$$n^{m+1}_{in}(\mathbf{r}) = (1 - Q) n^m_{in}(\mathbf{r}) + Q n^m_{out}(\mathbf{r}) \tag{1.38}$$
Where m are the number of iterations.

- The more efficient Broyden-II mixing scheme [78] provides better convergence properties and calculates the inverse Jacobian matrix J^m.

[3] $\sum_{\mathbf{k},\nu} w(\mathbf{k}) F_{\mathbf{k},\nu} = n_{tot}$

Finally, the total energy E_{tot} and the atomic forces $\mathbf{F} = -\frac{dE_{tot}}{d\mathbf{R}}$ are computed after adding the various contributions of the preceding steps from the last iteration. The forces can be used to optimize the internal parameters of the system.

Optimization of internal parameters

Within GGA, an optimization of internal parameters is implemented and controlled via the program mini. Obeying the symmetry constraints of the individual atoms, the equilibrium positions of all atoms can be determined: The atomic positions are shifted according to the calculated forces. The new positions of the atoms are written in the case.struct1 file. Recently an efficient optimization method using the PORT ("reverse-communication trust-region Quasi-Newton method") library was implemented.

1.2.5 Projector augmented-wave (PAW) method

This approach introduced by Blöchl [79] combines the accuracy of all-electron methods such as FLAPW with the efficiency of pseudopotentials by mixing two basis sets: planes waves and local orbitals. Within the PAW method the valence electronic wave functions are kept orthogonal to the core states. In particular, the complexity of the treatment of rapidly oscillating wave function close to the ion cores is reduced by a transformation into smooth pseudo wave functions. Here the physical valence wave functions are mapped onto the ficticious pseudo wave function. The all-electron wave function $|\Psi\rangle$ (a Kohn-Sham wave function) is obtained by applying the transformation $\mathcal{T}$ to the fictitious pseudo wave function $|\tilde{\Psi}\rangle$.

$$|\Psi\rangle = \mathcal{T}|\tilde{\Psi}\rangle \tag{1.39}$$

The transformation $\mathcal{T}$ is reversible:

$$\mathcal{T} = 1 + \sum_R \hat{\mathcal{T}}_R \tag{1.40}$$

where the sum is over all atomic sites R and each $\hat{\mathcal{T}}_R$ is non-zero within some spherical augmentation region Ω_R. Therefore, the calculation the eigenstates of the Kohn-Sham Hamiltonian both inside and outside atomic spheres is possible. This provides access to the full wave function holding not only information on the valence energy levels and wave functions in the bonding region, but also on the entire wave function and matrix elements of any operator on valence states of an atom in its new environment.

Analogous, a set of pseudo basis functions $|\tilde{\phi}_i\rangle$ is transformed upon operation of $\mathcal{T}$ to a set of all-electron basis functions $|\phi_i\rangle$.

$$|\phi_i\rangle = (1 + \sum_R \hat{\mathcal{T}}_R)|\tilde{\phi}_i\rangle \tag{1.41}$$

Thereby, the pseudo basis functions are identical to the all-electron basis functions outside the atomic spheres. Inside the atomic spheres, applying $\hat{\mathcal{T}}_R$ on the all-

electrons basis functions produces smoother pseudo basis functions.

The constructions of superpositions of the pseudo and all-electron bases lead to pseudo waves

$$|\tilde{\Psi}\rangle = \sum_i |\tilde{\phi}_i\rangle \tag{1.42}$$

and all-electrons waves

$$|\Psi\rangle = \sum_i |\phi_i\rangle c_i \tag{1.43}$$

respectively. The coefficients c_i of the transformation matrix $\mathcal{T}_R$ are scalars and are constructed from scalar products of pseudo basis functions with the projector functions, $|\tilde{p}_i\rangle$:

$$c_i = \langle \tilde{p}_i | \tilde{\Psi} \rangle \tag{1.44}$$

with $\langle p_i | \tilde{\phi}_j \rangle = \delta_{ij}$.

The PAW method is typically combined with the frozen core approximation where the core states are approximated by the free atom states.

1.2.6 The VASP code

VASP (Vienna *ab initio* simulation package)[43, 44, 45, 46, 47] is a density functional theory code based on a plane wave basis set with periodic boundary conditions. In order to describe the interaction between ions and electrons, pseudopotentials or in this case the PAW method [79] as introduced above are applied. The self consistent calculations are carried out within the generalized gradient approximation (GGA)[58]. The solution of the Kohn-Sham equations is obtained using an efficient matrix diagonalization method (blocked Davidson) [80, 81]. Stress and forces are calculated with VASP and, accordingly, a structural optimization is possible where the atoms relax into their equilibrium position. Here the conjugate gradient algorithm [82, 83] is applied.

These are four necessary input files for the calculations: POTCAR, POSCAR, INCAR, KPOINTS. [84] With the correct input files the calculation is invoked by executing the command `vasp`.

- **POTCAR** contains the PAW potentials for each atom specified in the POSCAR file. Furthermore, information on the atoms (e.g. atomic mass or valence) are included. For the energy cutoff (ENCUT), default values for the atoms are provided, but these can be modified in the INCAR file.

- **POSCAR** contains all structural information: the lattice parameters, the number of each atomic species, the atomic species, and the atomic positions.

- **INCAR** is the central input file and determines specifics of the calculation, e.g. the accuracy, the number of electronic steps or ionic relaxation cycles, or magnetic moments. Here modifications of the default values can be specified.

- **KPOINTS** contains the k point mesh size for creating the the k point grid.

1.3 Equation of state (EOS)

In solid materials, the equilibrium positions of the individual atoms, ions or radical groups are a consequence of the balance of the attractive and repulsive forces acting on the species. The total energy E_{tot} is calculated with respect to the lattice parameter. The minimum determines the equilibrium lattice parameters and volume V_0.

Bulk elastic properties under high pressure The bulk modulus gives information on the compressibility of a material exposed to an external pressure. Established as a material specific quantity, the bulk modulus B[4] is expressed as the change in pressure dP as a function of volume $\frac{dV}{V}$ (fractional volume compression). It is defined as:

$$B = -V\left(\frac{dP}{dV}\right)_T \tag{1.45}$$

The negative sign results from the demand on B remaining positive, while with an increase of pressure the volume decreases simultaneously. B is dependent on temperature T and pressure P and influences the speed of sound and other mechanical waves in the material. The reciprocal of the bulk modulus is the compressibility κ of the substance $\kappa = B^{-1}$.
The derivative of B with respect to P is:

$$B' = \left(\frac{dB}{dP}\right)_T \tag{1.46}$$

The demand is now to establish a sophisticated equation of state describing the (equilibrium) properties of a crystalline material in good agreement with experimental results. The Hooke's law has a limited range of applicability as it neglects the dependence of the elastic constants on the initial stress. Murnaghan [85] discarded this so called *action at a distance* theory and replaced it by a *differential* theory where the focus lies on the variation of the energy with respect to an infinitesimal volume change.

$$P = -\left(\frac{dE}{dV}\right) \tag{1.47}$$

Considering the bulk modulus pressure as a constant $B' = B'_0$, then

$$B = B_0 + B'_0 P \tag{1.48}$$

is obtained, where B_0 is the value of B at zero pressure ($P = 0$). Substituting this in Eq.(1.45) and integrating a rearranged expression, results in

$$P(V) = \frac{B_0}{B'_0}\left(\left(\frac{V_0}{V}\right)^{B'_0} - 1\right). \tag{1.49}$$

[4] in units of Pa: $[B] = Pa$

Substituting Eq.(1.49) with $E = E_0 - \int PdV$ gives the Murnaghan equation of state for the energy, normalized according to[86]

$$E(V) = E_0 + \left[\frac{B_0 V}{B_0'}\left(\frac{\eta^{B_0'}}{B_0' - 1} + 1\right) - \frac{B_0 V_0}{B_0' - 1}\right]\frac{1}{14703.6} \tag{1.50}$$

with $\eta = \left(\frac{V_0}{V}\right)^{\frac{1}{3}}$.

Birch-Murnaghan equation of state Birch developed Murnaghan's [85] theory of finite strain for a medium of cubic symmetry subjected to finite hydrostatic compression, plus an arbitrary homogeneous infinitesimal strain[87]. The free energy includes terms of the third order in the strain components. This so called *third-order Birch-Murnaghan* isothermal equation of state consists of:

$$P(V) = \frac{3}{2}B_0\left((\eta^7 - \eta^5)\left[1 + \frac{3}{4}(B_0' - 4)(\eta^2 - 1)\right]\right) \tag{1.51}$$

$$E(V) = E_0 + \frac{9}{16}\frac{B_0}{14703.6}V_0\left((\eta^2 - 1)^3 B_0' + (\eta^2 - 1)^2(6 - 4\eta^2)\right) \tag{1.52}$$

These equations of state (EOS) allow us to determine E_0, V_0, B_0, and B_0' from the calculated total energy for different volumes. These quantities can then be compared with experimental data.

1.4 *Ab initio* thermodynamics

In order to determine the stability of a particular surface structure depending on environmental parameters, a thermodynamic approach is used to extend the zero temperature and zero pressure results from the DFT calculations to realistic environmental conditions. [15, 48, 49, 50, 51]

In thermodynamic equilibrium the surface can exchange any amount of atoms with each reference phase (ad-/desorption)[5] without changing temperature, T, or pressure, p. The most stable structure and composition of the surface is the one that minimizes the total Gibbs free energy of the system.

$$G^{\text{slab}}(T, p, N_i) - \sum_i G_i(T, p, N_i^{\text{ref}}) = \min \tag{1.53}$$

Via the Euler equation the Gibbs free energy is replaced by the chemical potentials of the reference phases $\mu_i(T,p)$[6]:

$$G_i(T, p, N_i^{\text{ref}}) = (N_i^{\text{tot}} - N_i)\mu_i(T, p) \tag{1.54}$$

Since at thermodynamic equilibrium

[5] N_i^{tot} is constant: $N_i^{tot} = N_i + N_i^{ref}$ N_i^{tot}= total number of particles, N_i= number of atoms in the different species in the slab, N_i^{ref}= remaining atoms in the reference phases, i= atomic species

[6] chemical potential per atom i

$$\mu^{\text{slab}}(T,p) = \mu^{\text{ref}}(T,p), \tag{1.55}$$

the Gibbs free surface energy, $\gamma(T,p)$, is derived as

$$\begin{aligned}\gamma(T,p_i) =& \frac{1}{2A}\left(G^{\text{slab}}(T,p,N_i) - \sum_i N_i\mu_i(T,p)\right) \\ =& \frac{1}{2A}\left(G^{\text{slab}}(T,p,N_i) - N_{\text{Fe}}\mu_{\text{Fe}}(T,p_{\text{Fe}}) - N_{\text{O}}\mu_{\text{O}}(T,p_{\text{O}_2}) - N_{\text{H}}\mu_{\text{H}}(T,p_{\text{H}_2})\right)\end{aligned} \tag{1.56}$$

normalized to energy per unit area divided by the surface area, A[7]. Again, the most stable surface configuration minimizes the Gibbs free surface energy, $\gamma(T,p)$.

For the prediction of the most stable surface, first, the surface free energy of a series of model surfaces with different configurations as a function of their given chemical potentials is compiled in a phase diagram. The surface is in thermodynamic equilibrium with its bulk material and the surface model with the lowest surface free energy is most stable. Further, the chemical potentials are related to actual pressure and temperature conditions, under the assumption of thermodynamic equilibrium.

For bulk FeOOH the respective chemical potentials add up to the Gibbs free energy of the bulk unit cell:

$$\begin{aligned}G^{bulk}_{\text{FeOOH}}(T,p) &= n_{\text{Fe}}\mu_{\text{Fe}}(T,p_{\text{Fe}}) + n_{\text{O}}\mu_{\text{O}}(T,p_{\text{O}_2}) + n_{\text{H}}\mu_{\text{H}}(T,p_{\text{H}_2}) \\ \mu_{\text{Fe}}(T,p_{\text{Fe}}) &= \frac{1}{n_{\text{Fe}}}\left[G^{bulk}_{\text{FeOOH}}(T,p) - \frac{1}{2}\cdot n_{\text{O}}\mu_{\text{O}_2}(T,p_{\text{O}_2}) - \frac{1}{2}\cdot n_{\text{H}}\mu_{\text{H}_2}(T,p_{\text{H}_2})\right]\end{aligned} \tag{1.57}$$

With

$$\begin{aligned}\mu_{\text{O}} &= \frac{1}{2}\cdot\mu_{\text{O}_2} \\ \mu_{\text{H}} &= \frac{1}{2}\cdot\mu_{\text{H}_2}\end{aligned} \tag{1.58}$$

it comes to:

$$\begin{aligned}\mu_{\text{O}}(T,p_{\text{O}_2}) &= \frac{1}{n_{\text{O}}}\cdot\left[G^{bulk}_{\text{FeOOH}}(T,p) - n_{\text{Fe}}\mu_{\text{Fe}}(T,p_{\text{Fe}}) - n_{\text{H}}\mu_{\text{H}_2}(T,p_{\text{H}_2})\right] \\ \mu_{\text{H}}(T,p_{\text{H}_2}) &= \frac{1}{n_{\text{H}}}\cdot\left[G^{bulk}_{\text{FeOOH}}(T,p) - n_{\text{Fe}}\mu_{\text{Fe}}(T,p_{\text{Fe}}) - n_{\text{O}}\mu_{\text{O}}(T,p_{\text{O}_2})\right]\end{aligned} \tag{1.59}$$

For H_2O the chemical potentials can be expressed by its constituents.

$$\mu_{\text{H}_2\text{O}}(T,p_{\text{H}_2\text{O}}) = 2\cdot\mu_{\text{H}}(T,p_{\text{H}_2}) + \mu_{\text{O}}(T,p_{\text{O}_2}) \tag{1.60}$$

The Gibbs free surface energy can now be written as

[7] The slab possesses two equivalent surfaces, hence the factor of 1/2.

$$\begin{aligned}\gamma(T,p_i) = \frac{1}{2A}\cdot[&G^{slab}(T,p^{tot}) \\ &- \frac{N_{\mathrm{Fe}}}{n_{\mathrm{Fe}}}G^{bulk}(T,p^{tot}) \\ &- (N_{\mathrm{O}} - \frac{n_{\mathrm{O}}}{n_{\mathrm{Fe}}}N_{\mathrm{Fe}})\cdot\mu_{\mathrm{O}}(T,p_{\mathrm{O_2}}) \\ &- (N_{\mathrm{H}} - \frac{n_{\mathrm{H}}}{n_{\mathrm{Fe}}}N_{\mathrm{Fe}})\cdot\mu_{\mathrm{H}}(T,p_{\mathrm{H_2}})]\end{aligned} \tag{1.61}$$

This equation can be rearranged by replacing the expressions $\mu_{\mathrm{O}}(T,p_{\mathrm{O_2}})$ and $\mu_{\mathrm{H}}(T,p_{\mathrm{H_2}})$ according to Eq.1.60.

1. Replace $\mu_{\mathrm{H}} = 1/2\cdot(\mu_{\mathrm{H_2O}} - \mu_{\mathrm{O}})$ according to Eq.1.60:

$$\begin{aligned}\gamma(T,p_i) = \frac{1}{2A}\cdot\Bigg[&G^{slab}(T,p_{tot}) \\ &-\frac{N_{\mathrm{Fe}e}}{n_{\mathrm{Fe}}}\cdot G^{bulk}(T,p_{tot}) \\ &-\frac{1}{2}\cdot\left(N_{\mathrm{H}} - \frac{n_{\mathrm{H}}}{n_{\mathrm{Fe}e}}N_{\mathrm{Fe}}\right)\cdot\mu_{\mathrm{H_2O}} \\ &-\left(-\frac{1}{2}\cdot N_{\mathrm{H}} + \frac{1}{2}\cdot\frac{n_{\mathrm{H}}}{n_{\mathrm{Fe}}}N_{\mathrm{Fe}} + N_{\mathrm{O}} - \frac{n_{\mathrm{O}}}{n_{\mathrm{Fe}}}N_{\mathrm{Fe}}\right)\cdot\mu_{\mathrm{O}}\Bigg]\end{aligned} \tag{1.62}$$

2. Replace $\mu_{\mathrm{O}}{=}\mu_{\mathrm{H_2O}} - 2\cdot\mu_{\mathrm{H}}$ according to Eq.1.60:

$$\begin{aligned}\gamma(T,p_i) = \frac{1}{2A}\cdot\Bigg[&G^{slab}(T,p_{tot}) \\ &-\frac{N_{\mathrm{Fe}e}}{n_{\mathrm{Fe}}}\cdot G^{bulk}(T,p_{tot}) \\ &-\left(N_{\mathrm{O}} - \frac{n_{\mathrm{O}}}{n_{\mathrm{Fe}e}}N_{\mathrm{Fe}}\right)\mu_{\mathrm{H_2O}} \\ &-\left(N_{\mathrm{H}} - \frac{n_{\mathrm{H}}}{n_{\mathrm{Fe}}}N_{\mathrm{Fe}} - 2\cdot N_{\mathrm{O}} + 2\cdot\frac{n_{\mathrm{O}}}{n_{\mathrm{Fe}}}N_{\mathrm{Fe}}\right)\cdot\mu_{\mathrm{H}}\Bigg]\end{aligned} \tag{1.63}$$

Limits for the Chemical Potentials The chemical potential can be varied in the range between the lower and upper limit. The lower limit denotes the decomposition of the compound into its constituent elements

$$\mu_{\mathrm{FeOOH}}(T,p_{\mathrm{Fe,O,H}}) = n_{\mathrm{Fe}}\mu_{\mathrm{Fe}}(T,p_{\mathrm{Fe}}) + n_{\mathrm{O}}\mu_{\mathrm{O}}(T,p_{\mathrm{O_2}}) + n_{\mathrm{H}}\mu_{\mathrm{H}}(T,p_{\mathrm{H_2}}) \tag{1.64}$$

is set by the energy of formation of the compound FeOOH:

$$\Delta G^{formation}(T,p) = G^{bulk}_{\mathrm{FeOOH}}(T,p) - n_{\mathrm{Fe}} G^{bulk}_{\mathrm{bccFe}}(T,p) - n_{\mathrm{O}} G_{\mathrm{O}}(T,p) - n_{\mathrm{H}} G_{\mathrm{H}}(T,p) \tag{1.65}$$

While exceeding the upper limit leads to elemental phase condensation on the slab surface.

Limits with respect to μ_{O}

Because in experiment oxygen pressure and temperature are varied parameters, it is one way to express the limits with respect to $\mu_{\mathrm{O}_2}(\mathtt{T},p)$.

$$\min[\mu_{\mathrm{O}}(T,p)] =^{!} \frac{1}{n_{\mathrm{O}}} \cdot [G^{\mathrm{bulk}}_{\mathrm{FeOOH}}(0,0) - n_{\mathrm{Fe}} G^{\mathrm{bulk}}_{\mathrm{bccFe}}(0,0) - n_{\mathrm{H}} G_{\mathrm{H}}(0,0)] \tag{1.66}$$

If $\mu_{\mathrm{O}_2}(\mathtt{T},p)$ becomes too low, *i.e.*, the slab would decompose into its constituents and start to form Fe crystallites at the surface. Equ. 1.66 marks, therefore, the *oxygen poor* limit.

Than again under *oxygen poor* conditions, referred to as the upper limit, oxygen starts to condensate from the gas phase onto the slab surface. Still, it is inevitable to consider a reasonable T, p-range, where all constituents are thermodynamically stable. For oxygen an appropriate estimate of the maximum chemical potential is the total energy of an isolated O_2 molecule at T=0K:

$$\max[\mu_{\mathrm{O}}(T,p)] =^{!} \frac{1}{2} E^{\mathrm{total}}_{\mathrm{O}_2} \tag{1.67}$$

The range between the boundaries for μ_{O} is $\Delta G^{formation}(0,0)$:

$$\min[\mu_{\mathrm{O}}(T,p)] < \mu_{\mathrm{O}}(T,p) < \min[\mu_{\mathrm{O}}(T,p)] - \Delta G^{formation}(0,0) \tag{1.68}$$

This leads to the following expressions:

$$\begin{aligned}
\min[\mu_{\mathrm{O}}(0,0)] &= \frac{1}{n_{\mathrm{O}}} \cdot \left[G^{\mathrm{bulk}}_{\mathrm{FeOOH}}(0,0) - n_{\mathrm{Fe}} G^{\mathrm{bulk}}_{\mathrm{bccFe}}(0,0) - n_{\mathrm{H}} G^{\mathrm{gas}}_{\mathrm{H}}(0,0)\right] \\
\max[\mu_{\mathrm{O}}(0,0)] &= \frac{1}{n_{\mathrm{O}}} \cdot \left[G^{\mathrm{bulk}}_{\mathrm{FeOOH}}(0,0) - n_{\mathrm{Fe}} G^{\mathrm{bulk}}_{\mathrm{bccFe}}(0,0) - n_{\mathrm{H}} G^{\mathrm{gas}}_{\mathrm{H}}(0,0) - G^{\mathrm{formation}}(0,0)\right] \\
&= \frac{1}{n_{\mathrm{O}}} \cdot \Big[G^{\mathrm{bulk}}_{\mathrm{FeOOH}}(0,0) - n_{\mathrm{Fe}} G^{\mathrm{bulk}}_{\mathrm{bccFe}}(0,0) - n_{\mathrm{H}} G^{\mathrm{gas}}_{\mathrm{H}}(0,0) \\
&\quad - G^{bulk}_{\mathrm{FeOOH}}(0,0) + n_{\mathrm{Fe}} G^{\mathrm{bulk}}_{\mathrm{bccFe}}(0,0) + n_{\mathrm{O}} G_{\mathrm{O}}(0,0) + n_{\mathrm{H}} G_{\mathrm{H}}(0,0)\Big] \\
&= G_{\mathrm{O}}(0,0)
\end{aligned} \tag{1.69}$$

Limits with respect to $\mu_{\mathbf{H}}$

Further, limits for μ_{H_2} need to be set. In a UHV[8] chamber, residual gas as H_2 and N_2 is present.[9] The saturation limit of μ_H corresponds to an extremely H_2 rich environment, the upper limit:

$$\mu_H = 0 \tag{1.70}$$

For fixed chemical potentials of H_2O and O_2, lowering μ_{H_2} is equivalent to increasing μ_{OH} and μ_{O_2} which stabilizes OH and O rich surfaces. From the DFT energy, $E_{H_2}^{DFT,total}$, the limits are obtained as follows:

$$\begin{aligned} \min\Big[\mu_H\Big] &= \frac{1}{2}\cdot E_{H_2}^{DFT,total} + \Delta E_{H_2} \\ \Delta E_{H_2} &= \frac{1}{2}\cdot E_{H_2}^{DFT,total} + E_H^{DFT,total} \\ \max[\mu_H] &= \frac{1}{2}\cdot E_{H_2}^{DFT,total} \end{aligned} \tag{1.71}$$

$$\begin{aligned} \min[\mu_H(0,0)] &= \frac{1}{n_H}\cdot\Big[G_{FeOOH}^{bulk}(0,0) - n_{Fe}G_{bccFe}^{bulk}(0,0) - n_O G_O^{gas}(0,0)\Big] \\ \max[\mu_H(0,0)] &= \frac{1}{n_H}\cdot\Big[G_{FeOOH}^{bulk}(0,0) - n_{Fe}G_{bccFe}^{bulk}(0,0) - n_O G_O^{gas}(0,0) - G^{formation}(0,0)\Big] \\ &= G_H^{gas}(0,0) \end{aligned} \tag{1.72}$$

Limits with respect to $\mu_{\mathbf{H_2O}}$

Taking the formation energy as water

$$E_{H_2O}^{formation} = E_{H_2O}^{total} - E_{H_2}^{total} - {}^1\!/_2\cdot E_{O_2}^{total} \tag{1.73}$$

Water rich and poor conditions are calculated as follows

$$\begin{aligned} E_{H_2O}^{total} + E_{H_2O}^{formation} &< \mu_{H_2O}(T,p) < E_{H_2O}^{total} \\ 2\cdot E_{H_2O}^{total} - E_{H_2}^{total} - {}^1\!/_2\cdot E_{O_2}^{total} &< \mu_{H_2O}(T,p) < E_{H_2O}^{total} \end{aligned} \tag{1.74}$$

[8] UHV=Ultra High Vacuum

[9] reasonable pressure range between 10^{-9} to 10^{-9}mbar, very low is 10^{-10}mbar

2 The FeOOH Polymorphs: High Pressure Behavior and Adsorption Processes at Their Surfaces

- **Manuscript 1**
  Pressure Induced Structural and Electronic Transitions in FeOOH from First Principles, K. Otte, R. Pentcheva, W.W. Schmahl, and J.R. Rustad, Physical Review B **80**, 205116 (2009).

- **Manuscript 2**
  Density Functional Theory Study of Water Adsorption on FeOOH Surfaces, K. Otte, W.W. Schmahl, and R. Pentcheva, Surface Science **606**, 1623 (2012).

- **Manuscript 3**
  DFT+U Study of Arsenate Adsorption on FeOOH Surfaces: Evidence for a Monodentate Adsorption Configuration at Ambient Conditions, K. Otte, W.W. Schmahl, and R. Pentcheva, Journal of Physical Chemistry C, submitted (2012).

Manuscript 1: Pressure Induced Structural and Electronic Transitions in Bulk FeOOH

Pressure Induced Structural and Electronic Transitions in FeOOH from First Principles

K. Otte, R. Pentcheva, W.W. Schmahl, and J.R. Rustad,
Physical Review B **80**, 205116 (2009).

Pressure-induced structural and electronic transitions in FeOOH from first principles

Katrin Otte,[1,*] Rossitza Pentcheva,[1,†] Wolfgang W. Schmahl,[1] and James R. Rustad[2,‡]
[1]*Department of Earth and Environmental Sciences, University of Munich, Theresienstr. 41, 80333 Munich, Germany*
[2]*Geology Department, University of California–Davis, One Shields Avenue, Davis, California 95616, USA*
(Received 23 July 2009; revised manuscript received 23 September 2009; published 18 November 2009)

Using density-functional theory, we investigate the stability, structural, magnetic, and electronic properties of the iron oxyhydroxide polymorphs [α-, β-, γ-, and $hp(\epsilon)$-FeOOH] under hydrostatic pressure. At ambient conditions goethite (α) is the lowest energy phase, consistent with recent calorimetric measurements. Around 6–7 GPa we predict a transformation to the high-pressure $hp(\epsilon)$ phase. This structural transformation is followed by a high-spin to low-spin transition at 7.7 GPa, at much lower pressure than for other currently discussed iron-bearing minerals. While in the ground state the Fe^{3+} ions are coupled antiferromagnetically, at high pressures a strong competition to a ferromagnetic alignment is found in $hp(\epsilon)$-FeOOH. Concerning the electronic properties, including an on-site Coulomb repulsion parameter U (LDA/GGA+U method) improves the size of the zero-pressure band gaps substantially but shifts the spin transition to higher pressure (56.5 GPa). The predicted spin crossover is associated with a blueshift of 0.4 eV.

DOI: 10.1103/PhysRevB.80.205116 PACS number(s): 91.60.Gf, 71.30.+h, 75.30.Wx, 71.27.+a

I. INTRODUCTION

The iron oxyhydroxides (FeOOH) play an important role in nature and technology. They are common minerals in aquifers, sediments, and in the Earth's crust. In the soil they act as natural regulators of concentration and dissolution of nutrients or pollutants such as heavy metals[1,2] and arsenic complexes,[3] thus finding application in the treatment of contaminated water. FeOOH belongs to the group of *X*OOH minerals (X=Fe, Al, Mn, Co, and Cr), which crystallize in five canonical oxyhydroxide structures: diaspore, boehmite, akaganeite, guyanaite, and grimaldiite, named after the main representative. The iron oxyhydroxides have been identified crystallographically in the structures of diaspore as goethite (α),[4] of boehmite as lepidocrocite (γ),[5] as akaganeite (β),[6] and of guyanaite as the high-pressure [$hp(\epsilon)$] form.[7]

The FeOOH structures consist of corner-linked bands (single or double) of $FeO_3(OH)_3$ octahedra. The linkage of these bands results in different framework structures as shown in Fig. 1 (see also Table I). In the α phase the double bands of edge-sharing octahedra form 2×1 channels while in β-FeOOH the arrangement of double bands results in 2×2 channels, which are stabilized in nature by a variable amount of molecules such as H_2O and ions such as OH^-, Cl^-, F^-, or NO_3^-. In γ-FeOOH (lepidocrocite), the double bands along the c axis form zigzag layers, that are connected to each other via hydrogen bonds (OH$\cdots$O). The iron ions are surrounded by three nonequivalent oxygen atoms as a result of the zigzag sheets. The $hp(\epsilon)$ phase is isostructural to InOOH and the only structure composed of corner sharing single bands of octahedra. This results in a dense 1×1 arrangement along the c axis with interstitial hydrogen.

The polymorphs often have high surface areas and high adsorption affinities for aqueous solutes. Therefore, subtle changes in surface chemical environments in terms of temperature, humidity, impurity ions, and crystallization rates can have an important influence on the observed mineral assemblages in low-temperature environments. Their magnetic properties are sensitive to soil redox conditions and solution compositions.[8] Thus, the oxyhydroxide minerals can potentially serve as sensitive recorders of climate history, providing insights into crucial questions concerning the evolution of the Earth's atmosphere on geologic timescales.[9]

Despite the importance of this system in the Earth sciences, there is only one previous theoretical study on the relative stability of the FeOOH polymorphs at zero pressure based on DFT calculations using pseudopotentials.[10] An unexpected finding is that the $hp(\epsilon)$ phase was predicted to be the most stable polymorph at ambient conditions. The discrepancy to recent calorimetric measurements[11,12] has motivated us to revisit this problem employing an all-electron DFT method. Moreover, the high-pressure behavior of hydrous Fe-bearing minerals is important for understanding the processes in the Earth's crust and upper mantle. In this respect FeOOH can be regarded as a model system for achieving a better understanding of the role of hydrogen bonding at high pressures.[13,14] Hence, a main goal of this study is to explore the pressure dependence of the FeOOH polymorphs.

The theoretical description of iron-bearing minerals represents a challenge for first-principles methods due to their complex structure, the localized 3d orbitals of Fe, and the influence of correlation effects. Therefore, one aspect of this study is to examine how the level of treatment of electronic correlations influences the energetic, structural, and electronic properties.

In this paper we present a detailed study of the energetic stability of the polymorphs [α-, β-, γ-, and $hp(\epsilon)$-FeOOH] at ambient conditions and under pressure. Moreover, we determine the equation of state and compare the bulk moduli and equilibrium volumes to available experimental data. The focus of the present study lies on pressure-induced structural and spin transitions. We predict that the α phase (goethite) transforms at approximately 6–7 GPa to $hp(\epsilon)$-FeOOH. Furthermore, a collapse from a high-spin (HS) to a low-spin (LS) state is found for the $hp(\epsilon)$ phase. The transition takes place at considerably lower pressures than in magnesiowüstite[15,16] or silicate perovskites,[17,18] which are currently in the center of discussion of spin-crossover phenomena.

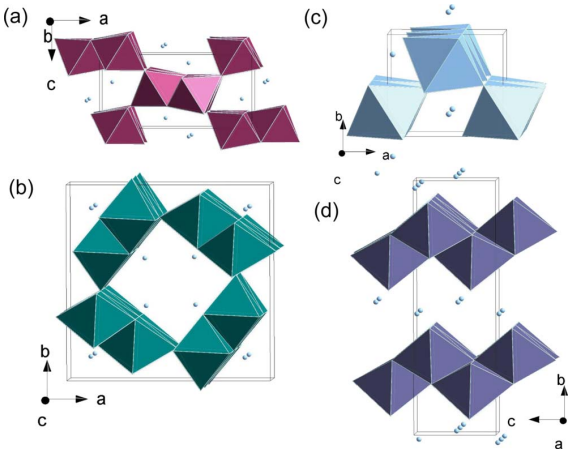

FIG. 1. (Color online) The structures of the FeOOH polymorphs represented in terms of $FeO_3(OH)_3$ octahedra where the hydrogen atoms (in light blue/gray) reside in the 2×1, 2×2, and 1×1 channels of (a) α-FeOOH (goethite), (b) β-FeOOH (akaganeite), and (c) $hp(\epsilon)$-FeOOH, respectively, or between the zigzag sheets of (d) γ-FeOOH (lepidocrocite)

In the following (Sec. II) we discuss briefly the calculational details. In Sec. III we compare the calculated relative energetic stability of the polymorphs to calorimetric measurements.[11] The equation of state of the polymorphs is determined in Sec. IV together with theoretical evidence for a transition from the α- to the $hp(\epsilon)$ phase between 5.9 and 7 GPa. We reexamine previous experimental data and find indications for such a phase transition. In Sec. V we describe the structural changes under pressure. The pressure-induced magnetic and spin transition in $hp(\epsilon)$-FeOOH is discussed in Sec. VI and related to the electronic properties in Sec. VII. The results are summarized in Sec. VIII.

II. CALCULATIONAL DETAILS

The DFT calculations were performed with the full-potential all-electron linear augmented plane-wave method in the WIEN2K implementation.[19] The generalized gradient approximation (GGA) (Ref. 20) of the exchange and correlation potential was used. Because electronic correlations play an important role in transition-metal oxides, we have explored their influence beyond GGA by including an on-site Coulomb repulsion parameter U within the GGA+U approach.[21] While U values obtained from constrained local-density approximation tend to be higher (7–8 eV),[22] a recent study of Fe^{2+} in magnesiowüstite determined U parameters between 5 and 6 eV from linear-response theory.[16] The authors reported also a pressure dependence of the U parameter but the absolute U value changes by less than 1 eV for a volume reduction of 30%. Therefore, in order to compare total energies as a function of pressure, we have used a consistent value of $U=5$ eV and $J=1$ eV on the Fe ions throughout the calculations, similar to other studies on iron oxides.[23,24] Due to the small muffin-tin (MT) radius of hydrogen [$R_{MT}(Fe)=1.9$ bohr, $R_{MT}(O)=1.0$ bohr, and $R_{MT}(H)=0.6$ bohr], a high energy cutoff of 36 Ry was chosen in order to achieve an accuracy of total energies of 1 mRy. For the integration in reciprocal space 48, 21, 84, and 32 $\boldsymbol{k}$ points were used in the irreducible part of the Brillouin zone for the α-, β-, γ-, and $hp(\epsilon)$ phase, respectively. Inside the MTs the wave functions were expanded in spherical harmonics with angular momenta up to $l_{max}^{wf}=10$. Nonspherical contributions to the electron density and potential up to $l_{max}^{pot.}=6$ were used within the MT and a cutoff of 196 Ry in the interstitial.

Information on the structural and magnetic parameters is given in Table I. An optimization of the internal parameters under hydrostatic pressure was performed both within GGA and GGA+U.

III. ENERGETIC STABILITY OF THE FeOOH POLYMORPHS

DFT calculations were carried out for the different polymorphs both for a ferromagnetic (FM) and an antiferromagnetic (AFM) coupling of the Fe ions. For all systems, except for the $hp(\epsilon)$ phase at high pressures, the AFM case is the ground state in agreement with experiment.[25] The energy volume, $E(V)$, as well as the enthalpy pressure, $\Delta H(p)$, relations of the polymorphs are presented in Fig. 2.

TABLE I. Experimental data on the (magnetic) structure of the different polymorphs showing the lattice parameters, volume, space group (SG), Wykoff letter, and multiplicity of the ions (site). The formula units per unit cell ($\frac{\text{f.u.}}{\text{u.c.}}$) correspond to the size of the simulation cell, except for γ-FeOOH, where only 2 f.u. remain in the reduced cell. Additionally, the type of octahedral arrangement and channels in the respective structures is given as well as the Néel temperature and orientation of the spins along the crystallographic axes.

	Lattice parameter								
Phase	a (Å)	b (Å)	c (Å)	V (Å)	SG	Site	$\frac{\text{f.u.}}{\text{u.c.}}$	Octahedra arrangements	T_N spin (K)
Goethite (α)	9.95	3.01	4.62	138.37	*Pnma*	4*c*	4	Double bands, 2×1 tunnels	400$\|b$
Akaganeite (β)	10.48	10.48	3.02	332.02	$I\frac{4}{m}$	8*h*	8	Double bands, 1×1 and 2×2 tunnels	270$\|c$
Lepidocrocite (γ)	3.07	12.52	3.87	148.91	*Cmcm*	4*a*	4	Zigzag layers	77$\|c$
$hp(\epsilon)$ [a]	4.94	4.43	2.99	65.5 1	$Pmn2_1$	2*a*	2	Single bands, 1×1 tunnels	470$\|c$

[a]Reference 7.

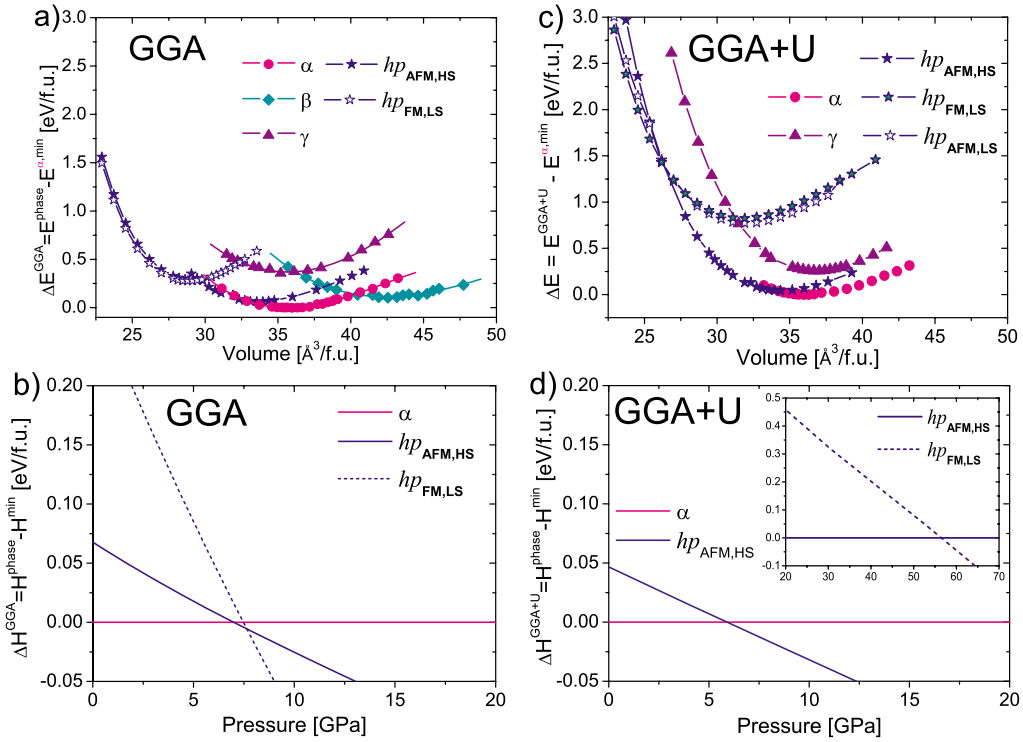

FIG. 2. (Color online) Energy as a function of volume and enthalpy-pressure relation $\Delta H(p)$ for the different polymorphs within GGA (left panels) and GGA+U (right panels). The total energy at the equilibrium volume, V_0, of the most stable α phase is set to zero. $\Delta H(p) < 0$ indicates phases that are more stable than the α-phase [or $hp(\epsilon)_{AFM,HS}$ in the inset in (d)] for a given pressure.

The relative stabilities of the different phases with respect to the α phase at zero pressure are displayed in Table II. Our results reveal that goethite is the most favorable phase at ambient conditions both within GGA and GGA+U. Within GGA the α phase is followed in stability by the $hp(\epsilon)$ (0.07 eV/f.u.), β- (0.11 eV/f.u.), and γ phase (0.37 eV/f.u.), which is the least stable one. A similar trend is obtained within GGA+U: $hp(\epsilon)$-FeOOH is 0.05 eV/f.u. less favorable than the α phase, followed by the γ phase (0.25 eV/f.u.).

These results agree with calorimetric measurements[11] which found energy differences with respect to the most stable α phase of $\Delta E^{\beta}=0.08$ eV/f.u. and $\Delta E^{\gamma}=0.14$ eV/f.u. [data for the $hp(\epsilon)$ phase were not reported in this study]. These relative stabilities indicate that the framework structure is more favorable than the layered one.

IV. EQUATION OF STATE: EVIDENCE FOR A PHASE TRANSITION

The equation of state is obtained through a third order Birch-Murnaghan (BM) fit.[27] To identify possible phase transitions, we have determined the enthalpy $H=E+pV$, where the pressure is obtained as an energy derivative with respect to the volume $p=-\frac{dE}{dV}$ from the third-order BM fit. In Figs. 2(b) and 2(d) we have plotted the enthalpy difference with respect to the α phase ($\Delta H=H^{phase}-H^{\alpha}$). While goethite is stable at ambient conditions, for negative pressures akaganeite becomes more favorable. At high pressures, our calculations predict that goethite transforms into the $hp(\epsilon)$ phase. The transition pressure is 7 GPa within GGA and slightly lower within GGA+U (5.9 GPa). Furthermore, a spin transition from a high-spin to a low-spin state is found which occurs within GGA at 7.7 GPa and within GGA+U at 56.5 GPa. The respective transition pressures are also listed in Table III.

Table II contains the equilibrium volume V_0, the bulk modulus B_0, and its pressure derivative B_0' for each phase. Experimentally determined volumes are also listed. Bulk moduli are available so far only for the α (Refs. 13 and 26) and the $hp(\epsilon)$ phase.[13] In the following we will discuss the properties of the FeOOH polymorphs and also reexamine previous experimental findings in the context of the predicted phase and spin transitions.

A. Equilibrium volume

Generally, both GGA and GGA+U overestimate the equilibrium volume. For goethite, the GGA/GGA+U values are 2.7%/4.3% larger than the V_0 determined by Szytula *et al.*[4] On the other hand, there is much better agreement to the data reported in a more recent synchrotron x-ray diffraction (XRD) study by Nagai *et al.*[26](1.1%/2.8%). A recent DFT study[28] of goethite obtained similar results (1.1%/5.1% larger than the ones reported by Szytula *et al.*[4]) while the values

TABLE II. Relative stability of the polymorphs ($\Delta E = E^{\text{phase}} - E^{\alpha,\text{min}}$) with respect to the most stable phase (α) calculated within GGA and GGA+U. The results for the equilibrium volume, bulk modulus, and B_0' of the different polymorphs are compared to available experimental data.

Phase	Method	ΔE ($\frac{\text{eV}}{\text{f.u.}}$)	V_0 ($\frac{\text{Å}^3}{\text{f.u.}}$)	B_0 (GPa)	B_0'
α	GGA	0.00	35.5	90.6	5.8
	GGA+U	0.00	36.1	108.8	5.9
	Experiment[a]		34.6		
	Experiment[b] (0–11.0 GPa)			108.5	4
	Experiment[b] (0–24.5 GPa)		35.1	111	4
	Experiment[c] (0–29.4 GPa)		34.7	140.3	4.6
β	GGA	0.11	42.6	76.4	2.1
	GGA+U	0.18	42.6	194.7	1.4
	Experiment[d]		41.5		
γ	GGA	0.37	35.7	107.1	0.7
	GGA+U	0.25	36.8	158.9	4.6
	Experiment[e]		37.0		
AFM coupling					
hp_{HS}	GGA	0.07	33.8	104.0	5.6
	GGA+U	0.05	34.5	123.2	5.7
hp_{LS}	GGA+U	0.76	32.0	152.7	4.6
FM coupling					
hp_{HS}	GGA+U	0.22	34.9	124.3	5.9
hp_{LS}	GGA	0.28	28.9	187.0	6.0
	GGA+U	0.83	31.7	135.1	5.9
hp	Experiment[f]		32.7		
	Experiment[c]		33.2	158	4

[a]Reference 4.
[b]Reference 26.
[c]Reference 13.
[d]Reference 6.
[e]Reference 5.
[f]Reference 7.

obtained by Kubicki *et al.*[29] coincide with the experimental data of Szytula *et al.*[4] both within GGA and GGA+U.

The theoretical equilibrium volume for the $hp(\epsilon)$ phase is 33.8 Å^3 (GGA) and 34.5 Å^3 (GGA+U) again larger than the experimental one (33.15 ± 0.5 Å^3).[13] We find that the predicted pressure-induced spin transition invokes a substantial volume reduction of 14.5%/8.1% within GGA/GGA+U to $V_0^{\text{FM,LS}} = 28.9/31.7$ Å^3.

TABLE III. Respective transition pressures within GGA and GGA+U for the phase transformation from α- to $hp(\epsilon)$-FeOOH as well as the spin crossover in the $hp(\epsilon)$ phase from a HS, AFM to an LS, FM state.

	Phase transition $\alpha \rightarrow hp(\epsilon)$ (GPa)		Spin crossover $hp(\epsilon) \rightarrow hp(\epsilon)$ (GPa)	
Method	HS, AFM	HS, AFM	HS, AFM	LS, FM
GGA	7		7.7	
GGA+U	5.9		56.5	

B. Compressibility

Concerning the bulk moduli, there is an excellent agreement between the GGA+U value for goethite (108.8 GPa) and the experimental bulk modulus determined by Nagai *et al.*[26] in the range 0–11 GPa (108.5 GPa). GGA tends to underestimate the bulk modulus ($B_0^{\text{GGA}} = 90.6$ GPa). Similar values were found by Russell *et al.*[28] We observe a strong dependence of the experimental B_0 on the pressure range used in the fit. For example, Nagai *et al.*[26] obtained 111 GPa using XRD data for 0–24.5 GPa. A substantially higher value of 140.3 ± 3.7 GPa was obtained by Gleason *et al.*[13] who applied a BM fit on XRD data in the pressure range 0–29.4

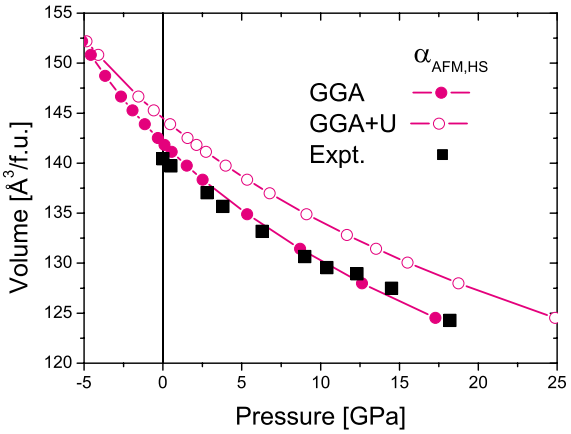

FIG. 3. (Color online) Volume as a function of pressure within GGA (filled circles) and GGA+U (open circles). For comparison, the experimental data of Nagai *et al.* (Ref. 26) (black squares) is added and shows very good agreement with the GGA results.

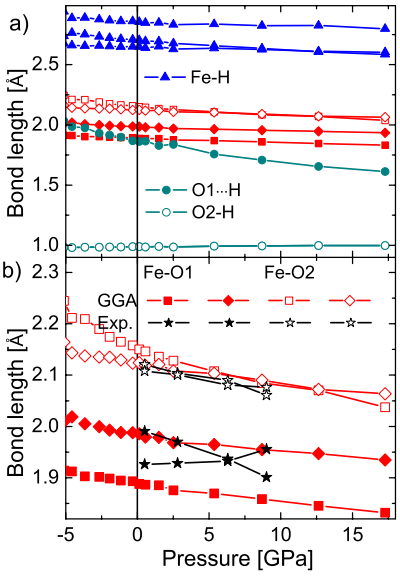

FIG. 4. (Color online) (a) Bond lengths in α-FeOOH as a function of pressure within GGA. (b) Pressure dependence of the Fe-O bonds in α-FeOOH within GGA: the filled symbols denote the different Fe-O1 bonds, the open symbols the different Fe-O2 bonds. Additionally, the bond lengths up to 9 GPa obtained by Nagai *et al.* (Ref. 26) from XRD measurements (black stars).

GPa. This value even exceeds the one for the isostructural diaspore [134.4 ± 1.4 GPa (Ref. 30) and 143.7 GPa (Ref. 31)], that has a substantially smaller volume and is thus expected to have a higher B_0 than goethite. We believe that this variation in the experimental bulk moduli with the pressure interval used in the BM fit is rather related to the phase transformation predicted here from the α- to the $hp(\epsilon)$ phase at 6–7 GPa.

For the $hp(\epsilon)$ phase the bulk moduli are higher than for α-FeOOH: 104 GPa/123 GPa for the HS AFM state within GGA/GGA+U, respectively. The transition to a low-spin state leads to a further increase in B_0. The value determined by Gleason *et al.*[13] (158 ± 5 GPa) is in agreement to the LS state with AFM coupling of the iron spins (152 GPa).

C. Volume-pressure dependence

Further indications for the predicted phase transition can be found in the volume versus pressure dependence presented in Fig. 3. In fact, the $V(p)$ data of Nagai *et al.*,[26] which are also plotted in Fig. 3, exhibit a kink at around 10–11 GPa accompanied by a discontinuous broadening of diffraction peaks. Similar features were observed also by Gleason *et al.*[13] above 8 GPa. Although these features were associated with a solidification of the pressure medium, they may be related to a beginning phase transformation.

V. PRESSURE DEPENDENCE OF THE BOND LENGTHS

In this section we discuss how the bond lengths change under pressure. In goethite there are two different types of oxygen atoms shared between the octahedra: O2 is part of the hydroxyl group in Fe-O2-H while O1 supplies the hydrogen bridge in Fe-O1···H. In Fig. 4(a), the different bond distances in goethite, namely, the Fe-O(1,2), O(1,2)-H, and Fe-H obtained from GGA are plotted as a function of pressure. Bond shortening is observed as a result of compression in all cases but the strongest effect occurs for the hydrogen-bridge distance (O1···H). This indicates that bulk compression takes place through contraction of the channels rather than the FeO_6 octahedra. A similar observation was made in the XRD study of Nagai *et al.*,[26] who found for a 7% volume reduction only 3% contraction of the FeO_6 octahedra.

Due to the different bonds of oxygen to H, there are four distinct Fe-O distances. Their pressure dependence from DFT and experiment is plotted in Fig. 4(b). The bond lengths at 0 GPa range from 1.9 Å (Fe-O1) to 2.15 Å (Fe-O2). We find that the longer Fe-O2 bonds decrease more rapidly than the Fe-O1 bonds with increasing pressure. The DFT-GGA bond lengths are in good agreement with the ones derived from XRD data[26] up to 9 GPa, which are also shown in Fig. 4(b).

OH bond-length variation with pressure

Because H is a weak x-ray scatterer, it is difficult to locate the H atoms from XRD experiments. DFT calculations can provide here useful information on the OH bonds. Fig. 5 presents the variation in the OH bond lengths for the different polymorphs with pressure obtained within GGA. As discussed above, for α-FeOOH the hydrogen bridge shows the strongest variation with pressure while the bond length of the hydroxyl group remains nearly constant (≈1.0 Å). This trend is also observed for the $hp(\epsilon)$ phase, which is the only polymorph, where a symmetrization of O2-H···O1 occurs above 40 GPa. Williams and Guenther[14] measured infrared (IR) spectra of goethite up to 24 GPa and found that a double peak feature at ≈900 cm^{-1} turns into a single peak at 9.8 GPa. Here, the hydrogen reaches a position equidistant to the

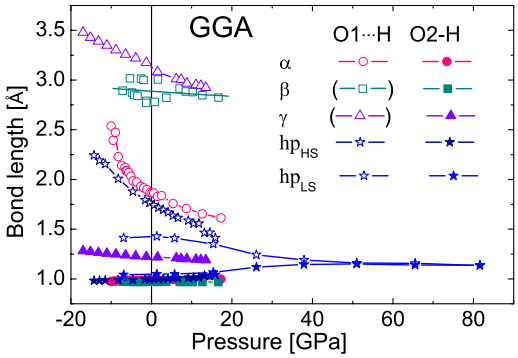

FIG. 5. (Color online) Variation in the hydroxyl bonds (O-H) and the hydroxyl bridges (O···H) for the different phases. The length of the hydrogen-bridge bond exhibits the strongest variation with pressure. In the case of $hp(\epsilon)$-FeOOH, a symmetrization of the OH bonds is observed above 40 GPa.

three Fe ions as in the $hp(\epsilon)$ phase. This feature may be related to the predicted phase transition.

In akaganeite, the oxygen-hydrogen distances remain nearly constant with pressure. This is also true for the O-H bond length in the layered γ-FeOOH of $\approx$1.2 Å, somewhat longer than the typical length in a hydroxyl group. On the other hand, the O···H bridge is reduced from 3.1 Å at ambient conditions to 2.9 Å at 15 GPa.

VI. MAGNETIC PROPERTIES AND PRESSURE-INDUCED SPIN CROSSOVER

The orientation of the spins with respect to the crystallographic axes are specified in Table I (last column). As mentioned previously, we have investigated both ferromagnetic and antiferromagnetic coupling of the Fe ions. For the latter case we have adopted the experimentally suggested magnetic structure.[25] This magnetic order is determined by two main interactions (following the scheme of Coey[32]): (i) a strong AFM coupling of Fe in corner sharing octahedra with an Fe-O-Fe bond angle close to 120° and (ii) a weak AFM coupling for edge-sharing octahedra (i.e., within the double bands) with a Fe-O-Fe bond angles close to 90°.

Table IV shows the magnetic moments of Fe ions in the different phases as well as the energy difference between the FM and AFM coupling ($\Delta E = E_{\mathrm{FM}} - E_{\mathrm{AFM}}$) at the experimental volume. At zero pressure the AFM order is clearly the ground state for all phases ($\Delta E > 0$), in agreement with experimental observations.[25] A stronger competition between the AFM and FM coupling is found only for lepidocrocite: $\Delta E_{\gamma} = 0.07$ eV compared to $\Delta E_{\alpha} = 0.42$ eV. This finding is consistent with the much lower Néel temperature for the γ phase ($T_{\mathrm{N}} = 77$ K) than for the α phase ($T_{\mathrm{N}} = 400$ K).

For all phases except for γ-FeOOH we observe a HS-LS transition in the FM case within GGA. We find that in the AFM state the magnetic moments at V_{exp} are higher (3.61 μ_B) than in the FM state (3.39 μ_B) and remain in a HS configuration under pressure with only a small reduction. The magnetic moments within GGA+U (4.14 μ_B) are larger compared to GGA. This is related to a reduced occupation in the minority-spin channel, as will be discussed in the next section. For goethite iron remains in HS state within the studied pressure range.

On the other hand, in the $hp(\epsilon)$ phase there is a transition from AFM coupled Fe ions in high-spin state to a FM coupling with a low-spin configuration and a magnetic moment of 0.97 μ_B. Within GGA the spin transition takes place at 7.7 GPa [see Fig. 2(b) dashed line] while within GGA+U

TABLE IV. Magnetic and electronic properties of the polymorphs. ΔE denotes the energy difference between the FM and AFM order in GGA ($\Delta E = E_{\mathrm{FM}} - E_{\mathrm{AFM}}$). Additionally, the magnetic moments as well as the calculated and experimental band gaps (Ref. 25) of all phases within GGA and GGA+U are displayed both for the experimental volume and the respective minimum volume, i.e., at maximum pressure. (m=metallic).

		ΔE ($\frac{\mathrm{eV}}{\mathrm{f.u.}}$)	Magnetic moments, M (μ_B)				Band gaps, Δ_g^{phase} (eV)				
		@V_{exp}	@V_{exp}		@V_{min}		@V_{exp}		@V_{min}		Expt. (Ref. 25)
		GGA	GGA	GGA+U	GGA	GGA+U	GGA	GGA+U	GGA	GGA+U	@p=0
α	FM	0.42	3.39	4.21	0.85	0.95	m	1.47	m	2.84	
	AFM		3.61	4.13	3.41	4.10	0.27	2.21	0.15	2.04	2.10
β	FM	0.55	2.87	4.21	0.86	0.96	m	1.43	m	1.79	
	AFM		3.58	4.12	3.21	4.05	0.57	2.44	0.12	1.43	2.12
γ	FM	0.07	3.72	4.21	3.20	3.24	m	1.61	m	m	
	AFM		3.85	4.18	2.79	4.01	m	1.69	m	m	2.06
hp_{HS}	FM			4.22		4.18		1.6		0.24	
	AFM		3.57	4.13		3.88	0.28	2.07		1.00	1.94
hp_{LS}	FM	0.21	0.88/0.84	0.99	0.86	0.93	m	2.40	m	2.46	
	AFM			1.02/0.96	0.84	0.93/0.90		1.90	m	1.30	

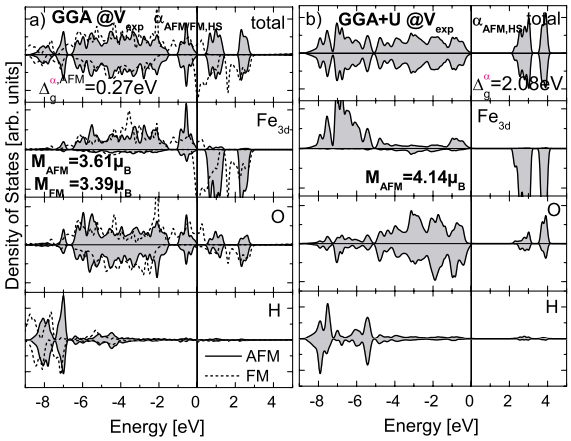

FIG. 6. (Color online) DOS of α-FeOOH at V_{exp}. The left panel shows the GGA results for the FM (dashed line) and AFM coupling (solid line, gray area), the right one the GGA+U results for AFM. V_{exp} corresponds to pressures of 2 GPa within GGA and 4 GPa within GGA+U, respectively.

the HS state collapses to the LS state at a much higher pressure of 56.5 GPa [inset in Fig. 2(d) dashed line]. The $E(V)$ relation within GGA+U [Fig. 2(c)] reveals for Fe in the low-spin state a strong competition between the ferromagnetic and the antiferromagnetic coupling in $hp(\epsilon)$-FeOOH.

We note that no intermediate spin states were obtained in FeOOH. Such have recently been reported for ferrous iron (Fe^{2+}) in lower mantle (post)perovskites.[33,34]

VII. ELECTRONIC PROPERTIES

A. Band gaps

The density of states (DOS) of the different phases were calculated at the experimental volume as well as under pressure. The DOS of the most stable polymorph goethite at the experimental volume within GGA [Fig. 6(a)] shows the sensitive influence of the magnetic coupling on the electronic properties: for FM order the system is metallic while the AFM ground state shows insulating character. However, GGA ($\Delta_g^{\alpha,\mathrm{GGA}}$=0.27 eV) substantially underestimates the experimental band gap of 2.1–2.5 eV.[25,35] Including correlation effects within GGA+U [see Fig. 6(b)] improves the size of the band gap to $\Delta_g^{\alpha,\mathrm{GGA}+U}$=2.08 eV in close agreement with the experimental value. Additionally, the type of band-gap changes from a Mott-Hubbard type (GGA) between empty and occupied Fe 3d states to a charge-transfer type (GGA+U), separating the occupied O 2p from unoccupied Fe 3d states. Analogous behavior was obtained for α-Fe_2O_3.[24,36]

The electronic properties of the other polymorphs given in Table IV show similar trends. While all FM coupled phases are metallic within GGA (except for β), the AFM coupled systems have nonzero band gaps (except for lepidocrocite), which are strongly underestimated compared to experiment. At high pressures, the small band gaps are further reduced to a pseudogap (α and β) or the system becomes metallic

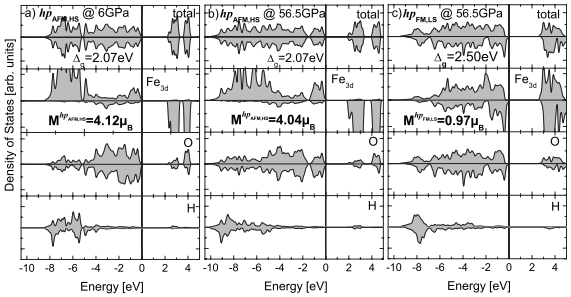

FIG. 7. DOS of $hp(\epsilon)$-FeOOH illustrating the spin transition associated with a change in magnetic order obtained within GGA+U: (a) $hp(\epsilon)$-FeOOH (AFM, HS) at the phase transition pressure of 5.9 GPa; at 56.5 GPa the spin crossover takes place in $hp(\epsilon)$-FeOOH from (b) an AFM, HS state to (c) an FM, LS state.

[$hp(\epsilon)$] within GGA. GGA+U reduces the hybridization between Fe 3d and O 2p bands and leads to a charge-transfer type of band gap with band widths in close agreement to the experimental values.

B. Pressure-induced spin transition in $hp(\epsilon)$-FeOOH

The DOS of $hp(\epsilon)$-FeOOH with antiferromagnetically coupled Fe in high-spin state obtained within GGA+U at the respective phase and spin transition pressures of 5.9 and 56.5 GPa is presented in Figs. 7(a) and 7(b). At 56.5 GPa the valence band is approximately 1.5 eV broader than at 6 GPa. Additionally, the hybridization between Fe 3d and O 2p states is substantially increased. For the HS state all Fe 3d orbitals in the majority-spin channel are occupied, the ones in the minority-spin channel are empty. A substantial rearrangement takes place with the spin transition [Fig. 7(c)]: two electrons now occupy t_{2g} states in the minority-spin channel while the e_g orbitals are empty for both spin directions. As a result, the lower Hubbard band is narrowed by approximately 1 eV and there is a blueshift of the band gap from 2.07 eV (AFM, HS) to 2.50 eV (FM, LS) at 56.5 GPa. A similar effect was reported, e.g., in $(Mg,Fe)SiO_3$.[18] The change in orbital occupation is visualized also in Fig. 8 which shows the spin-density distributions of Fe^{3+} at the spin transition pressure (GGA+U). While in the HS state [Fig. 8(a)] all Fe 3d orbitals are singly occupied leading to a spherical spin-density distribution, the LS state [Fig. 8(b)]

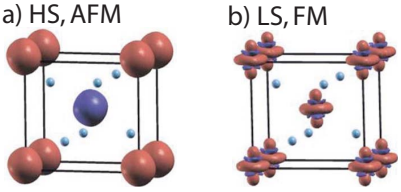

FIG. 8. (Color online) Spin-density distribution of $hp(\epsilon)$-FeOOH at 56.5 GPa for Fe^{3+} in (a) HS, AFM and (b) LS, FM state. Fe is octahedrally coordinated by oxygen (light blue/gray); the hydrogen positions are not shown.

exhibits a clear t_{2g} character with lobes pointing to the faces of the surrounding oxygen octahedron.

VIII. SUMMARY

In summary, we present a comprehensive DFT study of the bulk properties of the FeOOH polymorphs goethite (α), akaganeite (β), lepidocrocite (γ), and the $hp(\epsilon)$ phase at ambient conditions and under hydrostatic pressure. We find that at zero-pressure goethite is the lowest energy phase. Akaganeite becomes favorable only upon volume expansion, which suggests that it is stabilized at ambient conditions by additional ions in its channels. At ambient conditions the α phase is followed in stability by the $hp(\epsilon)$-, β-, and γ phases. The energetic relations among the phases show that the framework structures [α, $hp(\epsilon)$, and β] are more favorable than the layered one (γ) and are in agreement with the trends obtained from calorimetric measurements of Laberty and Navrotsky.[11] Thus, overall, the observed occurrences of these phases in the field are consistent with the calculated cohesive energies and do not appear to be governed primarily by kinetics or surface effects.

A pressure-induced transition from the α- to the $hp(\epsilon)$ phase is predicted at 6–7 GPa. This finding is supported by previous IR data by Ref. 14. Furthermore, Ref. 37 reported the synthesis the $hp(\epsilon)$-phase samples at pressures of 8 GPa, similar to the predicted transition pressure. Voigt and Will[38] determined the boundary line between α- and $hp(\epsilon)$-FeOOH in the range between 6 and 7.5 GPa at temperatures above 573 K. This is confirmed by recent XRD measurements[13] pointing also at a slow conversion from α- to $hp(\epsilon)$-FeOOH above 5 GPa and below 573 K. Further studies will be necessary to shed more light on this transition.

Furthermore, the structure influences not only the stability but also the compressibility. Due to its large 2×2 channels, akaganeite is most compressible. For goethite the bulk modulus obtained within GGA+U (108.8 GPa) is in very good agreement with the value obtained from XRD experiments (108.5 GPa).[26] The bulk modulus of the $hp(\epsilon)$ phase is significantly higher (152.7 GPa for HS AFM), again in good agreement with very recent experimental data (158 GPa).[13] We are not aware of any previous results in the literature for the other FeOOH phases.

The pressure dependence of the bond lengths for the α phase is in good agreement with experiment.[26] The O···H bridge of the α- and $hp(\epsilon)$ phase shows the strongest change with pressure indicating that compression takes place by contracting the channels. For the $hp(\epsilon)$ phase a symmetrization of the O-H bonds occurs beyond 40 GPa.

While GGA shows a closer agreement to experiment concerning the equilibrium volume as well as the pressure dependence of the volume and bond lengths, GGA+U provides a better description of the bulk moduli and improves considerably the band gaps. Under ambient conditions all phases are coupled antiferromagnetically and insulating. For the $hp(\epsilon)$ phase we find a HS-LS transition at 7.7 GPa within GGA. Because GGA+U tends to stabilize the HS state, this transition is shifted to 56.5 GPa. Still these pressures are significantly lower than the values reported, e.g., for iron-bearing perovskites or magnesiowüstite and may suggest that the presence of OH^- in the coordination shell of Fe^{3+} facilitates the HS-LS transition. One possible explanation may be the symmetry breaking caused by having both OH^- and O^{2-} in the coordination polyhedron. If this is a general phenomenon, it may indicate an unanticipated connection between water content and the spin-transition pressure in the Earth's mantle. We hope that the results presented here will inspire new experiments to explore the phase transition and possible spin crossover in FeOOH and to determine the bulk moduli of the FeOOH polymorphs.

ACKNOWLEDGMENTS

We acknowledge support through DOE under Grant No. DE-FG02-04ER15498. Simulations are performed on the high-performance supercomputer at the Leibniz Rechenzentrum.

*katrin.otte@lrz.uni-muenchen.de
†pentcheva@lrz.uni-muenchen.de
‡rustad@geology.ucdavis.edu

[1] B. A. Manning, J. R. Kiser, H. Kwon, and S. R. Kanel, Environ. Sci. Technol. **41**, 586 (2007).
[2] U. Schwertmann, NATO ASI Ser., Ser. B **217**, 267 (1988).
[3] M. Stachowicz, T. Hiemstra, and W. H. van Riemsdijk, J. Colloid. Interface Sci **302**, 62 (2006).
[4] A. Szytula, A. Burewicz, Z. Dimitrijevic, S. Krasnicki, H. Rzany, and J. Todorovic, Phys. Status Solidi **26**, 429 (1968).
[5] H. Christensen and A. N. Christensen, Acta Chem. Scand. **32a**, 87 (1978).
[6] A. L. MacKay, Mineral. Mag. J. Mineral. Soc. **32**, 545 (1960).
[7] M. Pernet, J. C. Joubert, and C. Berthet-Colominas, Solid State Commun. **17**, 1505 (1975).
[8] F. LaGroix and S. K. Banerjee, Earth Planet. Sci. Lett. **225**, 379 (2004).
[9] C. J. Yapp, Annu. Rev. Earth Planet Sci. **29**, 165 (2001).
[10] K. M. Rosso and J. R. Rustad, Am. Mineral. **86**, 312 (2001).
[11] C. Laberty and A. Navrotsky, Geochim. Cosmochim. Acta **62**, 2905 (1998).
[12] A. Navrotsky, L. Mazeina, and J. Majzlan, Science **319**, 1635 (2008).
[13] A. E. Gleason, R. Jeanloz, and M. Kunz, Am. Mineral. **93**, 1882 (2008).
[14] Q. Williams and L. Guenther, Solid State Commun. **100**, 105 (1996).
[15] J. Badro, J.-P. Rueff, G. Vanko, G. Monaco, G. Fiquet, and F. Guyot, Science **305**, 383 (2004).
[16] T. Tsuchiya, R. M. Wentzcovitch, C. R. S. da Silva, and S. de Gironcoli, Phys. Rev. Lett. **96**, 198501 (2006).
[17] S. Stackhouse, J. P. Brodholt, and G. D. Price, Earth Planet. Sci.

Lett. **253**, 282 (2007).
[18] K. Umemoto, R. M. Wentzkowitch, Y. G. Yu, and R. Requist, Earth Planet. Sci. Lett. **276**, 198 (2008).
[19] P. Blaha, K. Schwarz, G. K. H. Madsen, D. Kvasnicka, and J. Luitz, *wien2k, An Augmented Plane Wave plus Local Orbitals Program for Calculating Crystal Properties* (Karlheinz Schwarz, Technical University of Wien, Austria, 2001).
[20] J. P. Perdew, K. Burke, and M. Ernzerhof, Phys. Rev. Lett. **77**, 3865 (1996).
[21] V. I. Anisimov, I. V. Solovyev, M. A. Korotin, M. T. Czyzyk, and G. A. Sawatzky, Phys. Rev. B **48**, 16929 (1993).
[22] G. K. H. Madsen and P. Novak, Europhys. Lett. **69**, 777 (2005).
[23] I. Leonov, A. N. Yaresko, V. N. Antonov, M. A. Korotin, and V. I. Anisimov, Phys. Rev. Lett. **93**, 146404 (2004).
[24] G. Rollmann, A. Rohrbach, P. Entel, and J. Hafner, Phys. Rev. B **69**, 165107 (2004).
[25] R. M. Cornell and U. Schwertmann, *The Iron Oxides* (Wiley, Weinheim, 2001).
[26] T. Nagai, H. Kagi, and T. Yamanaka, Am. Mineral. **88**, 1423 (2003).
[27] F. D. Murnaghan, Proc. Natl. Acad. Sci. U.S.A. **30**, 244 (1944).
[28] B. Russell, M. Payne, and L. C. Ciacchi, Phys. Rev. B **79**, 165101 (2009).
[29] J. D. Kubicki, K. W. Paul, and D. L. Sparks, Geochem. Trans. **9**, 4 (2008).
[30] K.-D. Grevel, M. Burchard, D. W. Fasshauer, and T. Peun, J. Geophys. Res., [Solid Earth] **105**, 27877 (2000).
[31] A. Friedrich, D. J. Wilson, E. Haussühl, B. Winkler, W. Morgenroth, K. Refson, and V. Milmann, Phys. Chem. Miner. **34**, 145 (2007).
[32] J. M. D. Coey, in *Iron in Soils and Clay Minerals*, edited by J. W. Stucki, B. A. Goodman, and U. Schwertmann (D. Reidel, Dordrecht, 1988), p. 397–466.
[33] J.-F. Lin, H. Watson, G. Vankó, E. E. Alp, V. B. Prakapenka, P. Dera, V. V. Struzhkin, V. V. Kubo, J. Zhao, C. McCammon, and J. Evans, Nature Geoscience **1**, 688 (2008).
[34] C. McCammon, I. Kantor, O. Narygina, J. Rouquette, U. Ponkratz, I. Sergueev, M. Mezouar, V. Prakapenka, and L. Dubrovinsky, Nature Geoscience **1**, 684 (2008).
[35] D. M. Sherman, Geochim. Cosmochim. Acta **69**, 3249 (2005).
[36] J. Velev, A. Bandyopadhyay, W. H. Butler, and S. K. Sarker, Phys. Rev. B **71**, 205208 (2005).
[37] M. Pernet, J. Chenavas, and J. C. Joubert, Solid State Commun. **13**, 1147 (1973).
[38] R. Voigt and G. Will, Neues Jahrb. Mineral. Abh. **2**, 89 (1981).

Manuscript 2: Water Adsorption on FeOOH Surfaces

Density functional theory study of water adsorption on FeOOH surfaces

K. Otte, W.W. Schmahl, and R. Pentcheva,
Surface Science, **606**, 1623-1632 (2012).

Surface Science 606 (2012) 1623–1632

Contents lists available at SciVerse ScienceDirect

Surface Science

journal homepage: www.elsevier.com/locate/susc

Density functional theory study of water adsorption on FeOOH surfaces

Katrin Otte *, Wolfgang W. Schmahl, Rossitza Pentcheva

Section Crystallography, Department of Earth and Environmental Sciences, and Center of Nanoscience (CENS), University of Munich, Theresienstr. 41, 80333 Munich, Germany

ARTICLE INFO

Article history:
Received 13 March 2012
Accepted 1 July 2012
Available online 16 July 2012

Keywords:
Goethite
Akaganeite
Lepidocrocite
Water adsorption

ABSTRACT

Using density functional theory (DFT) calculations with an on-site Coulomb repulsion term, we study the composition, stability, and electronic properties of the most common FeOOH surfaces goethite(101), akaganeite(100), and lepidocrocite(010), and their interaction with water. Despite the differences in surface structure, the trends in surface stability of these FeOOH polymorphs exhibit remarkable similarities. We find that the reactivity and the binding configuration of adsorbates depend strongly on the coordination of surface iron: at the fourfold coordinated Fe2 site water is chemisorbed, whereas at the fivefold coordinated Fe1 water is only loosely bound with hydrogen pointing towards the surface. Our results show that the oxidation state of surface iron can be controlled by the surface termination where ferryl (Fe^{4+}) species emerge for oxygen terminated surfaces and ferrous iron (Fe^{2+}) at iron and water terminations leading to a reduced band gap. In contrast, the fully hydroxylated surfaces, identified as stable surface configurations at standard conditions from the surface phase diagram, show electronic properties and band gaps closest to bulk FeOOH with ferric surface iron (Fe^{3+}). Only in the case of goethite(101), a termination with mixed surface hydroxyl and aquo groups is stabilized.

1. Introduction

The iron oxyhydroxide (FeOOH) polymorphs are abundant in soil and sediments where they appear as nanoparticles with a high specific surface area [1]. They show high adsorption affinities for aqueous solutes [2,3] which turns them to attractive adsorbents. Prior to modeling the adsorption of contaminants such as heavy metals [1,4,5], it is necessary to understand the geometric and electronic structure as well as the stability of the water/FeOOH interface at the atomic level.

Goethite, α-FeOOH, is the most common and most stable [6,3,7,8] bulk FeOOH phase at ambient conditions and consists of $Fe(O,OH)_6$ double bands that form 2×1 channels. The acicular crystals are elongated along the [010] direction, terminate in {021} faces, and prism faces are predominantly {101} [9–11]. Note that the (101) surface in the setting of the space group *Pnma* used here is equivalent to the (110) surface in *Pbnm*. Considering only two surface terminations of α-FeOOH, previous DFT calculations found a fully hydroxylated (101) surface energetically favored over an oxygen termination [12], similar to findings for hydrated hematite(0001) [13]. A Fourier transform infrared (FTIR) spectroscopy study [14] identified different surface hydroxyl groups: singly, doubly (μ), and triply (μ_3) coordinated. On the other hand, at the goethite(100) surface a surface x-ray diffraction study [15] reported a mixed mononuclear water and binuclear hydroxyl group termination. While some properties as vibrational frequencies of these surface OH groups have been calculated using an embedded cluster approach [16] for the α-FeOOH(101), a detailed investigation of surface stability and porperties considering all possible surface terminations is lacking.

Akaganeite, β-FeOOH, follows goethite in stability [6,8] and exhibits wide 2×2 and small 1×1 channels with plenty of adsorption sites available both at the outer and inner surface. It is a microcrystalline material elongated along the *c*-direction exposing {100} surfaces in the setting of space group $I^4/_m$ [17]. In this study we explore the termination of the outer akaganeite(100) surface and its interaction with water. Adsorption of water, chloride, sulfate, and arsenate at the inner akaganeite channels goes beyond the scope of this study and will be addressed elsewhere [18]. Experimentally, the energetics of water adsorption on akaganeite was studied by calorimetric measurements [19]. Furthermore, a combined classical molecular dynamics and FTIR spectroscopy study [20] determined —OH, μ-OH and μ_3-OH surface terminal groups at the (100) and an additional configuration with multiple water molecules adsorbed at the same surface iron ion (η-OH_2 groups) of the (010) akaganeite surface.

Lepidocrocite (γ-FeOOH) crystals exhibit a platy shape with predominantly {010} surface [21] (space group *Cmcm*) and appear in biogeochemical processes of Fe^{3+} to Fe^{2+} transformation [22]. With its layered structure of zigzag sheets of edge sharing double bands of octahedra, γ-FeOOH is less stable in bulk than the framework FeOOH polymorphs (α, β) [6,8,23]. So far, the thermodynamic properties [24,25] and the energetics of water adsorption [26] at lepidocrocite were studied experimentally using calorimetry. A recent DFT study addressed proton transfer processes in the hydrogen

* Corresponding author.
E-mail addresses: katrin.otte@lrz.uni-muenchen.de (K. Otte), pentcheva@lrz.uni-muenchen.de (R. Pentcheva).

0039-6028/$ – see front matter © 2012 Elsevier B.V. All rights reserved.
doi:10.1016/j.susc.2012.07.009

bonded chains of bulk lepidocrocite with regard to its use as a proton conductor [27].

Calorimetric measurements [19,2,26] find similar enthalpies of water adsorption on the different FeOOH polymorph surfaces which suggests similar binding mechanisms. However, the exact water/FeOOH interface structure is not yet understood at the atomic level. In particular, we explore here how different surface iron sites and surface terminal groups affect surface reactivity. Using density functional theory (DFT), we provide a comprehensive, comparative study of the energetics and electronic properties of the most exposed FeOOH surfaces: goethite(101), akaganeite(100), and lepidocrocite(010), taking into account up to 17 surface terminations for each surface as described in Section 3. In Section 4 we compile a surface phase diagram in the framework of *ab initio* thermodynamics [28] and identify stable surface terminations for given oxygen and water pressures. Detailed information on the structure of different FeOOH terminations and adsorbate configurations considering both molecular and dissociative adsorption modes are provided in Section 5 together with the adsorption energy. In Section 6 the underlying electronic properties of the stable surface terminations are discussed. Previous studies on $Fe_3O_4(001)$ [29,30] have shown that the charge and orbital order of iron ions in the surface and subsurface layers depend sensitively on the surface termination and adsorbates like water and hydrogen. Here we investigate this aspect for the FeOOH polymorph surfaces and show how adsorbates control the Fe^{3+} to Fe^{2+} ratio at the surface.

2. Calculational details

The DFT calculations are performed with the Vienna *ab initio* Simulation Package (VASP) [31–35] using the generalized gradient approximation (GGA) of the exchange and correlation functional in the parameterization of Perdew et al. [36]. Because electronic correlations play an important role in transition-metal oxides, an on-site Coulomb repulsion parameter U within the GGA+U approach is included [37]. Throughout the calculations values of $U_{\mathrm{eff}}=5$ eV on the iron ions are used, similar to other studies on iron oxides [38,39]. In a previous DFT study we have found that this value correctly describes the experimental FeOOH band gaps [8]. We note that U values obtained from constrained LDA (local density approximation) tend to be higher (7–8 eV) [40], whereas U-parameters between 5 and 6 eV were determined from linear-response theory for Fe^{2+} in magnesiowüstite [41].

The systems are modeled in a supercell geometry with two inversion symmetric surfaces to avoid spurious electric fields and contain up to 74 atoms. A vacuum of at least 10 Å is used to prevent interactions between the slabs and their periodic images. We have tested convergence with respect to the number of iron layers: six iron layers for goethite(101) and eight iron layers for akaganeite(100) and lepidocrocite(010), respectively, are necessary to ensure that the central layers show bulk behavior. The lattice constants and internal parameters in the starting geometries correspond to the bulk ones obtained within GGA [8]. The atomic positions used in the surface slabs were obtained by matrix transformation of the bulk positions. The following lateral unit cell parameters are used throughout the calculations: $a=10.96$ Å and $b=3.02$ Å with $\gamma=90°$ (space group $P2_1/m$, $\beta=101.28°$) for α-FeOOH(101), $b=10.48$ Å and $c=3.023$ Å with $\alpha=90°$ (space group $P\bar{1}$) for β-FeOOH(100), and $a=3.06$ Å and $c=3.87$ Å with $\beta=90°$ (space group $P\bar{1}$) for γ-FeOOH(010). For the integration in reciprocal space 12, 12, and 30 k points were used in the irreducible part of the Brillouin zone for the α-, β-, and γ-FeOOH surfaces, respectively. An increased k mesh has been applied for the calculation of the density of states (54, 27, and 63 k points, respectively). An energy cut-off of 500 eV for the plane-wave basis set is used to achieve an accuracy of total energy differences of 10 meV. Selected cases were calculated with the full-potential all-electron linear augmented plane waves method as implemented in the WIEN2k [42] code showing good agreement of the electronic properties obtained with the two codes. A structural optimization of the two outer Fe double layers is performed up to a force convergence of 0.001 eV/Å, while the inner layers are kept fixed at their bulk positions to reproduce bulk behavior. In bulk the three FeOOH polymorphs show an antiferromagnetic order of iron spins [43–45]. This magnetic arrangement was also considered as a starting point for the surface calculations.

The total energy of an isolated water molecule, E_{H_2O}, needed as reference energy was calculated in a box of $10\times10\times10$ Å^3 while for oxygen, E_{O_2}, a box of $10\times10\times8$ Å^3 was used in order to obtain the correct ground state. We considered a bcc structure and ferromagnetic coupling to calculate the total energy of bulk iron, E_{Fe}.

3. Surface terminations

In this section we describe the surface terminations considered in our study. The iron terminated surfaces of the FeOOH polymorphs with truncated surface octahedra are displayed in the first panel of Figs. 2, 3, and 4 showing the characteristic linkage and orientation of the double bands of edge-sharing $Fe(O,OH)_6$ octahedra. Depending on the number of coordinating oxygen or hydroxyl groups, there are two distinct iron surface sites available at goethite(101) and akaganeite(100): Fe1 site in fivefold square pyramidal, $Fe(O,OH)_5$, and Fe2 site in fourfold, $Fe(O,OH)_4$, coordination. In contrast, at the lepidocrocite(010) surface only the fourfold coordinated Fe2 site is present. In the following the iron terminated surfaces are denoted according to the corresponding surface site as Fe/Fe termination for goethite(101) and akaganeite(100) or Fe termination in the case of lepidocrocite(010). In the open channels of α-FeOOH(101) and β-FeOOH(100) surface μ_3-OH groups are present with oxygens linked to three Fe ions referred to as O^C. Additionally, we have considered surfaces where O^C is deprotonated, denoted as Fe/Fe deprotonated termination. The stoichiometric surfaces of goethite(101) and akaganeite(100) correspond to oxygen added either mononuclear to Fe1 (apical surface oxygen, O^A) or binuclear to Fe2 (basal surface oxygen, O^B) and are called O/Fe or Fe/O terminations, respectively. The stoichiometric surface of lepidocrocite(010) corresponds to the hydroxyl termination where a μ-OH group is added at the surface iron.

We consider both molecular and dissociative adsorption of water at Fe1 and Fe2. This results in various combinations of the surface ions and end groups Fe, Fe–O, Fe–OH, and Fe–w or Fe+w*. Note that w and w* refer to chemisorbed and hydrogen bonded water molecules, respectively. Furthermore, the surface terminal groups can be coordinated mono-, bi- (μ), and trinuclear (μ_3) to the underlying iron ions.

In total 17 surface terminations each for α-FeOOH(101) and β-FeOOH(100) and 4 surface terminations for γ-FeOOH(010) were modeled.

4. Surface phase diagrams of the FeOOH surfaces

In this section we present the most stable surface configuration using the framework of *ab initio* atomistic thermodynamics [28]. The surface energy of each termination depends on the chemical potentials of the constituents and is defined in the following way:

$$\gamma(T,p_i)=\frac{1}{2A}\left(G^{\mathrm{slab}}_{\mathrm{FeOOH}}-n_{\mathrm{Fe}}\mu_{\mathrm{Fe}}-n_{\mathrm{O}}\mu_{\mathrm{O}}-n_{\mathrm{H}}\mu_{\mathrm{H}}\right) \quad (1)$$

where A is the surface area, the factor 2 accounts for the presence of two surfaces in the simulation cell, $G^{\mathrm{slab}}_{\mathrm{FeOOH}}$ is the Gibbs free energy of the system, and μ_i is the chemical potentials of the constituents. $G^{\mathrm{slab}}_{\mathrm{FeOOH}}$ can be expressed by the total energy from the DFT calculations. Entropic effects of the surface ions are expected to cancel to a large extent with their counterparts in the bulk in contrast to

adsorbates. In a previous study, the vibrational contributions γ^{vib} of hydroxyl and water species on the surface of $RuO_2(110)$ were estimated to amount to 15 meV/Å^2 and 30 meV/Å^2, respectively [46]. This results in an uncertainty in surface energies of 10–15 meV/Å^2. Furthermore, a DFT study of hydrated γ-MnOOH(010) by Oxford and Chaka [47] found that the vibrational contributions for different surface terminations differ by less than 0.1 eV per simulation cell.

For a given temperature the chemical potentials can be transferred into pressure using the following equation [48,28]:

$$\mu_i(T,p_i) = \mu_i\left(T,p^0\right) + \frac{1}{2}k_B T\cdot\ln\left(\frac{p_i}{p^0}\right) \quad (2)$$

where μ_O and μ_{H_2O} can vary between the poor limit determined by the stability of the respective bulk FeOOH phase and the rich limit defined by the energy of the molecule. For water the rich limit is defined by the critical point of water [46], which lies at 0.91 eV with respect to the energy of a gas phase isolated molecule, obtained from Eq. (2) using the JANAF tables [49] for $T=647$ K and $p=22$ MPa. The heat of formation of bulk α, β, and γ phases at 0 K calculated using the energy of liquid water is −6.38, −6.22, and −6.21 eV, respectively. These values are slightly higher than the experimental data (−5.82, −5.75, and −5.69 eV) [19], but show the same energetic trend.

The dependence of $\gamma(T,p_i)$ on μ_O and μ_{H_2O} results in a three dimensional surface phase diagram. To discuss the main trends, a two dimensional projection which renders the most stable surface configurations for given μ_O and μ_{H_2O} is shown in Fig. 1a, c, and e. Some of the surface configurations are higher in energy and do not appear in the surface phase diagrams of Fig. 1a, c, and e. On the other hand, all terminations are displayed in Fig. 1b, d, and f where $\gamma(T,p_i)$ is shown as a function of μ_O at water rich conditions.

There are some common trends observed for all FeOOH surfaces in Fig. 1a, c, and e: at μ_{H_2O}/μ_O poor conditions the phase diagrams are dominated by the iron terminations, for μ_{H_2O}/μ_O rich conditions by the hydroxyl terminated surfaces, and at μ_{H_2O} rich and μ_O poor conditions by water terminations. While for γ-FeOOH(010) the OH termination covers most of the phase diagram in Fig. 1e, for α-FeOOH(101) and β-FeOOH(100) further terminations appear due to the more complex surface structure and the presence of two distinct surface iron sites, Fe1 and Fe2. In Fig. 1a and c towards oxygen rich and water poor conditions the deprotonated Fe/Fe terminations are most stable. However, there are variations in the regions of stability for α- and β-FeOOH. In Fig. 1d the Fe/OH termination of β-FeOOH(100) is stable over a wide range at intermediate μ_{H_2O} and μ_O conditions, while for α-FeOOH(101) there is only a small region of stability for the OH/Fe termination in Fig. 1a. In Fig. 1b the small differences in surface energy reflect the competition between OH/Fe and Fe/OH terminations, whereas at β-FeOOH(100) there is a clear preference for a hydroxylated Fe2 site in the Fe/OH termination of 37 meV/Å^2 as shown in Fig. 1d. In contrast, hydroxylation of the Fe1 site at α-FeOOH(101) is preferred due to hydrogen bonding of O^A to H^{C2} as discussed in the next section.

Owing to the shorter distance between Fe1 and Fe2 at β-FeOOH(100) (initial: 3.46 Å) compared to α-FeOOH(101) (initial: 5.68 Å) an interaction of adsorbates with both iron surface sites is expected for the former. Indeed, for akaganeite(100) a further stable surface configuration appears at oxygen poor and intermediate μ_{H_2O} conditions in Fig. 1c: the Fe/w termination. Here binuclear molecular adsorbed water additionally forms a hydrogen bond to $O^{1/2}$ (Fig. 3) which leads to a stabilization of this termination. In contrast to the chemisorbed water at Fe2, at Fe1 water is only loosely bound through a hydrogen bond (w*). The stronger binding of water at Fe2 in Fe/w compared to Fe1 in Fe+w*/Fe

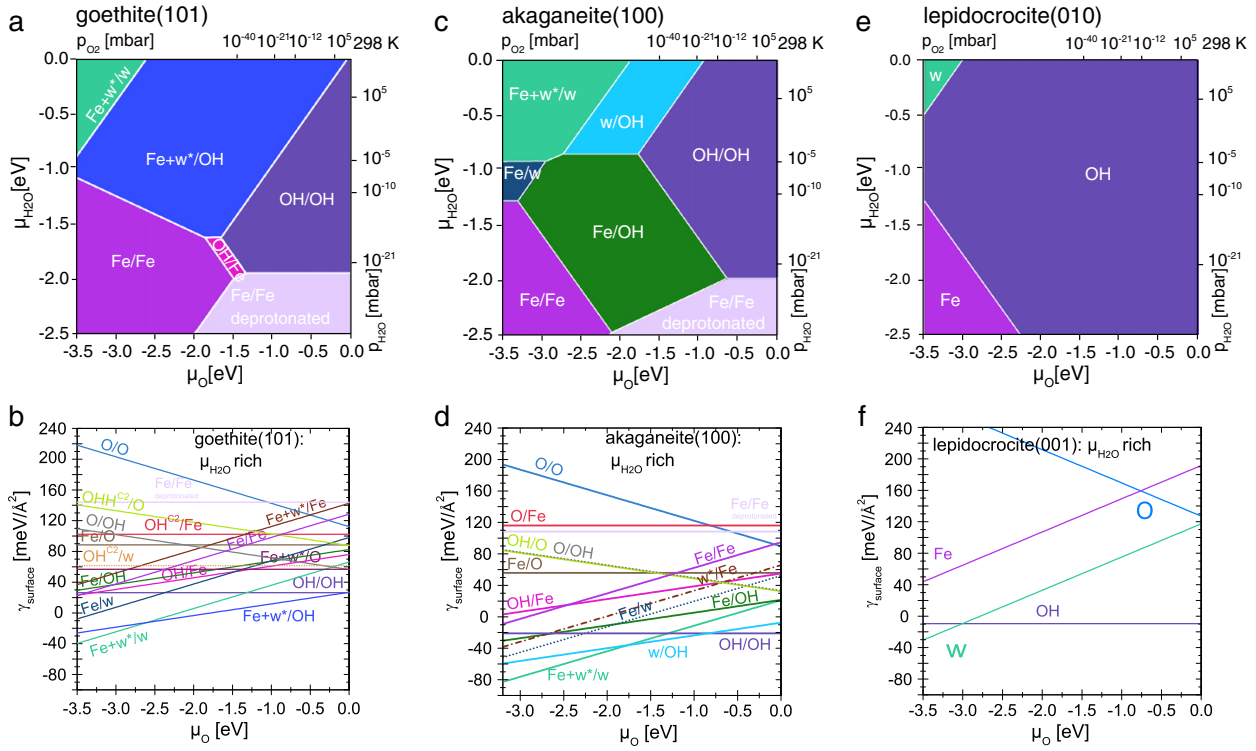

Fig. 1. Stable surface terminations at a) goethite(101), c) akaganeite(100), and e) lepidocrocite(010) with respect to μ_O and μ_{H_2O}. Additionally, μ_O and μ_{H_2O} are converted into pressures at room temperature (298 K). The surface energy as a function of μ_O at water rich conditions is displayed in b), d), and f). With increasing oxygen concentration there is a transition from water terminations to hydroxylated surface terminations. Stoichiometric terminations appear as horizontal lines and do not depend on μ_O. Note that oxygen terminal groups are energetically unfavorable. The color coding for the surface terminations corresponds to the frames used in Figs. 2, 3, and 4, respectively.

Table 1
Surface energies (meV/Å^2) of the most stable surface termination w.r.t μ_O and μ_{H_2O} in comparison with experiment at 298 K. Changes of μ_O and μ_{H_2O} with temperature at standard pressure are included using Eq. (2).

	Surface energy (meV/Å^2)		
	0 K	298 K	298 K
	DFT	DFT	Exp.
α(101)	26.4	42.2	37.4 [2]
β(100)	−19.1	−2.6	27.5 [19]
γ(010)	−9.4	−9.4	25.0 [26]

terminations is shown in Fig. 1d and will be discussed further in the following section. As mentioned above, at water rich conditions the Fe + w*/w terminations dominate and transform with increasing μ_O to a termination with either hydrogen bonded or chemisorbed water at Fe1 and hydroxylated Fe2 site, Fe+w*/OH and w/OH termination, for α-FeOOH(101) and β-FeOOH(100), respectively. Finally at high oxygen and water partial pressures, the fully hydroxylated surface, the OH/OH termination, is stabilized. This variation in the surface protonation state relates to changes in pH value from low (—OH_2) to intermediate (—OH, —OH_2) to high (—OH) pH.

In order to compare the surface stability of the FeOOH polymorphs at standard conditions, we calculate $\gamma(T, p_i)$ from Eq. (2) at $T = 298$ K and $p = 1$ bar, using experimentally determined values from the JANAF [49] tables. The lowest $\gamma(T, p_i)$ with respect to μ_O and μ_{H_2O} at 0 K and 298 K are listed in Table 1. Note that hydroxylated lepidocrocite(010) corresponds to the stoichiometric configuration and is, therefore, independent of pressure with $\gamma(T, p_i) = -9.4$ meV/Å^2. In bulk at ambient conditions the layered polymorph (γ-FeOOH) is less stable than the ones with framework structures (α- and β-FeOOH) [6,8]. The stability of the FeOOH surfaces at 298 K reveals the opposite order

$$E_{\gamma(010)} < E_{\beta(100)} < E_{\alpha(101)}$$

which is in accordance with calorimetric measurements [19,2,26]. Such a reverse relation between bulk and surface stability was recently shown, e.g. for Al_2O_3 [50].

5. Effect of water adsorption on the surface energetics and structure

After presenting the stable surface terminations in the previous section, we discuss here the binding strength and structural properties of molecular and dissociative adsorbed water at different FeOOH surface terminations and surface sites. The adsorption energy is calculated using

$$E_{ads} = \frac{1}{n}\left(E_{n_{H_2O}\cdot FeOOH} - E_{FeOOH} - n\cdot E_{H_2O}\right) \quad (3)$$

where E_{FeOOH} and $E_{n_{H2O}\cdot FeOOH}$ are the total energies of surfaces before and after adsorption of water. The results are summarized in Tables 2 and 3 for α-FeOOH(101) and β-FeOOH(100), respectively, where possible reaction pathways are listed. Depending on the starting configuration, different adsorption pathways can lead to the same stable surface configuration. In the following we discuss the energetics of water adsorption on goethite(101), akaganeite(100), and lepidocrocite(010).

5.1. Goethite(101)

Relaxed surface terminations of α-FeOOH(101) are displayed in Fig. 2 together with characteristic bond lengths. The stable Fe/Fe, Fe/Fe deprotonated, and OH/Fe terminations are the starting point for adsorption of water, whereas the stable Fe+w*/w, Fe+w*/OH, and OH/OH terminations are obtained either through molecular or dissociative water adsorption.

5.1.1. Energetics of water adsorption

At α-FeOOH(101) we find two distinct adsorption modes of molecular water depending on the adsorption site: water binds only binuclear at Fe2, but is hydrogen bonded at Fe1. This differs from results for the α-FeOOH(100) where only the Fe1 surface iron site is present and a mononuclear configuration is reported [51]. Both Fe/w or Fe+w*/Fe are obtained through adsorption of a single water molecule at Fe/Fe. We note that binuclear adsorption at the Fe2 site is preferred with $E_{ads} = -0.09$ eV (a2), while hydrogen bonded water at Fe1 (a1) is 1.47 eV higher in energy and strongly unfavorable. Increasing the coverage to two molecules results in the Fe+w*/w configuration where one water molecule connects to the Fe1 site via hydrogen bonding, w*, while the other water molecule binds binuclear at Fe2, μ-w. The adsorption energy is enhanced to −0.24 eV per water molecule (reaction

Table 2
Molecular and dissociative water adsorption paths at goethite(101) are summarized and consecutively numbered. For molecular adsorption on top of either Fe1 or Fe2 site, respectively, the corresponding adsorption energies E_{ads} are provided. For dissociative adsorption and higher coverages an average value per molecule is given. Stable terminations that appear in the surface phase diagram are given in bold letters. Bond lengths of Fe1,2–O are listed where oxygen can appear as adsorbed oxygen, as part of a hydroxyl group, or as hydrogen bonded or chemisorbed water, w* and w. For molecular water also $\angle_{HOH}$ is given.

Goethite(101)										
	Adsorption reaction initial	Adsorbate		Final	E_{ads} (eV)		d_{Fe-O} (Å)		$\angle_{HOH}$ (°)
					@ Fe1	@ Fe2	Fe1	Fe2	w*/w
a1	Fe/Fe	+	$1H_2O$	→	Fe+w*/Fe	+1.38		3.22	4.49	107.5
a2	Fe/Fe	+	$1H_2O$	→	Fe/w		−0.09		2.36	111.0
a3	Fe/Fe	+	$2H_2O$	→	Fe+w*/w	−0.24		4.58	2.33/3.51^{w*}	106.8/109.6
a4	Fe+w*/Fe	+	$1H_2O$	→	Fe+w*/w		−1.61			
a5	Fe/w	+	$1H_2O$	→	Fe+w*/w	−0.14				
a6	Fe/O	+	$1H_2O$	→	Fe+w*/O	−0.14		4.13	1.89, 3.47^{w*}	107.8
a7	OH^C/Fe	+	$1H_2O$	→	OH^C/w		−0.44		2.32	112.7
a8	Fe/OH	+	$1H_2O$	→	Fe+w*/OH	−0.97		3.22	2.04, 4.34^{w*}	104.6
a9	OH/Fe	+	$1H_2O$	→	Fe+w*/OH	−0.71				
a10	Fe/Fe deprotonated	+	$1H_2O$	→	OH^C/Fe	−0.47		1.85		
a11	Fe/Fe deprotonated	+	$1H_2O$	→	Fe/O	−0.93			1.87	
a12	OH^C/w	Dissociation		→	OH/OH	−1.16		1.91	1.96	
a13	Fe+w*/O	Dissociation		→	OH/OH	−1.01		1.91	1.96	

Table 3
Molecular and dissociative water adsorption paths at akaganeite(100) are summarized and consecutively numbered. For molecular adsorption on top of either Fe1 or Fe2 site, respectively, the corresponding adsorption energies E_{ads} are provided. For dissociative adsorption and higher coverages an average value per molecule is given. Stable terminations that appear in the surface phase diagram are given in bold letters. Bond lengths of Fe1,2–O are listed where oxygen can appear as adsorbed oxygen, as part of a hydroxyl group, or as hydrogen bonded (w*) or chemisorbed water (w). For molecular water also $\angle_{HOH}$ is given.

Akaganeite(100)										
	Adsorption reaction initial	Adsorbate		Final		E_{ads} (eV)		$d_{Fe\text{-}O}$ (Å)		$\angle_{HOH}$ (°)
						@ Fe1	@ Fe2	Fe1	Fe2	w*/w
b1	Fe/Fe	+	$1H_2O$	→	Fe+w*/Fe	+0.05		3.22		105.3
b2	Fe/Fe	+	$1H_2O$	→	Fe/w		−0.38		2.36	110.2
b3	Fe/Fe	+	$2H_2O$	→	Fe+w*/w	−0.06		3.57	2.34	104.8/112.2
b4	Fe+w*/Fe	+	$1H_2O$	→	Fe+w*/w		−0.44			
b5	Fe/w	+	$1H_2O$	→	Fe+w*/w	−0.02				
b6	Fe/OH	+	$1H_2O$	→	w/OH	+0.05		2.28	2.17	110.4
b7	OH/Fe	+	$1H_2O$	→	w/OH	−1.01		2.28	2.17	110.4
b8	Fe/Fe deprotonated	+	$1H_2O$	→	O/Fe	+1.22		1.75		
b9	Fe/Fe deprotonated	+	$1H_2O$	→	Fe/O	−0.69		1.86		
b10	O/Fe	+	$1H_2O$	→	OH/OH	−3.37		1.88	2.01	
b11	Fe/O	+	$1H_2O$	→	OH/OH	−1.47				

a3) due to hydrogen bonding between the molecules. This effect bears parallels to the increase in binding energy at metal surfaces owing to an attractive water–water interaction [52]. If we alternatively consider the binding of an additional water molecule to either Fe/w or Fe+w*/Fe configurations (reaction a5 or a4) we find that adsorption at the Fe2 site is clearly preferred with $E_{ads} = -1.61$ eV compared to Fe1 with $E_{ads} = -0.14$ eV.

Adsorption of water at either OH/Fe or Fe/OH leads in both cases to the Fe+w*/OH termination (reactions a8 and a9). Here water is linked via hydrogen bonding to the Fe1 site and the Fe2 site is hydroxylated. Water adsorbed at Fe1 in Fe/OH exhibits an adsorption energy of −0.97 eV, while adsorption at OH/Fe is 0.26 eV less favorable reflecting the difference in stability of the initial terminations Fe/OH and OH/Fe.

Starting from the deprotonated Fe/Fe surface, the stoichiometric α-FeOOH(101) terminations Fe/O or OH^C/Fe are formed by dissociation of water (reactions a11 and a10 with E_{ads} of −0.93 and −0.47 eV, respectively). In OH^C/Fe we find a preferential formation of a mononuclear coordinated surface hydroxyl group at O^A instead of a trinuclear μ_3-$O^{C2}H$. Such a lower proton affinity of μ_3-O compared to O^A was also found for the α(100) surface from DFT studies on extended surfaces [51] and clusters [53]. Water adsorbed on either of the latter configurations results in the configurations Fe+w*/O with $E_{ads} = -0.14$ eV (a6) or OH^C/w with $E_{ads} = -0.44$ eV (a7). Both chemisorbed water in OH^C/w and hydrogen bonded water in Fe1+w*/O dissociate to the OH/OH termination with a gain in energy of −1.16 eV and −1.01 eV, respectively.

5.1.2. Effect of adsorbate on the surface relaxation

The stable Fe/Fe termination is the starting point for molecular water adsorption on α-FeOOH(101). While Fe1–O/OH distances are only slightly changed (1.96/2.13 Å) compared to bulk α-FeOOH (1.95/2.11 Å), the bond lengths of Fe2 are decreased to $d_{Fe2-O/OH} =$ 1.87/2.03 Å as a result of the reduced fourfold coordination.

The main structural effect of adsorption of molecular water with respect to the Fe/Fe termination is that the remaining Fe2–O/OH bond lengths are nearly restored to bulk values. While in Fe/w water points with O towards Fe2 ($d_{Fe2-O^w} = 2.36$ Å), in Fe+w*/Fe the adsorption geometry at Fe1 is quite different with water pointing with H to Fe1 and a much larger distance $d_{Fe1-O^{w*}} = 3.22$ Å. Additionally, hydrogen bonds are formed to H^{C2} of $d_{O^{w*}\cdots H^{C2}} = 1.87$ Å. At the stable Fe+w*/w termination the distance of binuclear adsorbed μ-w to Fe2 is 2.33 Å. The gain in energy for this geometry is related to the formation of two hydrogen bonds: one between μ-w and w* with $d_{O^{w*}\cdots H^w} = 1.99$ Å and a second between w* and O^{C2} with $d_{O^{C2}\cdots H^{w*}} = 1.69$ Å. As a result of these hydrogen bonds the distance of w* to Fe2 (3.51 Å) is shorter than to Fe1 (4.58 Å). The close proximity of the two water molecules w* and μ-w is also reflected in $d_{O^{w*}-O^w} = 2.74$ Å. This value is similar to the one obtained in solvated water layers at α-FeOOH(100), i.e. $d_{O^{w1}-O^{w2}} = 2.68$ Å [15], but slightly shorter than the average O–O distance in liquid water of 2.81 Å found by Bergmann et al. [54].

In Fe+w*/OH the large energy gain goes hand in hand with a shorter distance of w* to Fe1 of $d_{Fe1\cdots O^w} = 3.22$ Å and additional hydrogen bonding to H^{C2} with $d_{H^{C2}\cdots O^w} = 1.90$ Å.

At the deprotonated Fe/Fe termination the hydrogens of the residual OH groups (H^{C1} and H^{C2}) at the Fe/Fe surface are removed and the surface now consists of Fe1, Fe2, and O^C as depicted in Fig. 2. The change in coordination compared to bulk leads to reduced surface Fe–O/OH bond lengths (Fe1: 1.96/2.01 Å, Fe2: 1.87/1.89 Å). On the other hand, the subsurface iron atoms Fe3 and Fe4 have increased distances to the apex oxygens on the bulk side (from 1.93/2.10 Å to 2.25/2.29 Å) as well as in the basal plane of the octahedron (from 1.96/1.95 Å to 2.13/2.03 Å).

At the stable OH/Fe termination where Fe1 is hydroxylated with $d_{Fe1-O^AH} = 1.94$ Å, the terminal mononuclear coordinated O^AH group forms additionally a short hydrogen bond to H^{C2} with $d_{H^{C2}\cdots O^B} =$ 1.52 Å. Note that the OH/Fe termination is energetically favored by 0.21 eV compared to a hydroxylated Fe2 site in the Fe/OH termination. At the Fe/OH termination the distance of the binuclear coordinated O^BH group, μ-O^BH, to Fe2 is $d_{Fe2-O^BH} = 1.96$ Å, comparable to bulk Fe–OH distances, while the remaining $d_{Fe2-O/OH}$ distances are reduced (1.89/2.03 Å). In contrast an enhanced $d_{Fe_2-OH} = 2.07$ Å was reported at α-FeOOH(100) where OH is linked to two iron ions [51].

Our results show that the OH/OH termination exhibits bond lengths closest to bulk, with relaxations of Fe–O^{SF} distances of only −2.1/+0.5%. The bond lengths of the surface Fe to the hydroxyl groups are $d_{Fe1-O^AH} = 1.91$ Å and $d_{Fe2-O^BH} = 1.96$ Å. Moreover, a hydrogen bond is formed between $O^{C2}H$ and O^AH with $d_{H^{C2}\cdots O^B} = 1.47$ Å.

5.2. Akaganeite(100)

The most stable β-FeOOH(100) surface terminations together with their characteristic bond lengths are displayed in Fig. 3. Analogous to α-FeOOH(101), the stable Fe/Fe, Fe/Fe deprotonated, and OH/Fe terminations are the starting points for adsorption reactions. Furthermore, the stable Fe/w, Fe+w*/w, Fe+w*/OH, and OH/OH terminations are obtained either through molecular or dissociative water adsorption.

5.2.1. Energetics of water adsorption

Reactions b1 and b2 in Table 3 describe adsorption of water either at Fe1 or Fe2 of β-FeOOH(100). Similar to α-FeOOH(101) water preferentially adsorbs binuclear at Fe2 in Fe/w with $E_{ads} = -0.38$ eV. The stable Fe/w termination is by 0.44 eV lower in energy compared to

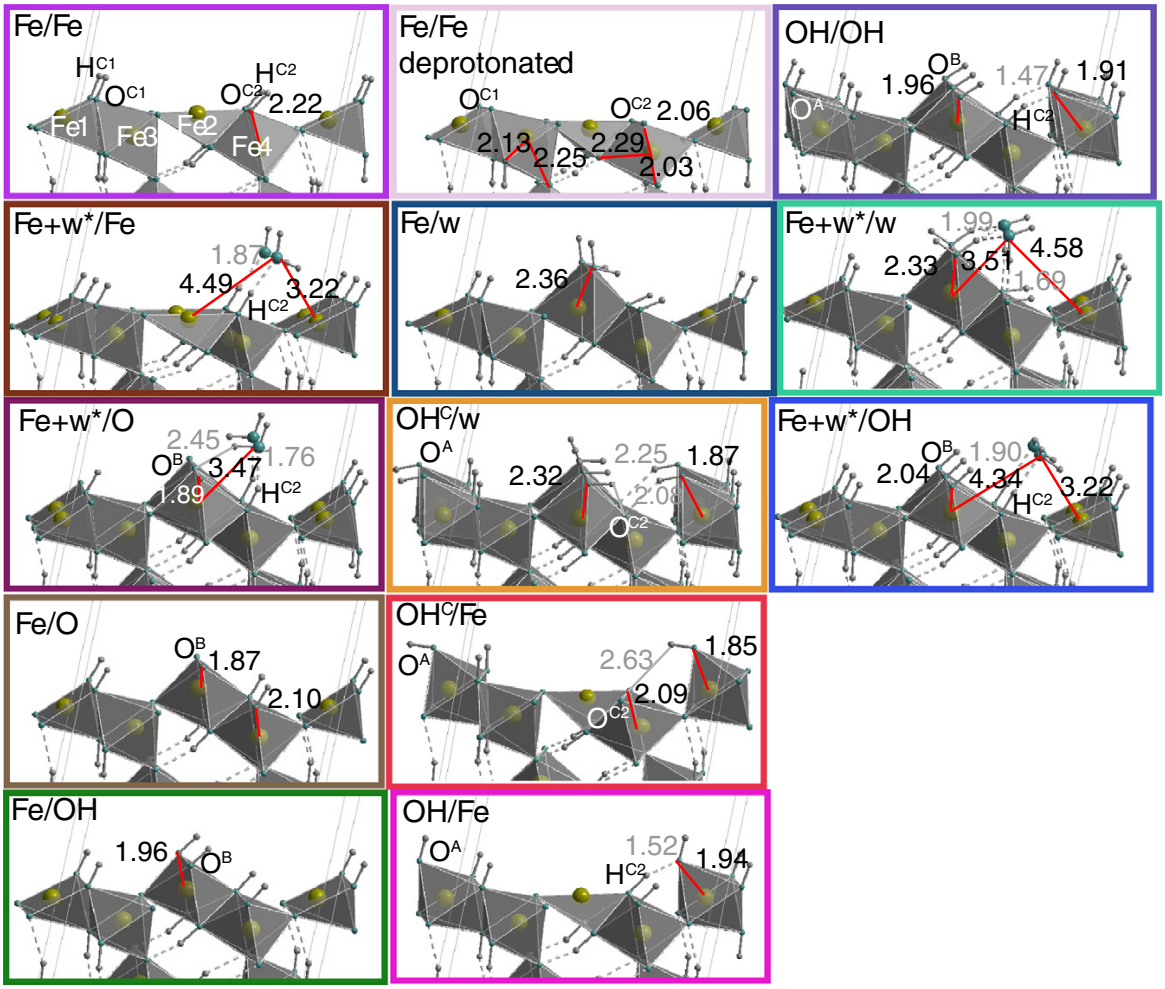

Fig. 2. Side views of the relaxed surface layers of α-FeOOH(101) before and after water adsorption. Relevant Fe–O/OH bond lengths are marked in red and hydrogen bonds are indicated by gray dashed lines. The Fe/Fe termination depicts the fivefold square pyramidal coordinated Fe1 and fourfold coordinated Fe2 with trinuclear hydroxyl groups (μ_3-O^{C}H) at the surface, whereas at the OH/OH termination the hydroxyl groups bind mononuclear at Fe1 (−O^{A}H) and binuclear at Fe2 (μ-O^{B}H) restoring the surface octahedra.

Fe+w*/Fe with hydrogen bonded water. This indicates also that the fourfold coordinated Fe2 is more reactive than the fivefold coordinated Fe1 site.

A second water molecule adsorbing at Fe1 in Fe/w or at Fe2 in Fe+w*/Fe leads to the Fe+w*/w termination. Here the adsorption energies of −0.02 and −0.44 eV for adsorbed water at Fe1 and Fe2, respectively, are significantly smaller compared to the corresponding energies at α-FeOOH(101) (E_{ads} of −0.14 eV at Fe1 and −1.61 eV at Fe2), but again the binding at Fe2 is stronger. The adsorption of two water molecules at Fe/Fe leads to the Fe+w*/w termination with E_{ads} per water molecule of −0.06 eV (b3).

Similar to the Fe/Fe termination, water added to the Fe/OH termination has a slightly positive binding energy to Fe1 (reaction b6). On the other hand, water adsorption at the OH/Fe termination results in w/OH (reaction b7) and is energetically favored with E_{ads} = −1.01 eV.

In contrast to α-FeOOH(101), at β-FeOOH(100) the fully hydroxylated OH/OH termination is directly obtained from the stoichiometric surfaces O/Fe or Fe/O through adsorption of a water molecule. The corresponding adsorption energies are significantly higher (E_{ads} = −3.37 and −1.47 eV for b10 and b11), compared to the analogous reactions at α-FeOOH(101) (E_{ads} = −1.16 and −1.01 eV for a5 and a6).

5.2.2. Effect of adsorbate on the surface relaxation

Similar to the iron termination of α-FeOOH(101), at the Fe/Fe termination the fivefold coordinated Fe1 has increased Fe1–O/OH distances (2.01/2.18 Å) in comparison to bulk (1.93/2.13 Å), while the fourfold coordinated Fe2 has shorter bonds, $d_{Fe2-O/OH}$ = 1.85/2.08 Å. On the other hand, the subsurface octahedra are hardly affected by the presence of the surface.

Upon water adsorption at Fe2 in Fe/w the distance between water and Fe2 is 2.36 Å. Additionally, water is hydrogen bonded to O$^{1/2}$ with $d_{O^{1/2}\cdots H}$ = 2.15 Å. In Fe+w*/w binuclear adsorbed water at Fe2 has a similar bond length of d_{Fe2-O^w} = 2.34 Å. At the Fe1 site w* points with one H towards Fe1 with d_{Fe2-O^w} = 3.57 Å. A further hydrogen bond is formed to H^{C1} with $d_{H^{C1}\cdots OwA}$ = 2.36 Å. The distance between w* and μ-w of 4.45 Å at β-FeOOH(100) is much larger compared to 2.74 Å at α-FeOOH(101) and there is no direct interaction between the two water molecules. This explains the significantly lower E_{ads}

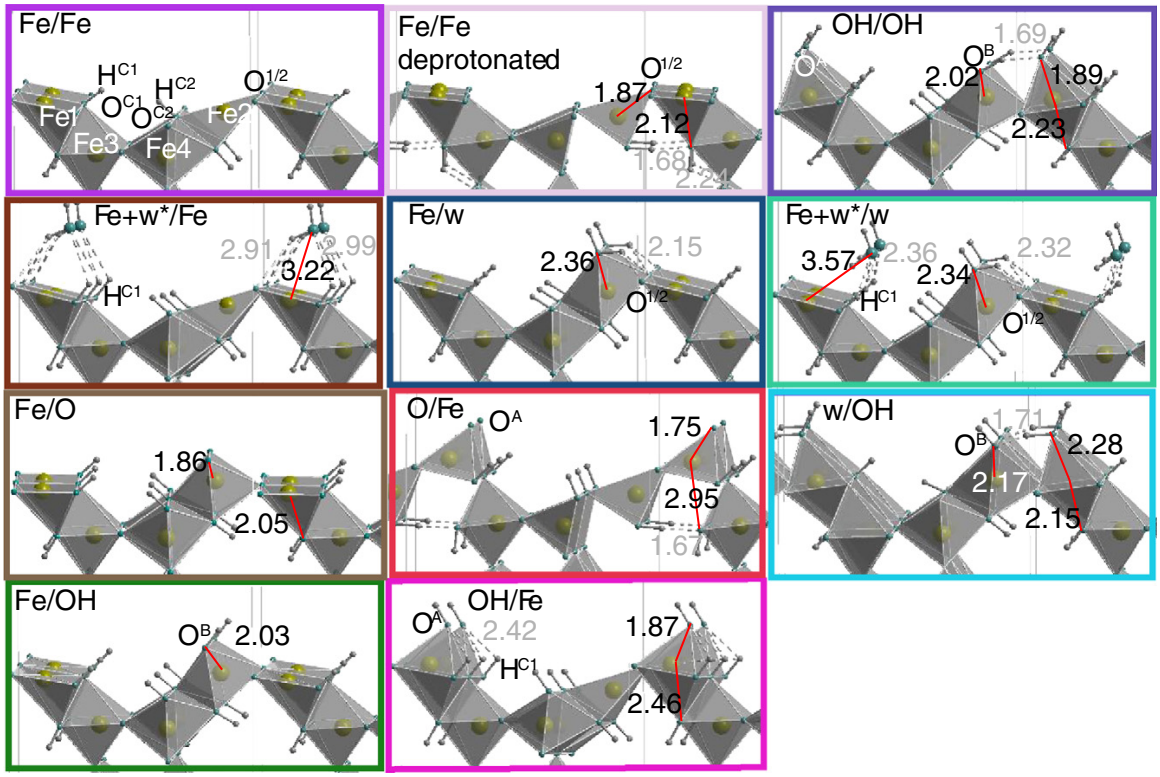

Fig. 3. Side views of the relaxed surface layers of β-FeOOH(100) before and after water adsorption. Relevant Fe–O/OH bond lengths are marked in red and hydrogen bonds are indicated by gray dashed lines. The Fe/Fe termination depicts the fivefold square pyramidal coordinated Fe1 and fourfold coordinated Fe2 with trinuclear hydroxyl groups (μ_3-O^{C}H) at the surface, whereas at the OH/OH termination the hydroxyl groups bind mononuclear at Fe1 ($-$O^{A}H) and binuclear at Fe2 (μ-O^{B}H) restoring the surface octahedra.

compared to goethite(101). We note that the w/OH termination is the only case where water is chemisorbed at Fe1 with $d_{Fe1-O^w} = 2.28$ Å, while the $d_{Fe2-OH} = 2.17$ Å. We attribute this adsorption mode to the hydrogen bonding between the water molecule and the μ-hydroxyl group at Fe2 with $d_{O^B\cdots H} = 1.71$ Å.

A μ-hydroxyl group at the Fe2 site in Fe/OH termination is energetically favored by 1.06 eV compared to a mononuclear OH group at the Fe1 site in OH/Fe. The corresponding distances are $d_{Fe2-OH^-} = 2.03$ Å in Fe/OH and $d_{Fe1-OH^-} = 1.87$ Å in OH/Fe.

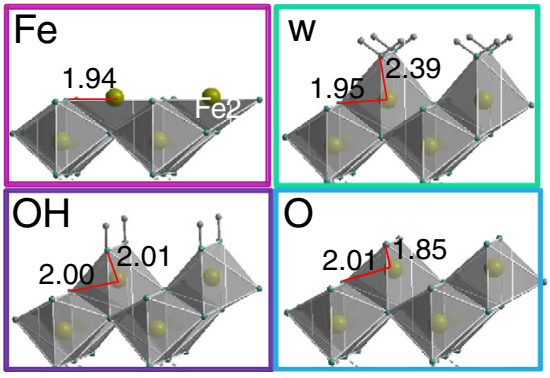

Fig. 4. Surface terminations of γ-FeOOH(010). The relaxed surface structures of the iron (Fe), the water (w), the stoichiometric hydroxyl (OH) as well as the oxygen (O) terminations are displayed.

The deprotonation of hydroxyl groups in the deprotonated Fe/Fe termination of the β-FeOOH(100) surface has a rather drastic effect on the surface relaxation. Fe2 and Fe4 are now tetrahedrally and square pyramidally coordinated by oxygen with shorter bond lengths of 1.87/1.83/1.98 Å (initial: 1.91/2.13/2.14 Å) and 2.08/1.88/1.98 Å (initial: 2.14/2.13/1.91 Å). The distance of Fe1 to the subsurface OH,

Table 4
Magnetic moments ($M_{Fe1/Fe2}$) for the surface irons and band gaps of the corresponding surface terminations of goethite(101) and akaganeite(100). Metallic behavior is denoted by m.

Goethite(101)				Akaganeite(100)			
SF	M_{Fe1} (μ_B)	M_{Fe2} (μ_B)	Δ (eV)	SF	M_{Fe1} (μ_B)	M_{Fe2} (μ_B)	Δ (eV)
Bulk	4.19	4.23	2.0	Bulk	4.26	−4.26	2.1
Fe/Fe	3.69	3.63	1.0	Fe/Fe	3.72	−3.65	1.0
Fe/w	3.69	3.68	0.4	Fe/w	3.73	−3.71	1.0
Fe+w*/Fe	3.70	3.75	0.1	Fe+w*/Fe	3.72	−3.66	1.0
Fe+w*/w	3.70	3.70	1.0	Fe+w*/w	3.74	−3.72	1.0
Fe/OH	3.68	4.29	1.0	Fe/OH	3.70	−4.28	1.2
OH/Fe	4.30	3.64	1.9	OH/Fe	4.27	−3.67	1.5
OH^{C2}/w	4.25	4.22	0.5				
Fe+w*/O	4.20	4.18	m				
Fe+w*/OH	3.69	4.31	1.2	w/OH	3.64	−4.20	m
Fe/FenoH	4.25	4.15	1.0	Fe/FenoH	4.25	−4.15	1.2
Fe/O	4.13	4.12	m	Fe/O	4.14	−4.14	m
OH^{C2}/Fe	4.25	4.14	0.2	O/Fe	4.09	−3.87	m
OH/OH	4.31	4.32	2.0	OH/OH	4.27	−4.29	1.2
O/OH	3.95	4.30	m	O/OH	3.70	−4.29	m
OH/O	4.31	2.42	0.7	OH/O	4.29	−4.01	2.0
OH^{C2}/O	3.70	3.99	m	O/O	3.62	−4.03	m

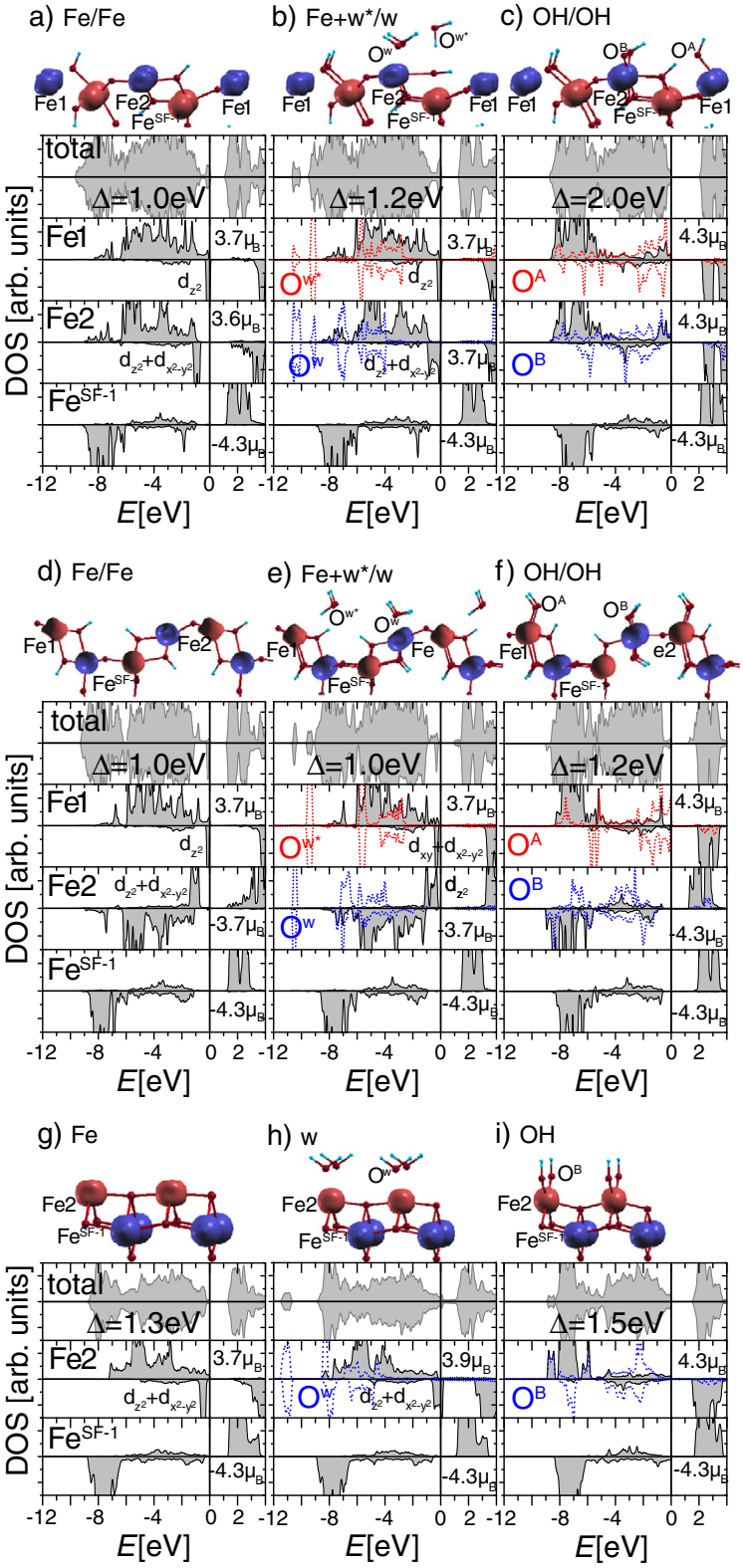

Fig. 5. Spin-density distribution and projected density of states (DOS) for iron, water and hydroxyl terminated surfaces of a–c) goethite(101), d–f) akaganeite(100), and g–i) lepidocrocite(010), respectively. The red and blue spheres in the spin-density plots show the antiferromagnetic coupling of iron ions. The top panel in the DOS plots displays the total DOS of the system, followed by the projected DOS of surface and subsurface iron together with the O *2p* bands of surface oxygens, denoted by dotted lines.

the tip of the square pyramid, is $d_{Fe1-OH} = 2.12$ Å. As shown in Fig. 3 this configuration with broken double band at the surface is stabilized via hydrogen bonding in the subsurface channels.

The surface Fe1 and Fe2 at OH/OH exhibit bond lengths to the oxygen of the corresponding surface hydroxyl groups of $d_{Fe1-O^AH} = 1.89$ Å and $d_{Fe2-O^BH} = 2.02$ Å (see also Table 3).

Similar to the goethite surfaces, different surface hydroxyl groups are identified at the akaganeite(100) surface depending on their coordination to iron ions: mono-, bi-, and trinuclear. These were associated with distinct bands in FTIR spectra [20]. Compared to classical MD simulations [20] where only small relaxations of 0.01 Å were obtained for Fe–O and Fe–OH distances, our periodic DFT calculations reveal strong surface relaxations, especially in the case of water terminated surfaces.

5.3. Lepidocrocite(010)

As a result of the zigzag layers of $Fe(O,OH)_6$ octahedra, the iron termination of lepidocrocite(010) only consists of Fe2 sites as displayed in Fig. 4. Relaxation of the surface atoms in the iron termination leads to slightly decreased Fe–O distances (1.94/2.07 Å) compared to bulk (2.00/2.11 Å). The subsurface octahedra are not affected by the presence of the surface. Molecular water adsorbs to Fe2 with $d_{Fe2-O^w} = 2.39$ Å, but the adsorption energy ($E_{ads} = +0.03$ eV) is slightly positive, likely due to the stability of the initial iron termination. At the stoichiometric hydroxyl termination the bond lengths (2.00/2.01 Å) are similar to bulk lepidocrocite.

We note that in several cases the adsorption energies are very small or even positive. This is attributed to the relative stability of the reference terminations, e.g. the Fe/Fe termination used in the calculations of E_{ads} and possibly to van der Waals interactions, that have not been considered here. A recent GGA study of water adsorption on metal surfaces showed that the inclusion of dispersion corrections enhances the binding energy by approximately 0.3 eV [55]. While this aspect has not been addressed for metal oxide surfaces so far, it deserves further attention in future studies.

6. Electronic and magnetic properties

In this section we focus on the electronic and magnetic properties of the FeOOH surfaces. The magnetic moments of surface iron ions and the band gaps for all terminations are summarized in Table 4. Fig. 5 displays the spin-density distribution at the surface and the corresponding total and projected density of states (DOS) for selected terminations: the iron, hydrated, and hydroxylated terminations of the FeOOH polymorphs. In bulk FeOOH all iron ions are octahedrally coordinated by O/OH and in Fe^{3+} state where all 3d orbitals are singly occupied leading to a spherical spin density distribution. Our results show that the subsurface layers consist exclusively of ferric iron, Fe^{3+}, with $M_{Fe} = 4.3$ μ_B as in bulk. At the surface, however, changes in coordination of Fe^{SF} can affect the occupation of the Fe 3d orbitals. In particular, ferrous iron, Fe^{2+}, is observed both at the Fe1 and Fe2 sites for the iron and water terminations in Fig 5 a, b, d, e, g, and h. At Fe^{2+} surface sites the spin density distribution deviates from spherical shape and the magnetic moment is reduced to 3.5–3.7 μ_B. The band associated with the sixth electron that appears in the opposite spin channel close to E_F in the PDOS reduces the bulk band gap of ~2.0 eV [1,8] to approximately 1.0 eV. Another interesting effect is a rearrangement of the crystal field (CF) splitting with respect to bulk at goethite(101) and akaganeite(100) when the coordination of surface iron is reduced. Here the d_{z^2} orbital of fivefold coordinated Fe1 as well as the d_{z^2} and $d_{x^2-y^2}$ orbitals of fourfold coordinated Fe2 are lowered in energy with respect to the t_{2g}-orbitals in contrast to the CF splitting in the bulk octahedral coordination.

Note that for some oxygen terminations we observe lowered magnetic moments, e.g. $M_{Fe2} = 2.42$ μ_B in the OH/O termination of goethite(101), indicating higher valence states of iron, Fe^{4+}, in a ferryl-oxo group.

There are strong parallels in electronic behavior for goethite(101), akaganeite(100), and lepidocrocite(010) despite the differences in surface structure as discussed in Section 5.

6.1. Iron termination

At the iron terminations of FeOOH stable at oxygen and water poor conditions the surface iron ions are reduced to Fe^{2+} with a magnetic moment of 3.7 μ_B. Fe1 at α-FeOOH(101) and β-FeOOH(100) is square pyramidally coordinated by oxygen with d_{z^2} states pinned at the Fermi level (second DOS panel in Fig. 5a and d). In contrast the sixth electron at the fourfold coordinated Fe2 (α-FeOOH(101), β-FeOOH(100), and γ-FeOOH(010)) occupies a state 0.5 eV below E_F (see third panel in Fig. 5a, d, and g). The occupied states of Fe^{3+} in the subsurface layer start at −1.0 eV below E_F. The band gap in these terminations is defined by the highest lying sixth orbital of Fe1 (or Fe2) in Fe^{2+} state and the unoccupied 3d states of Fe^{SF-1} and is significantly reduced with respect to bulk from 2.0 eV [8] to 1.0–1.2 eV.

6.2. Water termination

As illustrated in Fig. 5b, e, and h, water molecules are hydrogen bonded at the Fe1 site at the α-FeOOH(101) and β-FeOOH(100) surfaces, while at the Fe2 site water is chemisorbed. In this case we find that the sixth orbital at both Fe1 and Fe2 sites is just below E_F leading to a similar, reduced band gap as in the iron terminations. The peaks at −11.0 eV and −9.5 eV in the PDOS of oxygen correspond to molecular orbitals of w and w*. The different position of these bands indicates the stronger binding of water to Fe2 compared to hydrogen bonded water at the Fe1 site. Furthermore, the broadening of the bands of O^w and O^{w*} at α-FeOOH(101) reflects the formation of a hydrogen bond between w and w* as discussed in Section 5. This effect is missing for β-FeOOH(100) where the bands remain sharp consistent with a lower binding energy.

6.3. Hydroxyl termination

In contrast to the reduced Fe at the iron and hydrated terminations, at the hydroxyl termination with singly protonated O^A and O^B, all surface iron atoms are in a Fe^{3+} state with spherical spin density distributions. The charge-transfer type of band gap of 2.0 eV separates occupied O 2p and unoccupied Fe 3d states (see Fig. 5b, e, and h). Thus hydroxylated FeOOH surfaces exhibit properties closest to bulk FeOOH.

7. Conclusion

Based on periodic DFT calculations we present a comprehensive study on the surface configurations and properties of the FeOOH polymorph surfaces goethite(101), akaganeite(100), and lepidocrocite(100) and their interaction with water. A main finding is that the coordination of surface iron strongly influences the surface reactivity as well as the binding mechanism of water. In particular, a strong preference is found for binuclear water adsorption at the fourfold coordinated Fe2 site restoring the octahedron around Fe2. In contrast, water binds weaker to the fivefold coordinated Fe1 with hydrogen instead of oxygen pointing towards the surface. The surface phase diagrams obtained within the framework of *ab initio* thermodynamics reveal several stable terminations: iron terminations at oxygen and water poor conditions, water terminations at water rich and oxygen poor conditions, and a hydroxylated termination at ambient conditions. Different types of surface hydroxyl and aquo groups are identified according to their coordination at the FeOOH surfaces. The variation in protonation state can be directly related to changes in pH conditions. Furthermore, the surface energies show a reverse order in stability compared to the bulk FeOOH polymorphs with lepidocrocite(010) being most stable, followed by akaganeite(100) and goethite(101).

Our study provides detailed structural information of the surfaces that is relevant for interpretation of experimental data. Concerning the bond lengths of surface terminal groups we find the following variations: The shortest distances are obtained for oxygen terminations with Fe–O distances between 1.75 and 1.87 Å. For hydroxylated surfaces the Fe–OH bond length is shorter at Fe1 (1.91 Å at α(101) and 1.88 Å at β(100)) than at Fe2 (1.96 and 2.01 Å, respectively). The Fe2–OH distance at γ-FeOOH(010) is 2.01 Å. The distinct adsorption mechanism of water at Fe1 through hydrogen bonding results in longer Fe1–H_2O distances of 3.51 Å at goethite(101) and 3.23 Å at akaganeite(100), whereas the Fe2–H_2O bond lengths for chemisorbed water vary between 2.32 and 2.39 Å. We note that the explicit treatment of a solvation layer that goes beyond the scope of this study may enhance the bond lengths of chemisorbed water by up to 0.3 Å as shown for α-FeOOH(100) [15,51].

The results presented here show that the composition of the surface has a strong influence on the surface electronic and magnetic properties. In particular, iron and water terminated surfaces exhibit ferrous iron in the surface layer and a reduced band gap, while oxo species lead to higher valent cations. However, the fully hydroxylated FeOOH surfaces with restored surface octahedra that are stable surface configurations at standard conditions, show properties closest to bulk FeOOH where only ferric iron is present. Thus by varying the environmental of pH conditions, i.e. the partial pressures of water and oxygen, the ferric/ferrous iron ratio at the FeOOH surfaces can be controlled.

Acknowledgments

This work is funded by the BMBF Program Geotechnologies—Mineral Surfaces, project SURFTRAP as well as the Bavarian Elite Network. The calculations were performed at the supercomputer HLRBII, Leibniz Rechenzentrum, project h0721.

References

[1] R. Cornell, U. Schwertmann, The Iron Oxides: Structre, Properties, Reactions, Occurrences and Uses, Wiley-VCH GmBH & Co. KGaA, Weinheim, 2003.
[2] L. Mazeina, A. Navrotsky, Chem. Mater. 19 (2007) 825.
[3] A. Navrotsky, L. Mazeina, J. Majzlan, Science 319 (2008) 1635.
[4] G. Brown, V. Henrich, W. Casey, D. Clark, C. Eggleston, A. Felmy, D. Goodman, M. Gratzel, G. Maciel, M. McCarthy, et al., Chem. Rev. 99 (1999) 77.
[5] D. Sherman, S. Randall, Geochim. Cosmochim. Acta 67 (2003) 4223.
[6] C. Laberty, A. Navrotsky, Geochim. Cosmochim. Acta 62 (1998) 2905.
[7] K. Rosso, J. Rustad, Am. Mineral. 86 (2001) 312.
[8] K. Otte, R. Pentcheva, W. Schmahl, J. Rustad, Phys. Rev. B 80 (2009) 205116.
[9] U. Schwertmann, G. Pfab, Geochim. Cosmochim. Acta 58 (1994) 4349.
[10] U. Schwertmann, R. Cornell, Iron Oxides in the Laboratory, Weinheim, VCH, 2000.
[11] M. Villalobos, M. Cheney, J. Alcaraz-Cienfuegos, J. Colloid Interface Sci. 336 (2009) 412.
[12] B. Russell, M. Payne, L. Ciacchi, Phys. Rev. B 79 (2009) 165101.
[13] T. Trainor, A. Chaka, P. Eng, M. Newville, G. Waychunas, J. Catalano, G. Brownr, Surf. Sci. 573 (2004) 204.
[14] J.-F. Boily, A. Felmy, Geochim. Cosmochim. Acta 72 (2008) 3338.
[15] S. Ghose, G. Waychunas, T. Trainor, P. Eng, Geochim. Cosmochim. Acta 74 (2010) 1943.
[16] J. Rustad, J.-F. Boily, Am. Min. 95 (2010) 414.
[17] A. MacKay, Min. Mag. 33 (1962) 270.
[18] K. Otte, W. Schmahl, R. Pentcheva, in preparation.
[19] L. Mazeina, S. Deore, A. Navrotsky, Chem. Mater. 18 (2006) 1830.
[20] X. Song, J.-F. Boily, J. Phys. Chem. C 115 (2011) 17036.
[21] P. Ramdohr, H. Strunz, Lehrbuch der Mineralogie, In: 16th ed., Stuttgart, 0, 1978, p. 876.
[22] E. O'Loughlin, C. Gorski, M. Scherer, M.M., K. Kemner, Environ. Sci. Technol. 44 (2010) 4570.
[23] H. Guo, A. Barnard, Phys. Rev. B 83 (2011) 094112.
[24] J. Majzlan, B. Lang, R. Stevens, A. Navrotsky, B. Woodfield, J. Boerio-Goates, Am. Mineral. 88 (2003) 846.
[25] J. Majzlan, K.-D. Grevel, A. Navrotsky, Am. Mineral. 88 (2003) 855.
[26] J. Majzlan, L. Mazeina, A. Navrotsky, Geochim. Cosmochim. Acta 71 (2007) 615.
[27] H. Guo, A. Barnard, Phys. Chem. Chem. Phys. 13 (2011) 17864.
[28] K. Reuter, M. Scheffler, Phys. Rev. B 65 (2001) 035406.
[29] N. Mulakaluri, R. Pentchteva, M. Wieland, W. Moritz, M. Scheffler, Phys. Rev. Lett. 103 (2009) 176102.
[30] G. Parkinson, N. Mulakaluri, Y. Losovyj, P. Jacobson, R. Pentcheva, U. Diebold, Phys. Rev. B 82 (2010) 125413.
[31] G. Kresse, J. Hafner, Phys. Rev. B 47 (1993) 558.
[32] G. Kresse, J. Hafner, Phys. Rev. B 49 (1994) 14251.
[33] G. Kresse, J. Hafner, J. Phys. Condens. Matter 6 (1994) 8245.
[34] G. Kresse, J. Furthmüller, Comput. Mat. Sci. 6 (1996) 15.
[35] G. Kresse, J. Furthmüller, Phys. Rev. B 54 (1996) 11169.
[36] J. Perdew, K. Burke, M. Ernzerhof, Phys. Rev. Lett. 77 (1996) 3865.
[37] S. Dudarev, G. Botton, S. Savrasov, C. Humphreys, A. Sutton, Phys. Rev. B 57 (1998) 1505.
[38] G. Rollmann, A. Rohrbach, P. Entel, J. Hafner, Phys. Rev. B 69 (2004) 165107.
[39] I. Leonov, A. Yaresko, V. Antonov, M. Korotin, V. Anisimov, Phys. Rev. Lett. 93 (2004) 146404.
[40] G. Madsen, P. Novak, Europhys. Lett. 69 (2005) 777.
[41] T. Tsuchiya, R. Wentzcovitch, C. Dailva, S. Deironcoli, Phys. Rev. Lett. 96 (2006) 198501.
[42] P. Blaha, K. Schwarz, G. Madsen, D. Kvasnicka, J. Luitz, WIEN2k, An Augmented Plane Wave + Local Orbitals Program for Calculating Crystal Properties (K arlheinz Schwarz), Techn. Univ, Wien, Austria, 2001.
[43] A. Szytula, A. Burewicz, Z. Dimitrijevic, S. Krasnicki, H. Rzany, J. Todorovic, Phys. Status Solidi (a) 26 (1968) 429.
[44] A. MacKay, Mineral. Mag. J. Mineral. Soc. 32 (1960) 545.
[45] H. Christensen, A. Christensen, Acta Chem. Scand., Series A 32 (1978) 87.
[46] Q. Sun, K. Reuter, M. Scheffler, Phys. Rev. B 67 (2003) 205424.
[47] G. Oxford, A. Chaka, Phys. Rev. B 84 (2010) 205453.
[48] X.-G. Wang, A. Chaka, M. Scheffler, Phys. Rev. Lett. 84 (2000) 3650.
[49] M. Chaser, J. Curnutt, J. Downeyr, R. McDonald, A. Syverud, E. Valenzuela, J. Phys. Chem. Ref. Data 11 (1982) 695.
[50] J. McHale, A. Auroux, A. Perrotta, A. Navrotsky, Science 277 (1997) 788.
[51] J. Kubicki, K. Paul, D. Sparks, Geochem. Trans. 9 (2008) 4.
[52] A. Michaelides, Appl. Phys. A 85 (2006) 412.
[53] A. Aquino, D. Tunega, G. Haberhauer, M. Gerzabek, H. Lischka, Geochim. Cosmochim. Acta 72 (2008) 3587.
[54] U. Bergmann, A. Ciccoi, P. Wernet, E. Principi, P. Glatzel, A. Nilsson, J. Chem. Phys. 127 (2007) 174504.
[55] K. Tonigold, A. Groß, J. Comput. Chem. 33 (2012) 698.

Manuscript 3: Arsenate Adsorption on FeOOH Surfaces

DFT+U Study of Arsenate Adsorption on FeOOH Surfaces: Evidence for Competing Binding Mechanisms

K. Otte, W.W. Schmahl, and R. Pentcheva,
Journal of Physical Chemistry C, submitted (2012).

DFT+U Study of Arsenate Adsorption on FeOOH Surfaces: Evidence for Competing Binding Mechanisms

Katrin Otte,* Wolfgang W. Schmahl, and Rossitza Pentcheva*

Section Crystallography, Department of Earth and Environmental Sciences and Center of Nanoscience (CENS),

University of Munich, Theresienstr. 41, 80333 Munich, Germany

E-mail: katrin.otte@lrz.uni-muenchen.de; pentcheva@lrz.uni-muenchen.de

*To whom correspondence should be addressed

Abstract

Based on periodic density functional theory (DFT) calculations including an on-site Coulomb repulsion term U we study the adsorption mechanism of arsenate on the goethite(101), akaganeite(100), and lepidocrocite(010) surfaces. Mono- and bidentate binding configurations of arsenate complexes are considered at two distinct iron surface sites - directly at fivefold coordinated Fe1 and/or fourfold coordinated Fe2 as well as involving ligand exchange. The results obtained within *ab initio* thermodynamics shed light on the ongoing controversy on the arsenate adsorption configuration and we identify monodentate adsorbed arsenate complexes as stable configuration at ambient conditions and a strong preference for protonated arsenate complexes: a monodentate mononuclear complex at Fe1 ($d_{\mathrm{Fe1-As}}$=3.45 Å) at goethite(101) and a monodentate binuclear complex at Fe2 ($d_{\mathrm{Fe2-As}}$=3.29 Å) at akaganeite(100). Repulsive interactions between the complexes limit the loading capacity and promote configurations with maximized distances between the adsorbates. With decreasing oxygen pressures a mixed adsorption of bidentate binuclear complexes at Fe1 ($d_{\mathrm{Fe1-As}}$=3.26-3.34 Å) and monodentate binuclear arsenate at Fe2 ($d_{\mathrm{Fe2-As}}$=3.31-3.50 Å), and, finally, rows of protonated bidentate complexes at Fe1 with $d_{\mathrm{Fe1-As}}$=3.55-3.59 Å are favored at α-FeOOH(101) and β-FeOOH(100). At lepidocrocite(010) with only Fe2 sites exposed, the surface phase diagram is dominated by alternating protonated monodentate binuclear complexes ($d_{\mathrm{Fe2-As}}$=3.38 Å) and hydroxyl groups. At low oxygen pressures alternating rows of protonated bidentate mononuclear complexes ($d_{\mathrm{Fe2-As}}$=3.10 Å) and water are present. Hydrogen bond formation to surface hydroxyl groups and water plays a crucial role in the stabilization of these adsorbate configurations and leads to tilting of the arsenate complex that significantly reduces the Fe–As distance. Our results show that the Fe–As bond length is mainly determined by the protonation state, arsenate coverage, and hydrogen bonding to surface functional groups and to a lesser extent by the adsorption mode. This demonstrates that the Fe–As distance cannot be used as a unique criterion to discriminate between adsorption modes.

1 Introduction

Arsenic contamination of ground waters and mine wastes represents a significant environmental hazard.[1] An efficient method to control arsenic transport and distribution in aqueous environments is the binding at water/mineral interfaces. It is well established that arsenic species form predominantly inner sphere complexes at hydrous iron oxide surfaces.[2–6] In a recent study Catalano *et al.*[7] reported a two to one ratio between inner and outer sphere complexes adsorbed on hematite at saturation. However, the exact inner sphere bonding geometry of arsenate (mono- or bidentate) on the iron oxyhydroxide (FeOOH) surfaces is still a matter of ongoing debate.

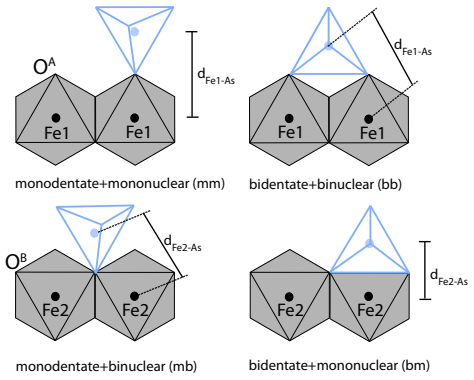

Figure 1: Schematic illustration of possible adsorption geometries of the AsO_4 complex (blue/light grey tetrahedron) at the tip/apex and in the basal plane of edge sharing FeO_6 octahedra, depicted in gray. Fe and As are represented as black and blue (gray) dots located in the center of the respective polyhedron. O^A and O^B refer to the oxygen at the tip and in the basal plane of the octahedra, respectively. Mono- or bidentate specify the linkage between tetra- and octahedra via one or two oxygen, whereas mono- or binuclear indicate the coordination of As to one or two Fe atoms via oxygen.

The FeOOH polymorphs are nanocrystalline materials with high surface area. Their structure is characterized by double bands of $Fe(O,OH)_6$ octahedra, resulting in 2×1 channels in goethite, α-FeOOH, 1×1 and large 2×2 tunnels in akaganeite, β-FeOOH, and zigzag-sheets in lepidocrocite, γ-FeOOH. The most common surfaces are obtained by cutting through the 2×1 channels in α-FeOOH(101),[8,9] the large 2×2 channels in β-FeOOH(100)[10] or between the zigzag sheets in γ-

FeOOH(010).[10,11] Thereby, two distinct iron sites are exposed at the iron terminated surfaces of α-FeOOH(101) and β-FeOOH(100), *i.e.* a fivefold coordinated Fe1 and a fourfold coordinated Fe2 site, while γ-FeOOH(010) has only Fe2 surface sites. Density functional theory (DFT) caculations of the FeOOH surfaces and their interaction with water reveal that Fe1 and Fe2 have significantly different reactivity and affinity for surface terminal groups (-OH/-OH_2).[12]

As displayed schematically in Figure 1, different possibilities for arsenate adsorption emerge depending on the orientation of $Fe(O,OH)_6$ octahedra at the FeOOH surface and the surface iron site. At Fe1 arsenate tetrahedra can bind monodentate mononuclear (mm, ^{1}V) or bidentate binuclear (bb, ^{2}C) while at Fe2 monodentate binuclear (mb) or bidentate mononuclear (bm,^{2}E) geometries are possible. Here mono- or bidentate specify the linkage between the AsO_4-tetrahedra and $Fe(O,OH)_6$ octahedra via one or two oxygens, whereas mono- or binuclear indicate the coordination of As to one or two iron atoms via oxygen. While the mm, bb, and bm configurations for arsenate adsorption have been extensively discussed in the literature, the mb mode has not been considered so far. Moreover, the schematic diagram suggests distinct Fe–As distances ($d_{\mathrm{Fe–As}}$) for each adsorption mode, but the idealized adsorbate geometry does not include relaxations of the atoms.

The most common technique to investigate the local environment of the adsorbed arsenate is EXAFS (extended x-ray absorption fine structure).[3,14–16] However, the interpretation of the extracted Fe–As distances is not unambiguous. In order to relate those to a particular adsorption geometry, one often relies on schematic bonding configurations as the ones shown in Figure 1 and/or on a comparison to known compounds that exhibit a similar environment as well as bond lengths, *e.g.*[3,16–18] Distances of 3.50 to 3.60 Å are thus commonly associated with a monodentate coordination, whereas distances of 2.70 to 3.45 Å with a bidentate one. According to this, the Fe–As distance of $\sim$3.30 Å measured in EXAFS experiments is related to a predominant bidentate binuclear adsorption geometry .[3,17,19,20] Waychunas et al.[3] included an additional monodentate component with a Fe–As distance of 3.60 Å in the fitting procedure. In contrast, Manceau[19] proposed rather a bidentate mononuclear configuration with a Fe–As distance of 2.80 Å to improve

the fit, similar to selenate adsorption geometries. In a reevaluation of their data Waychunas et al.[4] suggested a monodentate component with $d_{Fe–As}$=3.60 Å for low coverages at goethite. They[4] found several bonding configurations at lepidocrocite that were not closer identified as well as components with $d_{Fe–As}$=2.86 and 3.26 Å at akaganeite. Fendorf et al.[15] proposed a variation in the adsorption configuration with coverage at goethite surfaces: a monodentate mononuclear configuration with $d_{Fe–As}$=3.59 Å at low coverages, a dominating bidentate binuclear configuration ($d_{Fe–As}$=3.24 Å) at intermediate coverages and an additional bidentate mononuclear component ($d_{Fe–As}$=2.85 Å) at high coverages. On the other hand Sherman and Randall[17] suggested that the latter distance is rather related to As–O–O–As multiple scattering.[17] Furthermore, they concluded that arsenate binds bidentate binuclear both on goethite and lepidocrocit with a similar bond length of 3.31 Å. *Ab initio* calculations using clusters containing only two FeO_6 octahedra support this interpretation: a bb inner sphere complex is found to be energetically favored compared to a bm one, while the mm configuration was not stable.[17] The predominance of a bb complex with Fe–As distance of ∼3.30 Å was recently challenged by Loring et al.[18] that observed a striking similarity between the arsenate complex adsorbed at the goethite surface and pentaamminecobalt(III) arsenate with monodentate coordination and a much shorter Co–As distance of 3.25 Å.

Experimental results (*e.g.*[4]) suggest distinct adsorption modes depending on varying surface environments at the FeOOH polymorphs, but an exact atomic scale knowledge of the bonding geometries taking into account all possible relaxations of the arsenate tetrahedron and the surface is missing. DFT studies performed so far have used mostly clusters containing two iron ions.[17,21] While these capture some aspects of the adsorption process, the small cluster size does not allow realistic modeling of the FeOOH surface structure and the difference in surface morphology between the polymorphs. Additionally, the interaction with other adsorbates and surface functional groups cannot be fully taken into account.

To gain insight into the inner sphere adsorption mechanism of arsenate at the surfaces of the most common FeOOH polymorphs we present here DFT calculations where electronic correlations are taken into account within the GGA+U approach.[22] The objectives of the present study are: (i) to

determine the energetic stability of different arsenate adsorption configurations and adsorption sites at FeOOH surfaces and extract the corresponding structural changes (especially Fe–As distances and Fe–O–As angles); (ii) to identify similarities and differences in the adsorption process on the different FeOOH surfaces; (iii) to study surface loading/adsorption capacity of FeOOH surfaces by varying the adsorbate concentration; (iv) to investigate the effect of the adsorbate on the electronic properties of the FeOOH surfaces. Besides direct binding of arsenate complexes at surface iron sites, we have considered also ligand exchange of hydroxyl or aquo terminal groups. Different pH conditions are modeled by varying the protonation state of surface terminal groups. This allows also to explore the effect of surface functional groups (-O/-OH/-OH_2) on the stabilization of the arsenate complexes, an issue that has only recently been addressed for arsenate adsorption on TiO_2 surfaces.[23]

The paper is organized as follows: the details of the calculations are introduced in Section 2 and a description of the different arsenate adsorption geometries and their binding strength is given in Section 3.1. The energetics of the most stable surface configurations and structural details are discussed in Section 3.2. In Section 3.3 we describe the effect of the adsorbate on the magnetic and electronic properties of the systems. A discussion of the results and a comparison to previous findings both experimental and theoretical are presented in Section 4. Finally, the results are summarized in Section 5.

2 Calculational Details

The DFT calculations were carried out with the Vienna *ab initio* Simulation Package (VASP)[24–28] using a projected augmented wave (PAW) basis set [29,30] and the generalized gradient approximation (GGA)[31] for the exchange and correlation potential. Electronic correlations beyond GGA are treated by adding an on-site Coulomb repulsion parameter U within the GGA+U approach.[32] Throughout the calculations $U_{eff} = 5$ eV on iron has been employed that reproduces the experimental band gaps of ~ 2.0 eV[10] of the bulk FeOOH polymorphs.[33,34]

The systems are modeled in a supercell geometry with a vacuum of at least 10 Å between the surface slabs to prevent interactions between the surfaces and their periodic images. The slabs contain two inversion symmetric surfaces to avoid the formation of spurious electric fields. The thickness of the slabs amounts to six iron layers for goethite (101) and eight for akaganeite(100) and lepidocrocite(010), respectively. To allow a variation in the coverage of adsorbed arsenic complexes the lateral periodicity is extended to (1×2) for the surfaces of goethite(101) and akaganeite(100), and to (2×2) for lepidocrocite(010) with respect to models of the clean FeOOH surfaces.[12] This results in system sizes of 100 to 156 atoms which makes the calculations computationally very involved.

For the integration in reciprocal space 6, 8, and 11 k points were used in the irreducible part of the Brillouin zone for the α-, β-, and γ-FeOOH surfaces, respectively. For the calculation of density of states, an increased k-mesh of 30, 21, and 26 k-points, respectively, has been applied. An energy cut-off of 500 eV for the plane-wave basis set is used to achieve an accuracy of total energy differences of 10 meV per simulation cell.

The structure of the adsorbate complex and the two outer iron double layers are fully optimized up to a force convergence of 0.001 eV/Å, while the inner layers are kept fixed at their bulk positions to reproduce the properties of FeOOH bulk. While previous studies have used ferromagnetically coupled clusters[17] the FeOOH polymorphs exhibit an antiferromagnetic arrangement,[35–37] which is confirmed by DFT calculations.[33,34] This antiferromagnetic coupling was also adopted for the surfaces.

The relative stability of different adsorption configurations is determined using *ab initio* atomistic thermodynamics[38] where the surface energy, $\gamma(T, p_i)$ is defined in the following way:

$$\gamma(T, p_i) = \frac{1}{2A}\left(G^{\text{slab}}_{\text{FeOOH}} - \sum N_i \mu_i\right) \tag{1}$$

Here A is the surface area, the factor 2 accounts for the presence of two surfaces, $G^{\text{slab}}_{\text{FeOOH}}$ is the Gibbs free energy of the system, and μ_i are the chemical potentials of the constituents with i=

Fe, O, H, or As. μ_{As} is related to the Gibbs free energy of the H_3AsO_4 molecule. [1] $G^{\mathrm{slab}}_{\mathrm{FeOOH}}$ can be expressed by the total energy from the DFT calculations. The inclusion of vibrational contributions goes beyond the scope of this study. A previous study of water on $RuO_2(110)$[39] reported that neglecting vibrational contributions of surface hydroxyl and aquo groups leads to an uncertainty in surface energies of 10-15 meV/Å^2. A recent DFT study of γ-MnOOH(010) surfaces[40] showed that vibrational contributions vary by less than 0.1 eV per simulations cell between different terminations.

The adsorption energy, E_{ads}, of arsenate at FeOOH surfaces in [$^{\mathrm{eV}}/_{\mathrm{molecule}}$] is described as

$$E_{\mathrm{ads}} = \frac{1}{N}\left(E_{N\mathrm{H}_n\mathrm{AsO}_4\cdot\mathrm{FeOOH}} - E_{\mathrm{FeOOH}} - NE_{\mathrm{H_3AsO_4}}\right) \tag{2}$$

where E_{FeOOH} and $E_{N\mathrm{H}_n\mathrm{AsO}_4\cdot\mathrm{FeOOH}}$ are the total energies of surfaces before and after arsenate adsorption with n protons in H_nAsO_4. The total energy of an isolated water and a H_3AsO_4 molecule, needed as reference energies, are calculated in a box of $10\times10\times10$ Å^3, while for oxygen a box of $10\times10\times8$ Å^3 was used in order to obtain the correct ground state. The number n of hydrogen atoms is balanced by O_2 and H_2O molecules. The total energy of bulk iron, E_{Fe}, is calculated for bulk the ground state with a bcc structure and ferromagnetic coupling.

3 Results

3.1 Adsorption Geometries and Stability

In this section we describe the inner sphere arsenate adsorption geometries at the FeOOH surfaces considered in our study. Truncating the octahedra at the iron plane exposes a fivefold coordinated Fe1 with a missing apical oxygen (O^A) and a fourfold coordinated Fe2 with two missing oxygens in the basal plane (O^B). Goethite(101) and akaganeite(100) provide both Fe1 and Fe2 surface sites. At lepidocrocite(010), however, only Fe2 sites are present.

[1] $\mu_{\mathrm{As}} + 1.5\cdot\mu_{\mathrm{H_2O}} + 2.5\cdot\mu_{\mathrm{O}} = G_{\mathrm{H_3AsO_4}}$

As mentioned above and displayed in Figure 1, different adsorption geometries of the As complex are possible at the Fe1 and Fe2 sites. At Fe1 the arsenate can adsorb (i) monodentate mononuclear (mm), *i.e.* corner connected to the tip of the surface octahedron around Fe1 or (ii) bidentate binuclear (bb) via corner sharing at the tip of the surface octahedron around Fe1. On the other hand the adsorbate configurations at Fe2 are (i) monodentate binuclear (mb) via adsorption in the basal plane of the surface octahedron around Fe2 and (ii) bidentate mononuclear (bm) in the basal plane of the surface octahedron around Fe2. In the idealized starting adsorption configurations the Fe–O–As angles are: 180° (mm), 113° (bb), 130° (mb), and 67° (bm). Later we will report the changes upon structural relaxation.

The O–O^H (2.94 Å) and O^H–O^H distances (2.73 Å) of the gas phase H_3AsO_4 match well the Fe1–Fe1 and Fe2–Fe2 distances of approximately 3.00 Å at the akaganeite(100) and goethite(101) surfaces and thus allow bidentate adsorption. On the other hand the large Fe1–Fe2 distances of 3.46 Å at akaganeite(100) and 5.68 Å at goethite(101) preclude a mixed bidentate adsorption involving both Fe1 and Fe2 sites.

Owing to the larger lateral periodicity used in our study there are two Fe1 and two Fe2 sites at the goethite(101) and akaganeite(100) surfaces and four Fe2 sites at lepidocrocite(010). Taking into account the distinct adsorption geometries at Fe1 and Fe2 sites, discussed above, as well as different coverages and protonation states, in total 22 different configurations were investigated for goethite(101), 23 for akaganeite(100), and 13 for lepidocrocite(010). We denote the different terminations using the corresponding surface terminal groups/adsorbates, *e.g.* a deprotonated bidentate binuclear arsenate adsorbed at every second Fe1 and an oxo group at Fe2 is denoted as bb/O+O, while the protonated case is named H_2bb/OH+OH (H_2AsO_4 at Fe1 and hydroxyl groups at Fe2). At lepidocrocite(010) Fe2 surface sites are present in neighboring rows. The corresponding notation for two bidentate mononuclear arsenate complexes adsorbed at every second site in neighboring Fe2 rows is bm/bm or H_2bm/H_2bm in case of protonation.

In the following we discuss the adsorption energy of arsenate complexes at the different surfaces depending on adsorption site, protonation state and coverage. For selected cases we have

also considered adsorption of arsenate via ligand exchange of hydroxyl or aquo groups. Here the different protontation states determine the pH conditions: hydrated iron surface sites correspond to low pH, while a mixture of hydroxyl and aquo surface end groups are present at intermediate, and fully hyddoxylated surface sites (aquo groups) at higher pH. Furthermore, we show how the Fe–O–As angle ($\angle_{\mathrm{Fe–O–As}}$) influences the Fe–As bond lengths ($d_{\mathrm{Fe–As}}$). The supplementary material to this paper contains the adsorption energies of the studied adsorption pathways in Tables. S1, S3, S5. Side views for each surface configuration are shown in Figures S1–S3 and characteristic bond lengths are summarized in Tables. S2, S4, S6.

3.1.1 α-FeOOH(101)

Relative stability of adsorbate configurations Our results show that protonation leads to a strong stabilization of the arsenate complexes. For a mm complex at Fe1 on α-FeOOH(101) the adsorption energy changes from E_{ads}=-0.97 eV for O+mm/O+O to -2.25 eV if the complex is protonated in O+H_2mm/O+O and to -4.06 eV when additionally the surface is hydroxylated in OH+H_2mm/OH+OH. While the deprotonated mm complex is stronger bound at Fe1 (O+mm/O+O, E_{ads}=-0.97 eV) than an mb complex at Fe2 (O+O/mb+O, E_{ads}=-0.69 eV), the trend is reversed if the adsorbate is protonated: E_{ads}=-2.25 eV for O+H_2mm/O+O versus -2.65 eV for O+O/H_2mb+O. On the other hand bidentate complexes are bound stronger at Fe1 with -0.89 eV for bb/O+O and -0.73 eV for O+O/bm. The adsorption energies for the corresponding protonated cases are -4.21 eV for H_2bb/OH+OH and -3.83 eV for OH+OH/H_2bm, respectively.

Coverage dependence An interesting trend occurs when increasing the coverage of adsorbates. A significant reduction of E_{ads} is observed if the complexes are adsorbed at neighboring sites of the same type (either Fe1 or Fe2) indicating strong adsorbate-adsorbate repulsion. For example the adsorption energy changes from -4.21 eV for H_2bb/OH+OH to -0.91 eV for 2H_2bb/OH+OH. In the case of a bm complex the energy even becomes positive for OH+OH/2H_2bm (E_{ads}=+0.19 eV). Here the two bb complexes at Fe1 are more favorable than the two bm complexes at Fe2. On

the other hand, due to the larger distances between the adsorbates, mixed adsorption with mono- and bidentate complexes at both iron surface sites is significantly more favorable. For instance the mixed monodentate configuration O+H_2mm/H_2mb+O has an adsorption energy of -1.71 eV, whereas a mixed mono- and bidentate configuration OH+H_2mm/H_2bm is bound with -2.76 eV. However, the most favorable configuration comprises a protonated bidentate complex at Fe1 and a monodentate binuclear complex alternating with hydroxyl groups at Fe2, *i.e.* H_2bb/Hmb+OH with E_{ads}=-3.59 eV or H_2bb/H_2mb+OH with E_{ads}=-3.31 eV.

Ligand Exchange Besides the direct adsorption at exposed surface iron sites we have also considered ligand exchange scenarios. These can be related to different pH conditions. We find that the adsorption energy for a mm complex at a bare iron ion of *e.g.* E_{ads}=-4.06 eV in OH+H_2mm/OH+OH is reduced to -3.14 eV if the arsenate exchanges a water molecule bound via hydrogen bonding to Fe1 (H_2O*) and is further lowered to -2.66 eV in case of a substituted a hydroxyl group. For bidentate complexes where two surface end groups need to be substituted, the adsorption energy even turns positive in some cases. The adsorption energy for two protonated bb complexes (2H_2bb/OH+OH) changes from -0.91 eV for direct adsorption at Fe1 sites to positive values of +0.02 eV and +0.49 eV if two hydrogen bonded water molecules or two hydroxyl groups are exchanged, respectively. On the other hand, for the mixed protonated bb and mb complexes in H_2bb/H_2mb+OH the adsorption energy decreases from -3.31 eV for direct adsorption to -2.73 eV for exchange of hydrogen bonded and chemisorbed water, and, finally, to -1.38 eV for exchange of hydroxyl groups. The overall trend shows a decreasing affinity to bind arsenate complexes with increasing pH values.

Fe–As distances Concerning the bond lengths at α-FeOOH(101) we observe a noticeable increase with protonation. For a single mm complex at Fe1, the Fe–As distance changes from 3.25 Å ($\angle_{Fe1–O–As}$=120°) to 3.45 Å ($\angle_{Fe1–O–As}$ increased to 135°) upon protonation. Similarly, for a mb complex at Fe2 the distance increases from 3.16 Å ($\angle_{Fe2–O–As}$=111°) to 3.31 Å ($\angle_{Fe2–O–As}$ increased to 119°). The bb adsorption at Fe1 leads to Fe–As distances close to the mm case: $d_{Fe1–As}$=3.21 Å

($\angle_{Fe1–O–As}$=117°) for a single bb complex at Fe1 which is only slightly affected by protonation with $d_{Fe–As}$=3.24 Å ($\angle_{Fe1–O–As}$=124°) for a H_2bb complex. The shortest Fe–As distance is found for bm adsorption at Fe2 with bond lengths of 2.78 Å ($\angle_{Fe2–O–As}$=91°) and 2.85 Å ($\angle_{Fe2–O–As}$=87°) before and after protonation, respectively. The Fe–As distances increase with arsenate concentration, *e.g.* from 3.24 Å for H_2bb to 3.59 Å for $2H_2$bb ($\angle_{Fe1–O–As}$=122°) at each Fe1 and from 2.85 Å for H_2bm at Fe2 to 3.05 Å ($\angle_{Fe2–O–As}$=90°) in $2H_2$bm at each Fe2. However, the increase in Fe–As distance is much smaller for mixed adsorption at both Fe1 and Fe2 sites. Our results show that the Fe–As distances for mm and bb at Fe1 and mb at Fe2 are similar and vary between 3.20 Å and 3.60 Å depending on the protonation state and surface coverage. Moreover, Fe–As distances for bm adsorbed complexes at Fe2 sites are significantly shorter, $d_{Fe–As}$=2.80-3.00 Å.

3.1.2 β-FeOOH(100)

Relative stability of adsorbate configurations Most energetic trends of arsenate adsorption at β-FeOOH(100) are similar to α-FeOOH(101). The binding energy to the surface is enhanced with increasing protonation state, *e.g.* from -0.20 eV for bb/O+O to -2.20 eV for H_2bb/OH+OH. Furthermore, bb configurations at Fe1 are favored over bm at Fe2 by 0.7 eV in the deprotonated case (bb/O+O versus O+O/bm) and by 2.1 eV in case of protonation (H_2bb/OH+OH versus OH+OH/H_2bm). We note that the trend from the direct comparison of total energies in stiochiometrically identical terminations is not always reflected in the adsorption energies because the latter depend on the relative stability of the reference systems (*e.g.* Fe+Fe/O+O and O+O/Fe+Fe) prior to arsenate adsorption. Concerning the monodentate adsorption mode, we identify a stabilization of the mb complex, at variance with the behavior at α-FeOOH(101), where a mm adsorption mode prevails. At β-FeOOH(100) the mb adsorption at Fe2 in O+O/mb+O is favored by 0.3 eV over mm at Fe1 in O+mm/O+O. This preference is enhanced with increasing protonation state: OH+OH/Hmb+OH and H_2O+OH/Hmb+OH are by 1.3 and 0.7 eV more favorable than the corresponding systems with a mm complex. Interestingly, the stable protonated configuration is H_2O+OH/Hmb+OH with E_{ads}=-4.16 eV where instead of a doubly protonated mb complex at Fe2,

the second proton jumps to the hydroxyl group at Fe1 to form a water molecule.

Coverage dependence As already discussed for α-FeOOH(101), the adsorption energy decreases dramatically with surface loading at the same adsorption site due to adsorbate-adsorbate repulsion: from -2.20 eV for H_2bb/OH+OH to -0.28 eV for $2H_2$bb/OH+OH. On the other hand, mixed adsorption configurations at Fe1 and Fe2 sites are significantly more favorable: *e.g.* H_2bb/Hmb+OH with E_{ads}=-3.19 eV, H_2bb/H_2mb+OH with E_{ads}=-2.67 eV, and, finally, OH+H_2mm/H_2bm with E_{ads}=-3.48 eV.

Ligand exchange The trends for ligand exchange are similar to α-FeOOH(101). The adsorption energy for H_2bb/Hmb+OH consecutively decreases from -3.19 eV for direct adsorption at Fe sites to -3.02 eV for exchange of water and -1.41 eV for substitution of hydroxyl groups. In some cases as *e.g.* in H_2O+OH/Hmb+OH the exchange of water (E_{ads}=-4.54 eV) is even more favorable than the direct adsorption at exposed Fe sites (E_{ads}=-4.16 eV). Overall, the adsorption energy is only slightly changed in case of water substitution, but ligand exchange of hydroxyl groups costs significantly more energy and quickly becomes unfavorable.

Fe–As distances The bond distances show again similar trends to α-FeOOH(101). The Fe–As distance for the deprotonated mm complex at Fe1 is 3.32 Å in O+mm/O+O (Fe1-O-As bond angle is 132°) and increases to 3.46 Å upon protonation in OH+H_2mm/OH+OH (Fe-O-As bond angle is increased to 136°). For mb complexes at Fe2 the Fe–As distances vary between 3.18 Å ($\angle_{Fe2–O–As}$=112°) and 3.50 Å ($\angle_{Fe2–O–As}$=134°) depending on protonation state and concentration. A single deprotonated bb complex at Fe1 has a d_{Fe1-As} of 3.17 Å ($\angle_{Fe1–O–As}$=119°) for bb/O+O, which increases with protonation to 3.31 Å ($\angle_{Fe1–O–As}$=125°) for H_2bb/OH+OH and 3.55 Å ($\angle_{Fe1–O–As}$=127°) for $2H_2$bb/OH+OH. Analogous to α-FeOOH(101), the shortest Fe–As distances are observed for bm adsorption configurations at Fe2 where the deprotonated complex has a $d_{Fe–As}$ of 2.55 Å ($\angle_{Fe2–O–As}$=87°) in O+O/bm and 2.79 Å ($\angle_{Fe2–O–As}$=91°) in O+O/2bm with increasing coverage. For the protonated complexes the Fe–As distance varies from 2.73 Å

($\angle_{Fe2–O–As}$=85°) in OH+OH/H_2bm to 3.10 Å ($\angle_{Fe2–O–As}$=91°) in OH+OH/2H_2bm.

3.1.3 γ-FeOOH(010)

Relative stability of adsorbate configurations Arsenate adsorption at lepidocrocite(010) where only Fe2 surface sites are available shows some variation in trends. Monodentate binuclear arsenate adsorbed at one fourth of the Fe2 sites (O+mb/O+O) is bound by E_{ads}=-0.18 eV, but is significantly stabilized with protonation, E_{ads}=-3.57 eV for O+Hmb/O+OH and E_{ads}=-3.17 eV for OH+H_2mb/OH+OH. The enhancement in adsorption energy upon protonation can be attributed to the formation of hydrogen bonds between the complex and hydroxyl groups in the neighboring Fe2 row with $d_{O^{mb}\cdots HO^{B}}$=1.39 and 1.56 Å, respectively. Bidentate mononuclear complexes adsorbed at Fe2 in every second Fe2 row are stronger bound compared to the mb mode: -2.57 eV for bm/O+O, -3.17 eV for H_2bm/OH+OH, and -6.75 eV for H_2bm/H_2O+H_2O.

Coverage dependence Increasing the concentration of arsenate complexes, *e.g.* mb at half of the Fe2 sites staggered in neighboring rows (O+mb/mb+O), enhances the adsorption energy to -0.91 eV. With protonation of the adsorbates, O+H_2mb/H_2mb+O hydrogen bonds are formed between the adsorbates ($d_{OH^{mb}\cdots O^{mb}}$=1.35 Å) and between the adsorbate and the surface O^B ($d_{OH^{mb}\cdots O^{B}}$=1.83 Å). These stabilize the system further (E_{ads}=-1.62 eV). Increasing the coverage and protonating the remaining O^B in OH+H_2mb/H_2mb+OH reduces the adsorption energy to -1.31 eV compared to E_{ads}=-3.17 eV for OH+H_2mb/OH+OH.

For bm adsorption we have considered both rows of corner sharing arsenate tetrahedra adsorbed at all Fe2 in every second row as well as adsorption of arsenate tetrahedra at every second Fe2 in each row. As found for α-FeOOH(101) and β-FeOOH(100), the configuration with maximized distances between the adsorbates, bm/bm, is stronger bound compared (-2.28 eV) to the 2bm/O+O configuration (-0.01 eV). An analogous trend applies to the protonated systems H_2bm/H_2bm (E_{ads}=-2.55 eV) and 2H_2bm/H_2O+H_2O (E_{ads}=-1.55 eV), respectively.

Ligand exchange Similar to β-FeOOH(100) direct binding at an exposed surface iron and binding via ligand exchange of water are nearly equal in energy. In the case of OH+H_2mb/H_2mb+OH the corresponding adsorption energies are E_{ads}=-1.31 and -1.34 eV, for H_2bm/H_2O+H_2O E_{ads}=-6.75 and -6.81 eV, and for 2H_2bm/H_2O+H_2O E_{ads}= -1.55 and -1.56 eV. However, ligand exchange of hydroxyl groups is energetically highly unfavorable with positive adsorption energies in all cases. This indicates that arsenate adsorption is favored in particular at low pH.

Fe–As distances At the γ-FeOOH(010) surface where only Fe2 sites are available it is easier to discriminate between a mono- and bidentate geometry based on the Fe–As distances. For a doubly protonated H_2bm complex d_{Fe-As} is shortest for an isolated complex (2.80 Å, $\angle_{Fe2–O–As}$=91°) and increases with coverage to 3.10 Å ($\angle_{Fe2–O–As}$=89°). In contrast, the H_2mb complex has a bond length varying between 3.36 Å ($\angle_{Fe2–O–As}$=124°) and 3.46 Å ($\angle_{Fe2–O–As}$=129°) which is still below the range of 3.50–3.60 Å, commonly associated to monodentate adsorption.

3.2 Stability of Adsorption Configurations - Surface Phase Diagrams

While in the previous section we have discussed the adsorption strength of arsenate complexes in different adsorption modes and concentrations, here we address the energetic stability of different adsorption configurations at the FeOOH surfaces evaluated using the framework of *ab initio* thermodynamics. Figures 2 to 4 show side views of the most stable adsorbate configurations at goethite(101), akaganeite(100), and lepidocrocite(010) that appear in the two dimensional projection of the surface phase diagram in Figure 2a to Figure 4a as a function of the chemical potentials of oxygen and water, μ_O and μ_{H_2O}. Figure 2b to Figure 4b display the surface energy as a function of μ_O at water rich conditions and contain all considered surface terminations. A common feature for all studied FeOOH surfaces is that only protonated surface configurations appear in the surface phase diagrams in Figure 2a to Figure 4a, while the deprotonated surface configurations are higher in energy as can be seen from Figure 2b to Figure 4b. The most stable adsorbate configurations are analyzed in the following.

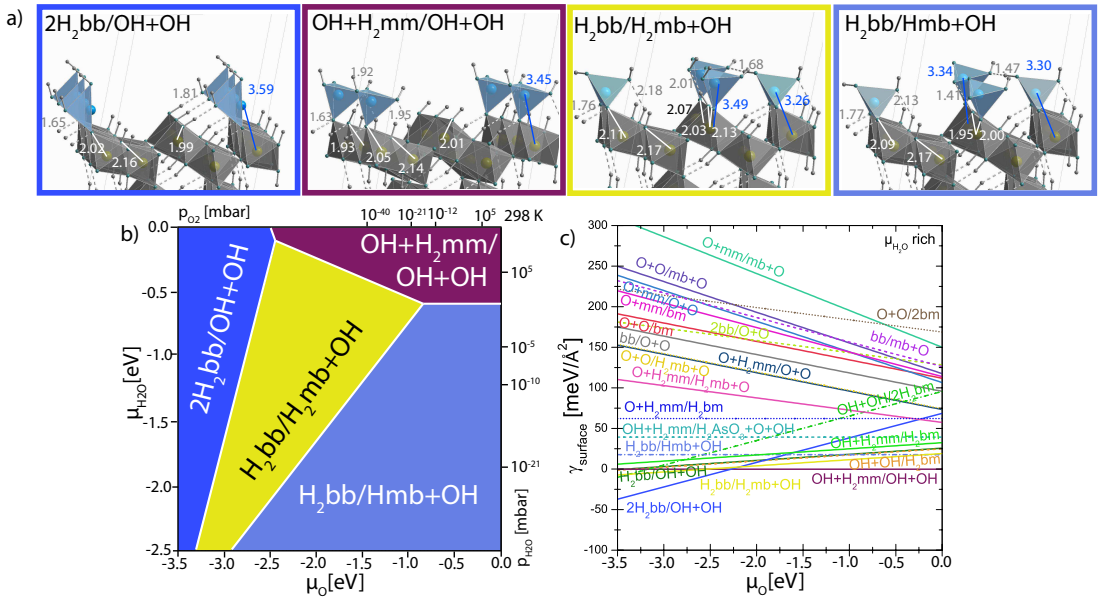

Figure 2: a) Side views of the relaxed structure of stable arsenate complexes at α-FeOOH(101). Relevant Fe–O/OH bond lengths are marked in white and hydrogen bonds are indicated by gray dashed lines. Additionally, the distances of As to the nearest and next nearest Fe ion are shown together with the corresponding Fe–O–As angle. The hydroxyl groups at the surfaces are coordinated either mononuclear to Fe1 (-O^{A}H) or binuclear to Fe2 (μ-O^{B}H) restoring the surface octahedra. The color of the frames corresponds to the color used in the surface phase diagram with stable surface terminations with respect to μ_O and μ_{H_2O} in b). In the top and right axis μ_O and μ_{H_2O} are converted into pressures for room temperature (298 K). c) Surface energy as a function of μ_O at water rich conditions. Note that oxygen terminated systems are energetically unfavorable. For more information see supplementary material.

3.2.1 Goethite(101) and Akaganeite(100)

As shown in Figure 2a and Figure 3a, α-FeOOH(101) and β-FeOOH(100) exhibit some common trends in surface stability. At oxygen poor conditions the surface phase diagram is dominated over nearly the whole range of μ_{H_2O} by the 2H$_2$bb/OH+OH configuration. This configuration is characterized by corner sharing arsenate tetrahedra connected bidentate binuclear to Fe1 and hydroxyl groups at Fe2. The rows of arsenate tetrahedra at the Fe1 site are significantly distorted, but stabilized by the formation of hydrogen bonds to neighboring surface hydroxyl groups: O^{B}H$\cdots$O (1.81 Å) and O^{C}H$\cdots$O^{A} (1.65 Å) for α-FeOOH(101) and O^{B}H$\cdots$O (2.19 Å) and O^{C}H$\cdots$O

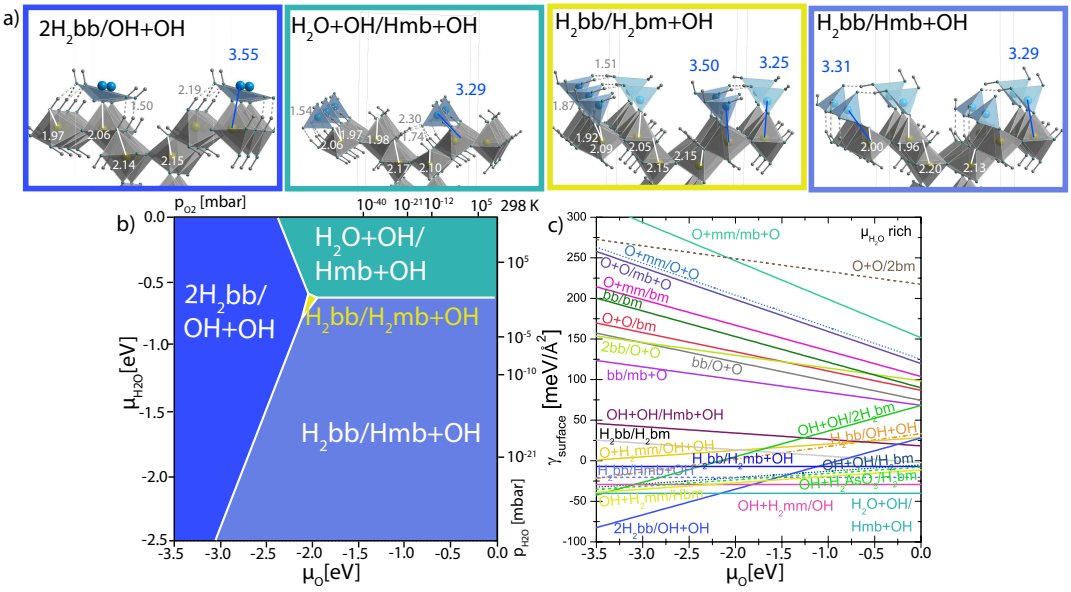

Figure 3: a) Side views of the relaxed structure of stable arsenate complexes at β-FeOOH(100). Relevant Fe–O/OH bond lengths are marked in white and hydrogen bonds are indicated by gray dashed lines. Additionally, the distances of As to the nearest and next nearest Fe ion are shown together with the corresponding Fe–O–As angle. The hydroxyl groups at the surfaces are coordinated either mononuclear to Fe1 (-$O^{A}H$) or binuclear to Fe2 (μ-$O^{B}H$) restoring the surface octahedra. The color of the frames corresponds to the color used in the surface phase diagram with stable surface terminations with respect to μ_O and μ_{H_2O} in b). In the top and right axis μ_O and μ_{H_2O} are converted into pressures for room temperature (298 K). c) Surface energy as a function of μ_O at water rich conditions. Note that oxygen terminated systems are energetically unfavorable. For more information see supplementary material.

(1.50 Å) for β-FeOOH(100). [2]

At water poor and oxygen rich conditions the H_2bb/Hmb+OH configuration with a mixed bidentate binuclear complex at Fe1 and a monodentate binuclear one at Fe2 is most stable. Here the mb adsorbed arsenate complex at Fe2 is singly and the bb complex at Fe1 is doubly protonated and the remaining surface oxygens are protonated. Hydrogen bonds are formed between the surface and H_2bb ($d_{O^{C}H\cdots O^{A}H_2bb}$=1.77, $d_{O^{C}H\cdots OH^{H_2bb}}$= 2.13 Å) and Hmb ($d_{O^{A}H\cdots O}$=1.41 Å at α-FeOOH and $d_{O^{C}H\cdots O^{Hmb}}$=1.75 at β-FeOOH) as well as between the adsorbate complexes ($d_{OH^{H_2bb}\cdots O^{Hmb}}$=1.47 Å

[2] O^{C} refers to a triply or trinclear coordinated surface oxygen.

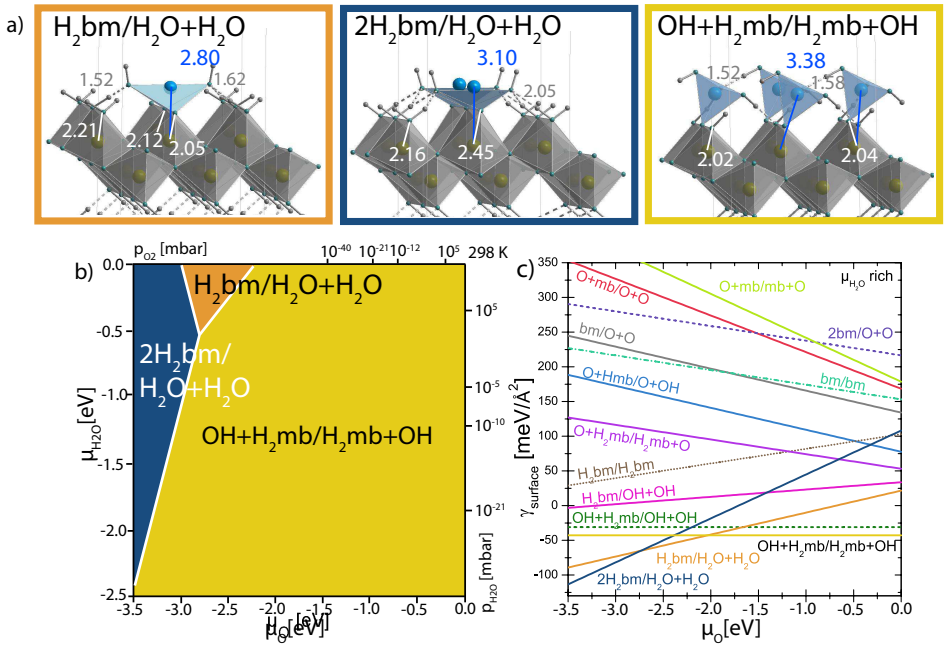

Figure 4: a) Side views of the relaxed structure of stable arsenate complexes at γ-FeOOH(010). Relevant Fe–O/OH bond lengths are marked in white and hydrogen bonds are indicated by gray dashed lines. Additionally, the distances of As to the nearest and next nearest Fe ion are shown together with the corresponding Fe–O–As angle. The hydroxyl groups at the surfaces are coordinated either mononuclear to Fe1 (-O^{A}H) or binuclear to Fe2 (μ-O^{B}H) restoring the surface octahedra. The color of the frames corresponds to the color used in the surface phase diagram with stable surface terminations with respect to μ_O and μ_{H_2O} in b). In the top and right axis μ_O and μ_{H_2O} are converted into pressures for room temperature (298 K). c) Surface energy as a function of μ_O at water rich conditions. Note that oxygen terminated systems are energetically unfavorable. For more information see supplementary material.

at α-FeOOH and $d_{\mathrm{OH^{H_2bb}\cdots O^{Hmb}}}$=1.50 Å at β-FeOOH). An interesting feature is that the Fe–As distances for mono- and bidentate adsorbed arsenate complexes almost coincide ($\sim$ 3.30 Å) both at goethite(101) and akaganeite(100). At β-FeOOH(100) the bidentate and monodentate configurations have distinct angles of $\angle_{\mathrm{Fe1–O–As}}$=127° and $\angle_{\mathrm{Fe2–O–As}}$=82°, while at α-FeOOH(101) both angles are approximately 121°.

H_2bb/H_2mb+OH with doubly protonated bb and mb complexes at Fe1 and Fe2, respectively, covers a wide range in the phase diagram of α-FeOOH(101) (Figure 2a) from μ_{H_2O}/μ_O poor to

intermediate conditions, whereas for β-FeOOH(100) it has only a very small stability range (Figure 3a). In this configuration the bb and mb complexes have different Fe–As distances both for goethite(101) and akaganeite(100): a shorter one for bidentate binuclear adsorption with 3.25 Å compared to 3.50 Å for monodentate binuclear adsorbed arsenate complexes. The corresponding Fe–O–As angles vary in the range of $\sim$127° to 134°.

Remarkably, at ambient conditions, for both surfaces the monodentate adsorption mode is favored. For α-FeOOH(101) the OH+H_2mm/OH+OH configuration where arsenate adsorbs monodentate mononuclear at Fe1 and all surface oxygens are protonated is most stable. The adsorbate is stabilized via hydrogen bonds to the surface hydroxyl groups. The Fe1–O^A distance to the arsenate $d_{Fe1–O^AAs}$=2.05 Å is larger compared to $d_{Fe1–O^AH}$=1.93 Å. The shortest Fe-As distance is $d_{Fe1–As}$=3.45 Å with $\angle_{Fe1–O^A–As}$=134°. In contrast at β-FeOOH(100) arsenate preferentially adsorbs monodentate binuclear at the Fe2 site resulting in the H_2O+OH/Hmb+OH configuration where hydroxyl and aquo terminal groups alternate at the Fe1 sites. The monodentate binuclear complex is singly protonated and tilts towards the open akaganeite channel to form hydrogen bonds to the triply coordinated O^CH (1.74 Å and 2.30 Å). This results in $d_{Fe2–As}$=3.29 Å and $\angle_{Fe2–O^B–As}$=116°.

3.2.2 Lepidocrocite(010)

As mentioned above, at γ-FeOOH(010) only Fe2 surface sites are available for arsenate adsorption. Hence the stable surface configurations show some differences to the other FeOOH polymorphs discussed above. The surface phase diagram is dominated by OH+H_2mb/H_2mb+OH. In this configuration staggered monodentate binuclear arsenate complexes adsorbed at Fe2 sites alternate with hydroxyl groups. The Fe–O^B distances are only slightly influenced by the adsorbates: $d_{Fe2–O^BH}$=2.02 Å and $d_{Fe2–O^BAs}$=2.04 Å. The arsenate complexes are tilted leading to $d_{Fe2–As}$=3.38 Å and a Fe2–O^BAs angle of $\angle_{Fe2–O^B–As}$=129° and are stabilized via hydrogen bonds, both between the adsorbates (1.52 Å) and to surface hydroxyl groups in the opposite row (1.58 Å).

At μ_O poor and μ_{H_2O} rich conditions the 2H_2bm/H_2O+H_2O configuration is favored. It com-

prises alternating rows of corner sharing bidentate mononuclear arsenate tetrahedra and monodentate binuclear water. The arsenate hydroxyl groups are connected to water via hydrogen bonding, but with increased bond lengths of $d_{\mathrm{OH\cdots OH^w}}$ =2.05 Å. In this case the Fe–O distances to the oxygen of water and the arsenate complex are similar with $d_{\mathrm{Fe2–O^w}}$=2.16 Å and $d_{\mathrm{Fe2–O^B As}}$=2.15 Å. Note also the strong deformation/flattening of the arsenate complex from the initial gas phase geometry leading to $d_{\mathrm{Fe2–As}}$=3.10 Å and $\angle_{\mathrm{Fe2–O^B–As}}$=89°.

At $\mu_{\mathrm{H_2O}}$ rich conditions with increasing μ_{O} there is a small region with a stable configuration of alternating rows of bidentate monoculear adsorbed arsenate at every second Fe2 site and binuclear adsorbed water, H_2bm/H_2O+H_2O. Both hydroxyl groups of the arsenate form hydrogen bonds to the hydrogen of water of 1.52 and 1.62 Å. The distance between Fe and oxygen of the water molecule $d_{\mathrm{Fe2–O^w}}$=2.21 Å is longer than to the oxygen of the arsenate $d_{\mathrm{Fe2–O^B As}}$=2.05 Å (for comparison in bulk FeOOH Fe–O/Fe–OH distances are 2.00 and 2.11 Å). For bidentate mononuclear adsorbed arsenate we find the shortest Fe–As distance with $d_{\mathrm{Fe2–As}}$=2.80 Å and $\angle_{\mathrm{Fe2–O^B–As}}$=93°. We note that this again is connected with a significant deformation of the arsenate tetrahedron.

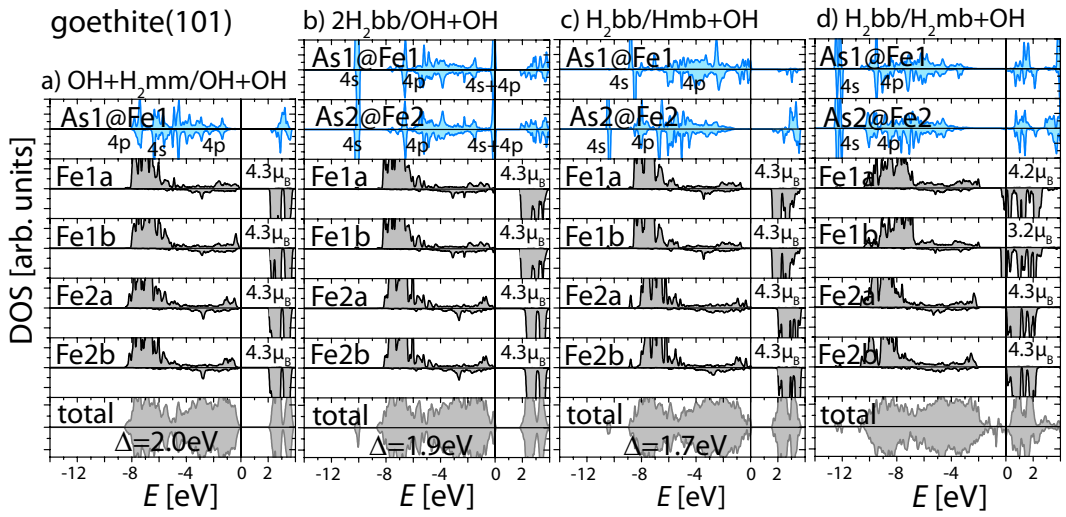

Figure 5: Density of states of the most stable surface configurations of arsenate adsorbed at goethite(101). The top panels represent the projected DOS of As in the arsenate complex. The surface irons are shown in the lower panels together with their magnetic moments. The total DOS is displayed in the bottom panel.

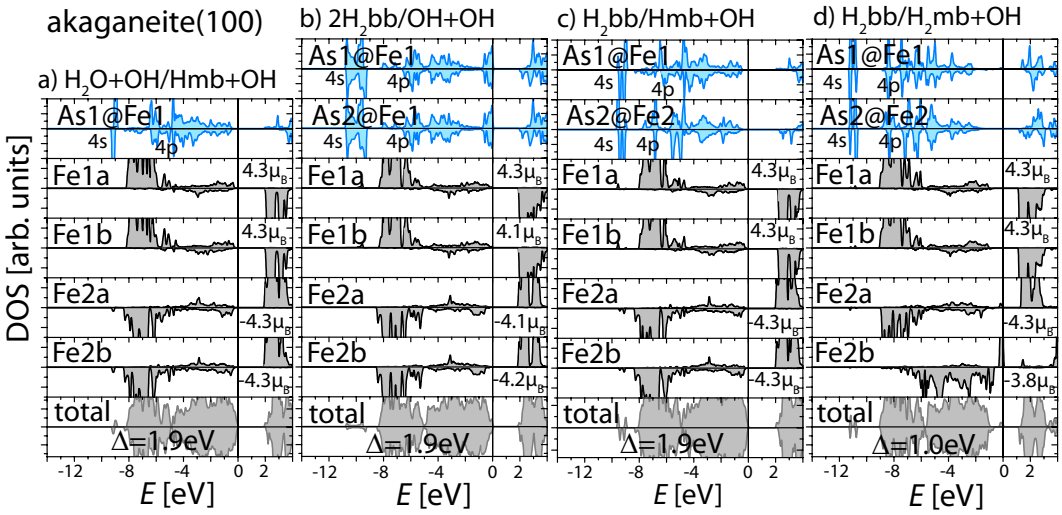

Figure 6: Density of states of the most stable surface configurations of arsenate adsorbed at akaganeite(100). The top panels represent the projected DOS of As in the arsenate complex. The surface irons are shown in the lower panels together with their magnetic moments. The total DOS is displayed in the bottom panel.

3.3 Electronic and Magnetic Properties

In this Section we discuss the electronic and magnetic properties of the stable adsorption configurations. In bulk FeOOH all iron ions are octahedrally coordinated by O/OH and in Fe^{3+} state. The subsurface layers show behavior close to bulk with only ferric iron and M_{Fe}=4.30 μ_B. On the other hand the altered coordination at the surface can affect the Fe 3*d* orbital occupation and lead *e.g.* to ferrous iron, Fe^{2+}, with a decreased magnetic moment of 3.5–3.7 μ_B. Our previous study on FeOOH surfaces [12] has shown that hydroxylated terminations have properties closest to bulk, while iron and water terminated surfaces lead to an enrichment of ferrous iron in the surface layer. The energy band associated with the sixth electron at the Fe^{2+} sites is pinned at E_F thereby reducing significantly the band gap of bulk FeOOH from ∼2.0 eV to ∼1.0 eV.

The total and projected density of states (DOS) of the most stable surface terminations of goethite(101), akaganeite(100), and lepidocrocite(010) upon arsenate adsorption are displayed in

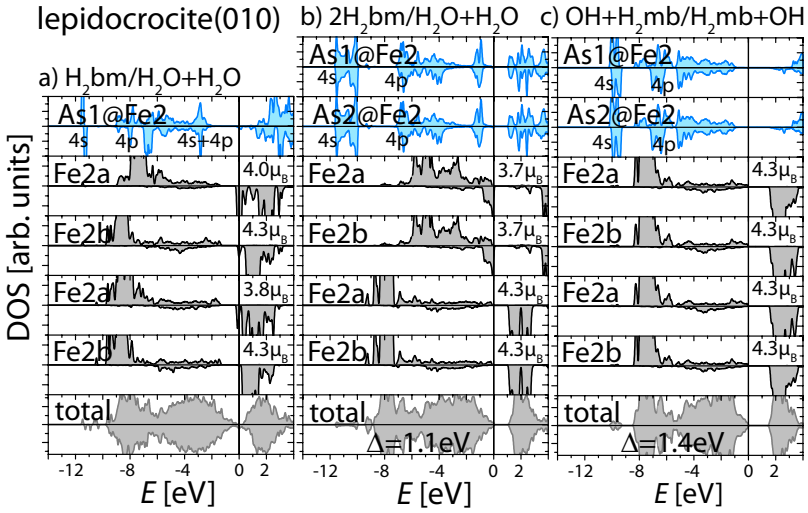

Figure 7: Density of states of the most stable surface configurations of arsenate adsorbed at lepidocrocite(010). The top panels represent the projected DOS of As in the arsenate complex. The surface irons are shown in the lower panels together with their magnetic moments. The total DOS is displayed in the bottom panel.

Figures 5 to 7, respectively. The configurations stable at ambient conditions, *i.e.*, OH+H_2mm/OH+OH at goethite(101), H_2O+OH/Hmb+OH at akaganeite(100), and OH+H_2mb/H_2mb+OH at lepidocrocite(010), in Figure 5a to Figure 7a exhibit only ferric iron at the surface and a band gap of ∼2.0 eV similar to bulk FeOOH. In contrast, ferrous iron, Fe^{2+}, emerges at half of the Fe1 sites below the arsenate complex in H_2bb/H_2mb+OH of goethite(101) as well as the Fe2 site below the hydroxyl group at akaganeite(100). Fe^{2+} is also found in H_2bm/H_2O+H_2O and 2H_2bm/H_2O+H_2O of lepidocrocite(010) below the water molecules. Similar to the Fe and water terminated FeOOH surfaces prior to arsenate adsorption, this reduces the band gap (now of a Mott-Hubbard type between occupied and unoccupied iron states) to ∼1.0 eV. We note that in H_2bb/H_2mb+OH of goethite(101) in Figure 5d and H_2bm/H_2O+H_2O of lepidocrocite(010) in Figure 7a, the Fermi level is pinned at the bottom of the conduction band. As a result the upper Hubbard band of Fe1 crosses E_F and gets partially occupied, leading to reduced magnetic moments of 3.2 and 3.7 μ_B, respectively, and a metallic state.

4 Discussion

As–O distances The As–O distances extracted from EXAFS are often used as a criterion to determine the As oxidation state with an average distance of 1.78 Å (As^{3+})[41] and 1.68 Å (As^{5+}),[4] respectively. For adsorbed complexes at α-FeOOH(101) the data displayed in Tables S2, S4, S6 reveal that the As-O(Fe) bond lengths are not only affected by the adsorption geometry (mono- or bidentate), but to an even larger extent by the coordination of surface oxygen (singly or bridging): Shorter distances are observed for adsorption of arsenate complexes at Fe1 with $d_{As\text{-}O(Fe1)}$=1.71±0.03 Å, where the linking oxygen is singly coordinated to Fe1, compared to adsorption at Fe2 with $d_{As\text{-}O(Fe2)}$=1.80±0.03 Å and an oxygen linked to two Fe2 ions. The longest As–O(Fe1) distances of 2.07 Å and 1.91 Å are observed for $2H_2$bb/OH+OH configurations of goethite(101) and akaganeite(100), respectively. These values correlate with the strong reduction of adsorption energy with increasing coverage due to repulsion between the complexes and are likely further influenced by the protonation state of the complex. Similarly, also the $2H_2$bm/H_2O+H_2O termination of lepidocrocite(010) shows a longer $d_{As–O(Fe2)}$=1.93 Å. Although the geometry of the arsenate complex is strongly affected by the bonding to the FeOOH surfaces, the remaining As–O and As–OH distances are similar to the ones for a gas phase arsenate molecule with $d_{As=O}$=1.65 Å and $d_{As–OH}$=1.78 Å. The shortest As–O bond lengths of ∼1.64 Å are obtained for As=O bonds in deprotonated complexes, whereas the As–OH bonds are significantly longer, 1.77-1.90 Å, due to the formation of hydrogen bonds. The values for the As–O shells agree with previous DFT and EXAFS results.[17,21,42,43]

Arsenate adsorbate geometries and Fe–As distances Results from previous DFT studies using two FeO_6 octahedra to model the FeOOH surface show that the small cluster is significantly more flexible than the extended surfaces studied here and rearranges around the arsenate complex. Moreover, the small size of the cluster limits the interaction with surface functional groups. As a consequence the arsenate geometry and bond lengths remain almost unchanged compared to the initial geometry. In contrast, the full relaxation performed here at extended FeOOH surfaces in the

presence of neighboring surface hydroxyl and aquo groups leads to a strong deformation and tilting of the arsenate complex caused by the formation of hydrogen bonds with surface functional groups. We find that the realistic modeling of the FeOOH surface has a crucial influence on the stability of the corresponding adsorption configuration. Furthermore, it affects the shape of the arsenate complex and most importantly the Fe–As distance and As–O–Fe tilt angle. In particular, we find that at the α-FeOOH(101) and β-FeOOH(010) surfaces the Fe–As distances of mixed bidentate binuclear (H_2bb) complexes at Fe1 (3.26-3.34 Å) and monodentate binuclear (H_2mb) at Fe2 (3.31-3.50 Å), stable at intermediate oxygen and water pressures, are nearly indistinguishable. Moreover, the 2H_2bb/OH+OH termination favored at high water and low oxygen chemical potentials shows Fe–As bond lengths of 3.59 Å (α-FeOOH(101)) and 3.55 Å (β-FeOOH(100)) that are significantly longer than the bond length associated with a bb adsorption geometry. Thus our results show that the bond lengths are affected primarily by the protonation state, coverage, and surrounding surface terminal groups. To this end, the H_2mm complex at Fe1 of α-FeOOH(101), found to be stable at ambient conditions, exhibits a bond length of 3.45 Å significantly shorter than the 3.50-3.60 Å, commonly assumed for monodentate complexes. While several studies use geometric/steric arguments to justify a linear Fe–O–As bond with zero tilt,[3,4,15] our results show that the shorter Fe–As bond is related to a significant reduction of the As–O–Fe tilt angle from the initial 180° to 134° upon relaxation. This is in agreement with Loring et al.[18] who suggested a monodentate configuration for arsenate on goethite similar to a pentaamminecobald-arsenate complex with Co–As distance of 3.25Å and an angle of 125°. They[18] report minor pH dependent variations of the Fe-As distance of 0.02 Å around the average value of 3.29 Å. This is consistent with our data: 3.24 Å for deprotonated and 3.23 Å for protonated mm complexes. However, at α-FeOOH(101) this distance is significantly increased to 3.45 Å if in addition the surface is hydroxylated. Our results show that the bm configurations are energetically unfavorable at α-FeOOH(101) and β-FeOOH(010), in agreement with previous studies.[3,4,17]

For lepidocrocite we find a dominating OH+H_2mb/H_2mb+OH termination and a 2H_2bm/H_2O+H_2O at low oxygen and high water pressures. The Fe–As distance is 3.38 Å in H_2mb and 3.10 Å in

$2H_2bm$. The former is closer to the experimentally determined Fe–As distance of 3.31 Å[17,43,44] which was previously interpreted as a bb complex. We note that this configuration is only possible at the edges of lepidocrocite crystallites. Randall and Sherman[44] argued that adsorption at other surface sites is unlikely due to a nearly complete coordination environment of the surface atoms. This is not confirmed by our results that show strong binding of the complexes at the Fe2 sites on the surface.

Hydrogen bond formation The DFT results show that hydrogen bond formation plays a central role in the stabilization of adsorbate configurations. In agreement with fourier transform infrared (FTIR) measurements Sun and Doner[5] we find a stronger affinity for arsenate adsorption at singly coordinated oxygen sites (corresponding to the Fe1 site) at goethite. Concerning the formation of hydrogen bonds, this study suggested stronger interaction (*i.e.* hydrogen bond formation) between the complex and triply coordinated surface hydroxyl groups. Indeed our results show that mainly the oxygen connecting the As complex to Fe forms hydrogen bonds to triply coordinated O^CH. Additionally, hydrogen bonds are formed both between the complexes as well as between the protonated oxygens of the complex and doubly coordinated hydroxyl groups at Fe2.

Ligand exchange Besides the adsorption at exposed iron surface sites, we have considered ligand exchange of different surface end groups. Hydrated iron surface sites correspond to low pH, while a mixture of hydroxyl and doubly protonated surface end groups is present at higher pH. In all cases water is substituted more easily from the surface, while hydroxyl groups are stronger bound and the arsenate adsorption energy is strongly reduced and even becomes positive in some cases. This is consistent with experimental results showing that anion adsorption is greater at lower pH and decreases with increasing pH[45] due to competition between adsorbate and surface hydroxyl groups.[2] In particular, almost 100 % adsorption of As^V around pH 4–6 was observed at ferrihydrite, but a rapid decrease at pH > 7.[46] Furthermore, our results are consistent with recent findings,[13] pointing at the role of doubly coordinated oxygen, typically considered inert, in ligand exchange at mineral surfaces.

5 Conclusions

The DFT+U results on extended surfaces of the FeOOH polymorphs presented here show that the arsenate adsorption configuration depends critically on the local environment, in particular the coordinaion of surface iron and the presence of surface functional groups (-OH/-OH_2). Some general trends are observed: Monodentate complexes are stabilized at ambient conditions, *e.g.* at goethite(101) a protonated monodentate mononuclear arsenate binds at Fe1. Such a configuration was considered in EXAFS studies (*e.g.*[3,15]), however, the relaxed geometry is consistent with the model proposed by Loring et al.[18] with a reduced Fe–As distance of 3.45 Å and a strong Fe–O–As tilt (134). On the other hand, a protonated mb complex at Fe2 is favored at akaganeite(100) with Fe–As of $d_{\mathrm{Fe2–As}}$=3.29 Å and staggered H_2mb complexes alternating with hydroxyl groups at lepidocrocite(010) with $d_{\mathrm{Fe2–As}}$=3.38 Å. With decreasing oxygen pressure a mixed protonated bb complex at Fe1 and mb at Fe2 site is stabilized at goethite(101) and akaganeite(100) with virtually indistinguishable Fe–As distances for bb ($d_{\mathrm{Fe1–As}}$=3.26-3.34 Å) and mb ($d_{\mathrm{Fe2–As}}$=3.31-3.50 Å), respectively. Finally, at low oxygen pressures two protonated bb complexes at Fe1 and hydroxyl groups at Fe2 are stabilized which show remarkably long Fe1–As bond distances of 3.55-3.59 Å due to adsorbate-adsorbate repulsion. While at α-FeOOH(101) and β-FeOOH(100) there is no evidence for a bm complex, protonated H_2bm rows alternating with water rows are stabilized at low oxygen pressure at lepidocrocite(010) with $d_{\mathrm{Fe1–As}}$=3.10 Å. Formation of hydrogen bonds to surface hydroxyl and aquo groups as well as to neighboring adsorbates plays an important role in the stabilization of the complexes. We note that the presence of further water molecules within a solvation layer, which is not considered here, may further influence the absolute values of relaxations. We find that the protonation state of the complex, the coverage, and the presence of surface functional groups are the main factors that determine the bond lengths and to a much lesser extent the bonding configuration. This indicates that the Fe–As bond length is not a reliable criterion to pinpoint the adsorption mode. The provided bond lengths of the relaxed surface structures for different adsorption configurations will be useful for interpretation of EXAFS data.

Concerning the electronic properties, the most stable adsorbate configurations at α-FeOOH(101)

and β-FeOOH(100) exhibit ferric iron in the surface layer and consequently band gaps close or slightly reduced with respect to bulk FeOOH (Δ=2.0 eV). Reduced magnetic moments, indicative of Fe^{2+}, are found underneath bidentate complexes or water molecules and lead to reduced band gaps and even a metallic state.

The explicit treatment of a solvation layer, calculation of vibrational spectra, and the investigation of outer sphere arsenate adsorption mechansims represent interesting topics for future studies.

Acknowledgement

We acknowledge funding by the BMBF Program Geotechnologies - Mineral Surfaces, project SURFTRAP as well as the Bavarian Elite Network. The calculations were performed at the supercomputer HLRBII, Leibniz Rechenzentrum, project h0721.

Supporting Information Available

The supporting material to this paper contains the adsorption energies of the studied adsorption pathways in Tables S1, S3, S5, side views for each surface configuration shown in Figures S1–S3, and characteristic bond lengths, summarized in Tables S2, S4, S6. Furthermore, information on the magnetic moments of surface iron as well as band gaps are also summarized in Tables S2, S4, S6.

References

(1) Carlson, L.; Bigham, J.; Schwertmann, U.; Kyek, A.; Wagner, F. *Environ. Sci. Technol.* **2002**, ***36***, 1712–1719.

(2) Grossl, P.; Eick, M.; Sparks, D.; Goldberg, S.; Ainsworth, C. *Environ. Sci. Technol.* **1997**, ***31***, 321–326.

(3) Waychunas, G.; Rea, B.; Fuller, C.; Davis, J. *Geochim. et Cosmochim. Acta* **1993**, ***1993***, 2251–2269.

(4) Waychunas, G.; Davis, J.; Fuller, C. *Geochim. et Cosmochim. Acta* **1995**, ***59***, 3655–3661.

(5) Sun, X.; Doner, H. *Soil Science* **1996**, ***161***, 865–872.

(6) Jain, A.; Raven, K.; Loeppert, R. *Environ. Sci. Technol.* **1999**, ***33***, 1179–1184.

(7) Catalano, J.; Park, C.; Fenter, P.; Zhang, Z. *Geochim. et Cosmochim. Acta* **2008**, ***72***, 1986–2004.

(8) Schwertmann, U.; Pfab, G. *Geochim. et Cosmochim. Acta* **1994**, ***58***, 4349.

(9) Villalobos, M.; Cheney, M.; Alcaraz-Cienfuegos, J. *J. Colloid Interface Sci.* **2009**, ***336***, 412.

(10) Cornell, R. M.; Schwertmann, U. *The Iron Oxides: Structure, Properties, Reactions, Occurrences and Uses*; Wiley-VCH GmBH & Co. KGaA, Weinheim, 2003.

(11) Ramdohr, P.; Strunz, H. *Lehrbuch der Mineralogie, 16th ed., Stuttgart* **1978**, *0*, 876.

(12) Otte, K.; Schmahl, W.; Pentcheva, R. *Surface Science* **2012**, ***606***, 1623ï£¡1632.

(13) Panasci, A.F.; Ohlin, C.A..; Harley, S.J., and Casey, W.H. *Inorganic Chemistry* **2012**, ***51***, 6731.

(14) Waychunas, G.; Trainor, T.; Eng, P.; Catalano, J.; Brown, G.; Davis, J.; Rogers, J.; Bargar, J. *Anal. Bioanal. Chem.* **2005**, ***383***, 12–27.

(15) Fendorf, S.; Eick, M.; Grossl, P.; Sparks, D. *Environ. Sci. Technol.* **1997**, ***31***, 315–320.

(16) Ona-Nguema, G.; Morin, G.; Juillot, F.; Calas, G.; Brown Jr., G. *Environ. Sci. Technol.* **2005**, ***39***, 9147–9155.

(17) Sherman, D.; Randall, S. *Geochim. et Cosmochim. Acta* **2003**, ***67***, 4223.

(18) Loring, J.; Sandström, M.; Norï£¡n, K.; Persson, P. *Chem. Eur. J.* **2009**, ***15***, 5063–5072.

(19) Manceau, A. *Geochim. et Cosmochim. Acta* **1995**, ***59***, 3647–3653.

(20) Arai, Y.; Sparks, D.; Davis, J. *Environ. Sci. Technol.* **2004**, ***38***, 817–824.

(21) Kubicki, J.; Kwon, K.; Paul, K.; Sparks, D. *European Journal of Soil Science* **2007**, ***58***, 932–944.

(22) Anisimov, V.; Solovyev, I.; Korotin, M. A.; Cryzyk, M. T.; Sawatzky, G. A. *Phys. Rev. B* **1993**, ***48***, 16929.

(23) He, G.; Zhang, M.; Pan, G. *J. Phys. Chem. C* **2009**, ***113***, 21679–21686.

(24) Kresse, G.; Hafner, J. *Phys. Rev. B* **1993**, *47*, 558.

(25) Kresse, G.; Hafner, J. *Phys. Rev. B* **1994**, *49*, 14251.

(26) Kresse, G.; Hafner, J. *J. Phys.: Condens. Matter* **1994**, *6*, 8245.

(27) Kresse, G.; Furthmüller, J. *Comput. Mat. Sci.* **1996**, *6*, 15.

(28) Kresse, G.; Furthmüller, J. *Phys. Rev. B* **1996**, *54*, 11169.

(29) Blöchl, P. *Phys. Rev. B* **1994**, *50*, 17953.

(30) Kresse, G.; Joubert, D. *Phys. Rev. B* **1999**, *59*, 1758.

(31) Perdew, J.; Burke, K.; Ernzerhof, M. *Phys. Rev. Lett.* **1996**, ***77***, 3865–3868.

(32) Dudarev, S.; Botton, G.; Savrasov, S.; Humphreys, C.; Sutton, A. *Phys. Rev. B* **1998**, ***57***, 1505–1509.

(33) Otte, K.; Pentcheva, R.; Schmahl, W.; Rustad, J. *Phys. Rev. B* **2009**, ***80***, 205116.

(34) Russell, B.; Payne, M.; Ciacchi, L. *Phys. Rev. B* **2009**, ***79***, 165101.

(35) Szytula, A.; Burewicz, A.; Dimitrijevic, Z.; Krasnicki, S.; Rzany, H.; Todorovic, J. *Phys. Status Solidi* **1968**, ***26***, 429.

(36) MacKay, A. *Mineral. Mag. J. Mineral. Soc.* **1960**, ***32***, 545.

(37) Christensen, H.; Christensen, A. *Acta Chem. Scand., Series A* **1978**, ***32***, 87.

(38) Reuter, K.; Scheffler, M. *Phys. Rev. B* **2001**, ***65***, 035406.

(39) Sun, Q.; Reuter, K.; Scheffler, M. *Phys. Rev. B* **2003**, ***67***, 205424.

(40) Oxford, G.; Chaka, A. *Phys. Rev. B* **2010**, ***84***, 205453.

(41) Manning, B.; Fendorf, S.; Goldberg, S. *Environ. Sci. Technol.* **1998**, ***32***, 2383–2388.

(42) Stachowicz, M.; Hiemstra, T.; van Riemsdijk, W. *J. Coll. Int. Sci,* **2006**, ***302***, 62.

(43) Farquhar, M.; Charnock, J.; Livens, F.; Vaughan, D. *Environ. Sci. Technol.* **2002**, ***36***, 1757–1762.

(44) Randall, S. R.; Sherman, K. V., D. M.and Ragnarsdottir *Geochim. et Cosmochim. Acta* **2001**, ***65***, 1015–1023.

(45) Hayes, K.; Papelis, C.; Leckie, J. *J. Colloid Interface Sci.* **1988**, ***125***, 717–726.

(46) Pierce, M.; Moore, C. *Water Res.* **1982**, ***16***, 1247–1253.

This material is available free of charge via the Internet at `http://pubs.acs.org/`.

Supporting information for:

DFT+U Study of Arsenate Adsorption on FeOOH Surfaces:

Evidence for Competing Binding Mechanisms

Katrin Otte,* Wolfgang W. Schmahl, and Rossitza Pentcheva*

Section Crystallography, Department of Earth and Environmental Sciences and Center of Nanoscience (CENS),

University of Munich, Theresienstr. 41, 80333 Munich, Germany

E-mail: katrin.otte@lrz.uni-muenchen.de; pentcheva@lrz.uni-muenchen.de

*To whom correspondence should be addressed

The relaxed structures of all considered surface configurations of arsenate adsorbed at goethite(101), akaganeite(100), and lepidocrocite(010), respectively, are displayed in Figures S1 to S3. From left to right the surface protonation state increases. For systems with identical stoichiometry we show also the energy differences, ΔE, with an arrow pointing to the more favorable configuration. The stable surface configurations that appear in the surface phase diagrams in Figures 2 to 4 are discussed in the manuscript and are framed in the corresponding color.

The arsenate adsorption reactions are summarized in Tables S1, S3, and S5 together with the adsorption energies, E_{ads}. Adsorption energies are calculated with respect to a termination where the arsenate binds directly at an exposed iron site. Ligand exchange scenarios are also considered for the most stable surface terminations that relate to different pH conditions. Hydrated iron surface sites correspond to low pH, while a mixture of hydroxyl and aquo surface end groups are present at intermediate, and fully hyddoxylated surface sites at higher pH. Tables S2, S4, and S6 contain information on the Fe−As distances, $d_{\mathrm{Fe–As}}$, the Fe−O−As angles, $\angle_{\mathrm{Fe–O–As}}$, and the As−O bond lengths, $d_{\mathrm{As–O}}$. The tilt of the complex is associated with the formation of hydrogen bonds to surface hydroxyl groups. In particular, hydrogen bonds are formed to the trinuclear coordinated surface hydroxyls, $\mathrm{HO^C}$, in the open channels at the surface and/or to the mono- or binculear coordinated OH groups at the Fe1 and Fe2 sites ($\mathrm{HO^A}$ and $\mathrm{HO^B}$), respectively. This tilting influences the Fe−O−As angle and changes the Fe–As distances. Furthermore, an increase of $\mathrm{d_{Fe-As}}$ with protonation is observed. Tables S2, S4, and S6 contain information on the Fe−As distances, $\mathrm{d_{Fe–As}}$, the Fe−O−As angles, $\angle_{\mathrm{Fe–O–As}}$, and the As−O bond lengths, $\mathrm{d_{As–O}}$.

The magnetic moments of surface iron as well as band gaps are also summarized in Tables S2, S4, and S6. Specifically, a reduction of surface iron $\mathrm{Fe^{3+}}$ to $\mathrm{Fe^{2+}}$ leads to a narrowing/closing of the band. We note that for some oxygen terminated surface sites we observe lowered magnetic moments, *e.g.* $\mathrm{M_{Fe}}$=2.71 μ_B in the O+O/bm configuration of akaganeite(100), indicating higher valence states of iron, $\mathrm{Fe^{4+}}$, in a ferryl-oxo group.

Table S1: Arsenate adsorption reactions for the surface terminations of goethite(101) (a1-a22). The configurations that appear as stable terminations in the surface phase diagrams of the manuscript are given in bold letters. The corresponding adsorption energies $E_{\mathbf{ads}}$ of the adsorbates on different iron sites are provided. Note that the energies of H_2 and OH are expressed through $E_{\mathbf{H_2O}}$ and $E_{\mathbf{O_2}}$ using $E_{\mathbf{H_2}} = E_{\mathbf{H_2O}} - 1/2 \cdot E_{\mathbf{O_2}}$ and $E_{\mathbf{OH}} = 1/2 \cdot E_{\mathbf{H_2O}} + 1/4 \cdot E_{\mathbf{O_2}}$, respectively.

Adsorption configurations of arsenate at different terminations of the goethite(101) surface						E_{ads} (eV)	
	initial		adsorbate		final	Fe1	Fe2
a1	O+Fe/O+O	+	$1H_3AsO_4$	→	O+mm/O+O	+1.5H_2	-0.97
a2	O+Fe/O+O	+	$1H_3AsO_4$	→	O+H_2mm/O+O	+0.5H_2	-2.25
a3	**OH+Fe/OH+OH**	**+**	**$1H_3AsO_4$**	**→**	**OH+H_2mm/OH+OH**	**+0.5H_2**	**-4.06**
	OH+H_2O*/OH+OH	**+**	**$1H_3AsO_4$**	**→**	**OH+H_2mm/OH+OH**	**+1.5H_2+0.5O_2**	**-3.14**
	OH+OH/OH+OH	**+**	**$1H_3AsO_4$**	**→**	**OH+H_2mm/OH+OH**	**+1H_2O**	**-2.66**
a4	O+O/Fe+O	+	$1H_3AsO_4$	→	O+O/mb+O	+1.5H_2	-0.69
a5	O+O/Fe+O	+	$1H_3AsO_4$	→	O+O/H_2mb+O	+0.5H_2	-2.64
a6	Fe+Fe/O+O	+	$1H_3AsO_4$	→	bb/O+O	+1.5H_2	-0.89
a7	Fe+Fe/OH+OH	+	$1H_3AsO_4$	→	H_2bb/OH+OH	+2OH	-4.21
a8	O+O/Fe+Fe	+	$1H_3AsO_4$	→	O+O/bm	+1.5H_2	-0.73
a9	OH+OH/Fe+Fe	+	$1H_3AsO_4$	→	OH+OH/H_2bm	+2OH	-3.83
a10	O+Fe/Fe+O	+	$2H_3AsO_4$	→	O+mm/mb+O	+3H_2	+0.44
a11	O+Fe/Fe+O	+	$2H_3AsO_4$	→	O+H_2mm/H_2mb+O	+1H_2	-1.71
a12	OH+Fe/O+OH	+	$2H_3AsO_4$	→	OH+H_2mm/ H_2AsO_3+O+OH	+1H_2	-1.77
a13	Fe+Fe/O+O	+	$2H_3AsO_4$	→	2bb/O+O	+3H_2+1O_2	-0.05
a14	**Fe+Fe/OH+OH**	**+**	**$2H_3AsO_4$**	**→**	**2H_2bb/OH+OH**	**+2OH**	**-0.91**
	H_2O*+H_2O*/OH+OH	**+**	**$2H_3AsO_4$**	**→**	**2H_2bb/OH+OH**	**+3H_2+2O_2**	**+0.02**
	OH+OH/OH+OH	**+**	**$2H_3AsO_4$**	**→**	**2H_2bb/OH+OH**	**+2H_2+2O_2**	**+0.49**
a15	O+O/Fe+Fe	+	$2H_3AsO_4$	→	O+O/2bm	+3H_2+1O_2	+0.83
a16	OH+OH/Fe+Fe	+	$2H_3AsO_4$	→	OH+OH/2H_2bm	+2OH	+0.19
a17	Fe+Fe/Fe+O	+	$2H_3AsO_4$	→	bb/mb+O	+3H_2	-0.78
a18	**Fe+Fe/Fe+OH**	**+**	**$2H_3AsO_4$**	**→**	**H_2bb/Hmb+OH**	**+H_2**	**-3.59**
	H_2O*+H_2O*/H_2O+OH	**+**	**$2H_3AsO_4$**	**→**	**H_2bb/Hmb+OH**	**+3H_2O+1.5H_2**	**-3.00**
a19	**Fe+Fe/Fe+OH**	**+**	**$2H_3AsO_4$**	**→**	**H_2bb/H_2mb+OH**	**+H_2**	**-3.31**
	H_2O*+H_2O*/H_2O+OH	**+**	**$2H_3AsO_4$**	**→**	**H_2bb/H_2mb+OH**	**+3H_2O+H_2**	**-2.73**
	OH+OH/OH+OH	**+**	**$2H_3AsO_4$**	**→**	**H_2bb/H_2mb+OH**	**+2H_2+O_2**	**-1.38**
a20	O+Fe/Fe+Fe	+	$2H_3AsO_4$	→	O+mm/bm	+3H_2	-1.42
a21	OH+Fe/Fe+Fe	+	$2H_3AsO_4$	→	O+H_2mm/H_2bm	+1.5H_2	-2.22
a22	OH+Fe/Fe+Fe	+	$2H_3AsO_4$	→	OH+H_2mm/H_2bm	+1H_2	-2.76

Table S2: The distances of As to the next Fe ion together with the corresponding Fe−O−As angle (θ^1 = $\angle_{\mathbf{Fe1–O^A–As}}$ and θ^2 = $\angle_{\mathbf{Fe2–O^B–As}}$) as well as the As−O bond lengths (As−O(Fe)/As−O or As=O/As−OH) are listed. Additionally, the magnetic moments of the surface iron ions, M_{Fe}, together with the band gap are given. The configurations that appear as stable terminations in the surface phase diagrams of the manuscript are given in bold letters.

Structural, magnetic and electronic properties of arsenate at goethite(101)							
configuration	$d_{Fe1–As}$ (Å), θ^1	$d_{Fe2–As}$ (Å), θ^2	$d_{As1–O}$ (Å)	$d_{As2–O}$ (Å)	M_{Fe1} (μ_B)	M_{Fe2} (μ_B)	Δ (eV)
O+mm/O+O	3.25,120°		1.76/1.70,1.66/ –		4.30/4.26	3.00/4.24	0.2
O+H_2mm/O+O	3.23,119°		1.74/1.70/1.76		4.29/3.73	2.98/4.23	0.3
OH+H_2mm/OH+OH	**3.45,134°**		**1.70/1.67/1.80**		**4.30/4.30**	**4.30/4.30**	**2.0**
O+O/mb+O		3.16,111°		1.82/1.66/ –	3.70/3.71	4.26/4.26	m
O+O/H_2mb+O		3.31,119°		1.80/1.68/1.75	3.71/3.70	4.19/4.25	m
bb/O+O	3.21,117°		1.76/1.71/ –		4.29/4.30	2.98/4.24	0.1
H_2bb/OH+OH	3.24,124°		1.75/ – /1.99		4.28/4.29	4.30/4.30	m
O+O/bm		2.78, 91°		1.85/1.68/ –	3.69/3.70	4.27/4.28	m
OH+OH/H_2bm		2.85, 87°		1.76/ – /1.71,1.78	4.31/4.31	4.22/3.78	1.2
O+mm/mb+O	3.51,142°	3.27,119°	1.73/1.64,1.86/–	1.77/1.66,1.75,1.82/ –	4.31/4.26	4.26/2.90	m
O+H_2mm/H_2mb+O	3.49,140°	3.35,126°	1.73/1.67/1.78	1.82/1.65/1.76	3.64/4.30	4.27/3.81	m
OH+H_2mm/H_2AsO_3+O+OH	3.45,137°	5.05,115°	1.72/1.66/1.77,1.81	1.89/1.68/1.81	4.30/4.31	3.76/4.28	0.1
2bb/O+O	3.56,117°		1.94/1.67/ –		4.30/4.30	3.96/3.96	m
2H_2bb/OH+OH	**3.59,122°**		**2.07/ – /1.88**		**4.29/4.29**	**4.30/4.30**	**1.9**
O+O/2bm		2.95, 88°		2.07/1.63/ –	3.63/3.63	4.24/4.24	0.2
OH+OH/2H_2bm		3.03, 90°		2.19/ – /1.82,1.89	4.30/4.30	4.26/4.26	1.0
bb/mb+O	3.26,121°	3.11,110°	1.77/1.68/1.76	1.82/1.67/–	4.23/4.16	4.26/2.91	m
H_2bb/Hmb+OH	**3.30,121°**	**3.34,122°**	**1.72/ – /1.78**	**1.82/1.67/1.88**	**4.31/4.31**	**4.29/4.29**	**1.7**
H_2bb/H_2mb+OH	**3.26,118°**	**3.49,132°**	**1.70/ – /1.77**	**1.68/1.65/1.82**	**4.21/3.15**	**4.31/4.29**	**m**
O+mm/bm	3.34,125°	2.80, 92°	1.74/1.64/ –	1.86/1.65,1.70/ –	4.30/4.25	4.28/4.26	m
O+H_2mm/H_2bm	3.47,135°	2.73, 87°	1.70/1.65/1.81	1.71/ – /1.77	3.64/4.30	4.23/3.76	m
OH+H_2mm/H_2bm	3.39,129°	2.88, 96°	1.69/1.67/1.81	1.70/ – /1.77	4.30/4.30	4.21/3.78	1.7

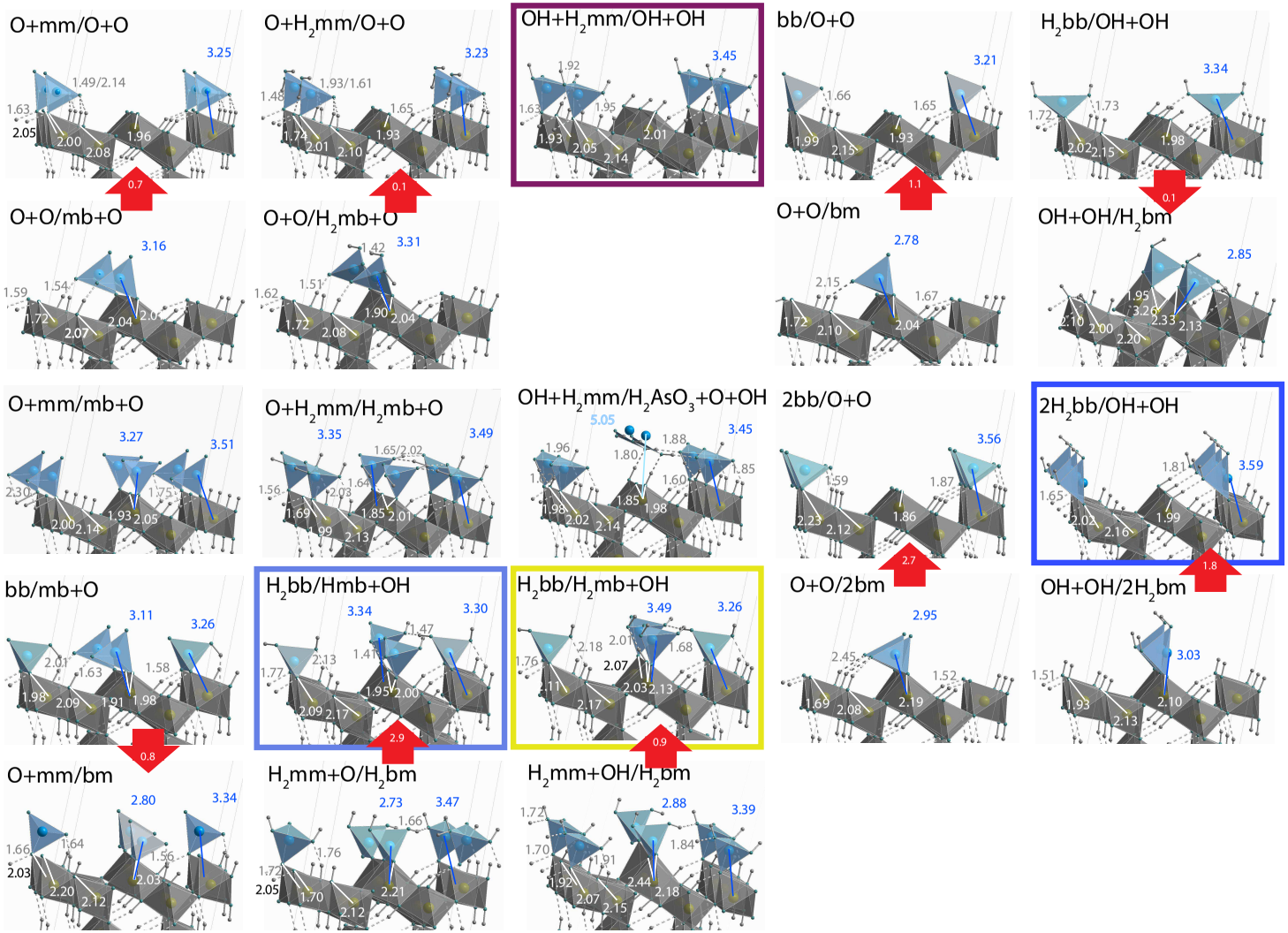

Figure S1: DFT optimized surface structure of all studied arsenate adsorption configurations at goethite(101). The most stable configurations are framed in the corresponding color of the surface phase diagram. For configurations with the same number of atoms additionally the energy difference, ΔE, is given.

Table S3: Arsenate adsorption reactions for surface configurations of akaganeite(100) (b1-b23). The configurations that appear as stable terminations in the surface phase diagrams of the manuscript are given in bold letters. The corresponding adsorption energies $E_{\mathbf{ads}}$ of the arsenate complexes on different iron sites are provided. Note that the energies of H_2 and OH are expressed through $E_{\mathbf{H_2O}}$ and $E_{\mathbf{O_2}}$ using $E_{\mathbf{H_2}} = E_{\mathbf{H_2O}} - 1/2 \cdot E_{\mathbf{O_2}}$ and $E_{\mathbf{OH}} = 1/2 \cdot E_{\mathbf{H_2O}} + 1/4 \cdot E_{\mathbf{O_2}}$, respectively.

Adsorption configurations of arsenate at different terminations of the akaganeite(100) surface						E_{ads} (eV)	
	initial		adsorbate		final	Fe1	Fe2
b1	O+Fe/O+O	+	$1H_3AsO_4$	→	O+mm/O+O +$1.5H_2$	+1.94	
b2	O+Fe/OH+OH	+	$1H_3AsO_4$	→	O+H_2mm/OH+OH +$0.5H_2$	-1.09	
b3	OH+Fe/OH+OH	+	$1H_3AsO_4$	→	OH+H_2mm/OH+OH +$0.5H_2$	-2.42	
b4	O+O/Fe+O	+	$1H_3AsO_4$	→	O+O/mb+O +$1.5H_2$		-0.30
b5	OH+OH/Fe+OH	+	$1H_3AsO_4$	→	OH+OH/Hmb+OH +$0.5H_2$		-1.61
b6	**H_2O+OH/Fe+OH**	**+**	**$1H_3AsO_4$**	**→**	**H_2O+OH/Hmb+OH +H_2**		**-4.16**
	H_2O*+OH/H_2O+OH	**+**	**$1H_3AsO_4$**	**→**	**H_2O+OH/Hmb+OH +$1.5H_2$+$0.5O_2$**		**-4.54**
	OH+OH/OH+OH	**+**	**$1H_3AsO_4$**	**→**	**H_2O+OH/Hmb+OH +1OH**		**-2.24**
b7	Fe+Fe/O+O	+	$1H_3AsO_4$	→	bb/O+O +$1.5H_2$	-0.20	
b8	Fe+Fe/OH+OH	+	$1H_3AsO_4$	→	H_2bb/OH+OH +2OH	-2.20	
b9	O+O/Fe+Fe	+	$1H_3AsO_4$	→	O+O/bm +$1.5H_2$		-3.22
b10	OH+OH/Fe+Fe	+	$1H_3AsO_4$	→	OH+OH/H_2bm +2OH		-2.20
b11	O+Fe/Fe+O	+	$2H_3AsO_4$	→	O+mm/mb+O +$3H_2$	+0.71	
b12	Fe+Fe/O+O	+	$2H_3AsO_4$	→	2bb/O+O +$3H_2$+$1O_2$	-0.02	
b13	**Fe+Fe/OH+OH**	**+**	**$2H_3AsO_4$**	**→**	**2H2bb/OH+OH +2OH**	**-0.28**	
	H_2O*+H_2O*/OH+OH	**+**	**$2H_3AsO_4$**	**→**	**2H2bb/OH+OH +2H_2O+2OH**	**-0.33**	
	OH+OH/OH+OH	**+**	**$2H_3AsO_4$**	**→**	**2H2bb/OH+OH +4OH**	**+0.59**	
b14	O+O/Fe+Fe	+	$2H_3AsO_4$	→	O+O/2bm +$3H_2$+$1O_2$		+1.84
b15	OH+OH/Fe+Fe	+	$2H_3AsO_4$	→	OH+OH/2H_2bm +2OH		-0.07
b16	Fe+Fe/Fe+Fe	+	$2H_3AsO_4$	→	bb/bm +$3H_2$	-2.21	
b17	Fe+Fe/Fe+Fe	+	$2H_3AsO_4$	→	H_2bb/H_2bm +$1H_2$	-2.40	
b18	Fe+Fe/Fe+O	+	$2H_3AsO_4$	→	bb/mb+O +$3H_2$	-0.46	
b19	**Fe+Fe/Fe+OH**	**+**	**$2H_3AsO_4$**	**→**	**H_2bb/Hmb+OH +$1.5H_2$**	**-3.19**	
	H_2O*+H_2O*/H_2O+OH	**+**	**$2H_3AsO_4$**	**→**	**H_2bb/Hmb+OH +3H_2O+$1.5H_2$**	**-3.02**	
	OH+OH/OH+OH	**+**	**$2H_3AsO_4$**	**→**	**H_2bb/Hmb+OH +$2.5H_2$+O_2**	**-1.41**	
b20	**Fe+Fe/Fe+OH**	**+**	**$2H_3AsO_4$**	**→**	**H_2bb/H_2mb+OH +H_2**	**-2.67**	
	H_2O*+H_2O*/H_2O+OH	**+**	**$2H_3AsO_4$**	**→**	**H_2bb/H_2mb+OH +3H_2O+H_2**	**-2.05**	
	OH+OH/OH+OH	**+**	**$2H_3AsO_4$**	**→**	**H_2bb/H_2mb+OH +2H_2O**	**-0.89**	
b21	O+Fe/Fe+Fe	+	$2H_3AsO_4$	→	O+mm/bm +$3H_2$	-1.86	
b22	OH+Fe/Fe+Fe	+	$2H_3AsO_4$	→	O+H_2mm/H_2bm +$1.5H_2$	-3.30	
b23	OH+Fe/Fe+Fe	+	$2H_3AsO_4$	→	OH+H_2mm/H_2bm +$1H_2$	-3.48	

Table S4: The distances of As to the next Fe ion together with the corresponding Fe−O−As angle ($\theta^1 = \angle_{\mathbf{Fe–O^A–As}}$ and $\theta^2 = \angle_{\mathbf{Fe2\text{-}O^B\text{-}As}}$) as well as the As−O bond lengths (As−O(Fe)/As−O or As=O/As−OH) are listed. Additionally, the magnetic moments of the surface iron ions, M_{Fe}, together with the band gap are given. The configurations that appear as stable terminations in the surface phase diagrams of the manuscript are given in bold letters.

Structural, magnetic and electronic properties of arsenate at akaganeite(100)							
configuration	$d_{Fe1–As}$ (Å), θ^1	$d_{Fe2–As}$ (Å), θ^2	$d_{As1–O}$ (Å)	$d_{As2–O}$ (Å)	M_{Fe1} (μ_B)	M_{Fe2} (μ_B)	Δ (eV)
O+mm/O+O	3.32,132°		1.72/1.73,1.80/ –		4.28/4.08	-4.07/-4.07	m
O+H_2mm/OH+OH	3.55,153°		1.71/1.65/1.77,1.84		1.79/4.28	-4.31/-4.31	1.2
OH+H_2mm/OH+OH	3.46,136°		1.74/1.65/1.81		4.28/4.30	-4.30/-4.30	2.0
O+O/mb+O		3.26,121°		1.83/1.71/ –	3.65/3.60	-4.16/-4.16	m
OH+OH/Hmb+OH		3.38,124°		1.81/1.68/1.77	4.29/4.28	-4.20/-4.29	2.0
H_2O+OH/Hmb+OH		**3.29,116°**		**1.81/1.68/1.76**	**4.31/4.30**	**-4.30/-4.29**	**1.9**
bb/O+O	3.17,119°		1.75/1.68/1.78		4.27/4.27	-4.24/-3.02	m
H_2bb/OH+OH	3.31,125°		1.69/ – /1.80		4.20/4.30	-3.75/-4.20	0.4
O+O/bm		2.55, 87°		1.83/1.63/1.77	2.71/3.71	-4.28/-4.28	m
OH+OH/H_2bm		2.73, 85°		1.70/ – /1.80	4.26/4.26	-3.74/-4.21	0.4
O+mm/mb+O	3.20,122°	3.35,121°	1.72/1.71,1.77/ –	1.82/1.72/ –	4.26/4.08	-4.12/-4.12	m
2bb/O+O	3.17,119°		1.92/1.68/ –		4.29/4.29	-4.00/-4.00	m
2H_2bb/OH+OH	**3.55,127°**		**1.91/ – /1.99**		**4.26/4.08**	**-4.12/-4.23**	**1.9**
O+O/2bm		2.79, 91°		1.73/1.83/ –	4.29/4.29	-4.21/-4.21	m
OH+OH/2H_2bm		3.10, 91°		2.20/ – /1.85	4.26/4.26	-4.27/-4.27	1.0
bb/bm	3.08,117°	3.01, 97°	1.75/1.68/ –	1.81/1.63/1.77	4.29/4.29	-4.19/-4.26	m
H_2bb/H_2bm	3.24,118°	2.80, 86°	1.69/ – /1.81	1.68/ – /1.81	4.31/4.31	-3.70/-3.72	1.0
bb/mb+O	3.31,125°	3.18,112°	1.73/1.64/ –	1.78/1.64,1.73,1.91/ –	4.29/4.29	-4.18/-2.99	0.1
H_2bb/Hmb+OH	**3.25,127°**	**3.31,134°**	**1.71/ – /1.77**	**1.79/1.67/1.80**	**4.29/4.29**	**-4.26/-4.28**	**1.9**
H_2bb/H_2mb+OH	**3.29,123°**	**3.50,134°**	**1.70/ – /1.79**	**1.71/1.69/1.79**	**4.30/4.30**	**-3.75/-4.29**	**1.0**
O+mm/bm	3.50,153°	2.80, 92°	1.68/1.64,1.88/ –	1.78/1.66,1.80/ –	4.27/4.21	-4.25/-4.27	0.7
O+H_2mm/H_2bm	3.31,140°	2.80, 92°	1.73/1.70/1.77	1.80/ – /1.70	4.30/4.30	-3.81/-4.24	0.5
OH+H_2mm/H_2bm	3.34,124°	2.80, 90°	1.72/ – /1.80,1.85	1.76/ – /1.76	4.30/4.30	-3.75/-4.29	1.1

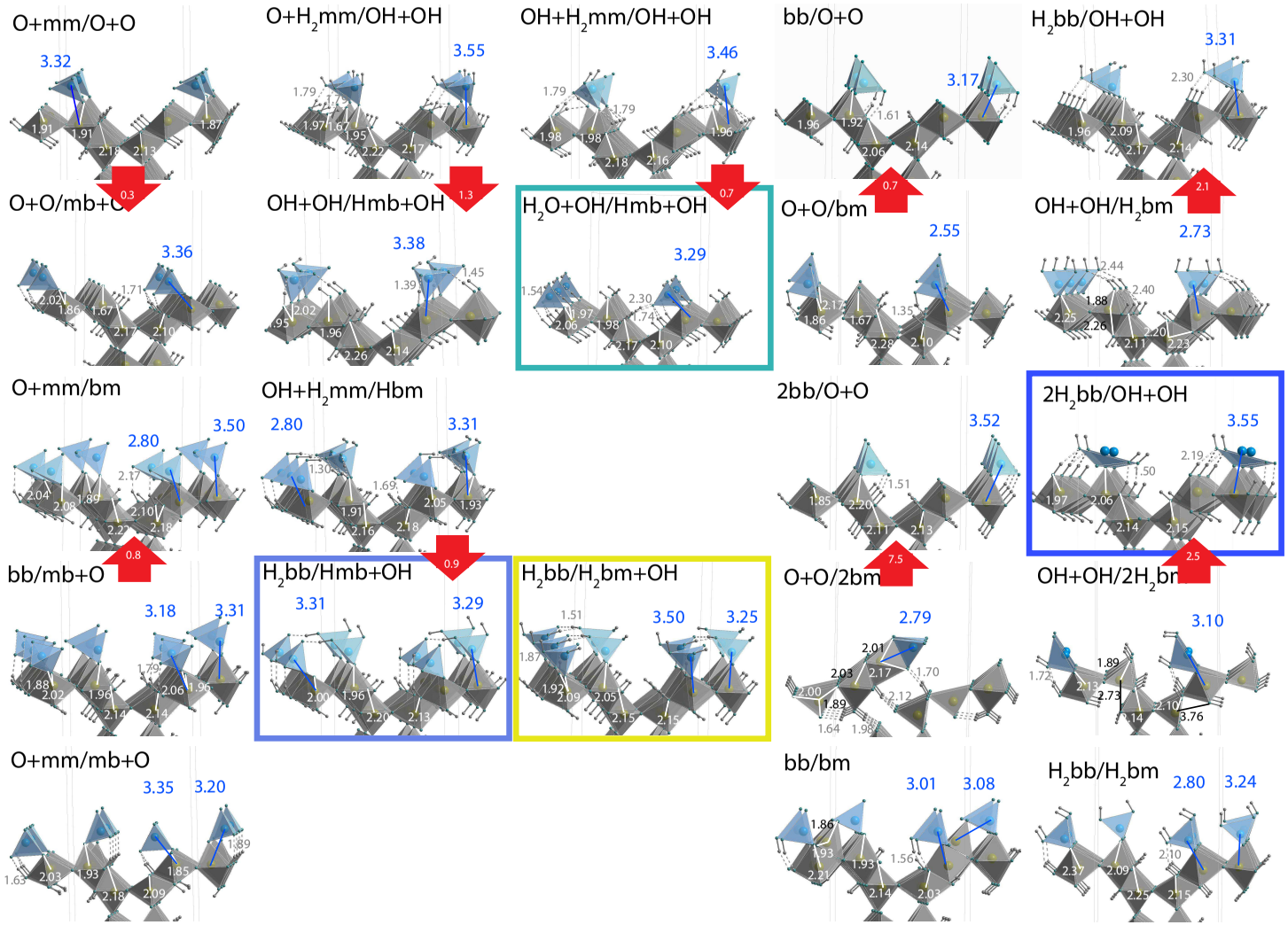

Figure S2: DFT optimized surface structure of all studied arsenate adsorption configurations at akaganeite(100). The most stable configurations are framed in the corresponding color of the surface phase diagram. For configurations with the same number of atoms additionally the energy difference, Δ_E, is given.

Table S5: Arsenate adsorption reactions for surface configurations of lepidocrocite(100) (g1-g13). The configurations that appear as stable terminations in the surface phase diagrams of the manuscript are given in bold letters. The corresponding adsorption energies $E_{\mathbf{ads}}$ (eV) of the arsenate complexes on different iron sites are provided. Note that the energies of H_2 and OH are expressed through $E_{\mathbf{H_2O}}$ and $E_{\mathbf{O_2}}$ using $E_{\mathbf{H_2}} = E_{\mathbf{H_2O}} - 1/2 \cdot E_{\mathbf{O_2}}$ and $E_{\mathbf{OH}} = 1/2 \cdot E_{\mathbf{H_2O}} + 1/4 \cdot E_{\mathbf{O_2}}$, respectively.

Adsorption configurations of arsenate at different terminations of the lepidocrocite(010) surface					
	initial	adsorbate	final		E_{ads} Fe2
g1	O+Fe/O+O	+ $1H_3AsO_4$	→ O+mb/O+O	+1.5H_2	-0.18
g2	O+Fe/O+OH	+ $1H_3AsO_4$	→ O+Hmb/O+OH	+0.5H_2	-3.57
g3	OH+Fe/OH+OH	+ $1H_3AsO_4$	→ OH+H_2mb/OH+OH	+0.5H_2	-3.17
g4	O+Fe/Fe+O	+ $2H_3AsO_4$	→ O+mb/mb+O	+3H_2	-0.91
g5	O+Fe/Fe+O	+ $2H_3AsO_4$	→ O+H_2mb/H_2mb+O	+1H_2	-2.97
g6	**OH+Fe/Fe+OH**	**+ $2H_3AsO_4$**	**→ OH+H_2mb/H_2mb+OH**	**+1H_2**	**-1.31**
	OH+H_2O/H_2O+OH	**+ $2H_3AsO_4$**	**→ OH+H_2mb/H_2mb+OH**	**+1H_2+2H_2O**	**-1.34**
	OH+OH/OH+OH	**+ $2H_3AsO_4$**	**→ OH+H_2mb/H_2mb+OH**	**+2H_2O**	**+0.61**
g7	Fe+Fe/O+O	+ $1H_3AsO_4$	→ bm/O+O	+1.5H_2	-2.57
g8	Fe+Fe/OH+OH	+ $1H_3AsO_4$	→ H_2bm/OH+OH	+0.5H_2	-3.17
g9	**Fe+Fe/H_2O+H_2O**	**+ $1H_3AsO_4$**	**→ H_2bm/H_2O+H_2O**	**+0.5H_2**	**-6.75**
	H_2O+H_2O/H_2O+H_2O	**+ $1H_3AsO_4$**	**→ H_2bm/H_2O+H_2O**	**+0.5H_2+2H_2O**	**-6.81**
	OH+OH/H_2O+H_2O	**+ $1H_3AsO_4$**	**→ H_2bm/H_2O+H_2O**	**+1H_2+1H_2O**	**-2.89**
g10	Fe+Fe/O+O	+ $2H_3AsO_4$	→ 2bm/O+O	+3H_2+1O_2	-0.01
g11	**Fe+Fe/H_2O+H_2O**	**+ $2H_3AsO_4$**	**→ 2H_2bm/H_2O+H_2O**	**+2OH**	**-1.55**
	H_2O+H_2O/H_2O+H_2O	**+ $2H_3AsO_4$**	**→ 2H_2bm/H_2O+H_2O**	**+2H_2O+2OH**	**-1.56**
	OH+OH/H_2O+H_2O	**+ $2H_3AsO_4$**	**→ 2H_2bm/H_2O+H_2O**	**+4OH**	**+0.37**
g12	Fe+Fe/Fe+Fe	+ $2H_3AsO_4$	→ bm/bm	+3H_2	-2.28
g13	Fe+Fe/Fe+Fe	+ $2H_3AsO_4$	→ H_2bm/H_2bm	+1H_2	-2.55

Table S6: The distances of As to the next Fe ion together with the corresponding Fe−O−As angle (θ^2 = $\angle_{\mathbf{Fe2–O^B–As}}$) as well as the As−O bond lengths (As−O(Fe)/As−O or As=O/As−OH) are listed. Additionally, the magnetic moments of the surface iron ions, M_{Fe}, together with the band gap are given. The configurations that appear as stable terminations in the surface phase diagrams of the manuscript are given in bold letters.

Structural, magnetic and electronic properties of arsenate at lepidocrocite(010)					
final	$d_{Fe2–As}$ (Å), θ^2	$d_{As–O}$ (Å)	M_{Fe2} (μ_B)	M_{Fe2} (μ_B)	Δ (eV)
O+mb/O+O	3.29,119°	1.80/1.73/ –	3.94/3.85	4.17/4.18	m
O+Hmb/O+OH	3.24,115°	1.80/1.68/1.78	3.92/4.25	4.10/4.20	m
OH+H_2mb/OH+OH	3.36,124°	1.77/1.67/1.76	4.32/4.32	4.32/4.33	1.4
O+mb/mb+O	3.44,128°	1.76/1.63,1.85/ –	4.24/4.14	4.16/2.89	m
O+H_2mb/H_2mb+O	3.46,129°	1.80/1.67/1.74	4.05/4.28	4.24/4.03	m
OH+H_2mb/H_2mb+OH	**3.38,125°**	**1.78/1.70/1.73**	**4.32/4.32**	**4.32/4.32**	**1.5**
bm/O+O	2.81, 94°	1.75/1.73/ –	3.85/4.14	4.18/4.29	m
H_2bm/OH+OH	2.80, 91°	1.84/ – /1.86,1.94	4.33/4.33	4.29/4.22	0.7
H_2bm/H_2O+H_2O	**2.80, 93°**	**1.86/ – /2.13**	**4.28/4.13**	**4.26/3.99**	**m**
2bm/O+O	2.96, 88°	2.06/1.65/ –	4.01/4.01	4.23/4.23	m
2H_2bm/H_2O+H_2O	**3.10, 89°**	**1.93/2.03/ –**	**4.30/4.30**	**3.72/3.72**	**1.1**
bm/bm	2.81, 93°	1.86/1.68/ –	4.29/4.29	4.29/4.29	m
H_2bm/H_2bm	2.79, 91°	1.85/ – /1.96	4.22/4.29	4.29/4.22	0.5

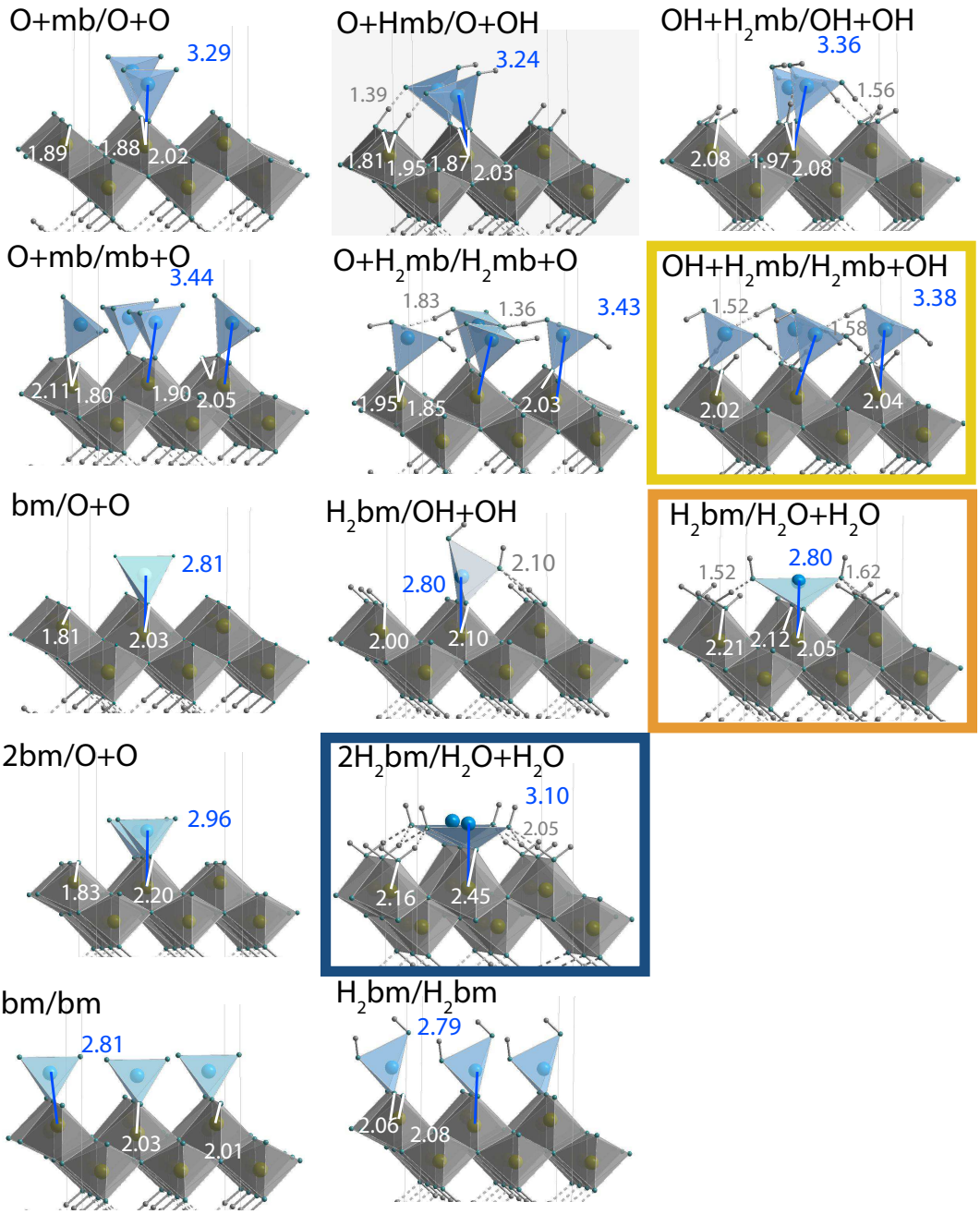

Figure S3: DFT optimized surface structure of all studied arsenate adsorption configurations at lepidocrocite(010). The most stable configurations are framed in the corresponding color of the surface phase diagram.

3 Influence of a $SrTiO_3$ Capping Layer on the Electronic Reconstruction at the $LaAlO_3/SrTiO_3(001)$ Interface

- **Manuscript 4**
  Parallel Electron-Hole Bilayer Conductivity from Electronic Interface Reconstruction, R. Pentcheva, M. Huijben, K. Otte, W. E. Pickett, J. E. Kleibeuker, J. Huijben, H. Boschker, D. Kockmann, W. Siemons, G. Koster, H. J. W. Zandvliet, G. Rijnders, D. H. A. Blank, H. Hilgenkamp, and A. Brinkman, Physical Review Letters **104**, 166804 (2010).

- **Manuscript 5**
  Termination Control of Electronic Phases in Oxide Thin Films and Interfaces: $LaAlO_3/SrTiO_3(001)$, R. Pentcheva, R. Arras, K. Otte, V.Ruiz, and W. E. Pickett, Philosophical Transactions of the Royal Society A **370**, 4904-4926 (2012).

Manuscript 4: $SrTiO_3/LaAlO_3/SrTiO_3(001)$

Parallel Electron-Hole Bilayer Conductivity from Electronic Interface Reconstruction

R. Pentcheva, M. Huijben, K. Otte, W. E. Pickett, J. E. Kleibeuker, J. Huijben, H. Boschker, D. Kockmann, W. Siemons, G. Koster, H. J. W. Zandvliet, G. Rijnders, D. H. A. Blank, H. Hilgenkamp, and A. Brinkman,
Physical Review Letters **104**, 166804 (2010).

Parallel Electron-Hole Bilayer Conductivity from Electronic Interface Reconstruction

R. Pentcheva,[1] M. Huijben,[2] K. Otte,[1] W. E. Pickett,[3] J. E. Kleibeuker,[2] J. Huijben,[2] H. Boschker,[2] D. Kockmann,[2] W. Siemons,[4] G. Koster,[2] H. J. W. Zandvliet,[2] G. Rijnders,[2] D. H. A. Blank,[2] H. Hilgenkamp,[2] and A. Brinkman[2]

[1]*Department of Earth and Environmental Sciences, University of Munich, D-80333 Munich, Germany*
[2]*MESA+ Institute for Nanotechnology, University of Twente, 7500 AE Enschede, The Netherlands*
[3]*Department of Physics, University of California, Davis, California 95616, USA*
[4]*Department of Physics, University of California, Berkeley, California 94720, USA*

(Received 22 December 2009; published 23 April 2010)

The perovskite $SrTiO_3$-$LaAlO_3$ structure has advanced to a model system to investigate the rich electronic phenomena arising at polar oxide interfaces. Using first principles calculations and transport measurements we demonstrate that an additional $SrTiO_3$ capping layer prevents atomic reconstruction at the $LaAlO_3$ surface and triggers the electronic reconstruction at a significantly lower $LaAlO_3$ film thickness than for the uncapped systems. Combined theoretical and experimental evidence (from magnetotransport and ultraviolet photoelectron spectroscopy) suggests two spatially separated sheets with electron and hole carriers, that are as close as 1 nm.

DOI: 10.1103/PhysRevLett.104.166804 PACS numbers: 73.20.−r, 71.30.+h, 71.35.−y, 77.55.−g

Polarity discontinuities at the interfaces between different crystalline materials are usually compensated by atomic reconstructions via defects or adsorbates as in conventional semiconductor interfaces. However, in complex oxides the mixed valence states provide an extra option for charge rearrangement by redistributing electrons at lower energy cost than redistributing ions. The remarkable electronic transport properties that occur at the interface between the band insulators $SrTiO_3$ (STO) and $LaAlO_3$ (LAO) [1–8] have been attributed to this so called electronic reconstruction [9,10] but direct evidence has not yet been found.

The polarity of LAO arises from the LaO and AlO_2 layers being not charge neutral in the [001] direction, unlike the formally neutral TiO_2 and SrO layers of STO. In the ionic limit, LaO has a charge $q = +e$ and AlO_2 $q = -e$ per unit cell. The screened dipole per unit cell is then $D = q\Delta z/\epsilon$, where the spacing $\Delta z = c/2$ ($c = 3.9$ Å is the out of plane lattice parameter) and $\epsilon = 25$ is the dielectric constant of LAO [11]. Screening contributions come primarily from a strong lattice polarization of the LAO film (their contribution can be as high as ~62% [12]), supplemented by electronic cloud deformation [13]. For STO-LAO systems, the remaining screened dipole of 0.08 eÅ per cell is expected to give rise to an internal electric field of 2.4×10^7 V/cm, and a resulting buildup of electric potential of 0.9 V per LAO unit cell.

This potential shift explains quantitatively why, above a threshold of 3–4 unit cells, electrons are transferred from the surface, across the LAO slab, into the STO conduction band. The resulting insulator-to-metal transition has been observed experimentally for the *n*-type LaO/TiO_2 interface [4]. However, the corresponding potential shifts across LAO have not been detected so far in experiments [14], which suggests that possibly nonelectronic reconstructions occur during the growth. To avoid potential buildup also the LAO surface itself needs to reconstruct, either structurally, electronically, or chemically. After electronic charge transfer one would expect holes at the surface, which have also never been observed.

In this Letter we show that an additional STO capping layer circumvents structural and chemical reconstructions at the LAO surface. The O $2p$ band in the STO capping layer allows for hole doping, so that an electronic reconstruction mechanism comes into play. By means of the STO capping layer one enters a new regime in the field of electronically reconstructed oxide interfaces with two spatially separated 2D conducting sheets, one electronlike and the other holelike, that can display new electronic behavior including the possibility of a 2D excitonic liquid phase.

The system consisting of a varying number of LAO monolayers (ML), $n = 1$–5 ML, and of a STO capping layer, $m = 0$–2 ML, stacked on an STO(001) substrate, was studied by density functional theory (DFT) calculations in the generalized gradient approximation (GGA) (for details see Refs. [12,15]). The calculated layer-resolved densities of states are presented in Fig. 1(a) for 2 ML LAO with and without 1 ML STO capping. The effect of the electric field within the LAO film is apparent from the shifts of bands, e.g., by ~0.4 eV per LAO unit-cell for the uncapped system [12]. Note, that this potential shift is smaller than the mentioned 0.9 eV due to effects related to the well-known underestimation of band gaps by DFT.

Adding a single unit-cell STO capping layer is found to have a dramatic impact on the calculated electronic structure: the band gap, being 1.2 eV for STO(001)/2LAO, is nearly closed for STO(001)/2LAO/1STO. While the ionic relaxation pattern [12] changes significantly when a capping layer is added [15], the net contribution of the buckled TiO_2 and SrO layers does not affect appreciably the total ionic dipole moment of the film (which scales with the

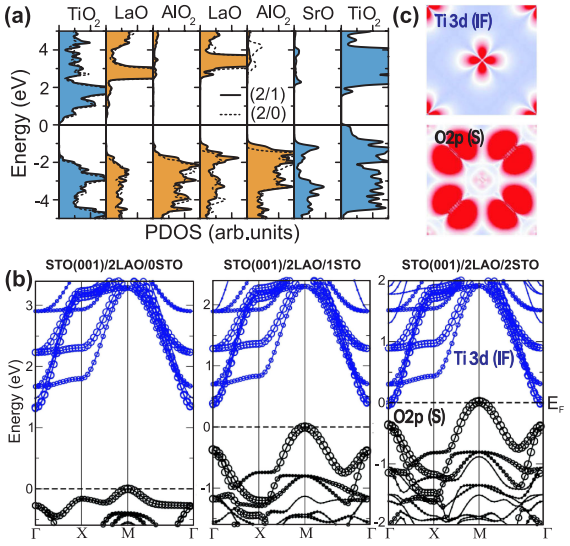

FIG. 1 (color online). (a) Layer-resolved density of states (DOS) of STO(001)/2LAO (dotted line), and STO(001)/2LAO/1STO (black line, colored area) aligned at the bottom of the Ti $3d$ band at the interface. (b) Influence of $m = 0$–2 STO capping layers on the band structure of STO(001)/2LAO/mSTO The band gap closes due to overlap between surface O $2p$ states (black circles) and interface Ti $3d$ states (blue circles). (c) The electron density for the $m = 2$ system, integrated between -0.6 and 0.0 eV, shows electrons in the Ti $3d_{xy}$ orbitals at the interface (top) and holes in the O $2p_{\pi}$ bands at the surface (bottom).

number of LAO layers). Hence, the gap reduction has mainly an electronic origin.

The evolution of the band structure of STO(001)/2LAO/mSTO with increasing number of capping layers is depicted in Fig. 1(b). The valence band maximum is defined by the O $2p$ states at the $M(\pi, \pi)$ point in the surface layer, while Ti $3d$ states at Γ at the n-type interface mark the bottom of the conduction band. In the capped systems a dispersive O $2p$ surface band extends 0.8 eV above the subsurface O $2p$ band and effectively reduces the band gap driving the insulator-to-metal transition at an LAO thickness of only 2 ML compared to 4 ML in the uncapped case. This surface state is analogous to the one on the clean STO (001) surface [16,17]. Further STO layers (e.g., STO(001)/2LAO/2STO [15]) increase the band overlap at the Fermi level, but have an overall weaker influence due to the lack of internal field in STO. The reduction of the band gap, and finally its closing, is thus due to three *electronic* effects: (i) the steady upward shift of the O $2p$ states as they approach the surface [12] due to the internal polarity of LAO, (ii) the band discontinuity at the interface between LAO and the capping STO layer, and (iii) the dispersive O $2p$ surface band in the capped systems that extends 0.8 eV above the subsurface O $2p$ band.

Experimentally, we confirm the crucial influence of a single monolayer of nonpolar material on the electronic interface reconstruction. STO(001)/nLAO/mSTO samples were made by pulsed laser deposition of n ML of LAO and m ML of STO on TiO_2-terminated STO(001) substrates (for fabrication details, see Refs. [3,6]). While uncapped STO(001)/2LAO samples are found to be insulating (sheet resistance above 1 G$\Omega/\square$), samples with an additional single ML of STO are conducting [see Fig. 2(a)]. The conductivity is further enhanced in STO(001)/2LAO/2STO samples, but the influence of increasing the STO capping layer thickness weakens, as expected from the DFT results: the STO(001)/2LAO/10STO sample has almost the same conductivity as the STO(001)/2LAO/2STO sample. Samples with a single ML of LAO were found to be insulating except for the sample with a thick STO capping ($m \geq 10$).

It is known that the sheet resistance in STO/LAO samples depends critically on the oxygen pressure during growth [6,18–21] and can vary over many orders of magnitude [6]. Figure 2(b) shows the sheet resistance for two different sets of STO/LAO/STO heterostructures with varying LAO interlayer thickness, grown at a relatively high oxygen pressure (2×10^{-3} mbar) and at lower oxygen pressure (3×10^{-5} mbar). For the coupled-interface samples, the influence of the oxygen pressure is now found to be much weaker. Apparently, the STO capping protects the underlying LAO surface against reconstruction via defects or adsorbates.

In order to obtain spectroscopic evidence for the *electronic* reconstruction, ultraviolet photoelectron spectroscopy (UPS) was performed *in situ* immediately after the growth of a STO(001)/2LAO/1STO sample. Figure 3(a)

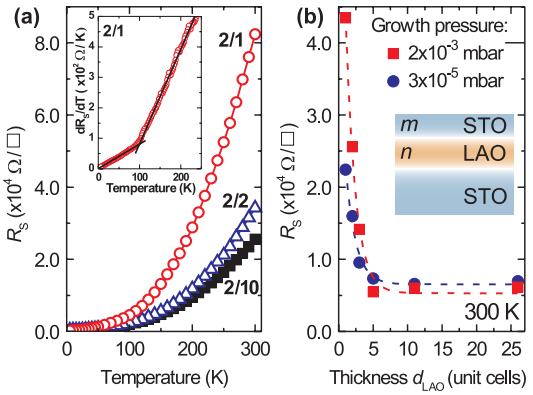

FIG. 2 (color online). (a) Sheet resistance as a function of temperature for STO(001)/2LAO/1STO (red circles), STO(001)/2LAO/2STO (blue triangles), and STO(001)/2LAO/10STO (black squares). All samples are grown at 2×10^{-3} mbar of oxygen. Inset: dR/dT as function of temperature with different linear fits below and above 100 K. (b) Sheet resistance at room temperature of STO(001)/nLAO/10STO samples for varying n LAO thickness and a fixed number of 10 unit cells of STO capping. Red squares/blue circles correspond to oxygen pressure of 2×10^{-3} mbar/3×10^{-5} mbar during growth.

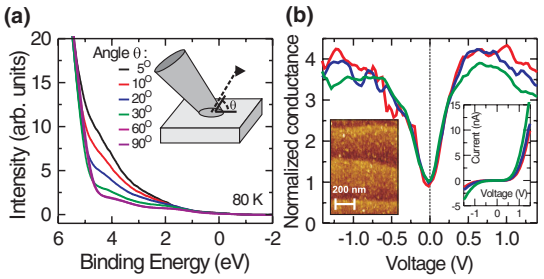

FIG. 3 (color online). (a) UPS spectra of a STO(001)/2LAO/1STO sample taken at 80 K *in situ* after growth under various detector angles (the inset shows how the angle towards the detector is defined). A gradual filling of the valence band towards the Fermi energy is found in the surface-sensitive lower angle spectra. (b) STS conductance $(dI/dV)/(I/V)$ at 300 K for different tip-sample distances (current set-point, respectively, 1.5, 2.0, and 4.0 nA at a bias voltage of -1.5 V). Right inset: I/V curve; left inset shows an STM image recorded at -1.0 V and 300 K.

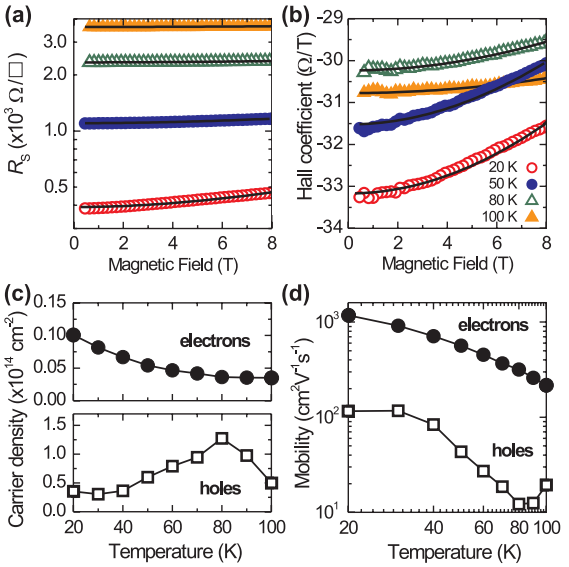

FIG. 4 (color online). (a) Sheet resistance and (b) Hall coefficient (R_H/H) as a function of magnetic field at different temperatures for a STO(001)/2LAO/1STO sample. (c) Sheet carrier densities and (d) mobilities as obtained from a two-band fit to the magnetoresistance and Hall data at each temperature.

shows a gradual increase in intensity for the more surface sensitive measurements at lower detector angles. These states originate from the valence band of LAO as well as the valence band of the STO surface ML. Note, that the valence band states penetrate all the way to E_F, unlike studies on doped STO [22], where only trapped states close to the conduction band are usually observed.

To probe states around the Fermi level, scanning tunneling spectroscopy (STS) was performed in ultra high vacuum using a variable temperature cryostat. Figure 3(b) shows the local DOS, $(dI/dV)/(I/V)$, of a STO(001)/2LAO/1STO sample. At room temperature, the Fermi energy lies between the valence band of the STO surface and the conduction band of the substrate-LAO interface. The bandgap is (almost) closed, as predicted in Fig. 1 by DFT (see also [15]). The observed density of states just below E_F, as measured by both UPS and STS, is consistent with the electronic reconstruction scenario and suggests the presence of holes in transport.

To explore the nature of charge carriers in capped systems, magnetoresistance and Hall data were analyzed. Because the intrinsic coupling between the layers would not allow us to probe the transport properties of the layers individually, unless structures are realized on a submicron length scale, our measurements contain information on the layers in parallel. Figure 4 displays a positive nonquadratic magnetoresistance and a Hall resistance whose slope increases for higher fields for all conducting STO/LAO/STO samples. Quantum oscillations can still be excluded because of the low mobility. A negative magnetoresistance contribution, observed for single-interface samples deposited at high oxygen pressure [6], only appears below 10 K. It is natural to interpret the observations in terms of multiband conductivity. Indeed, in the temperature range up to 100 K, the magnetoresistance as well as the Hall resistance can be fitted with a two-band model [15] [solid lines in Figs. 4(a) and 4(b)]. Two carrier concentrations and two mobilities could be obtained for the STO(001)/2LAO/1STO sample from fitting as a function of temperature [Figs. 4(c) and 4(d)].

The positive carrier sign of one of the bands at low temperatures indicates hole-type conductivity, while the other band is of electron-type. We note that no fit to the data could be obtained for equal signs of the two carrier densities. Neither oxygen vacancy doping, nor doping by cation substitution, have ever been shown to give rise to hole conductivity in the STO/LAO system. The calculated electron density distribution in Fig. 1(c) displays electrons of Ti $3d_{xy}$ orbital character in the interface TiO_2 layer, while holes of O $2p_\pi$ type are present in the surface TiO_2 layer. Consequently, we attribute the hole band to the surface layer, while the electron band, with a lower carrier density but a much larger mobility, is naturally attributed to the Ti $3d_{xy}$ states at the interface to the substrate, consistent with the observations in Ref. [23].

Note, that the hole density is about an order of magnitude larger than the electron density. However, the Hall effect is dominated by the electron band because of its large mobility (10^3 cm^2 V^{-1} s^{-1}). The unequal number of electrons and holes illustrates that not all charge carriers are visible in transport measurements. While the effective electron and hole masses cannot be directly inferred from our data, the band structure calculations (neglecting strong correlation effects and defects) render $0.4m_e$ for the electrons (both in the capped and uncapped system) and a significantly higher effective mass of $1.2m_e$ for the holes.

Above 100 K, neither magnetoresistance, nor a nonlinear Hall resistance were observed, because the mobilities become so low that no magnetoresistance effects are expected any longer ($\mu^2 H^2 \ll 1$ in the two-band equations of [15]). Therefore, no two-band fitting analysis can be performed in this case, and no statement can be done on the presence of electrons and holes.

In the STO(001)/2LAO/1STO sample evidence from different experimental techniques point to an electronic reconstruction mechanism. At the same time, we know that for uncapped thick LAO samples no potential buildup has been observed [14], suggestive of nonelectronic reconstruction scenarios. In order to verify whether it is only the capping that makes a difference, the magnetotransport was studied for a large number of samples with either thicker LAO or thicker capping STO [15]. While for defect-free systems DFT predicts an increase in the band overlap, and hence in the number of electrons and holes, no hole contribution was found experimentally beyond $n = 2$ and $m = 1$. Apparently, during growth structural reconstruction occurs whenever the potential buildup exceeds a few eV. While conductivity arises also in this case, no evidence for pure electronic reconstruction exists any longer. The STO(001)/2LAO/1STO sample might be an example of a system where the potential buildup during growth of just 2 ML of LAO is just not yet large enough for a reconstruction. The subsequent capping ML protects the LAO surface from structural or chemical reconstruction, provides another potential increase (either during growth or cool down), and can accommodate mobile holes, resulting in electronic reconstruction. This conclusion provides guidelines to enhance electronic reconstruction effects in general.

As shown in Fig. 1, the surface valence band has its maximum at the $M = (\pi, \pi)$ zone corner, whereas the substrate-LAO interface conduction band has its minimum at the zone center. This makes the band overlap distant not only in real space (across 12 Å or more, depending on capping layer thickness) but also indirect in momentum. As a practical consequence, an electron at the surface cannot move to the substrate without some mechanism to supply the momentum transfer. The obvious mechanism is via phonons, specifically $M = (\pi, \pi)$ phonons. These are zone boundary optical phonons, which typically lie at a few tens of meV energy. Equilibration of electrons and holes across the LAO slab will be slow at low temperature, but will occur rapidly as soon as optical phonons are excited.

In summary, the STO capping has enabled us to show the presence of holes at electronically reconstructed oxide interfaces. Their mobility is low and it is expected that the holes can become localized or eliminated in uncapped STO/LAO systems more strongly (e.g., by absorbed molecules or other defects). This possibly explains the large sensitivity of uncapped samples to growth conditions and the possibility to manipulate the interface conductivity by an atomic force microscope tip [24,25].

A further consequence of this 2D electron-hole bilayer is that it provides the conditions necessary for formation of a 2D excitonic liquid [26,27] comprised of interacting indirect excitons. In this oxide nanostructure the separation of the 2D electron and hole gases can be varied by the choice of polar material as well as capping material. In analogy to other oxides, such as ZnO [28], it is expected that higher mobilities can be obtained by reducing the defect density. Furthermore, the carrier densities can be tuned by gating, allowing a substantial parameter range to be probed.

This work is supported by the Dutch Foundation for Fundamental Research on Matter (FOM), the Netherlands Organization for Scientific Research (NWO) through VIDI and VICI grants, NANONED, the Bavaria-California Technology Center (BaCaTeC), German Science Foundation (TRR80) and DOE's Computational Materials Science Network, DOE grant DE-FG02-04ER46111, NSF grant PHY05-51164, and a grant for computational time at the Leibniz Rechenzentrum.

[1] A. Ohtomo and H. Y. Hwang, Nature (London) **427**, 423 (2004); **441**, 120 (2006).
[2] N. Nakagawa, H. Y. Hwang, and D. A. Muller, Nature Mater. **5**, 204 (2006).
[3] M. Huijben *et al.*, Nature Mater. **5**, 556 (2006).
[4] S. Thiel *et al.*, Science **313**, 1942 (2006).
[5] N. Reyren *et al.*, Science **317**, 1196 (2007).
[6] A. Brinkman *et al.*, Nature Mater. **6**, 493 (2007).
[7] A. D. Caviglia *et al.*, Nature (London) **456**, 624 (2008).
[8] M. Basletić *et al.*, Nature Mater. **7**, 621 (2008).
[9] R. Hesper *et al.*, Phys. Rev. B **62**, 16046 (2000).
[10] S. Okamoto and A. J. Millis, Nature (London) **428**, 630 (2004).
[11] S. A. Hayward *et al.*, Phys. Rev. B **72**, 054110 (2005).
[12] R. Pentcheva and W. E. Pickett, Phys. Rev. Lett. **102**, 107602 (2009).
[13] S. Ishibashi and K. Terakura, J. Phys. Soc. Jpn. **77**, 104706 (2008).
[14] Y. Segal *et al.*, Phys. Rev. B **80**, 241107(R) (2009).
[15] See supplementary material at http://link.aps.org/supplemental/10.1103/PhysRevLett.104.166804.
[16] S. Kimura *et al.*, Phys. Rev. B **51**, 11049 (1995).
[17] J. Padilla and D. Vanderbilt, Surf. Sci. **418**, 64 (1998).
[18] W. Siemons *et al.*, Phys. Rev. Lett. **98**, 196802 (2007).
[19] G. Herranz *et al.*, Phys. Rev. Lett. **98**, 216803 (2007).
[20] A. Kalabukhov *et al.*, Phys. Rev. B **75**, 121404(R) (2007).
[21] M. Huijben *et al.*, Adv. Mater. **21**, 1665 (2009).
[22] W. Maus-Friedrichs *et al.*, Surf. Sci. **515**, 499 (2002).
[23] M. Salluzzo *et al.*, Phys. Rev. Lett. **102**, 166804 (2009).
[24] C. Cen *et al.*, Nature Mater. **7**, 298 (2008).
[25] C. Cen *et al.*, Science **323**, 1026 (2009).
[26] L. V. Keldysh and Y. V. Kopaev, Sov. Phys. Solid State **6**, 2219 (1965).
[27] J. des Cloizeaux, J. Phys. Chem. Solids **26**, 259 (1965).
[28] A. Tsukazaki *et al.*, Science **315**, 1388 (2007).

Supplementary information for "Parallel electron-hole bilayer conductivity from electronic interface reconstruction"

R. Pentcheva,[1] M. Huijben,[2] K. Otte,[1] W.E. Pickett,[3] J.E. Kleibeuker,[2] J. Huijben,[2] H. Boschker,[2] D. Kockmann,[2] W. Siemons,[4] G. Koster,[2] H.J.W. Zandvliet,[2] G. Rijnders,[2] D.H.A. Blank,[2] H. Hilgenkamp,[2] and A. Brinkman[2]

[1]*Department of Earth and Environmental Sciences, University of Munich, Germany*
[2]*Faculty of Science and Technology and MESA+ Institute for Nanotechnology, University of Twente, The Netherlands*
[3]*Department of Physics, University of California, Davis, USA*
[4]*Department of Physics, University of California, Berkeley, USA*

EVOLUTION OF DENSITY OF STATES

Figure 1 shows the evolution of the total density of states (DOS) as a function of the number, m, of STO capping layers in STO(001)/2LAO/mSTO samples. While the first layer has the dominating effect of reducing the band gap by 1.2 eV, a second STO layer leads to a clear band overlap and an enhancement of the DOS at the Fermi level.

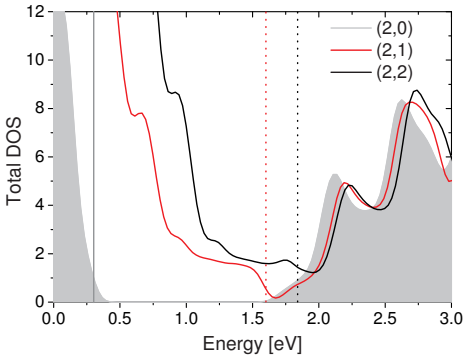

FIG. 1: Total density of states (DOS) of STO(001)/2LAO/mSTO, aligned at the bottom of the Ti 3d band at the interface. Vertical lines mark the positions of the Fermi level for each system. By adding a STO capping layer, the band gap of STO(001)/2LAO is reduced by 1.2 eV. Further capping layers lead to an increase of DOS at the Fermi level.

IONIC RELAXATIONS

Figure 2 shows the calculated layer resolved ionic displacements [1] in STO(001)/2LAO/mSTO. Additionally, the relaxations of a STO(001)-surface are plotted. For the uncapped systems Al and O both relax inwards by similar amounts without a ferroelectric distortion. In contrast, there is a strong buckling in the surface TiO_2 layer in the case of STO capping. The relaxation pattern in the capping layers bears a striking resemblance to the structure of the STO(001) surface, where the total dipole is relatively small $D_{ionic}^{\mathrm{STO(001)}} = -0.19$ eÅ [2]. As mentioned previously, also the electronic structure of the

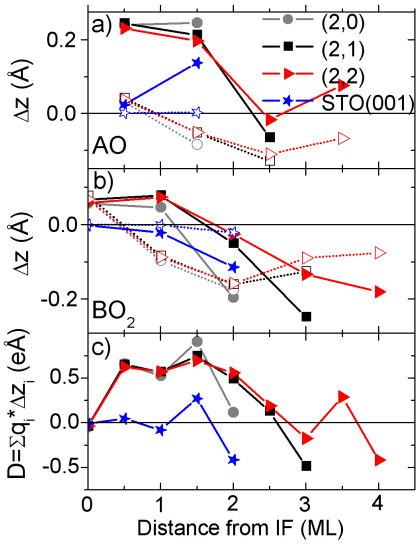

FIG. 2: Ionic relaxations in STO(001)/2LAO/mSTO and the bare STO(001)-surface. Vertical displacements Δz are shown with respect to the bulk position in the (a) AO and (b) BO_2 layers, (c) layer-resolved dipole moments as a function of the distance from the interface (IF) TiO_2-layer. The filled (open) symbols mark cation (anion) relaxations. (n, m) denotes the number n of LAO and m of STO layers in the respective system.

STO(001) surface [3, 4] and the capping layer are similar, in particular a dispersive O 2p surface state with maximum at the M-point appears. Due to the small ionic contribution of the capping layer the total dipole moment is not affected appreciably by the capping layer: $D_{ionic}^{(2,0)} = 2.15$ eÅ, $D_{ionic}^{(2,1)} = 2.05$ eÅ, and $D_{ionic}^{(2,2)} = 2.28$ eÅ. The latter turns out to be determined by the total number of LAO layers, e.g. $D_{ionic}^{(1,1)} = 1.02$ eÅ, $D_{ionic}^{(2,1)} = 2.05$ eÅ, and $D_{ionic}^{(3,1)} = 3.30$ eÅ.

SPECTROSCOPIC DETAILS

Figure 3 shows the current-voltage tunneling characteristics of a STO(001)/2LAO/1STO sample and the derived normal-

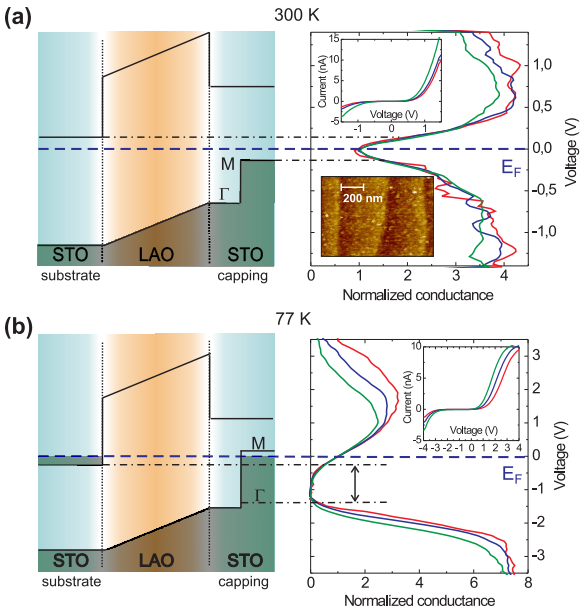

FIG. 3: (a) Scanning tunneling normalized conductance $(dI/dV)/(I/V)$ measurements of a STO(001)/2LAO/1STO sample at 300 K for different tip-sample distances (current set-point respectively 1.5 nA, 2.0 nA, and 4.0 nA at a bias voltage of -1.5 V). The schematic drawing explains the small gap between the valence band at the M-point of the STO capping surface and the conduction band at the substrate-LAO interface. The Fermi energy, E_F, at $V = 0$ V (blue dashed line) lies in the gap. The upper inset shows the current-voltage characteristics from which the conductance was derived and the lower inset shows an STM topography image taken at 300 K with a bias voltage of -1.0 V. (b) Normalized conductance at 77 K (current set-point respectively 1.5 nA, 2.5 nA, and 4.0 nA at a bias voltage of -4.0 V). The schematic drawing explains the larger gap between the valence band Γ point at the STO capping surface and the substrate-LAO interface conduction band. The Fermi energy (blue dashed line) lies now in the conduction band. Band bending is not depicted on this scale. The inset shows the current-voltage characteristics.

ized conductivity $(dI/dV)/(I/V)$, which can be interpreted as the sample local density of states (LDOS). Assuming that tunneling occurs both to the surface and to the substrate-LAO interface, these spectroscopic features can be understood on the basis of the band structure calculations. At 300 K, the Fermi energy lies between the valence band at the M-point in the surface and the conduction band at the Γ-point in the substrate-LAO interface. At 77 K, see Fig. 3b, the valence band seems to have shifted to lower energy. We will elaborate below that this is due to the momentum-resolving capabilities of STS.

The apparent increase of the STS band gap when cooling down from room temperature to 77 K can be understood from an analysis of measurements of the tunnel current, I, versus the tip-sample separation, z, at fixed (negative) sample bias. The tunnel current $I \propto e^{-2\kappa z}$ is measured at negative sample biases in the range from -1 V to -3 V. The inverse decay length, κ, is substantially larger at room temperature (~ 80 %) than at 77 K. The inverse decay length is given by $\kappa = \sqrt{C + k_{\parallel}^2}$, where C only depends on the temperature independent tunnel barrier height and $k_{\parallel}$ is the parallel momentum of the surface electronic structure [5]. The relatively large κ at room temperature strongly supports the idea that at room temperature tunneling occurs from filled surface electronic states with a nonzero parallel momentum (*i.e.* regions near the M point of the surface Brillouin zone) to empty states of the tip. Accordingly, at 77 K tunneling mainly occurs from filled electronic states near the Γ point of the surface Brillouin zone to empty states of the tip, leading to substantial increase of the measured band gap. The latter analysis emphasizes that the electrons that are transferred across the STO/LAO/STO structure upon reconstruction indeed originate from the M point of the surface STO Brillouin zone.

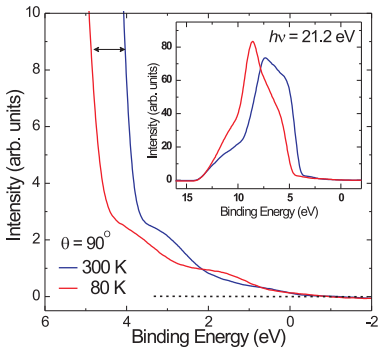

FIG. 4: UPS spectra of a STO(001)/2LAO/1STO sample taken *in situ* after growth, at 300 K and 80 K with the detector at 90°. The inset shows the zoomed-out full spectra. The data has been normalized to the integrated peak height. The arrows indicate a significant shift that was observed between the spectra.

The STS measurements also reveal that, upon lowering the temperature, the Fermi energy is slightly shifted to higher energies. At 77 K, E_F is found to ly in the conduction band. This finding was confirmed by the temperature dependence of the UPS spectra. While the overall spectra (see inset of Fig. 4) resemble those for bulk STO [6], a clear 1 eV peak shift to higher binding energy is observed for 80 K when compared to 300 K. This can be interpreted as an upward shift of the Fermi energy relative to the valence band maximum in the bulk of STO when lowering the temperature, analogous to the observation by STS.

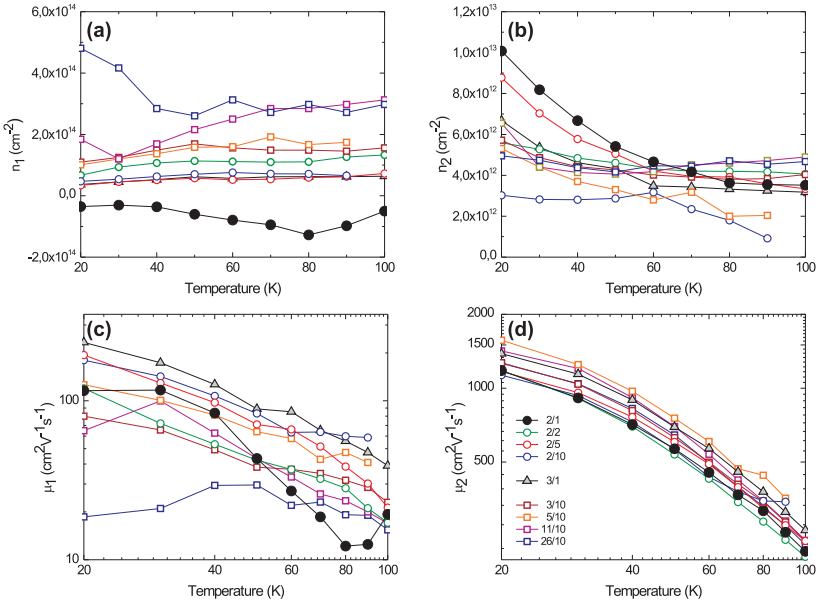

FIG. 5: Two-band fitting results for different STO(001)/nLAO/mSTO samples. The magnetoresistance and Hall effect field dependence were fitted with a two-band model. The fitting provides two carrier densities (a-b) and two mobilities (c-d) for each n/m sample.

TWO-BAND FITTING RESULTS

For every electronic band n, that contributes to conductivity, the induced current $\boldsymbol{j_n}$ is given by the electric field $\boldsymbol{E_n}$ times the band conductivity $\boldsymbol{\sigma_n}$, $\boldsymbol{j_n} = \boldsymbol{\sigma_n}\boldsymbol{E_n}$. The band resistivity $\boldsymbol{\rho_n} = \boldsymbol{\sigma_n^{-1}}$ is defined as

$$\boldsymbol{\rho_n} = \begin{pmatrix} \rho_n & -R_n H \\ R_n H & \rho_n \end{pmatrix}, \tag{1}$$

where ρ_n is the longitudinal resistance, R_n the transverse Hall coefficient and H the magnetic field. The *total* resistivity tensor $\boldsymbol{\rho}$, defined as

$$\boldsymbol{\rho_n} = \begin{pmatrix} \rho & -RH \\ RH & \rho \end{pmatrix}, \tag{2}$$

is given by $\boldsymbol{\rho} = \boldsymbol{\sigma}^{-1} = \left(\sum_n \boldsymbol{\sigma_n}\right)^{-1} = \left(\sum_n \boldsymbol{\rho_n^{-1}}\right)^{-1}$. When only two bands contribute to conductivity, it follows that the total longitudinal and Hall resistances can be expressed as

$$\rho = \frac{\rho_0 + \rho_\infty \mu^2 H^2}{1 + \mu^2 H^2}, \tag{3}$$

$$R_H = \frac{R_0 + R_\infty \mu^2 H^2}{1 + \mu^2 H^2}, \tag{4}$$

where $R_0 = \left(R_1\sigma_1^2 + R_2\sigma_2^2\right)(\sigma_1+\sigma_2)^{-2}$, $R_\infty = R_1 R_2 (R_1+R_2)^{-1}$, $\mu = (R_1+R_2)\sigma_1\sigma_2(\sigma_1+\sigma_2)^{-1}$, $\rho_0 = (\sigma_1+\sigma_2)^{-1}$, and $\rho_\infty = \left(R_1^2\sigma_2^{-1} + R_2^2\sigma_1^{-1}\right)(R_1+R_2)^{-2}$.

The band conductivities are given by $\sigma_{1,2} = |n_{1,2}|\,\mu_{1,2}$ and the band Hall resistivities by $R_{1,2} = (n_{1,2})^{-1}$, where n is negative for electrons (negative curvature in the band dispersion relation) and positive for holes (positive band curvature).

Equations (3) and (4) were fitted simultaneously to the measured sheet resistance and Hall resistance by means of a least square fitting routine. The resistivity data was symmetrized (average over values at positive and negative fields) in order to exclude a transverse resistance contribution to the longitudinal resistance. The Hall resistivity was anti-symmetrized (difference between values at positive and negative fields) in order to exclude longitudinal components. All the different samples could be fitted within the experimental error bars. The results for all measured STO(001)/nLAO/mSTO samples are shown in Fig. 5.

[1] The DFT calculations are performed in a tetragonal unit cell with a full relaxation of the vertical positions of the atoms. Further distortions such as tilting and rotations of the octahedra have not been included and are assumed not to be relevant to our main conclusions. Due to the small occupation of the Ti $3d$ band no further symmetry lowering is observed by using a larger lateral periodicity in a $c(2\times2)$ unit cell.

[2] The dipole moment is determined from the ionic displacements using the formal ionic charges. Although Born effective charges may be more appropriate, we use this approach as a rough estimate of the ionic contribution to the total dipole.

[3] S. Kimura, J. Yamauchi, M. Tsukada, S. Watanabe, Phys. Rev. B

51, 11049 (1995).
[4] J. Padilla, D. Vanderbilt, Surf. Sci. **418**, 64 (1998).
[5] H.J.W. Zandvliet, A. van Houselt, Ann. Rev. Anal. Chem. **2**, 37 (2009).
[6] W. Siemons *et al.*, Phys. Rev. B **76**, 155111 (2007).

Manuscript 5: $LaAlO_3/SrTiO_3(001)$

Termination Control of Electronic Phases in Oxide Thin Films and Interfaces: $LaAlO_3/SrTiO_3(001)$

R. Pentcheva, R. Arras, K. Otte, V. Ruiz, and W. E. Pickett, Philosophical Transactions of the Royal Society A **370**, 4904-4926 (2012).

PHILOSOPHICAL TRANSACTIONS OF THE ROYAL SOCIETY A MATHEMATICAL, PHYSICAL & ENGINEERING SCIENCES

Termination control of electronic phases in oxide thin films and interfaces: $LaAlO_3/SrTiO_3(001)$

R. Pentcheva, R. Arras, K. Otte, V. G. Ruiz and W. E. Pickett

Phil. Trans. R. Soc. A 2012 **370**, doi: 10.1098/rsta.2012.0202, published 17 September 2012

PHILOSOPHICAL TRANSACTIONS OF THE ROYAL SOCIETY A

CrossMark click for updates

Phil. Trans. R. Soc. A (2012) **370**, 4904–4926
doi:10.1098/rsta.2012.0202

Review

Termination control of electronic phases in oxide thin films and interfaces: $LaAlO_3/SrTiO_3(001)$

By R. Pentcheva[1,*], R. Arras[1], K. Otte[1], V. G. Ruiz[1] and W. E. Pickett[2]

[1]*Department of Earth and Environmental Sciences, Section Crystallography and Center of Nanoscience, University of Munich, Theresienstrasse 41, 80333 Munich, Germany*
[2]*Department of Physics, University of California, Davis, One Shields Avenue, Davis, CA 95616, USA*

A wealth of intriguing properties emerge in the seemingly simple system composed of the band insulators $LaAlO_3$ and $SrTiO_3$ such as a two-dimensional electron gas, superconductivity and magnetism. In this paper, we review the current insight obtained from first principles calculations on the mechanisms governing the behaviour of thin $LaAlO_3$ films on $SrTiO_3(001)$. In particular, we explore the strong dependence of the electronic properties on the surface and interface termination, the finite film thickness, lattice polarization and defects. A further aspect that is addressed is how the electronic behaviour and functionality can be tuned by an $SrTiO_3$ capping layer, adsorbates and metallic contacts. Lastly, we discuss recent reports on the coexistence of magnetism and superconductivity in this system for what they might imply about the electronic structure of this system.

Keywords: oxide interfaces; density functional theory; magnetic thin oxide films; metal–insulator transition; metal-insulator contacts; Schottky barrier

1. Introduction

The advance of thin-film growth techniques such as pulsed laser deposition (PLD) and molecular beam epitaxy allows the fabrication of single terminated oxide interfaces on the atomic scale. Understanding the novel phenomena arising in these artificial materials is not only of fundamental interest, but is also relevant for the development of future electronics and spintronics devices. A system that has attracted most of the interest so far is composed of the simple band insulators $LaAlO_3$ (LAO) and $SrTiO_3$ (STO), where a two-dimensional electron gas (2DEG) [1], superconductivity [2], magnetism [3] and even signatures of their coexistence [4–6] have been reported. A further feature of interest and potential importance is that the electronic properties can be tuned by the LAO thickness,

*Author for correspondence (rossitza.pentcheva@lrz.uni-muenchen.de).

One contribution of 10 to a Discussion Meeting Issue ‘The new science of oxide interfaces’.

and the system undergoes a transition from insulating to conducting behaviour at around four monolayers (ML) LAO [7]. This insulator–metal transition (IMT) can be controlled reversibly via an electric field, e.g. by an atomic force microscope (AFM) tip [8–10], and several electronic devices based on this feature have been proposed [11,12]. The electronic properties can be further tuned by an additional STO capping layer that triggers the IMT already at 2 ML, thereby stabilizing an electron–hole bilayer [13]. The electronic properties show a strong dependence on the growth conditions: varying the oxygen partial pressure in the PLD chamber from 10^{-6} to 10^{-3} mbar induces an increase in sheet resistance by seven orders of magnitude [3]. This enormous change implies that oxygen defects play a controlling role during low-pressure growth.

Extensive theoretical and experimental efforts aim at explaining the origin of these interfacial phenomena. A central feature is the polar discontinuity that emerges at the interface: in the (001) direction, LAO consists of charged $(LaO)^+$ and $(AlO_2)^-$ planes, while in STO, formally neutral $(SrO)^0$ and $(TiO_2)^0$ planes alternate. Because both cations change across the interface, two distinct interfaces can be realized: an electron-doped n-type with an LaO layer next to a TiO_2 layer and a hole-doped p-type interface with an SrO and AlO_2 next to each other. Assuming formal ionic charges, the electrostatic potential produced by an infinite stack of charged planes would grow without bounds, a phenomenon known as the *polar catastrophe* [14,15]. This polar catastrophe cannot of course actually occur, and it may be avoided in several ways: a mechanism also common to semiconductors is an *atomic reconstruction* via introduction of defects or adsorbates. In transition metal oxides, electronic degrees of freedom may lead to an alternative compensation mechanism, i.e. an *electronic reconstruction*. The latter can give rise to exotic electronic states—for example, the observed 2D conductivity in LAO/STO, charge/spin/orbital order, excitonic or superconducting phases. A further question that arises is whether a thin film of LAO with only a few layers approaches the regime of the *polar catastrophe*. Sorting out the many possibilities is challenging owing to the strong dependence on growth method and conditions.

In this paper, we review the progress made so far in understanding the mechanisms that determine the electronic behaviour of LAO/STO(001) based on density functional theory (DFT) calculations. For further reviews on the experimental and theoretical work, the reader is referred to Pauli *et al.* [16], Huijben *et al.* [17], Pentcheva & Pickett [18], Chen *et al.* [19] and Zubko *et al.* [20]. In particular, we address finite size effects and the role of electrostatic boundary conditions [21] in thin LAO films on STO(001). We first discuss intrinsic mechanisms that arise at defect-free n- and p-type interfaces providing a possible explanation for the thickness-dependent IMT. Moreover, we explore the effect of the surface termination on the band diagram. In §§3 and 5, we address the role of an STO capping layer and a metallic electrode. A controversially discussed issue is the presence of an internal potential build-up within the LAO film, as predicted by DFT calculations on LAO/STO(001) with abrupt interfaces. While recent AFM experiments provide evidence for such an internal field in terms of a polarity-dependent asymmetry of the signal [22], X-ray photoemission studies [23–25] have not been able to detect shifts or broadening of core-level spectra that would reflect an internal electric field. This discrepancy implies that besides the electronic reconstruction, extrinsic effects play a role, e.g. oxygen defects [26,27],

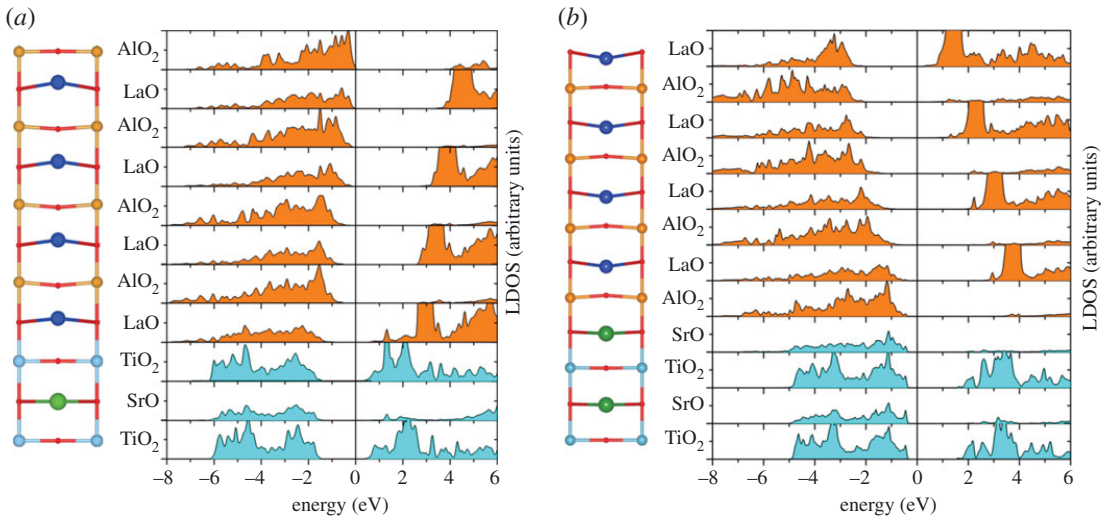

Figure 1. Side view of the relaxed structure and layer-resolved density of states (LDOS) of 4LAO/STO(001) with an (*a*) n-type and (*b*) p-type interface. Note the emergence of a potential build-up and a lattice polarization within the LAO film of opposite sign for the n- and p-type interface. (Online version in colour.)

adsorbates such as water or hydrogen [28] or cation disorder [29,30]. An overview of the current theoretical understanding of the role of such extrinsic mechanisms is provided in §4. Finally, in §6, we address recent reports on the coexistence of superconductivity and ferromagnetism in LAO/STO—a phenomenon that may be helpful in understanding the underlying electronic structure in these nanoscale systems.

2. Polar oxide films on a nonpolar substrate: $LaAlO_3/SrTiO_3(001)$

An intriguing experimental finding in LAO/STO(001) is the thickness-dependent IMT in thin LAO films on STO(001) [7]. DFT calculations demonstrate that an internal electric field emerges in thin polar LAO overlayers on STO(001) [18,31–33]. As shown in the layer-resolved density of states (LDOS) of a 4 ML LAO film on STO(001) with an n-type interface (figure 1*a*), this is expressed in an upward shift of the O 2p bands as they get closer to the surface. Interestingly, a large electric field of opposite sign arises in an analogous manner in a defect-free 4 ML LAO/STO(001) overlayer with a p-type interface (figure 1*b*). The internal electric field of the polar LAO film is screened to a large degree (but not completely) by a strong lattice polarization. As can be seen from the side view of the relaxed structure in figure 1*a* and the anion–cation buckling displayed in figure 2, for an n-type interface, this lattice polarization is characterized by a strong outward shift of La by 0.2–0.3 Å and buckling in the subsurface AlO_2 layers, while the surface layer shows similar relaxations for anions and cations. Experimental evidence for an internal electric field within the LAO film seems contradictory. Segal *et al.* [23] and Chambers *et al.* [25] found no evidence for the expected core-level shifts due to an internal field. However, evidence for a lattice polarization as a response to an internal electric field has been obtained from

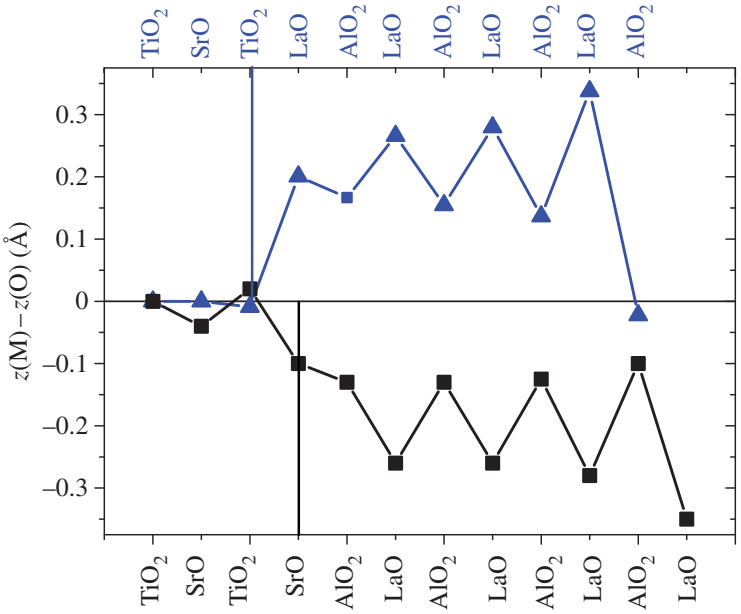

Figure 2. Oxygen–cation buckling in 4LAO/STO(001) with an n- (triangles) and a p-type interface (squares). As already shown in the side view in figure 1, the lattice polarization has an opposite sign for the n- and p-type interfaces. (Online version in colour.)

surface X-ray diffraction (SXRD) by Pauli *et al.* [34]. The latter study detected also a dependence of the lattice response on the LAO thickness with a maximum buckling in a 2 ML LAO film. This indicates possibly a stronger role of cation interdiffusion or higher affinity for adsorbates in the thicker films. Such extrinsic mechanisms can reduce the internal potential and thereby the lattice polarization (see discussion in §4).

The lattice relaxation has a crucial effect on the electronic properties: if the atoms are fixed at their ideal bulk positions, all systems are metallic [32]. The lattice polarization in the relaxed system allows several layers of LAO to remain insulating with a band gap of 1.7 eV for 1 ML LAO/STO(001) and a gradual decrease by ~ 0.4 eV per added LAO ML. Finally, at around 5 ML of LAO, an electronic reconstruction takes place. However, the closing of the band gap is *indirect* in real space, as it is due to the overlap of the valence band defined by the O 2p band in the surface layer and the conduction band marked by Ti 3d states at the interface. Consequently, the carrier density is much lower than the one expected if 0.5e were transferred to the interface. Furthermore, the results suggest carriers of two different types: electrons at the interface and holes in the surface layer. We will return to the possibility of excitonic effects later when discussing the role of an STO capping layer in §3.

For a defect-free 4LAO/STO(001) with a p-type interface, the ionic relaxations are of similar magnitude but of opposite sign (note the inward relaxation of the La ions and the anion cation buckling shown in figure 2). A very similar thickness-dependent insulator-to-metal transition is expected, which involves different states: La 5d states in the surface LaO layer and O 2p states at the interface. In experiments, the p-type interface has been found so far insulating [1] and has therefore attracted much less attention. The analysis of O K-edge spectra

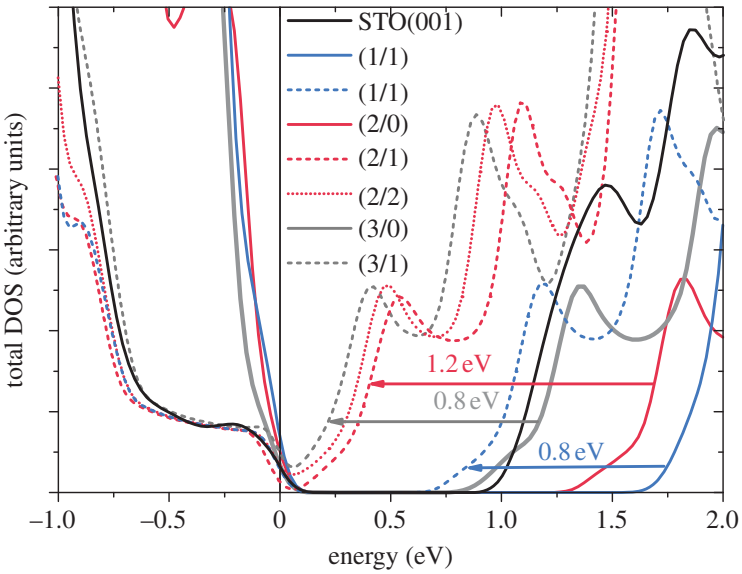

Figure 3. Total density of states (DOS) nLAO/STO(001), capped by m STO layers. Note that the band gap closes for $n > 2$ ML as soon as a capping STO layer is added. Thereby, the effect of the first STO layer is most pronounced. (Online version in colour.)

by Nakagawa *et al.* [35] suggested that compensation takes place via oxygen vacancies, that is, by atomic reconstruction. Still, the results above and those by Ishibashi & Terakura [31] show that provided defect-free LAO/STO interfaces with a p-type interface can be realized, they would exhibit just as interesting thickness-dependent properties as the ones for the n-type interface.

So far, we have considered stoichiometric 4 ML LAO films on STO(001), where, e.g. for an n-type interface, the LAO film is terminated by an AlO_2 surface layer. Pavlenko & Kopp [36] recently investigated LAO/STO(001) with an n-type interface and an LaO surface termination. Note that, here, both the surface and the interface are electron doped. Not surprisingly, the system is found to be metallic for 2.5 and 3.5 ML LAO with finite occupation of Ti $3d_{xy}$ states in the interface layer and La $5d_{x^2-y^2}$ states in the surface layer. The authors interpreted the surface La 5d occupation as a result of surface tensile stress. While the latter influences, e.g. the vertical relaxation of ions, the polarity discontinuity at the surface and interface is likely to be the dominating effect.

3. Influence of an $SrTiO_3$ capping layer

In contrast to the sharp IMT in LAO films on STO, Huijben *et al.* [37] observed a much smoother transition from insulating to conducting behaviour that starts already at 2 ML LAO if the latter is covered by a non-polar STO layer. The total DOS of n ML LAO/STO(001) covered by m layers of STO [denoted in the following as (n/m)] is displayed in figure 3. The DFT results reveal that for $n = 2$ ML, already a single STO capping layer leads to an IMT. Increasing the number of STO capping layers m or LAO layers n enhances the DOS at the Fermi level, but the first STO capping layer has the most dramatic effect, reducing the band gap by ~ 1.0 eV.

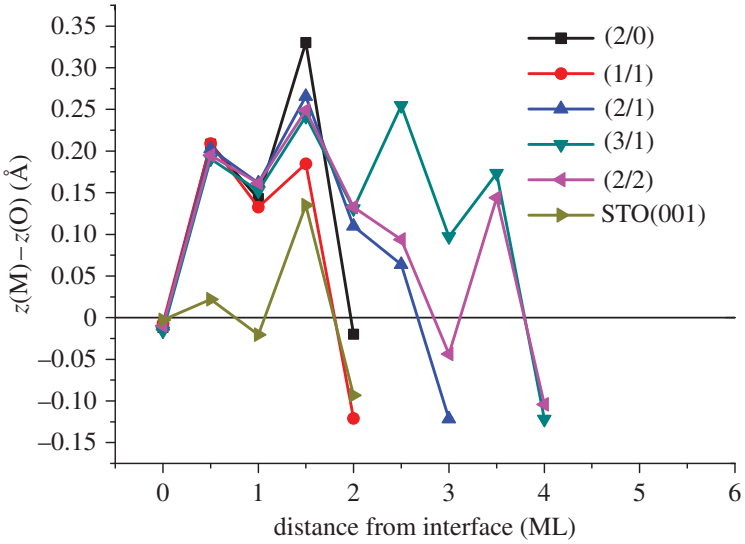

Figure 4. Cation–anion vertical buckling in mSTO/nLAO/STO(001) and at the STO(001) surface for comparison. (Online version in colour.)

In order to gain more insights into the mechanism of closing of the gap, we analyse first the lattice relaxations. Figure 4 shows the cation–anion displacements in mSTO/nLAO/STO(001). We observe slight reduction in the buckling within the LAO film compared with the (2/0) system and a polarization within the STO layer. The relaxation pattern in the STO capping layer is in fact similar to the one of the STO(001) surface [38] (for comparison, the relaxations at an STO(001) surface are added to figure 4). However, the total contribution of the STO capping layer is small as the ionic dipole moments of the SrO and TiO_2 layers are of opposite sign (negative dipole moment in the surface TiO_2 layer and a positive one in the subsurface SrO layer) and nearly cancel. The results show that the ionic contribution to the dipole moment in mSTO/nLAO/STO(001) scales with the number n of LAO layers and increases roughly by 1 eÅ per added LAO layer.

The impact of the STO capping layer turns out to be of electronic origin: Figure 5 shows the LDOS of (2/0) (dashed line) and (2/1) (solid line) lines aligned at the bottom of the Ti 3d band at the interface. In both the capped and the uncapped system, the O 2p bands within the LAO film exhibit a gradual upward shift of 0.4 eV per LAO as they approach the surface. In the capped system, there is an additional strong shift/broadening of the O 2p band in the surface TiO_2 layer of $\sim$0.8 eV that closes the band gap and induces an electronic reconstruction [13].

Indeed, the band structure in figure 6*b* shows that, once the STO capping layer is added, a dispersive O 2p surface band appears similar to a surface state in STO(001) [38,39]. This band extends 0.8 eV above the subsurface O 2p band and marks the top of the valence band at the M point of the Brillouin zone. On the other hand, the bottom of the conduction band lies at the Γ point and is determined by Ti 3d states in the interface layer. Thus, the closing of the band gap is indirect in both real and reciprocal space. Increasing the number of LAO and STO capping layers enhances the overlap of the valence and conduction bands at the Fermi level.

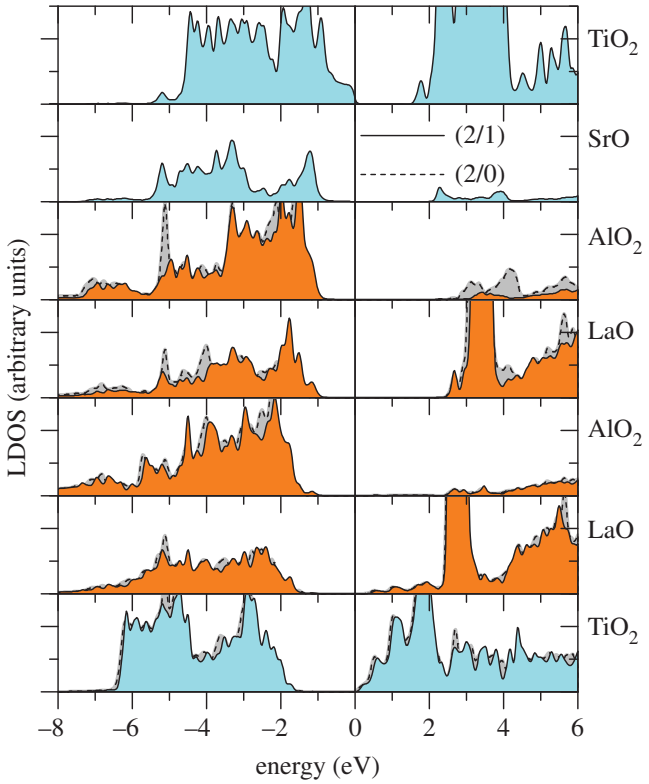

Figure 5. Layer-resolved density of states (LDOS) of 2LAO/STO(001) with (solid line) and without (dashed line) a single STO capping layer. A dispersive O 2p band in the surface TiO_2 layer leads to a closing of the band gap in the capped system [13]. (Online version in colour.)

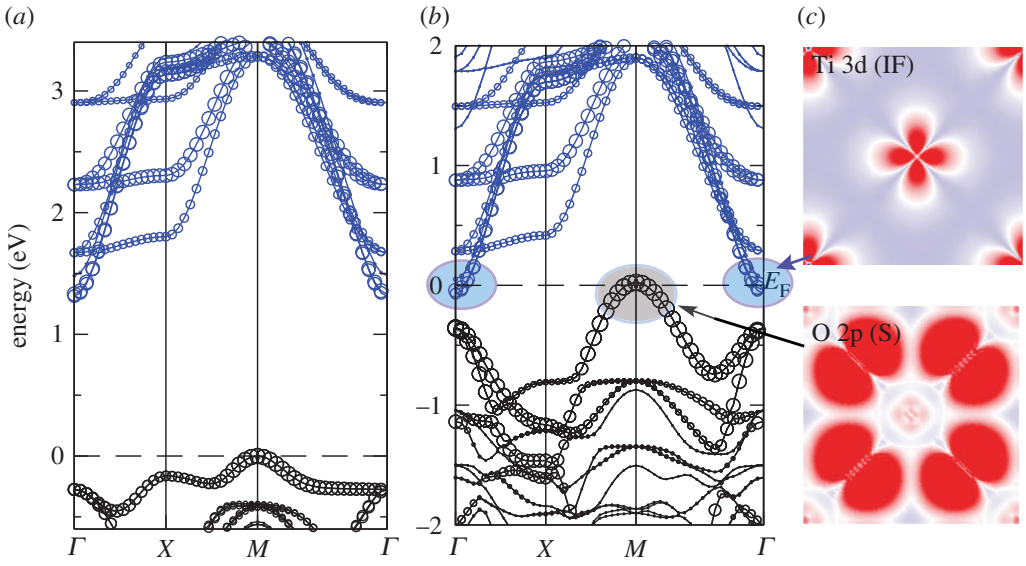

Figure 6. Band structure of (*a*) 2LAO/STO(001) with an indirect band gap and (*b*) 2STO/2LAO/STO(001) with a closed band gap due to the overlap of an electron band at Γ and a holes band at M; (*c*) integrated electron density around the Fermi level shows electrons of Ti $3d_{xy}$ character at the interface (IF) at Γ and holes of O $2p_\pi$ type at the surface (S) M. Adapted from Pentcheva *et al.* [13]. (Online version in colour.)

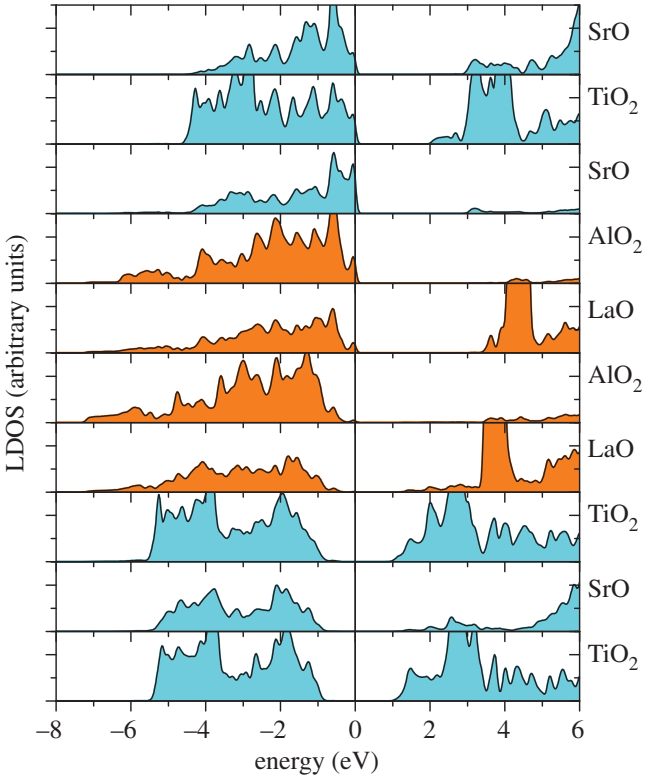

Figure 7. Layer-resolved density of states (LDOS) of an SrO terminated 1.5 ML STO/2LAO/STO(001), showing insulating behaviour. (Online version in colour.)

The electron density distribution in 2STO/2LAO/STO(001) integrated between −0.3 and 0 eV shows electrons of Ti $3d_{xy}$ character in the interface layer and holes in the O $2p_{\pi}$ bands at the surface. From the curvature of the electron and hole bands at the Γ and M points, we determine a significantly higher effective mass of the holes ($1.4\,m_e/1.2\,m_e$ in the uncapped/capped system, respectively) than for the lighter electrons ($0.4\,m_e$). The presence of two types of carriers with different mobilities is confirmed in Hall and magnetoresistance measurements [13], where the data between 0 and 100 K can be fitted only by using a two-band model with one hole and one electron band. Photoemission experiments give further evidence for the presence of holes in the surface layer [13]. Thus, the presence of a non-polar oxide capping layer seems to stabilize the system with respect to surface defects and adsorbates that are likely to eliminate holes in the uncapped systems.

In contrast, when the system is terminated by an SrO layer (using a 1.5 ML STO overlayer), the LDOS in figure 7 shows that the band gap of ∼1 eV of the uncapped (2/0) system is preserved. The reduction of the band gap is solely due to the potential build-up within the LAO film, while the valence band (VB) of the STO capping layer aligns with the VB in the top AlO_2 layer without the surface state characteristic of the TiO_2-terminated capping layer. This system exhibits a behaviour that is closer to what one would expect when adding a 'non-polar' oxide overlayer on top of LAO/STO(001).

4. Role of lattice defects and adsorbates

(a) Cationic intermixing

The systems considered so far contained abrupt interfaces. However, several studies suggest significant cation intermixing at the interface [29,30,34]. Intermixing has been discussed as an alternative mechanism to the electronic reconstruction to compensate polarity, but the role of intermixing in cancelling the potential divergence is questioned [40]. Qiao *et al.* [30] proposed as main sources of defects the deviations from a 1:1 La:Sr ratio due to strong angular dependence during the PLD process, Sr vacancy formation and La interdiffusion into the STO substrate. They investigated La→Sr and Al→Ti substitution both near and far from the interface, using up to 4 ML LAO on a 6 ML thick STO substrate in a $c(2 \times 2)$ lateral unit cell. The DFT results indicate that coupled La–Sr, Al–Ti exchange processes involving both the surface and interface region lower the energy of the system, and the energy gain is dependent on the LAO thickness, being ~ 1.0 eV for $n = 3$ LAO and ~ 1.6 eV for $n = 4$ LAO layers, respectively. A comparison of the calculated and measured valence band offset was used as a further criterion to prove the presence of intermixing.

Pauli *et al.* [34] performed SXRD experiments, and DFT calculations on films with thickness between 2 and 5 ML LAO. The experimental data indicated an 80% filling of the surface layer with 20% of a layer on top of that. Futhermore, the results were consistent with cation intermixing exceeding 5% throughout 3 ML around the interface layer. In contrast to the study of Qiao *et al.* [30], DFT calculations on abrupt and intermixed interfaces did not show significant differences in electronic behaviour.

(b) Oxygen defects

As mentioned in the introduction, a number of experimental studies have shown the strong influence of the oxygen partial pressure during deposition or post-deposition annealing on the transport properties. Despite its importance, there are only a few studies that have addressed the role of oxygen vacancies. Cen *et al.* [8] considered a 3 ML LAO/STO(001) with a vacancy in the surface AlO_2 layer and found a dramatic difference in the electronic properties with reduction/cancellation of the electric field within the LAO film and an accumulation of carriers at the interface, in contrast to the insulating defect-free 3 ML LAO/STO(001). Chen *et al.* [41] modelled LAO/STO superlattices with a p-type interface and observed that oxygen vacancies are repelled from the interface towards bulk STO. On the other hand, Zhong *et al.* [26] studied oxygen vacancies in an $(LAO)_m/(STO)_m$ superlattice with alternating n- and p-type interfaces. In contrast to Chen *et al.* [41], they found that the formation energy of vacancies is lowest at the p-type interface and ~ 2 eV higher at the n-type interface with a nonlinear dependence in between. Furthermore, the vacancy formation tends to be more favourable in BO_2 layers than in AO layers of the perovskite ABO_3 lattice. The formation energy at the p-type interface becomes negative with respect to the one in the STO bulk at a critical thickness $m = 3$–4 ML. The electrons released by the vacancy are transferred to the conduction band minimum at the n-type interface (which now moves below the Fermi level with a significant orbital polarization in the interface and more distant TiO_2 layers), while the

p-type interface is insulating. This result implies separation between regions where impurity scattering takes place and regions of enhanced carrier density. The authors also observed that the vacancy formation reduces the core-level shifts within the superlattice and proposed this as a possible explanation of the lacking broadening in X-ray photoemission measurements [23–25].

Zhang *et al.* [42] studied the formation of vacancies in thin LAO overlayers on STO(001) using an asymmetric setup with dipole correction, and varied the position of the vacancies within the LAO film. Note that only the Γ point was used for integration within the Brillouin zone. In systems with a p-type interface, vacancies are formed preferentially at the interface, thereby compensating the valence discontinuity and leaving the system insulating. In contrast, for systems with an n-type interface, the formation energy was significantly higher. Furthermore, vacancies tend to be formed rather in the surface LAO layer than at the interface. This has two consequences: it compensates the p-type surface AlO_2 layer and enhances the carrier density at the interface. On the basis of a phenomenological electrostatic model, Bristowe *et al.* [27] showed that there is a critical thickness for surface vacancy formation, in agreement with DFT calculations [43]. Furthermore, they proposed that surface defects generate a trapping potential for carriers whose strength depends on the LAO-film thickness.

DFT calculations [44] introducing an oxygen vacancy in the interface TiO_2 layer within a 2×1 lateral unit cell indicate spin polarization of the carriers in the Ti 3d band, and propose this as a possible explanation of the recently reported coexistence of ferromagnetism and superconductivity in the LAO/STO(001) system (see also discussion in §6). Further studies are necessary to explore lower concentrations of vacancies and other thermodynamically more stable sites for the vacancy (e.g. in the surface AlO_2 layer).

(*c*) *H adsorption*

In most of the experiments so far, the samples are exposed to air; thus, the interfacial properties can be significantly affected by adsorbates. These are considered as a possible origin of reversible writing and erasing of conducting regions on LAO/STO(001) by an AFM tip [8]. Son *et al.* [33] investigated the H adsorption using DFT and the generalized gradient approximation (GGA) [45]. They found that the adsorption energy increases with LAO thickness and that beyond a critical thickness of ~ 5 ML, the energy gain exceeds the energy needed for H_2 or H_2O dissociative adsorption. An interesting feature is the planar adsorption geometry with the H–O bond being nearly parallel to the surface reflecting a maximized overlap between the H 1s orbitals and the planar O $2p_\pi$ states. H is found to donate electrons to the STO conduction band. Furthermore, the size and sign of the internal potential build-up can be tuned by the H concentration on the surface, e.g. the latter is exactly cancelled for a (2×1) surface unit cell (this coverage corresponds to 0.5e transfer per (1×1) lateral unit cell). The impact of H adsorption bears strong parallels to the influence of a metallic contact layer on the interfacial properties that is discussed in the next section. The influence of further adsorbates such as water has not been considered so far, but needs to be addressed in order to obtain a comprehensive picture of all effects that may determine the properties of LAO/STO(001).

5. Impact of metallic contacts on the electronic properties of $LaAlO_3/SrTiO_3(001)(001)$

In §§3 and 4, we have seen that the presence of a non-polar oxide overlayer or defects can significantly alter the electronic properties of the LAO/STO system. For device applications, metallic overlayers are important, and several experimental studies have used setups with metallic contacts on LAO/STO(001) [10,46,47]. The coupling between metallic thin films and semiconductors or ferroelectric oxides have been widely studied [48–52]. In order to gain understanding of the impact of metallic contacts on the electronic behaviour of an oxide interface, we have recently performed DFT calculations on a series of metal electrodes on LAO/STO(001) [53]. Here, we discuss how the electronic properties can be influenced by the metallic contact.

All the calculations presented in this section have been performed with the full potential linearized augmented plane wave method in the WIEN2K implementation [54] using the GGA [45]. We have also explored the influence of an on-site Coulomb repulsion parameter (local density approximation/GGA + U method [55]) with $U = 5\,\mathrm{eV}$ and $J = 1\,\mathrm{eV}$ for the Ti 3d orbitals, and $U = 7\,\mathrm{eV}$ for the La 4f orbitals. The irreducible part of the Brillouin zone was sampled with 21 k-points. The systems were modelled by a symmetric slab, with a 2 and 4 ML LAO film on a TiO_2-terminated STO substrate with a lateral lattice parameter set to the GGA value of bulk STO (3.92 Å). The influence of the substrate thickness was probed by using a system with a thin (2.5 ML) and thick (6.5 ML) STO slab. The metal atoms were adsorbed on top of the oxygen atoms in the top AlO_2 layer. These sites were found to be energetically favourable in previous studies of metallic overlayers on LAO(001) [56] and for other transition metal/perovskite oxide interfaces [57–59]. Further metallic layers are deposited, assuming a face-centred cubic stacking of the layers. A vacuum of at least 10 Å was used to separate the supercell from its periodic images and avoid spurious interactions. The atomic positions were relaxed within tetragonal symmetry. A side view of the relaxed systems with an Al (1 ML), Ti (1 and 2 ML) and Pt (1 ML) overlayer is shown in figure 8.

As discussed in §2, in the nLAO/STO(001) system, a central feature is the upward shift of the O 2p bands within the polar LAO film. The LDOS of Al, Ti and Pt contact layers on top of 2 ML LAO/STO(001) are shown in figure 9. Upon adsorption of an Al or Ti overlayer, this potential build-up is largely cancelled. In contrast, for Pt, there is a non-vanishing shift of the unoccupied La 4f and 5d bands. In all cases, both the surface contact layer and the interface (IF) layer are metallic with a significant occupation of the Ti 3d band at the interface and a decreasing occupation in deeper layers.

As can be seen from the band structure in figure 10, multiple bands contribute to conductivity: the lowest lying bands at the interface are of Ti $3d_{xy}$ character, in the IF-1 layer all t_{2g} states contribute, while in deeper layers d_{xz}, d_{yz} bands lie lowest in energy. The d_{xy} bands have a strong dispersion along $M-\Gamma-X$, whereas d_{xz} and d_{yz} are heavier along $\Gamma-X$. This difference in velocities (masses) suggests different mobilities of the carriers. Further bands between E_F and $E_F - 2.0\,\mathrm{eV}$ stem from the surface metallic layer. We observe that the occupation of Ti 3d bands at the interface depends strongly on the type of metal contact on the

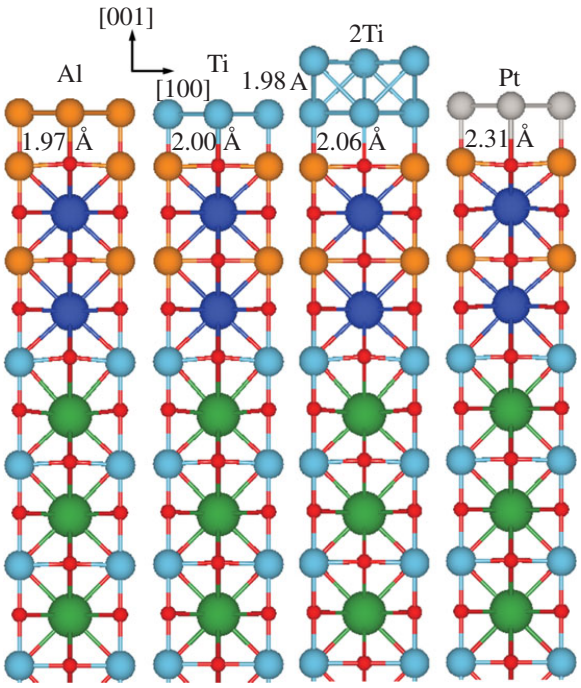

Figure 8. Side view of the relaxed structures for M/LAO/STO systems (M = Al, Ti, 2Ti and Pt). Only half of our symmetric slab is shown. M–O bond lengths near the surface increase from Al to Pt. In contrast, the buckling in the interface TiO_2 layer decreases. (Online version in colour.)

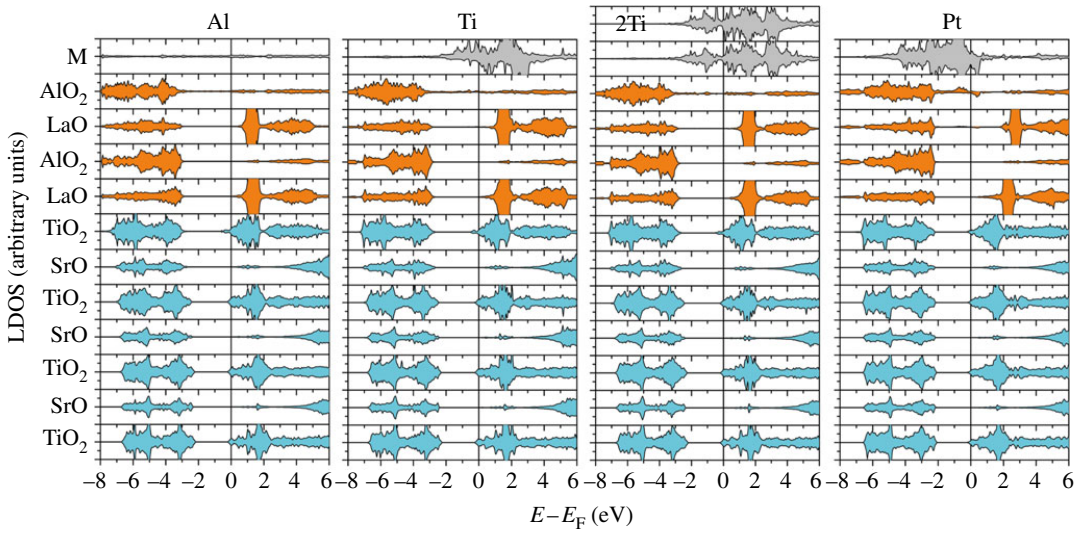

Figure 9. Layer-resolved density of states (LDOS) for 2 ML LAO/STO(001) with Al (1 ML), Ti (1 and 2 ML) and Pt (1 ML). The internal electric field, observed in the uncovered films, is cancelled for an Al and Ti contact. A residual field is obtained for a Pt electrode. (Online version in colour.)

surface: for an Al, Ti and Pt overlayer, the band edge is 0.65, 0.5 and 0.25 eV below the Fermi level at Γ.

Further insights into the influence of the contact layer on the structural and electronic properties of LAO/STO(001) can be obtained from figure 11. The buckling within the layers expressed as a relative shift of anion and cation

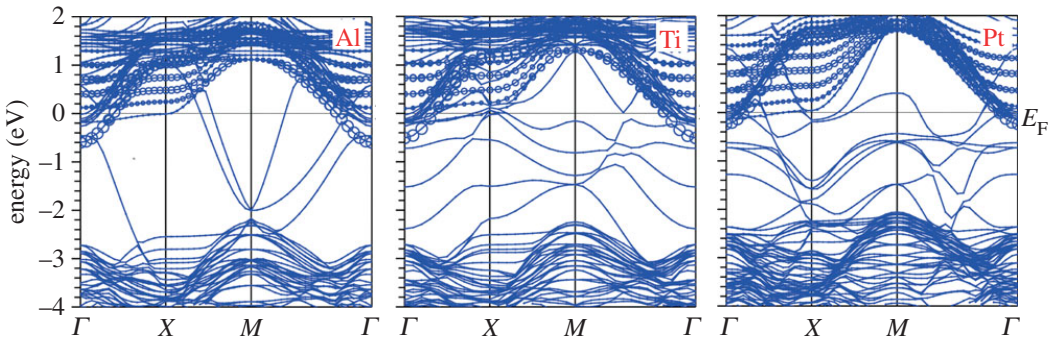

Figure 10. Majority spin band structures for M/LAO/STO systems (M = Al, Ti and Pt). The contribution of Ti 3d states from the interface TiO_2 layer is marked by circles. (Online version in colour.)

z-coordinate in figure 11 differs significantly compared with the systems without a metallic contact. As discussed in §2, in the uncovered LAO films on STO(001), the lattice polarization is confined to the LAO film where it plays a decisive role to counteract the divergence of the electric potential, while the buckling is negligible within the STO substrate (see lines with empty symbols). In contrast, after adsorbing the metallic overlayer, the potential build-up in LAO is largely cancelled and hence the anion–cation buckling is strongly reduced in size (Pt contact) and even changes sign (Al and Ti overlayer).

On the other hand, a notable polarization emerges within STO that is strongest at the interface and decays in deeper layers. The pattern is similar to the one in $LaTiO_3$/STO and LAO/STO superlattices with an n-type interface [60,61]. This lattice polarization in STO correlates directly with the occupation of Ti 3d bands (figure 11*b*), which is highest in the interface TiO_2 layer and decays in deeper layers. Concerning the chemical effects of the overlayer, the lattice polarization and band occupation at the interface are highest for the system with an Al overlayer, followed by Ti and lowest for a Pt overlayer. The position of O 1s level, which is a monitor of the local potential, shows a similar trend with the strongest binding energy in the interface TiO_2 layer for an Al contact layer. The strength in binding to the surface is reflected also in the M–O bond lengths, Al–O being the shortest (1.97 Å), followed by Ti–O (2.00 Å) and Pt–O being longest (2.31 Å) (see figure 8).

(*a*) *Dependence on the metallic contact thickness*

To investigate the dependence on the metallic contact thickness, we have varied the thickness of the Ti overlayer. The calculations for 2 ML Ti/2LAO/STO(001) show a similar occupation of the Ti 3d band at the interface but a stronger band bending in the deeper layers leading to a lower total number of electrons within STO. This correlates with a slightly larger distance between Ti in the contact layer and oxygen in the top AlO_2 layer of 2.00 Å versus 2.06 Å for 1 ML and 2 ML Ti/2LAO/STO(001), respectively.

(*b*) *Schottky barriers*

Another illuminating characteristic of the M/LAO/STO(001) system, important for understanding the variation of band lineups and in view of device

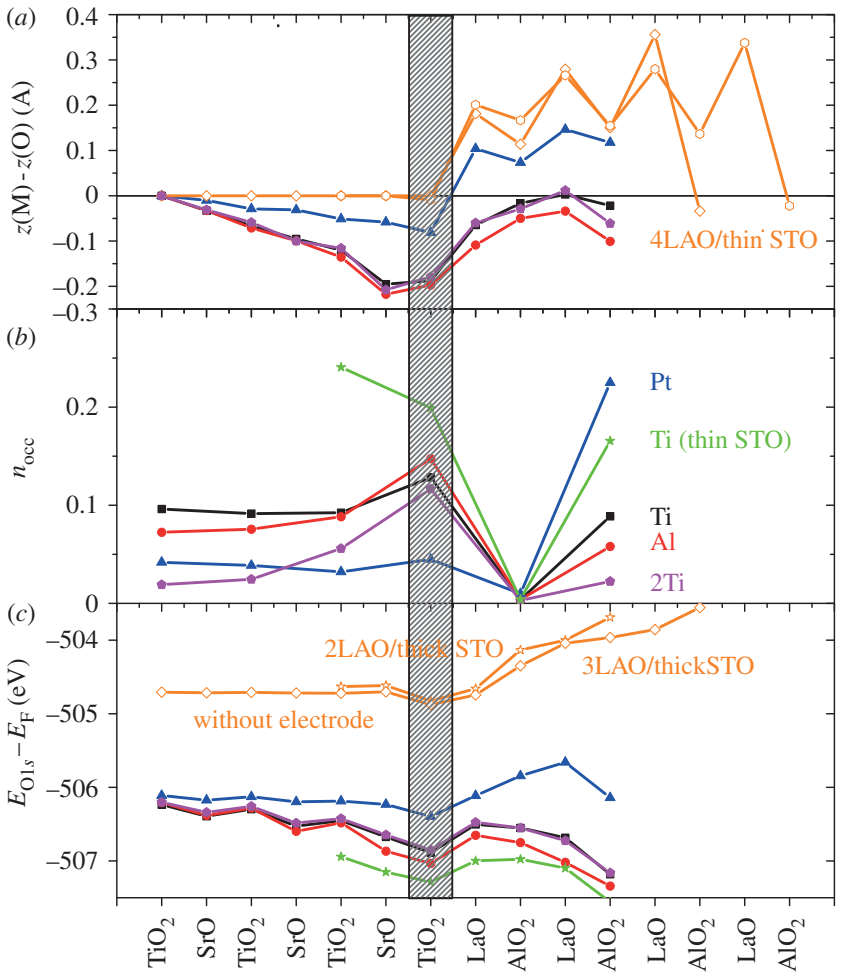

Figure 11. (*a*) Oxygen–cation buckling along the [001] direction. (*b*) Layer-resolved electron occupation integrated between $E_F - 0.65\,eV$ and E_F. Charge on the LaO and SrO layers is zero (not shown). (*c*) Positions of O 1s states with respect to E_F. Data for 1 ML Ti and thin/thick STO substrate is marked by stars/squares; 2 ML Ti (pentagons), as well as 1 ML Pt (triangles) and 1 ML Al (circles). Results for *n*LAO/STO(001) without a metallic overlayer are displayed with empty symbols (stars, diamonds and hexagons for $n = 2, 3, 4$ ML, respectively). (Online version in colour.)

applications, are the Schottky barrier heights (SBHs). As displayed in Table 1, these correlate with the strength of the chemical bond and, most importantly, with the work function: Al has the highest p-SBH (3.0 eV), followed by Ti (2.8 eV) and finally Pt (2.2 eV). As the well-known underestimation of band gaps within GGA is mostly related to the position of the conduction band minimum, the n-SBH tend to be too small. Taking the experimental band gap of LAO, the n-SBHs are 2.6 eV (Al), 2.8 eV (Ti) and 3.4 eV (Pt). The relevance of the chemical bonding between *M* and LAO/STO(001) is in line with previous findings for metal–oxide interfaces [62].

Figure 12 displays the schematic band diagrams of three distinct mechanisms of formation of a 2DEG in LAO/STO(001), STO/LAO/STO(001) and *M*/LAO/STO(001). For LAO/STO(001), a thickness-dependent IMT occurs as

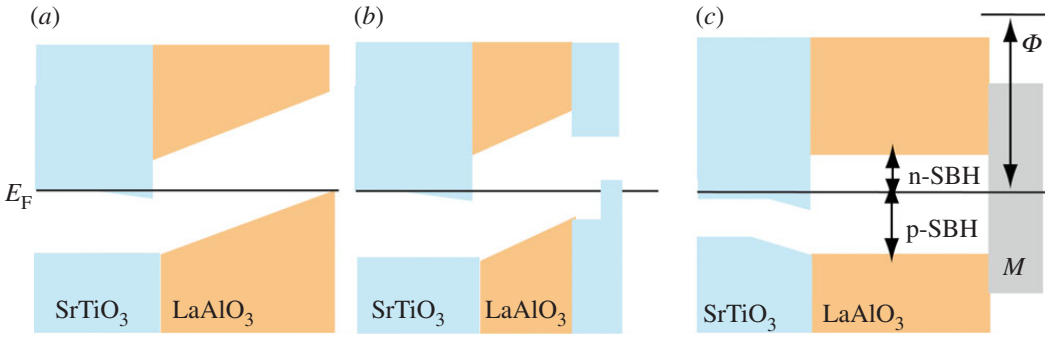

Figure 12. Schematic band diagram of (*a*) LAO/STO(001) at the verge of an electronic reconstruction at the critical LAO thickness; LAO/STO(001) covered by (*b*) an STO overlayer which leads to IMT already at 2 ML LAO and (*c*) a metallic contact layer (*M*). Note that the potential build-up that leads to an electronic reconstruction in (*a*) and (*b*) beyond a critical LAO thickness is eliminated in *M*/LAO/STO(001). (Online version in colour.)

Table 1. Calculated *M*–O bond lengths, Ti–O buckling (difference in *z*-coordinate between cations and oxygen) and Ti 3d band occupation in the interface layer, integrated between $E_F - 0.65$ eV and E_F. Work functions and Schottky barrier heights for the different contact overlayers are also displayed.

metallic layer	O–*M* distance (Å)	$z_{Ti} - z_O$ (IF) (Å)	n_{occ}	Φ (eV)	p-SBH (eV)
Al	1.97	−0.20	0.15	3.53	3.0
Ti	2.00	−0.19	0.13	4.05	2.8
2Ti	2.06	−0.18	0.11	4.05	2.8
Pt	2.31	−0.08	0.04	5.60	2.2

a result of the potential build-up within the LAO film, where the electronic reconstruction involves the formation of holes at the surface and electrons at the interface. In STO/LAO/STO(001) due to an additional surface state in the top TiO_2 layer, the IMT takes place at a much lower LAO critical thickness, leading to the formation of an electron–hole bilayer. In contrast, for *M*/LAO/STO(001) (*M* = Al, Ti), the potential in LAO is flat, regardless of the LAO or STO thickness. Simultaneously, a 2DEG with higher carrier density is formed at the interface. In the case of Pt (and other transition and noble metals, for more details see [53]), likely due to the weaker bonding and smaller charge transfer to the oxide layer, a residual slope within LAO is found, consistent with the recently measured potential build-up in Pt/LAO/STO(001) [47].

The evolution of the system due to deposition of the contact can be considered in several steps. Beginning with the internal field in 2 ML LAO/STO(001) [~ 0.8 eV potential rise], the metal layer is added and allowed to equilibrate with the outer LAO layer, determining the work function and the Schottky barrier (contact Fermi level with respect to the LAO band edges). On the basis of the final result shown in figure 9, the contact Fermi level would be ~ 1 eV above the STO conduction band minimum. Now, allowing exchange of charge with the interface—full self-consistency—electrons will flow from the contact layer to the

interface until the Fermi levels coincide. As charge is transferred, the internal field and accompanying ionic polarization decrease. The determining factor is the lineup of the surface and interface Fermi levels, which is accompanied by the (near-) disappearance of the electric field within the LAO slab. This charge transfer between the metal and the surface AlO_2 layer, leaving a slightly positive contact layer, will renormalize the work function of the metal and Schottky barrier somewhat. The self-consistent calculation gives only this final result, shown in figure 9.

(*c*) *Thin SrTiO$_3$ substrate: spin polarization*

While the results for M/LAO/STO(001) presented earlier were obtained using a 6.5 ML STO substrate, we have also performed calculations with a thin (2.5 ML) STO and observe there interesting confinement effects, which will be described later. As shown in figure 11*b*, a much higher Ti 3d band occupation is obtained at the interface for the thin STO substrate. However, the most prominent effect is a spin polarization of the 2DEG at the interface for the thin STO substrate. When adsorbing a single Ti layer, Ti displays a significant magnetic moment of $0.60\mu_B$ owing to the reduced coordination of the metal atom at the surface. We note that also a single Pt overlayer is spin polarized with $0.49\mu_B$ owing to polarization of the holes in the 5d shell. For a Ti overlayer, this effect induces a moment of 0.10 $(0.24)\mu_B$ at the Ti sites in IF (IF-1) layer. The values obtained within GGA + U, where effects of strong intra-atomic interaction are included, are enhanced: 0.20 $(0.30)\mu_B$ in IF (IF-1). Such polarization seems surprising because the interface and surface layers are separated by the insulating LAO slab, precluding (or vastly reducing) exchange coupling between the layers, but indeed the effect depends on the LAO spacer thickness. An increase in the width of the LAO layer reduces the influence of the contact layer: for a 4 ML thick LAO film, the spin polarization of the 2DEG decreases to $0.05/0.11\mu_B$ for IF/IF-1.

This spin polarization is a result of two effects. First, the fact that spin-up and spin-down Fermi levels at the surface and interface must be separately aligned (as well as with each other, finally). Second, a quantum confinement effect creates discrete bands, and a classical confinement effect leads to enhanced charge occupation at the IF and IF-1 layers.

As mentioned above, the magnetic moment of Ti in the surface contact layer is approximately $0.6\mu_B$ due to reduced coordination. This value decreases once the contact thickness is increased to 2 ML: the magnetic moment of the surface and subsurface Ti layer is reduced to $0.25\mu_B$ and $-0.05\mu_B$, respectively, owing to the enhanced Ti coordination. For other electrodes with lower surface magnetic moment, for example, 1 ML of Al (no magnetic moment) or 2 ML of Ti, the spin polarization of the 2DEG is quenched.

6. Broader functionalities of these interfacial systems

The range of unexpected phenomena that has been observed in these nanostructures has systematically been broadened by new discoveries. In the preceding sections, we have discussed how unusual properties, such as two-type carrier conduction or magnetism, may arise in these nanostructures. These theoretical studies are based, with a few exceptions, on atomically abrupt,

structurally ideal interfaces. It is understood that most (if not, all) samples are more complicated than this. We provide here an overview of the discoveries of magnetism at the interface, then of the reports of superconductivity and finally of the recent reports of coexistence of these two distinct, and usually strongly competing, types of long-range order. Understanding these phenomena will shed light on the underlying electronic structure at and near the interface. Specifically, several of these studies point out the importance of inhomogeneities in the samples, complications that should be kept in mind and will finally have to be taken into account. From the theorist's viewpoint, this emphasizes the importance of controlling defect concentration and distribution, to allow a closer connection of theory to experiment.

(*a*) *Hysteresis reflecting magnetic order*

Soon after the initial reports on conductivity in the LAO/STO system raised interest and research activity on this system, Brinkman *et al.* reported magnetic hysteresis in transport properties at the LAO/STO interface of PLD-deposited films [3]. This hysteresis, and an associated large negative magnetoresistance, reflects magnetic order arising at a few Kelvins and moves this oxide interface towards spintronics applications. Even prior to this study, the prospect of magnetism at this interface had been raised by Pentcheva & Pickett [63] in theoretical studies of LAO/STO superlattices with either n- or p-type interfaces. The question they faced at the time was this: at the polar LAO/STO interface, there is 0.5 carrier per interface cell too many (n-type) or too few (p-type) to fill bands. Therefore, the interface will be conducting unless other considerations come into play. For an n-type interface, it was demonstrated that correlation effects within GGA + U give rise to a charge and orbitally ordered state with magnetic moments of $0.7\mu_B$ at the Ti^{3+} sites. Later, Zhong & Kelly [64] investigated the effects of structural distortion beyond tetragonal symmetry and its impact on charge and spin ordering, finding an antiferromagnetic ground state. The relationship of the observed magnetism (due to Ti^{3+} local moments at the n-type interface) to the conduction by carriers remains to be clarified. We note that samples grown at high oxygen pressure, where the effect of oxygen vacancies is minimized, are nearly insulating with a sheet resistance that is seven orders of magnitude higher [3] than the initial samples studied by Ohtomo & Hwang [1]. On the other hand, the p-type interface had been found *always* to be non-conducting, independent of growth parameters. For a defect-free interface suggested by the initial reports, Pentcheva & Pickett proposed that correlation effects on the O 2p orbitals, resulting in charge order of oxygen holes with a magnetic moment $0.68\mu_B$, provided a plausible mechanism for insulating behaviour. While this is an interesting case of d^0-magnetism, the insulating behaviour of the p-type interface has been generally ascribed to O vacancies [35].

The possibility of magnetism at these interfaces was highlighted in *Physics Today* in 2007 [65], and remains an enigma. Magnetism was further discussed by Huijben *et al.* [17], who provided a broader overview of work on oxide interfaces up to that time. Subsequently, Seri & Klein [66] reported antisymmetric magnetoresistance at this interface, and noted magnetic-field-induced inhomogeneous magnetism, but did not characterize it as spontaneous ferromagnetism. Ariando *et al.* [67] detected dia-, ferro- and paramagnetic signals

interpreted in terms of phase separation. In particular, the ferromagnetic phase persisted beyond room temperature. Li *et al.* [6] reported magnetic effects persisting up to 200 K, which raises new questions, beginning with how such apparently weak magnetism can maintain spin order to such high temperatures.

(*b*) *Superconductivity*

The observation of superconductivity at the n-type interface by Reyren *et al.* [2] further enriched the variety of phenomena that have been reported. The superconducting state in PLD-grown samples at intermediate pressures (10^{-4} mbar) arose below 200 mK. Because bulk n-type STO superconducts in that range (up to 400 mK), one might initially question how new the phenomenon really is. The magnetic field directional dependence established that the superconductivity was highly two dimensional, and so in that manner, its behaviour is quite unlike that of bulk STO; as a 2D system, it is characterized by a 2D carrier concentration rather than a three-dimensional (3D) one. As with the magnetism, the degree of localization around the interface, and origin and character of the carriers, have become objects of scrutiny.

Subsequent reports by Caviglia *et al.* [68] and Ben Shalom *et al.* [69] confirmed superconductivity arising at this interfacial system. The latter report, where 15 unit cells of LAO were deposited with a pulsed laser and the carrier density was varied with gating, mapped out a portion of the phase diagram where T_c decreases as the carrier density increases. Kim *et al.* [70] studied, by Shubnikov-de Haas oscillations, the (presumably) related superconducting state in δ-doped STO films deposited by PLD. The doping by Nb (for Ti) was performed in a varying number of TiO_2 layers, and a 2D to 3D crossover in the superconducting state was monitored. This still very new topic of oxide interface superconductivity has been reviewed by Gariglio & Triscone [71]

(*c*) *Coexistence*

Historically, magnetism and superconductivity were mutual anathema, but the high-temperature superconductivity discovered in cuprates changed that. The latest big discovery in superconductivity, the Fe-based pnictides and chalcogenides also display magnetic phases next to superconducting ones. These, as well as some other materials classes such as heavy fermion metals [72], raise questions about possible connections between these ordered phases. In these examples, the magnetism is antiferromagnetism (or correlations). Superconductivity coexisting with *ferromagnetism* is very rare, having been reported only in the past decade or so in $RuSr_2GdCu_2O_8$ [73] and in the three uranium compounds UGe_2, URhGe and UCoGe. Aoki *et al.* have provided a recent overview summarizing several of the phenomena and some of the issues to account for observations [74]. There are several challenges to be overcome for superconductivity to arise in a ferromagnet (see discussion in Pickett *et al.* [75]): exchange splitting of up and down bands that disrupts pairing, magnetic field disruption of superconducting order, etc. In the following, we return briefly to some of these issues.

The first observation of coexistence by Dikin *et al.* [5] involved superconducting onsets around $T_c \approx 150$ mK on PLD films of 10 unit cells of LAO on TiO_2-terminated STO(001) substrates. They observed hysteresis in $T_c(H)$ curves

(H is the magnetic field) attributed to underlying ferromagnetic order. Their interpretation focuses on two parallel conduction channels: one consists of localized, magnetic states that are intrinsic to the interface (*viz.* Ti^{3+} moments, likely in the immediate interface region), while the other carriers are itinerant electrons contributed by defects (a likely candidate being oxygen vacancies). While previous reports indicated quenching of magnetism at a few Kelvin, Li *et al.* [6] report high-resolution magnetic torque magnetometry measurements, showing evidence of magnetic ('superparamagnetic-like') order up to 200 K. The superconducting signal in their samples arises below 120 mK.

Most recently, Bert *et al.* [4] provided a real space picture of their PLD grown films. They performed imaging with a scanning superconducting quantum interference device (SQUID) over $\sim 200\,\mu m$ square regions on samples of 10 ML LAO on STO(001) substrates. They report strong inhomogeneity, with sub-micron regions of ferromagnetism in a background of paramagnetic carriers that show a diamagnetic superconducting signal around 100 mK; thus, superconductivity and magnetism coexist in the sample, but not in the same region. For comparison, no magnetic dipoles were observed in a reference sample of δ-doped STO. From their transport and thermodynamic measurements, they infer that most of the intrinsic carriers ($4 \times 10^{14}\,cm^{-2}$ per interface cell for an atomically perfect interface) are localized because an order-of-magnitude fewer carriers contribute to the Hall conductivity.

Some early attempts to account for this coexistence have appeared [44,76,77]. The coexistence seems an even more delicate question here than in the ferromagnetic superconductors mentioned earlier. The ~ 200 mK critical temperature reflects a Bardeen–Cooper–Schrieffer gap of a few μeV, a truly tiny energy scale that appreciable exchange splitting of the bands would overwhelm. The critical magnetic field should be very small. There are aspects of the interfaces that suggest the means to avoid these pair breakers. The magnetic electrons and the superconducting carriers may reside in different bands, requiring a generalization of models applied to the previously known ferromagnetic superconductors. Inhomogeneity or phase separation may play a role, and coexistence in the same sample may not imply local coexistence (in the same region of the sample). The superconducting state may be inhomogeneous of the Fulde–Farrel–Larkin–Ovchinnikov type [78,79].

7. Summary

The LAO/STO system shows a remarkable spectrum of electronic phenomena, some of which seem to be understood and others require further study. We have provided an overview on the basis of DFT results addressing how the electrostatic boundary conditions determine charge (re-)distribution and the electronic state. A variety of parameters are identified (such as the surface and interface termination and stoichiometry, the presence of metallic or oxide overlayers, as well as defects and adsorbates) that enable tuning the electronic behaviour of this system. Understanding and controlling these parameters, and especially defects, dopants [80] and adsorbates, remain a challenging area that needs further attention in future theoretical and experimental studies.

We acknowledge financial support through the DFG SFB/TR80 (project C3) and grant h0721 for computational time at the Leibniz Computational Center Garching. V.G.R. acknowledges financial support from CONACYT (Mexico) and DAAD (Germany). W.E.P. was supported by U.S. Department of Energy grant no. DE-FG02-04ER46111.

References

1 Ohtomo, A. & Hwang, H. Y. 2004 A high-mobility electron gas at the $LaAlO_3/SrTiO_3$ heterointerface. *Nature* **427**, 423–426. (doi:10.1038/nature02308)
2 Reyren, N. *et al.* 2007 Superconducting interfaces between insulating oxides. *Science* **317**, 1196–1199. (doi:10.1126/science.1146006)
3 Brinkman, A. *et al.* 2007 Magnetic effects at the interface between non-magnetic oxides. *Nature Mater.* **6**, 493–496. (doi:10.1038/nmat1931)
4 Bert, J. A., Kalisky, B., Bell, C., Kim, M., Hikita, Y., Hwang, H. Y. & Moler, K. A. 2011 Direct imaging of the coexistence of ferromagnetism and superconductivity at the $LaAlO_3/SrTiO_3$ interface. *Nat. Phys.* **7**, 767–771. (doi:10.1038/nphys2079)
5 Dikin, D. A., Mehta, M., Bark, C. W., Folkman, C. M., Eom, C. B. & Chandrasekhar, V. 2011 Coexistence of superconductivity and ferromagnetism in two dimensions. *Phys. Rev. Lett.* **107**, 056802. (doi:10.1103/PhysRevLett.107.056802)
6 Li, L., Richter, C., Mannhart, J. & Ashoori, R. C. 2011 Coexistence of magnetic order and two-dimensional superconductivity at $LaAlO_3/SrTiO_3$ interfaces. *Nat. Phys.* **7**, 762–766. (doi:10.1038/nphys2080)
7 Thiel, S., Hammerl, G., Schmehl, A., Schneider, C. W. & Mannhart, J. 2006 Tunable quasi-two-dimensional electron gases in oxide heterostructures. *Science* **313**, 1942–1945. (doi:10.1126/science.1131091)
8 Cen, C., Thiel, S., Hammerl, G., Schneider, C. W., Andersen, K. E., Hellberg, C. S., Mannhart, J. & Levy, J. 2008 Nanoscale control of an interfacial metal-insulator transition at room temperature. *Nat. Mater.* **7**, 298–302. (doi:10.1038/nmat2136)
9 Bi, F., Bogorin, D. F., Cen, C., Bark, C. W., Park, J. W., Eom, C. B. & Levy, J. 2010 'Water-cycle' mechanism for writing and erasing nanostructures at the $LaAlO_3/SrTiO_3$ interface. *Appl. Phys. Lett.* **97**, 173110. (doi:10.1063/1.3506509)
10 Chen, Y. Z., Zhao, J. L., Sun, J. R., Pryds, N. & Shen, B. G. 2010 Resistance switching at the interface of $LaAlO_3/SrTiO_3$. *Appl. Phys. Lett.* **97**, 123102. (doi:10.1063/1.3490646)
11 Cen, C., Thiel, S., Mannhart, J. & Levy, J. 2009 Oxide nanoelectronics on demand. *Science* **323**, 1026–1030. (doi:10.1126/science.1168294)
12 Bogorin, D. F., Irvin, P., Cen, C. & Levy, J. 2010 $LaAlO_3/SrTiO_3$-based device concepts. (http://arxiv.org/abs/1011.5290)
13 Pentcheva, R. *et al.* 2010 Parallel electron-hole bilayer conductivity from electronic interface reconstruction. *Phys. Rev. Lett.* **104**, 166804. (doi:10.1103/PhysRevLett.104.166804)
14 Hwang, H. Y. 2006 Tuning interface states. *Science* **313**, 1895–1896. (doi:10.1126/science.1133138)
15 Goniakowski, J., Finocchi, F. & Noguera, C. 2008 Polarity of oxide surfaces and nanostructures. *Rep. Prog. Phys.* **71**, 016501. (doi:10.1088/0034-4885/71/1/016501)
16 Pauli, S. A. & Willmott, P. R. 2008 Conducting interfaces between polar and non-polar insulating perovskites. *J. Phys., Condens. Matter* **20**, 264012. (doi:10.1088/0953-8984/20/26/264012)
17 Huijben, M., Brinkman, A., Koster, G., Rijnders, G., Hilgenkamp, H. & Blank, D. H. A. 2009 Structure–property relation of $SrTiO_3/LaAlO_3$ interfaces. *Adv. Mater.* **21**, 1665–1677. (doi:10.1002/adma.200801448)
18 Pentcheva, R. & Pickett, W. E. 2010 Electronic phenomena at complex oxide interfaces: insights from first principles. *J. Phys., Condens. Matter* **22**, 043001. (doi:10.1088/0953-8984/22/4/043001)
19 Chen, H., Kolpak, A. M. & Ismail-Beigi, S. 2010 Electronic and magnetic properties of $SrTiO_3/LaAlO_3$ interfaces from first principles. *Adv. Mater.* **22**, 2881–2899. (doi:10.1002/adma.200903800)

20 Zubko, P., Gariglio, S., Gabay, M., Ghosez, P. & Triscone, J. M. 2011 Interface physics in complex oxide heterostructures. *Annu. Rev. Condens. Matter Phys.* **2**, 141–165. (doi:10.1146/annurev-conmatphys-062910-140445)

21 Stengel, M. 2011 First-principles modeling of electrostatically doped perovskite systems. *Phys. Rev. Lett.* **106**, 136803. (doi:10.1103/PhysRevLett.106.136803)

22 Xie, Y., Bell, C., Yajima, T., Hikita, Y. & Hwang, H. Y. 2010 Charge writing at the $LaAlO_3/SrTiO_3$ surface. *Nano Lett.* **10**, 2588–2591. (doi:10.1021/nl1012695)

23 Segal, Y., Ngai, J. H., Reiner, J. W., Walker, F. J. & Ahn, C. H. 2009 X-ray photoemission studies of the metal-insulator transition in $LaAlO_3/SrTiO_3$ structures grown by molecular beam epitaxy. *Phys. Rev. B* **80**, 241107. (doi:10.1103/PhysRevB.80.241107)

24 Sing, M. *et al.* 2009 Profiling the interface electron gas of $LaAlO_3/SrTiO_3$ heterostructures with hard X-ray photoelectron spectroscopy. *Phys. Rev. Lett.* **102**, 176805. (doi:10.1103/PhysRevLett.102.176805)

25 Chambers, S. *et al.* 2010 Instability, intermixing and electronic structure at the epitaxial heterojunction. *Surf. Sci. Rep.* **65**, 317–352. (doi:10.1016/j.surfrep.2010.09.001)

26 Zhong, Z., Xu, P. X. & Kelly, P. J. 2010 Polarity-induced oxygen vacancies at $LaAlO_3/SrTiO_3$ interfaces. *Phys. Rev. B* **82**, 165127. (doi:10.1103/PhysRevB.82.165127)

27 Bristowe, N. C., Littlewood, P. B. & Artacho, E. 2011 Surface defects and conduction in polar oxide heterostructures. *Phys. Rev. B* **83**, 205405. (doi:10.1103/PhysRevB.83.205405)

28 Son, W., Cho, E., Lee, J. & Han, S. 2010 Hydrogen adsorption and carrier generation in $LaAlO_3$–$SrTiO_3$ heterointerfaces: a first-principles study. *J. Phys., Condens. Matter* **22**, 315501. (doi:10.1088/0953-8984/22/31/315501)

29 Willmott, P. R. *et al.* 2007 Structural basis for the conducting interface between $LaAlO_3$ and $SrTiO_3$. *Phys. Rev. Lett.* **99**, 155502. (doi:10.1103/PhysRevLett.99.155502)

30 Qiao, L., Droubay, T. C., Shutthanandan, V., Zhu, Z., Sushko, P. V. & Chambers, S. A. 2010 Thermodynamic instability at the stoichiometric $LaAlO_3/SrTiO_3$(001) interface. *J. Phys., Condens. Matter* **22**, 312201. (doi:10.1088/0953-8984/22/31/312201)

31 Ishibashi, S. & Terakura, K. 2008 Analysis of screening mechanisms for polar discontinuity for $LaAlO_3/SrTiO_3$ thin films based on *ab initio* calculations. *J. Phys. Soc. Jpn.* **77**, 104706. (doi:10.1143/JPSJ.77.104706)

32 Pentcheva, R. & Pickett, W. E. 2009 Avoiding the polarization catastrophe in $LaAlO_3$ overlayers on $SrTiO_3$(001) through polar distortion. *Phys. Rev. Lett.* **102**, 107602. (doi:10.1103/PhysRevLett.102.107602)

33 Son, W.-J., Cho, E., Lee, B., Lee, J. & Han, S. 2009 Density and spatial distribution of charge carriers in the intrinsic *n*-type $LaAlO_3$–$SrTiO_3$ interface. *Phys. Rev. B* **79**, 245411. (doi:10.1103/PhysRevB.79.245411)

34 Pauli, S. A. *et al.* 2011 Evolution of the interfacial structure of $LaAlO_3$ on $SrTiO_3$. *Phys. Rev. Lett.* **106**, 036101. (doi:10.1103/PhysRevLett.106.036101)

35 Nakagawa, N., Hwang, H. Y. & Muller, D. A. 2006 Why some interfaces cannot be sharp. *Nat. Mater.* **5**, 204–209. (doi:10.1038/nmat1569)

36 Pavlenko, N. & Kopp, T. 2004 Structural relaxation and metal-insulator transition at the interface between $SrTiO_3$ and $LaAlO_3$. *Surf. Sci.* **605**, 1114–1121. (doi:10.1016/j.susc.2011.03.016)

37 Huijben, M., Rijnders, G., Blank, D. H. A., Bals, S., Van Aert, S., Verbeeck, J., Van Tendeloo, G., Brinkman, A. & Hilgenkamp, H. 2006 Electronically coupled complementary interfaces between perovskite band insulators. *Nat. Mater.* **5**, 556–560. (doi:10.1038/nmat1675)

38 Padilla, J. & Vanderbilt, D. 1998 *Ab initio* study of $SrTiO_3$ surfaces. *Surf. Sci.* **418**, 64–70. (doi:10.1016/S0039-6028(98)00670-0)

39 Kimura, S., Yamauchi, J., Tsukada, M. & Watanabe, S. 1995 First-principles study on electronic structure of the (001) surface of $SrTiO_3$. *Phys. Rev. B* **51**, 11 049–11 054. (doi:10.1103/PhysRevB.51.11049)

40 Takizawa, M., Tsuda, S., Susaki, T., Hwang, H. Y. & Fujimori, A. 2011 Electronic charges and electric potential at $LaAlO_3/SrTiO_3$ interfaces studied by core-level photoemission spectroscopy. *Phys. Rev. B* **84**, 245124. (doi:10.1103/PhysRevB.84.245124)

41 Chen, H., Kolpak, A. M. & Ismail-Beigi, S. 2009 Fundamental asymmetry in interfacial electronic reconstruction between insulating oxides: an *ab initio* study. *Phys. Rev. B* **79**, 161402. (doi:10.1103/PhysRevB.79.161402)

42 Zhang, L., Zhou, X. F., Wang, H. T., Xu, J. J., Li, J., Wang, E. G. & Wei, S. H. 2010 Origin of insulating behavior of the *p*-type $LaAlO_3/SrTiO_3$ interface: polarization-induced asymmetric distribution of oxygen vacancies. *Phys. Rev. B* **82**, 125412. (doi:10.1103/PhysRevB.82.125412)

43 Li, Y., Na Phattalung, S., Limpijumnong, S., Kim, J. & Yu, J. 2009 Formation of oxygen vacancies and charge carriers induced in the *n*-type interface of a $LaAlO_3$ overlayer on $SrTiO_3$(001) *Phys. Rev. B* **84**, 245307. (doi:10.1103/PhysRevB.84.245307)

44 Pavlenko, N., Kopp, T., Tsymbal, E. Y., Sawatzky, G. A. & Mannhart, J. 2012 Magnetic and superconducting phases at the $LaAlO_3/SrTiO_3$ interface: the Ti 3d interface electrons. *Phys. Rev. B* **85**, 020407. (doi:10.1103/PhysRevB.85.020407)

45 Perdew, J. P., Burke, K. & Ernzerhof, M. 1996 Generalized gradient approximation made simple. *Phys. Rev. Lett.* **77**, 3865–3868. (doi:10.1103/PhysRevLett.77.3865)

46 Jany, R. *et al.* 2010 Diodes with breakdown voltages enhanced by the metal-insulator transition of $LaAlO_3$–$SrTiO_3$ interfaces. *Appl. Phys. Lett.* **96**, 183504. (doi:10.1063/1.3428433)

47 Singh-Bhalla, G., Bell, C., Ravichandran, J., Siemons, W., Hikita, Y., Salahuddin, S., Hebard, A. F., Hwang, H. Y. & Ramesh, R. 2011 Built-in and induced polarization across $LaAlO_3/SrTiO_3$ heterojunctions. *Nat. Phys.* **7**, 80–86. (doi:10.1038/NPHYS1814)

48 Campbell, C. T. 1997 Ultrathin metal films and particles on oxide surfaces: structural, electronic and chemisorptive properties. *Surf. Sci. Rep.* **27**, 1–111. (doi:10.1016/S0167-5729(96)00011-8)

49 Goniakowski, J. & Noguera, C. 2004 Electronic states and Schottky barrier height at metal/MgO(100) interfaces. *Interf. Sci.* **12**, 93–103. (doi:10.1023/B:INTS.0000012298.34540.50)

50 Duan, C. G., Jaswal, S. S. & Tsymbal, E. Y. 2006 Predicted magnetoelectric effect in Fe/$BaTiO_3$ multilayers: ferroelectric control of magnetism. *Phys. Rev. Lett.* **97**, 047201. (doi:10.1103/PhysRevLett.97.047201)

51 Fu, Q. & Wagner, T. 2007 Interaction of nanostructured metal overlayers with oxide surfaces. *Surf. Sci. Rep.* **62**, 431–498. (doi:10.1016/j.surfrep.2007.07.001)

52 Fechner, M., Maznichenko, I. V., Ostanin, S., Ernst, A., Henk, J., Bruno, P. & Mertig, I. 2008 Magnetic phase transition in two-phase multiferroics predicted from first principles. *Phys. Rev. B* **78**, 212406. (doi:10.1103/PhysRevB.78.212406)

53 Arras, R., Ruiz, V. G., Pickett, W. E. & Pentcheva, R. 2012 Tuning the two-dimensional electron gas at the $LaAlO_3/SrTiO_3$(001) interface by metallic contacts. *Phys. Rev. B* **85**, 125404. (doi:10.1103/PhysRevB.85.125404)

54 Blaha, P., Schwarz, K., Madsen, G., Kvasnicka, D. & Luitz, J. 2001 *WIEN2k, an augmented plane wave plus local orbitals program for calculating crystal properties*. Technische Universität Wien, Austria: Karlheinz Schwarz.

55 Anisimov, V. I., Solovyev, I. V., Korotin, M. A., Czyżyk, M. T. & Sawatzky, G. A. 1993 Density-functional theory and NiO photoemission spectra. *Phys. Rev. B* **48**, 16 929–16 934. (doi:10.1103/PhysRevB.48.16929)

56 Asthagiri, A. & Sholl, D. S. 2006 Pt thin films on the polar $LaAlO_3$(100) surface: a first-principles study. *Phys. Rev. B* **73**, 125432. (doi:10.1103/PhysRevB.73.125432)

57 Asthagiri, A. & Scholl, D. S. 2002 First principles study of Pt adhesion and growth on SrO- and TiO_2-terminated $SrTiO_3$(100). *J. Chem. Phys.* **116**, 9914–9925. (doi:10.1063/1.1476322)

58 Ochs, T., Köstlmeier, S. & Elsässer, C. 2001 Microscopic structure and bonding at the Pd/$SrTiO_3$ (001) interface an ab-initio local-density-functional study. *Integr. Ferroelectr.* **32**, 267–278. (doi:10.1080/10584580108215697)

59 Oleinik, I. I., Tsymbal, E. Y. & Pettifor, D. G. 2001 Atomic and electronic structure of Co/$SrTiO_3$/Co magnetic tunnel junctions. *Phys. Rev. B* **65**, 020401. (doi:10.1103/PhysRevB.65.020401)

60 Okamoto, S., Millis, A. J. & Spaldin, N. A. 2006 Lattice relaxation in oxide heterostructures: $LaTiO_3/SrTiO_3$ superlattices. *Phys. Rev. Lett.* **97**, 056802. (doi:10.1103/PhysRevLett.97.056802)

61 Pentcheva, R. & Pickett, W. E. 2008 Ionic relaxation contribution to the electronic reconstruction at the *n*-type $LaAlO_3/SrTiO_3$ interface. *Phys. Rev. B* **78**, 205106. (doi:10.1103/PhysRevB.78.205106)

62 Stengel, M., Vanderbilt, D. & Spaldin, N. A. 2009 Enhancement of ferroelectricity at metal-oxide interfaces. *Nat. Mater.* **8**, 392–397. (doi:10.1038/NMAT2429)

63 Pentcheva, R. & Pickett, W. E. 2006 Charge localization or itineracy at $LaAlO_3/SrTiO_3$ interfaces: hole polarons, oxygen vacancies, and mobile electrons. *Phys. Rev. B* **74**, 035112. (doi:10.1103/PhysRevB.74.035112)

64 Zhong, Z. & Kelly, P. 2008 Electronic-structure-induced reconstruction and magnetic ordering at the $LaAlO_3/SrTiO_3$ interface. *Europhys. Lett.* **84**, 27001. (doi:10.1209/0295-5075/84/27001)

65 Goss Levi, B. 2007 Interface between nonmagnetic insulators may be ferromagnetic and conducting. *Phys. Today* **60**, 23. (doi:10.1063/1.2754590)

66 Seri, S. & Klein, L. 2009 Antisymmetric magnetoresistance of the $SrTiO_3/LaAlO_3$ interface. *Phys. Rev. B* **80**, 180410. (doi:10.1103/PhysRevB.80.180410)

67 Ariando *et al.* 2011 Electronic phase separation at the $LaAlO_3/SrTiO_3$ interface. *Nature Commun.* **2**, 188. (doi:10.1038/ncomms1192)

68 Caviglia, A. D. *et al.* 2008 Electric field control of the $LaAlO_3/SrTiO_3$ interface ground state. *Nature* **456**, 624–627. (doi:10.1038/nature07576)

69 Ben Shalom, M., Sachs, M., Rakhmilevitch, D., Palevski, A. & Dagan, Y. 2010 Tuning spin-orbit coupling and superconductivity at the $SrTiO_3/LaAlO_3$ interface: a magnetotransport study. *Phys. Rev. Lett.* **104**, 126802. (doi:10.1103/PhysRevLett.104.126802)

70 Kim, M., Bell, C., Kozuka, Y., Kurita, M., Hikita, Y. & Hwang, H. Y. 2011 Fermi surface and superconductivity in low-density high-mobility δ-doped $SrTiO_3$. *Phys. Rev. Lett.* **107**, 106801. (doi:10.1103/PhysRevLett.107.106801)

71 Gariglio, S. & Triscone, J. M. 2011 Oxide interface superconductivity. *C. R. Phys.* **12**, 591–599. (doi:10.1016/j.crhy.2011.03.006)

72 Sarrao, J. L. *et al.* 2002 Plutonium-based superconductivity with a transition temperature above 18 K. *Nature* **420**, 297–299. (doi:10.1038/nature01212)

73 Bernhard, C. 1999 Coexistence of ferromagnetism and superconductivity in the hybrid ruthenate-cuprate compound $RuSr_2GdCu_2O_8$ studied by muon spin rotation and DC magnetization. *Phys. Rev. B* **59**, 14099–14107. (doi:10.1103/PhysRevB.59.14099)

74 Aoki, D., Hardy, F., Miyake, A., Taufour, V., Matsuda, T. D. & Flouquet, J. 2011 Properties of ferromagnetic superconductors. *C. R. Phys.* **12**, 573–583. (doi:10.1016/j.crhy.2011.04.007)

75 Pickett, W. E., Weht, R. & Shick, A. B. 1999 Superconductivity in ferromagnetic $RuSr_2GdCu_2O_8$. *Phys. Rev. Lett.* **83**, 3713–3716. (doi:10.1103/PhysRevLett.83.3713)

76 Michaeli, K., Potter, A. C. & Lee, P. A. 2012 Superconductivity and ferromagnetism in oxide interface structures: possibility of finite momentum pairing. *Phys. Rev. Lett.* **108**, 117003. (doi:10.1103/PhysRevLett.108.117003)

77 Stephanos, C., Kopp, T., Mannhart, J. & Hirschfeld, P. J. 2011 Interface-induced d-wave pairing. *Phys. Rev. B* **84**, 100510. (doi:10.1103/PhysRevB.84.100510)

78 Fulde, P. & Ferrell, R. A. 1964 Superconductivity in a strong spin-exchange field. *Phys. Rev.* **135**, A550–A563. (doi:10.1103/PhysRev.135.A550)

79 Larkin, A. I. & Ovchinnikov, Y. N. 1964 *Zh. Eksp. Teor. Fiz*, **47**, 1136–1146.

80 Fix, T., Schoofs, F., MacManus-Driscoll, J. L. & Blamire, M.G. 2009 Charge confinement and doping at $LaAlO_3/SrTiO_3$ interfaces. *Phys. Rev. Lett.* **103**, 166802. (doi:10.1103/PhysRevLett.103.166802)

Bibliography

[1] R. M. Cornell and U. Schwertmann. *The Iron Oxides: Structure, Properties, Reactions, Occurrences and Uses*. Wiley-VCH GmBH & Co. KGaA, Weinheim, 2003.

[2] Q. Williams and L. Guenther. *Solid State Commun.*, **100**:105, 1996.

[3] A.E. Gleason, R. Jeanloz, and M. Kunz. *Am. Mineral.*, **93**:1882, 2008.

[4] L. Carlson, J.M. Bigham, U. Schwertmann, A. Kyek, and F. Wagner. *Environ. Sci. Technol.*, **36**:1712–1719, 2002.

[5] L. Mazeina and A. Navrotsky. *Chem. Mater.*, **19**:825–833, 2007.

[6] A. Navrotsky, L. Mazeina, and J. Majzlan. *Science*, **319**:1635–1638, 2008.

[7] G.E. Brown Jr., V.E. Henrich, W.H. Casey, D.L. Clark, C. Eggleston, A. Felmy, D.W. Goodman, M. Gratzel, G. Maciel, M.I. McCarthy, K.H. Nealson, D.A. Sverjensky, M.F. Toney, and J.M Zachara. *Chem. Rev.*, **99**:77, 1999.

[8] D.M. Sherman and S.R. Randall. *Geochim. et Cosmochim. Acta*, **67**:4223, 2003.

[9] B.A. Manning, J.R. Kiser, H. Kwon, and S.R. Kanel. *Environ. Sci. Technol.*, **41**:586, 2007.

[10] U. Schwertmann. *NATO ASI Ser.*, **217**:267–302, 1988.

[11] C. Laberty and A. Navrotsky. *Geochim. et Cosmochim. Acta*, **62**:2905, 1998.

[12] M. Pernet, J. Chenavas, and J.C. Joubert. *Solid State Commun.*, **13**:1147, 1973.

[13] R. Voigt and G. Will. *Neues Jahrb. Mineral. Abh.*, **2**:89, 1981.

[14] J.-F. Lin, V.V. Struzhkin, S.D. Jacobsen, M.Y. Hu, P. Chow, J. Kung, H. Liu, H.-k. Mao, and R.J. Hemley. *Nature*, **436**:377–380, 2005.

[15] K. Reuter and M. Scheffler. *Phys. Rev. B*, **65**:035406, 2001.

[16] J. Majzlan, L. Mazeina, and A. Navrotsky. *Geochim. et Cosmochim. Acta*, **71**: 615–623, 2007.

[17] L. Mazeina, S. Deore, and A. Navrotsky. *Chem. Mater.*, **18**:1830, 2006.

[18] P.R. Grossl, M. Eick, D.L. Sparks, S. Goldberg, and C.C. Ainsworth. *Environ. Sci. Technol.*, **31**:321–326, 1997.

[19] G.A. Waychunas, B.A. Rea, C.C. Fuller, and J.A. Davis. *Geochim. et Cosmochim. Acta*, **1993**:2251–2269, 1993.

[20] G.A. Waychunas, J.A. Davis, and C.C. Fuller. *Geochim. et Cosmochim. Acta*, **59**:3655–3661, 1995.

[21] X. Sun and H.E. Doner. *Soil Science*, **161**:865—872, 1996.

[22] A. Jain, K.P. Raven, and R.H. Loeppert. *Environ. Sci. Technol.*, **33**:1179–1184, 1999.

[23] G. Waychunas, T. Trainor, P. Eng, J. Catalano, G. Brown, J. Davis, J. Rogers, and J. Bargar. *Anal. Bioanal. Chem.*, **383**:12–27, 2005.

[24] S. Fendorf, M.J. Eick, P. Grossl, and D.L. Sparks. *Environ. Sci. Technol.*, **31**: 315–320, 1997.

[25] G. Ona-Nguema, G. Morin, F. Juillot, G. Calas, and G.E. Brown Jr. *Environ. Sci. Technol.*, **39**:9147–9155, 2005.

[26] S. Graeser, H. Schwander, F. Demartin, C.M. Gramacciolli, T. Pilati, and E. Reusser. *Am. Mineral.*, **79**:996–1002, 1994.

[27] M.A. Cooper and F.C. Hawthorne. *Can. Mineral.*, **34**:79–89, 1996.

[28] F.C. Hawthorne. *Can. Mineral.*, **23**:675–679, 1985.

[29] A. Manceau. *Geochim. et Cosmochim. Acta*, **59**:3647–3653, 1995.

[30] Y. Arai, D.L. Sparks, and J.A. Davis. *Environ. Sci. Technol.*, **38**:817–824, 2004.

[31] J.S. Loring, M.H. Sandström, K. Norén, and P. Persson. *Chem. Eur. J.*, **15**: 5063–5072, 2009. doi: 10.1002/chem.200900284.

[32] A. Ohtomo and H.Y. Hwang. *Nature*, **427**:423, 2004.

[33] N. Reyren, S. Thiel, A. D. Caviglia, L. Fitting Kourkoutis, G. Hammerl, C. Richter, C. W. Schneider, T. Kopp, A.-S. Rüetschi, D. Jaccard, M. Gabay, D. A. Muller, J.-M. Triscone, and J. Mannhart. Superconducting interfaces between insulating oxides. 317(5842):1196–1199, 2007.

[34] A. Brinkman and *et al. Nature Mater.*, **6**:493, 2007.

[35] J.A. Bert, B. Kalisky, C. Bell, M. Kim, Y Hikita, H.Y. Hwang, and K.A. Moler. *Nature Physics*, **7**:767–771, 2011.

[36] D.A Dikin, M. Mehta, C.W. Bark, C.M. Folkman, C.B. Eom, and V. Chandrasekhar. *Phys. Rev. Lett.*, **107**:056802, 2011.

[37] L. Li, C. Richter, J. Mannhart, and R. C. Ashoori. *Nature Physics*, **7**:762–766, 2011.

[38] S. Thiel, G. Hammerl, A. Schmehl, C.W. Schneider, and J. Mannhart. *Science*, **212**:1942, 2006.

[39] R. Pentcheva and W.E. Pickett. *Phys. Rev. Lett.*, **102**:107602.

[40] M. Huijben, G. Rijnders, D.H. Blank, S. Bals, S. Van Aert, J. Verbeeck, G. Van Tendeloo, A. Brinkman, and H. Hilgenkamp. *Nat. Materials*, **5**:556, 2006.

[41] R. Pentcheva, M. Hujben, K. Otte, W.E. Pickett, J.E. Kleibeuker, J. Huijben, H. Boschker, D. Kockmann, W. Siemons, G. Koster, H.J.W. Zandvliet, G. Rijnders, D.H.A. Blank, H. Hilgenkamp, and A. Brinkman. *Phys. Rev. Lett.*, **104**: 166804, 2010.

[42] P. Blaha, K. Schwarz, G.K.H. Madsen, D. Kvasnicka, and J. Luitz. *WIEN2k, An Augmented Plane Wave + Local Orbitals Program for Calculating Crystal Properties*. Karlheinz Schwarz, Techn. Univ. Wien, Austria, 2001.

[43] G. Kresse and J. Hafner. *Phys. Rev. B*, 47:558, 1993.

[44] G. Kresse and J. Hafner. *Phys. Rev. B*, 49:14251, 1994.

[45] G. Kresse and J. Hafner. *J. Phys.: Condens. Matter*, 6:8245, 1994.

[46] G. Kresse and J. Furthmüller. *Comput. Mat. Sci.*, 6:15, 1996.

[47] G. Kresse and J. Furthmüller. *Phys. Rev. B*, 54:11169, 1996.

[48] E. Kaxiras, Y. Pandey, K.C.and Bar-Yam, and J.D. Joannopoulos. *Phys. Rev. Lett.*, **56**:2819, 1986.

[49] E. Kaxiras, Y. Pandey, K.C.and Bar-Yam, and J.D. Joannopoulos. *Phys. Rev. B*, **35**:9625, 1987.

[50] G.-X. Qian, R.M. Martin, and D.J. Chadi. *Phys. Rev. B*, **38**:7649, 1988.

[51] B. Meyer. *Phys. Rev. B*, **69**:045416, 2004.

[52] P. Hohenberg and W. Kohn. *Phys. Rev. B*, **136**:864–871, 1964.

[53] W. Kohn and L. J. Sham. *Phys. Rev. A*, **144**:864–871, 1965.

[54] T. C. Leung, C. T. Chan, and B. N. Harmon. *Phys. Rev. B*, **44**:2923–2927, 1991.

[55] R. M. Martin. *Electronic Structure: Basic Theory and Practical Methods*. Cambridge University Press, 2008.

[56] A. D. Becke. *Phys. Rev. A*, **38**:3098–3100, 1988.

[57] J. P. Perdew and Y. Wang. *Phys. Rev. B*, **45**:13244–13249, 1992.

[58] Perdew J. P., K. Burke, and M. Ernzerhof. *Phys. Rev. Lett.*, **77**:3865–3868, 1990.

[59] V. I. Anisimov, I. V. Solovyev, and M. A. Korotin. *Phys. Rev. B*, **48**:16929, 1993.

[60] A. I. Liechtenstein, V. I. Anisimov, and J. Zaanen. *Phys. Rev. B*, **52**:R5467, 1995.

[61] E. K. Andersen. *Phys. Rev. B*, **12**:3060, 1975.

[62] D.D. Koelling and G.O. Arbman. *J. Phys. F: Met. Phys*, **5**:2041, 1975.

[63] M. Weinert, E. Wimmer, and A. J. Freeman. *Phys. Rev. B*, **26**:4571–4578, 1982.

[64] L. F. Mattheiss and D. R. Hamann. *Phys. Rev. B*, **33**:823–840, 1986.

[65] P. Blaha, Schwarz. K., P. Sorantin, and S. B. Trickey. *Computer Phys. Commun.*, **59(3)**:399, 1990.

[66] M. Weinert. *J. Math. Phys.*, **22**:2433, 1981.

[67] V.I. Anisimov, I.V. Solovyev, M. A. Korotin, M. T. Cryzyk, and G. A. Sawatzky. *Phys. Rev. B*, **48**:16929, 1993.

[68] M. T. Cryzyk and G. A. Sawatzky. *Phys. Rev. B*, **49**:14211, 1994.

[69] G. Lehmann, P. Rennert, M. Taut, and H. Wonn. *Phys. Status Solidi*, **37**:K27, 1970.

[70] G. Lehmann, J. T. Waber, and D. T. Cromer. *Phys. Status Solidi*, **54**:469, 1972.

[71] O. Jepsen and O. K. Andersen. *Solid State Commun.*, **9**:1763, 1971.

[72] G. Gilat. *J. Comp. Phys.*, **10**:432, 1072.

[73] J. Rath and A. J. Freeman. *Phys. Rev. B*, **11**:2109, 1975.

[74] A. Baldereschi. *Phys. Rev. B*, **7**:5212, 1973.

[75] D. J. Chadi and M. L. Cohen. *Phys. Rev. B*, **8**:5747, 1973.

[76] H. J. Monkhorst and J. D. Pack. *Phys. Rev. B*, **13**:5188, 1976.

[77] G. W. Pratt. *Phys. Rev.*, **88**:1217, 1952.

[78] D. Singh, H. Karkauer, and C.-S. Wang. *Phys. Rev. B*, **34**:8391, 1986.

[79] P.E. Blöchl. *Phys. Rev. B*, 50:17953, 1994.

[80] B. Liu. *Report on Workshop "Numerical Algorithms in Chemistry: Algebraic Methods"*, :49, 1978.

[81] E.R. Davidson. *NATO Advanced Study Institute, Series C*, **113**:95, 1983.

[82] M.P. Teter, M.C. Payne, and D.C. Allan. *Phys. Rev. B*, **40**:12255, 1989.

[83] D.M. Bylander, L. Kleinman, and S. Lee. *Phys. Rev. B*, **42**:1394, 1990.

[84] G. Kresse, M. Marsman, and J. Furthmüller. Vasp the guide. 2012. URL `http://cms.mpi.univie.ac.at/VASP/`.

[85] F.D. Murnaghan. *Proc. Nat. Acad. Sci.*, **30**:244–247, 1944.

[86] D. M. Teter, G. V. Gibbs, M. B. Boisen Jr., D. C. Allen, and M. P. Teter. *Phys. Rev. B*, **52**:8064–8073, 1995.

[87] F. Birch. *Phys. Rev.*, **71**:809–824, 1947.

List of Publications

FeOOH polymorphs:

- *Pressure Induced Structural and Electronic Transitions in FeOOH from First Principles*, K. Otte, R. Pentcheva, W.W. Schmahl, and J.R. Rustad, Physical Review B **80**, 205116 (2009).
- *Density Functional Theory Study of Water Adsorption on FeOOH Surfaces*, K. Otte, W.W. Schmahl, and R. Pentcheva, Surface Science **606**, 1623 (2012).
- *DFT+U Study of Arsenate Adsorption on FeOOH Surfaces: Evidence for Competing Binding Mechanisms*, K. Otte, W.W. Schmahl, and R. Pentcheva, Journal of Physical Chemistry C, submitted.

$LaAlO_3/SrTiO_3$ interfaces:

- *Parallel Electron-Hole Bilayer Conductivity from Electronic Interface Reconstruction*, R. Pentcheva, M. Huijben, K. Otte, W. E. Pickett, J. E. Kleibeuker, J. Huijben, H. Boschker, D. Kockmann, W. Siemons, G. Koster, H. J. W. Zandvliet, G. Rijnders, D. H. A. Blank, H. Hilgenkamp, and A. Brinkman, Physical Review Letters **104**, 166804 (2010).
- *Termination Control of Electronic Phases in Oxide Thin Films and Interfaces: $LaAlO_3/SrTiO_3(001)$*, R. Pentcheva, R. Arras, K. Otte, V.Ruiz, and W. E. Pickett, Philosophical Transactions of the Royal Society A **370**, 4904-4926 (2012).

Danksagung

An diser Stelle möchte ich mich ganz herzlich bei meiner Betreuerin PD Dr. Rossitza Pentcheva dafür bedanken, dass ich in ihrer Arbeitsgruppe "Computational Materials Science" diese Arbeit anfertigen konnte. Ihre kontinuierliche Förderung und Unterstützung waren für den Fortschritt meiner Arbeit von unschätzbarem Wert. Zahlreiche Anregungen haben die Arbeit immer wieder vorangetrieben und mich neu motiviert.

Herrn Prof. Dr. Wolfgang Schmahl danke ich für die Übernahme der Rolle als Zweitgutachter und sein Interesse an meiner Arbeit.

Ein Großteil der Rechnungen wurde am Leibniz Rechenzentrum (LRZ) durchgeführt, und an dieser Stelle möchte ich an die Mitarbeiter ein großes Dankeschön aussprechen für die durchweg freundliche und bereitwillige Unterstützung.

Prof. Warren Pickett (UC Davis, Kalifornien) danke ich für zahlreiche Diskussionen während meines Forschungsaufenthaltes an der UC Davis und die Zusammenarbeit bei der Untersuchung der Perowskit Grenzflächen.

Finanzielle Unterstützung, ohne die diese Arbeit nicht möglich gewesen wäre, habe ich durch das SURFTRAP-Projekt (BMBF) und vom Elitenetzwerk Bayern erhalten. Weiterhin möchte ich hier das LMU Mentoring Programm GeoSciences und das International Center of Materials Research (ICMR) erwähnen.

Meinen Kollegen/innen, insbesondere Carmen Quiroga, Dr. Narasimham Mulakaluri, Dr. Melanie Kaliwoda, Dr. Ariadna Blanca Romero, David Doennig, Maria Wieland, Victor Ruiz López, Ulf-Niklas Berninger, Dr. Maike Lübbe, Dr. Casjen Merkel und Dr. Hasan Sadat Nabi, danke ich für die freundschaftliche Arbeitsatmosphäre, ihre Hilfsbereitschaft und auch für nicht wissenschaftliche Gespräche.

Besonders dankbar bin ich all den lieben und mir liebsten Personen aus meinem privaten Umfeld, die mich während der Zeit, in der ich diese Arbeit angefertigt habe, immer bedingungslos untertützt haben. Ihr habt Euch mit mir gefreut und mit mir gelitten. Euer Zuspruch, Eure Geduld und Euer Glaube an mich haben mir immer Rückhalt gegeben. Vielen Dank.